UNIVERSITY OF OKLAHOMA

GRADUATE COLLEGE

QUANTIFYING UNCERTAINTIES IN GLOBAL AND NORTH AMERICAN REGIONAL CLIMATE CHANGE PROJECTIONS USING A MULTI-THOUSAND MEMBER GLOBAL CLIMATE MODEL PERTURBED PHYSICS ENSEMBLE

A DISSERTATION

SUBMITTED TO THE GRADUATE FACULTY

in partial fulfillment of the requirements for the

Degree of

DOCTOR OF PHILOSOPHY

By

DEREK HAROLD ROSENDAHL
Norman, Oklahoma
2013

Downloaded from SHAREOK. Persistent Handle URL: https://hdl.handle.net/11244/7890

QUANTIFYING UNCERTAINTIES IN GLOBAL AND NORTH AMERICAN REGIONAL CLIMATE CHANGE PROJECTIONS USING A MULTI-THOUSAND MEMBER GLOBAL CLIMATE MODEL PERTURBED PHYSICS ENSEMBLE

A DISSERTATION APPROVED FOR THE
SCHOOL OF METEOROLOGY

BY

_____
Dr. Susan Postawko, Chair

_____
Dr. David Karoly, Co-Chair

_____
Dr. Berrien Moore III

_____
Dr. Mark Morrissey

_____
Dr. William Hooke

_____
Dr. Yiqi Luo

© Copyright by DEREK HAROLD ROSENDAHL 2013
All Rights Reserved.

ACKNOWLEDGMENTS

I would like to acknowledge those who have helped make the completion of this dissertation possible. I would first like to thank my research advisor David Karoly for providing me this opportunity and for his mentoring and research guidance. I would also like to thank Susan Postawko for her assistance and my other doctoral committee members: Berrien Moore, Mark Morrissey, William Hooke, and Yiqi Luo.

I would also like to thank the Climate*prediction*.net team based at the University of Oxford: particularly Myles Allen, Milo Thurston, Dan Rowlands, Hiro Yamazaki, Jonathan Miller, and William Ingram. Frank Drost also provided beneficial support throughout the early stages of this project.

Funding for this research was supported by the National Science Foundation's Division of Atmospheric Sciences under award number ATM-0111234. Funding also was provided by the U.S. Department of Interior's South Central Climate Science Center and I am grateful for all of their encouragement and support.

I would like to thank Research Computing Services at the University of Oklahoma (OU) for computing assistance, particularly the help provided by Kyle Keys.

Thanks also go to the OU School of Meteorology faculty and staff: especially Marcia Pallutto, Celia Jones, Nancy Campbell, and Becky Steely.

I also must thank Alan Czarnetzki, my advisor and mentor at the University of Northern Iowa, who early on inspired me to pursue a career in meteorology.

I also would like to thank all of my family for their love and support, especially my grandparents, Mert and Elsie Rosendahl and Galin and Wilma Barth, as well as my siblings, Kari (and husband Roger), Jodi, and Todd. A special thanks also to my many supportive aunts and uncles, Wally and Merlene, Phyl, Marc and Kathy, Gary and Chris, Jerry and Jackie, Ken and Bette, my Godparents Don and DiAnn and Wayne and Arletta, and the many others in my extended family.

My father- and mother-in-law, Bob and Marcia Thornburg, have given constant love and support and I am very thankful to have them in my life. With me living so far away from my own family they have always done everything they could to make sure I knew that I had family close by, which I have sincerely appreciated.

My parents, Harold and Marlys Rosendahl, have completely supported me in everything I have done and have taught me more than they could ever know. They instilled in me a strong sense of self-discipline and the desire to work hard in everything I do. Growing up, my parents constantly encouraged me to believe there was nothing I could not accomplish if I set my mind to it. They always believed in me, even in those times when I may have doubted myself. It is for these reasons and so many more that I have become the person I am today. I am forever grateful for the life lessons they taught me, which could never have been taught in a classroom or found in a textbook.

And to the most important person in my life, my wonderful and beautiful wife Becca, I am continually amazed at your love, patience and kindness. You have been by my side every step of the way and I truly am blessed to have you in my life. Your encouragement and support has been unsurpassed. I love you so much.

Finally, I thank God for guiding me through life's many crossroads to bring me to where I am today.

TABLE OF CONTENTS

LIST OF TABLES ..... **X**

LIST OF FIGURES ..... **XIV**

ABSTRACT ..... **XXIV**

CHAPTER 1: INTRODUCTION **1**

CHAPTER 2: CLIMATE MODELING OVERVIEW **20**

2.1 CLIMATE MODEL HIERARCHY 20
2.1.1 Lower Complexity Models *21*
2.1.2 Earth Models of Intermediate Complexity (EMIC) *21*
2.1.3 Global Climate Models (GCMs) *22*
2.1.4 Regional Downscaled Models *24*
2.2 MODEL UNCERTAINTY IN FUTURE PROJECTIONS 25
2.2.1 Internal Variability Uncertainty *26*
2.2.2 External Forcing Uncertainty *29*
2.2.3 Model Uncertainty *31*
2.3 MULTI-MODEL ENSEMBLES 32
2.4 PERTURBED PHYSICS ENSEMBLES 35

CHAPTER 3: CLIMATE*PREDICTION*.NET CLIMATE MODEL AND EXPERIMENT DESIGN **42**

3.1 CLIMATE*PREDICTION*.NET 42
3.1.1 CPDN Project Design *42*
3.1.2 Overview of CPDN Experiments *44*
3.2 HADCM3L MODEL DESIGN 46
3.2.1 Atmospheric Model *49*
3.2.2 Ocean Model *54*
3.3 BBC CLIMATE CHANGE EXPERIMENT 59
3.3.1 Physics Parameter Perturbations *60*
3.3.2 Atmosphere-Ocean Coupling and Flux Adjustments *75*
3.3.3 Control and Transient Simulations *77*
3.3.4 Model Output *80*

CHAPTER 4: OBSERVATIONAL DATA SETS **83**

4.1 TEMPERATURE 83
4.1.1 HadCRUT3 ..... *83*
4.1.2 NOAA-MLOST *85*
4.1.3 NASA-GISTEMP *86*
4.2 PRECIPITATION RATE 86
4.2.1 GPCP *87*
4.2.2 NOAA-PREC *87*
4.3 NORTH AMERICAN REGIONAL REANALYSIS (NARR) 88

CHAPTER 5: CONTROL SIMULATION ANALYSIS 90

5.1 QUALITY CONTROL OF CONTROL SIMULATION ENSEMBLE 91
5.1.1 NetCDF File Errors *91*
5.1.2 Erroneous Outliers *92*
5.1.3 Duplicates *96*
5.1.4 Final Ensemble *104*
5.2 MODEL DRIFT 108
5.2.1 Drift Due to Initial Model Coupling Adjustment *108*
5.3 MEAN 116
5.3.1 Annual Mean *116*
5.3.2 Seasonal Means *125*
5.4 SEASONAL CYCLE 127
5.4.1. Mean Seasonal Cycle *128*
5.4.2 Magnitude of the Seasonal Cycle (JJA-DJF) *131*
5.5 VARIABILITY 132
5.5.1 Interannual Variability *133*
5.5.2 Monthly Interannual Variability *137*
5.6 REGIONAL AND VARIABLE RELATIONSHIPS 140
5.6.1 Temperature and Precipitation Relationships within the same Regions *140*
5.6.2 Relationships between Regions *145*
5.6.3 NAO and ENSO Teleconnections *148*
5.7 SENSITIVITY TO PHYSICAL PARAMETER VALUES 157
5.7.1 Mean, Variability, and Seasonal Cycle *157*
5.7.2 Long-term Mean Drift *167*
5.8 INITIAL CONDITIONS UNCERTAINTY 170
5.9 SUMMARY 174

CHAPTER 6: NORTH AMERICAN PALEOCLIMATE COMPARISON 177

6.1 PROXY DATA SOURCES 178
6.1.1 Tree Rings *178*
6.1.2 Varved Lake and Ocean Sediments *184*
6.2 PALEOCLIMATE RECONSTRUCTION METHOD 186
6.3 NORTH AMERICAN PALEOCLIMATE RECONSTRUCTIONS 190
6.4 PALEOCLIMATE VARIABILITY COMPARED TO CPDN AND OBSERVATIONS 195
6.5 SUMMARY 200

CHAPTER 7: TRANSIENT SIMULATION ANALYSIS 202

7.1 QUALITY CONTROL OF TRANSIENT SIMULATION ENSEMBLE 203
7.1.1 NetCDF File Errors *203*
7.1.2 Erroneous Outliers *204*
7.1.3 Duplicates *206*
7.2 LONG-TERM MEAN DRIFT REMOVAL 207
7.3 TRANSIENT SIMULATIONS VS. OBSERVATIONS 218
7.3.1 Transient Observational Period Ensemble *218*

7.3.2 Transient Observational Period Trends *226*
7.4 TRANSIENT (PAST AND FUTURE) AND CONTROL TRENDS 229
7.5 TRANSIENT TREND RELATIONSHIPS 236
7.5.1 Global vs. Regional Trends (Same Time Period) *236*
7.5.2 Past Global Trends vs. Future Global and Regional Trends *238*
7.5.3 Past vs. Future Trends in Same Region *240*
7.6 CHANGES IN SEASONAL CYCLE AND VARIABILITY 242
7.7 SENSITIVITY TO PHYSICAL PARAMETER VALUES 245
7.7.1 Parameter Variations and Observational Period Trends *245*
7.7.2 Parameter Variations and Future Trends *250*
7.8 CONSTRAINED TRANSIENT ENSEMBLE 255
7.8.1 Constrained by 30 Year Global Temperature Trend *255*
7.8.2 Constrained by 70 Year Global Temperature Trend Performance *258*
7.8.3 Constrained by Parameters with Greatest Sensitivity (70yr Global Trends) *259*
7.8 SUMMARY 264

CHAPTER 8: CPDN VERSUS CMIP ENSEMBLES **267**

8.1 CONTROL SIMULATIONS (CPDN VS. CMIP5) 267
8.1.1 Mean *268*
8.1.2 Seasonal Cycle *272*
8.1.3 Variability *273*
8.2 TRANSIENT SIMULATIONS (CPDN VS. CMIP3 & CMIP5) 280
8.2.1 Historical Time Period *280*
8.2.2 Future Projections *285*
8.2.3 CMIP3 versus Constrained CPDN Ensembles *292*
8.3 SUMMARY 300

CHAPTER 9: CONCLUSIONS **306**

9.1 CONTROL ANALYSIS 306
9.2 TRANSIENT ANALYSIS 309
9.3 COMPARISON TO CMIP ENSEMBLES 312
9.4 BROAD IMPLICATIONS 315
9.5 FUTURE WORK 315

REFERENCES **318**

APPENDIX A: INFERRED TRANSIENT SIMULATION ENSEMBLE **338**

LIST OF TABLES

Table 3.1: Summary of key components in the HadCM3L model design. 48

Table 3.2: The σ-p hybrid vertical grid of Simmons and Burridge (1981) used to generate the HadCM3L atmospheric model's vertical structure. The hybrid coordinate (H) is calculated using the equation $H = (A/10^5 \text{ Pa}) + B$. (From Johns et al. (1997).) 50

Table 3.3: Vertical levels in the HadCM3L ocean model as well as background vertical diffusivity of tracers between a given level and the level directly above it. (From Johns et al. (1997).) 55

Table 3.4: CPDN perturbed parameters, associated parameterization schemes and perturbation values. Default parameter values are highlighted in bold. 61

Table 3.5: Empirically adjusted cloud fraction (EACF) parameter perturbation values, which vary with height. The EACF parameter perturbation value identifier is the average of all values across the 19 vertical layers in the atmosphere. 65

Table 3.6: Critical relative humidity (RHCRIT) parameter perturbation values, which vary with height. The RHCRIT parameter perturbation value identifier is the average of all values across the 19 vertical layers in the atmosphere. 71

Table 3.7: Boundaries used in the area-averaged monthly mean time series output for the CPDN North American regions. 81

Table 3.8: Model output variables available for the globe and over North America for the HadCM3L area-averaged monthly mean time series. 82

Table 4.1: Observational data sets and one reanalysis (i.e., NARR) used in this study. 89

Table 5.1: CPDN perturbed parameters and the number of control simulations out of 1,214 that have a particular parameter value. Atmosphere and ocean parameters are grouped separately and the initial condition parameter is given at the end. Default parameter values are highlighted in bold. 105

Table 5.2: The 95% range of control simulation 140 year trends in annual mean temperature (°C/century) and precipitation rate ((mm/day)/century) for the globe and NA regions. All three observational temperature data set trends are from 1921-2010 and precipitation rate trends are from 1981-2010 for GPCP and 1951-2010 for NOAA-PREC. Refer to Chapter 4 for further discussion of the observational data sets. 114

Table 5.3: Temperature (C) and precipitation rate (mm/day) correlations for a given region and time period. CPDN correlations are shaded and contain the mean and 2.5%-97.5% range of the distribution of correlations from each simulation (i.e., 140-year comparison) in brackets with observational data set correlations directly beneath them with their mean and minimum and maximum values from the correlation calculated within each data set in parentheses. Asterisks (*) mark the largest mean correlation magnitude for both CPDN and observations within each given season and yellow shading identifies the mean largest correlation magnitude for both CPDN and observations within each given region (both for NA regions only). ……..142

Table 5.4: Regional annual mean temperature (°C) correlations of annual means for CPDN gray shading; mean [2.5%, 97.5%]) and observations (second line, white; mean (min, max)). Yellow shading indicates a mean correlation magnitude ≥ 0.3. 147

Table 5.5: Same as Table 5.4 but for precipitation rate (mm/day). Global temperature correlations per region also are included. 147

Table 5.6: Regional temperature (°C) correlations of JJA means (upper-right) and DJF means (lower-left) for CPDN (shaded: mean [2.5%, 97.5%]) and observations (second line, white; mean (min, max)). Yellow shading indicates a mean correlation magnitude ≥ 0.3. 148

Table 5.7: Same as Table 5.6 but for precipitation rate (mm/day). Global temperature correlations per region also are included. 148

Table 5.8: Correlations between NAO and global and NA regional temperatures across seasons for 1,214 control simulations (shaded; mean[2.5%,97.5%]) and observations (directly beneath; mean[min,max]). Correlation magnitudes ≥0.3 are highlighted yellow. 152

Table 5.9: Same as Table 5.8 but for correlations between NAO and precipitation. 152

Table 5.10: Correlations between Niño 3.4 temperatures and global and NA regional temperatures across seasons for 1,214 control simulations (shaded; mean[2.5%,97.5%]) and observations (directly beneath; mean[min,max]). Correlation magnitudes ≥0.3 are highlighted yellow. 156

Table 5.11: Same as Table 5.10 but for correlations between Niño 3.4 temperatures and precipitation. 156

Table 5.12: Model physics parameters with correlation magnitude ≥ to 0.4 between their variations and climate indices over a defined region. The climate indice information is provided showing the variable of either temperature (T) or precipitation rate (P); the indice of either mean, interannual variability (Int Var), or magnitude of seasonal cycle (JJA-DJF); and the time period of either annual or one of the four seasons. Correlations are listed with magnitudes ≥ to 0.5 (yellow) and 0.7 (red) highlighted. Parameters are listed in order of generally higher sensitivity to lower. All correlations shown have $p<<0.00001$. 158

Table 5.13: Model physics parameters with correlation magnitude ≥ to 0.2 between their variations and climate long-term mean drift of temperature (Temp) or precipitation (Precip) over a defined region. Correlations with magnitudes greater than 0.4 are highlighted yellow. Parameters are listed in order of generally higher sensitivity to lower. All correlations shown have $p<<0.00001$. 168

Table 5.14: Ratios of initial condition uncertainty in 70-year control drift compared to the full range of 70 year drift for the 50% and 95% range. Larger ratio values indicate an increased influence of the initial conditions variations (i.e., internal variability) to the 70-year trends. 174

Table 6.1: Information for each proxy-based paleoclimate reconstruction shown in Figure 6.5. 191

Table 7.1: CPDN perturbed parameters and the number of transient simulations having each particular parameter value for the 1,692 transient simulations. Parameters are separated into their respective atmosphere, ocean, or initial condition groups. Default parameter values are highlighted in bold. 212

Table 7.2: Correlations between simulated global temperature trends and regional temperature and precipitation rate trends over the same time period for the 1,692 transient simulations. Correlations are provided for 70 year past (1941-2010) and future (2011-2080) trends and for 30 year past (1981-2010) and two future time period (2011-2050; 2051-2080) trends. Correlations with magnitude ≥ 0.6 (0.8) are highlighted in gray (yellow). All p-values are <<0.001. 237

Table 7.3: Correlations between simulated past global temperature trends and future regional temperature and precipitation rate trends and for the 1,692 transient simulations. Correlations are provided for 70 year past (1941-2010) global and future (2011-2080) regional trends and for 30 year past (1981-2010) global and two future time period (2011-2050; 2051-2080) regional trends. Correlations with magnitude ≥ 0.25 are highlighted in blue. All p-values are <<0.001 except for those denoted with a (*). 239

Table 7.4: Correlations between past and future trends within a given region for temperature and precipitation rate for the 1,692 transient simulations. The 70 year trends are compared between 1941-2010 and 2011-2080 and the 30 year trends are compared from the past time period 1981-2010 and future periods 2011-2040 and 2051-2080. Correlations ≥0.25 are highlighted in blue. All p-values are <<0.001 except for those with a (*). 241

Table 7.5: Model physics parameters with correlation magnitude ≥ 0.3 between their variations and 30-year (1981-2010) or 70-year (1941-2010) observational period trends in annual mean temperature or precipitation rate over a defined region. Parameters are listed in order of generally higher sensitivity to lower. All correlations shown have p<<0.00001… 246

Table 7.6: Model physics parameters with correlation magnitude ≥ 0.3 between their variations and 30-year (2051-2080) or 70-year (2010-2080) future trends in annual mean temperature or precipitation rate over a defined region. Parameters are listed in order of generally higher sensitivity to lower and correlation magnitudes ≥ 0.4 are highlighted yellow. All correlations shown have p<<0.00001. 251

Table 8.1: Decadal mean temperature anomalies for CMIP5, CPDN, CPDN constrained by 30-year global temperature trends (CPDN C-Trends), and CPDN constrained by parameters with greatest impact on 70-year global temperature trends (CPDN C-Parameters). Decadal means for each ensemble are given in terms of their mean [2.5% (25%-75%) 97.5%] and are given for three time periods (2001-2010), (2041-2050), and (2071-2080). 299

Table 8.2: Decadal mean precipitation anomalies for CMIP5, CPDN, CPDN constrained by 30-year global temperature trends (CPDN C-Trends), and CPDN constrained by parameters with greatest impact on 70-year global temperature trends (CPDN C-Parameters). Decadal means for each ensemble are given in terms of their mean [2.5% (25%-75%) 97.5%] and are given for three time periods (2001-2010), (2041-2050), and (2071-2080). 301

Table A.1: CPDN perturbed parameters and the number of transient simulations having each particular parameter value for the 1,692 transients with a "direct" atmosphere/ocean matching control and for the 2,106 transients with an "inferred" match based on parameter sensitivity to control simulation long-term drift (see Chapter 5, Section 5.7.2). Default parameter values are highlighted in bold. 339

Table A.2: Model parameter matching information for matching all atmosphere and ocean parameters ("Direct") and multiple options for matching a reduced number of parameters ("Inferred"). The number of parameters matched, number of transient-control matches, and

average number of controls matching a single transient are given. The “Inferred” match options originate from the parameter sensitivity analysis for control long-term mean drift in Chapter 5 (Section 5.7.2). 343

LIST OF FIGURES

Figure 1.1: Various interacting components making up the Earth's climate system. The most important components include the atmosphere, hydrosphere, cryosphere, land surface, biosphere, and anthrosphere. (From Stocker 2011.) 2

Figure 1.2: Observed annual mean global (land and ocean) temperature anomalies from 1850-2012. Data sets include HacCRUT4 (black; Morice et al. 2012), GISSTEMP (blue; Hansen et al. 2010), and NOAA NCDC MLOST (orange; Vose et al. 2012). Anomalies are from 1961-1990 base period average. (Adapted from Alexander et al. (2013).) 4

Figure 1.3: Observed surface temperature change from 1901-2012 from NOAA NCDC MLOST (Vose et al. 2012). Trends were calculated for grid cells with greater than 70% complete records and those cells with trends significant at the 10% level contain a "+" sign. (From Alexander et al. (2013).) 4

Figure 1.4: A number of indicators of a warming world. See citation for detailed data set information. (From www.ncdc.noaa.gov/bams-state-of-the-climate/; Updated from Arndt et al. (2010).) 6

Figure 1.5: Trends in land-based precipitation for 1901-2010 (left) and 1951-2010 (right) from the Global Precipitation Climatology Centre (GPCC) data set (Becker et al. 2013; Schneider et al. 2013). Trends are calculated within grid cells with greater than a70% complete record. White areas (on land) indicate incomplete or missing data. Dark colored individual grid cells indicate cells with significant trends (i.e., zero trend is outside 90% confidence interval. (From IPCC (2013).) 7

Figure 1.6: Measurements of atmospheric carbon for (a) CO2 concentrations from Mauna Loa, HI (red) and the South Pole (black) from 1958- 2012 (Alexander et al. 2013), (b) anthropogenic carbon emissions from burning coal, oil and natural gas and cement production (Boden et al. 2010)), and (c) reconstructions of atmospheric CO2 over the last 20,000 years based on a variety of paleoclimate records combined with current direct measurements (See Figure 6.4 from Jansen et al. (2007) for data set descriptions and references). 8

Figure 1.7: Radiative Forcing of various climate drivers from their changes between 1750-2011 in Wm-2. Best estimates are shown as black diamonds and uncertainty ranges as extended lines. Levels of confidence are given on the right hand side as very high (VH), high (H), medium (M), low (L), and very low (VL). See reference for additional details for each individual forcing. (From Alexander et al. (2013).) 10

Figure 1.8: Comparison of simulated climate change across the historical time period for simulations CMIP5 simulations that use both natural and anthropogenic forcings (pink) and those that use only natural forcings (blue). Simulated quantities are temperature (light brown backgrounds), ocean heat content (blue backgrounds) and sea ice extent (white background). (From IPCC (2013).) 12

Figure 1.9: CMIP5 ensemble annual mean global surface temperature anomaly time series (from 1986-2005 mean) simulated over the historic period (black) and for two future RCP scenarios with ensemble mean and uncertainty range. The number of models used to calculate the mean is shown for each distribution. Distributions on the right show ensemble

mean and uncertainty range for mean temperature from 2081-2100 for the four different RCP scenarios (From Alexander et al. (2013).) 13

Figure 1.10: Spatial maps of CMIP5 multi-model mean for (a) annual mean surface temperature change and (b) percent change in annual mean precipitation from 1986-2005 to 2081-2100 for the lower (RCP 2.6) and higher (RCP 8.5) emissions scenarios. Hatching indicates where the multi-model mean change is small compared to internal variability (i.e., change is less than 1 standard deviation of the range of internal variability) and stippling indicates where the change is large compared to internal variability (i.e., change is greater than 2 standard deviations of the range of internal variability). The number of models used to create the mean is shown in upper right corner. (Adapted from Alexander et al. (2013).) 14

Figure 2.1: Illustration of the development of coupled climate models since the mid-1970's and when various components were introduced into the model. Cylinder height represents the complexity the processes and how it has increased over time. The timing of the five IPCC reports is given along the top. (From IPCC (2013).) 24

Figure 2.2: Total variance for global mean decadal surface air temperature predictions split into uncertainty in internal variability (orange), model (blue), and forcing scenario (green). Global and North American 20 projections are shown in the two smaller panels with variance in annual mean temperatures over the first five years given as well. (From Hawkins and Sutton (2009).) 27

Figure 2.3: Ratio of the variability in trends (2005-2060) between an ensemble varying only its atmospheric initial conditions (i.e., internal variability) and the CMIP3 ensemble for (a) precipitation and (b) surface temperature. Stippling indicates ratios significantly different than 1 at the 95% confidence level. (Adapted from Deser et al. (2012).) 28

Figure 2.4: Alternative future scenarios from the four Representative Concentration Pathways (RCPs) described in Vuuren et al. (2011). Examples are shown for (a) the primary energy type used across the globe from 2000-2100, including a comparison between the various energy sources between 2000 and 2100 levels for each scenario (right plot) and (b) atmospheric concentrations of the three main anthropogenic greenhouse gases. Dotted lines represent the previous SRES scenarios and gray shading indicates results from other literature sources (see reference for details). (From Vuuren et al. (2011).) 30

Figure 2.5: MMD multi-model mean temperature and precipitation changes over North America for the A1B scenario. Temperature change (top), fractional change in precipitation (middle) and number of models out of 21 that project increases in precipitation (bottom) for annual mean (left), DJF (center) and JJA (right) mean. Changes are given in terms of difference between 1980-1999 and 2080-2090. (From Christensen et al. (2007).) 34

Figure 2.6: Global mean temperature anomalies (from 1961-1990 mean) for 2,752 simulation from the HadCM3L BBC CCE. Blue shading indicates a calculated goodness-of-fit metric (r2) with dark blue lines indicating the 66% confidence range. Global mean observations are shown as the thick black line and red bars indicate the CMIP3 ensemble likely range and multi-model mean (center red dash). (From Rowlands et al. (2012).) 41

Figure 3.1: Supercomputer Performance over time. Performance is calculated in terms of Floating-point Operations Per Second (FLOPS) and shown for the top performer for a given year (red), 500th top performer (pink) and the sum FLOPS over all 500 top supercomputers (green). (From top500.org.) 44

Figure 3.2: Illustration of the HadCM3L atmospheric model's σ-p hybrid coordinate vertical structure (left) with an enlarged view of the lowest 100 mb (right). Vertical layers transition from σ (i.e., terrain-following) layers near surface to pure pressure layers at the top boundary with higher resolution near the surface. Hybrid coordinate values are provided at the layer centers across the lowest 100 mb (refer to Table 3.2). (From Cullen (1993).) 51

Figure 3.3: Natural and anthropogenic forcing and SO2 emissions scenarios applied to the BBC-CCE HadCM3L transient simulations. (a) Radiative forcing due to well mixed greenhouse gases using 1921-2000 historical values and the 2001-2080 SRES A1B future scenario. (b) Radiative forcing from volcanic sulphate aerosol emissions. Five historical scenarios are included based on Sato et al. (1993) (S), Ammann et al. (2003) (A), a logarithmic average of the two (Avg S+A), lower magnitude version (Sato-), and higher magnitude version (Ammonn+). Ten future volcanic emission scenarios are created based on the same two data sets (S,A) as well as Crowley (2000) (C). The time periods used from each data set are listed in the legend. (c) Five versions of historical and SRES A1B annual average global anthropogenic SO2 emissions scaled by parameter "anthsca." (d) Five historical solar forcing scenarios from 1920-2003 are included based on Hoyt and Schatten (1993) (HS), Lean et al. (1995) (LBBx2), Solanki and Krivova (2003) (SK) and the other two based on expert elicitation (ML1, ML2), (see Frame et al. 2009). Fifteen future scenarios are created based on three versions of each of the historical five; a continuation of the historical trend (Repeated), a reversal of the historical trend (Reversed), and zero trend (No-Trend). (From Rowlands et al. 2012, Supplementary Information.) 79

Figure 3.4: North American regions investigated containing area-averaged monthly mean time-series output. 82

Figure 5.1: Initial ensemble of all control simulations acquired from CPDN for annual mean absolute (a) temperature (°C) and (b) precipitation rate (mm/day) for the globe and five NA regions. Each plot shows time series for 1,216 individual simulations. 93

Figure 5.2: Two simulations containing outliers (black) and a typical simulation (red, green) for annual mean absolute (a) temperature (°C) and (b) precipitation rate (mm/day) for the globe and five NA regions. 95

Figure 5.3: Two simulations with identical model parameters but with different output for annual average absolute (a) temperature (°C) and (b) precipitation rate (mm/day) for the globe and five NA regions. 97

Figure 5.4: Two simulations that have identical output initially but then subsequently diverge for annual mean (a) temperature (°C) and (b) precipitation rate (mm/day) for the globe and five NA regions. 100

Figure 5.5: Standardized differences between interannual variability within corresponding 30-year periods in simulation pairs having identical parameters (red, green) compared to multi-decadal differences within all control simulations (gray) for (a) temperature (°C) and (b) precipitation rate (mm/day). Distributions are standardized by the distribution of 30-year interannual variability values from all control simulations and the two distributions are rescaled on the y-axis because of the sample size difference (1,065 duplicate; 12,140 multi-decadal). 103

Figure 5.6: Control simulation 1,214 member ensemble of annual mean global absolute temperature (°C) for (a) the full 160 year period and (b) the initial 30-year period. 109

Figure 5.7: Control simulation 1,214 member ensemble of the initial 30-year period for annual mean absolute (a) temperature (°C) and (b) precipitation rate (mm/day) for the globe and five NA regions. 110

Figure 5.8: Trends per decade for the 1,214 control simulation's global mean annual mean temperature (°C/century). The boxplots indicate the mean and 25%-75% range within the box with whiskers out to the 95% range and subsequent trends in the outer 5% as black dots. 111

Figure 5.9: Same as Figure 5.8 but including the NA regions for (a) temperature (°C/century) and (b) precipitation ((mm/day)/century). 112

Figure 5.10: Control simulation long-term mean trends from years 21-160 in annual mean (a) temperature (°C/century) and (b) precipitation rate ((mm/day)/century) for the globe and NA regions. There is one drift value for each of the 1,214 simulations. 115

Figure 5.11: Annual 30-yr mean (a) temperature (°C) and (b) precipitation rate (mm/day) for the globe and five NA regions from the 1,214 control simulations (five samples per simulation) and observational bootstrap distributions (same number of overall samples). The upper x-axis in each region is standardized values based on the CPDN distribution in that region. The y-axis is set to highlight the CPDN distributions (i.e., observations can be cut off). 118

Figure 5.12: Annual 30-yr mean (a) temperature (°C) and (b) precipitation rate (mm/day) for the globe and five NA regions from the 1,214 control simulations (five samples per simulation) and observational bootstrap distributions (same number of samples). Boxplots provide 25-75% (inner) and 2.5%-97% (outer) ranges and dots for samples outside the 95% range. 123

Figure 5.13: Same as Figure 5.12 but including seasonal 30-yr means for (a) temperature (°C) and (b) precipitation rate (mm/day). 126

Figure 5.14: Mean seasonal cycle 30-yr averages for (a) temperature (°C) and (b) precipitation rate (mm/day) for the globe and five NA regions for the 1,214 control simulations (five samples per simulation) and observational bootstrap distributions (same number of samples). The y-axis is the same in all regions for a given variable. 129

Figure 5.15: Magnitude of the seasonal cycle (JJA-DJF) of temperature for the globe and five NA regions for the 1,214 control simulations (five samples per simulation) and observational bootstrap distributions (same number of samples). Boxplots provide 25-75% (inner) and 2.5%-97% (outer) ranges and dots for samples outside the 95% range. 132

Figure 5.16: Annual 30-yr interannual variability for (a) temperature (°C) and (b) precipitation rate (mm/day) for the globe and five NA regions from the 1,214 control simulations (five samples per simulation) and observational bootstrap distributions (same number of samples). Boxplots provide 25-75% (inner) and 2.5%-97% (outer) ranges and dots for samples outside the 95% range. 134

Figure 5.17: Same as Figure 5.16 but including both annual and seasonal 30-yr interannual variability for (a) temperature (°C) and (b) precipitation rate (mm/day). 136

Figure 5.18: Monthly interannual variability 30-yr averages for (a) temperature (°C) and (b) precipitation rate (mm/day) of the globe and five NA regions for the 1,214 control

simulations (five samples per simulation) and observational bootstrap distributions (same number of samples). The y-axis for the global plots differs from the regional plots. 138

Figure 5.19: Interannual variability in NAO calculated for CPDN control simulations (five 30-year samples per simulation) and observations (six 30-year samples; 10 year overlapping blocks from 80 years of data). 150

Figure 5.20: Interannual variability in Niño 3.4 SST anomalies calculated for CPDN control simulations (five 30-year samples per simulation) and observations (four 30-year samples; 10 year overlapping blocks from 60 years of data). 154

Figure 5.21: Annual mean (a) temperature (°C) and (b) precipitation rate (mm/day) of the globe and five NA regions for the 1,214 control simulations (five 30-yr samples per simulation) split into distributions corresponding with model parameter values. Actual parameter values are not listed but are arranged in the same order as that given in Table 5.1. Boxplots provide 25-75% (inner) and 2.5%-97% (outer) ranges and dots for samples outside the 95% range. The 95% range of observational (plus NARR) bootstrap distributions is shown as a vertical gray bar. 161

Figure 5.22: Same as Figure 5.21 but for interannual variability. 165

Figure 5.23: Same as Figure 5.21 but for the magnitude of the seasonal cycle (JJA-DJF) of temperature (°C). 167

Figure 5.24: Long-term mean drift in temperature (°C/Century) for the globe and five NA regions for the 1,214 control simulations split into distributions corresponding with model parameter values. Actual parameter values are not listed but are arranged in the same order as that given in Table 5.1. Boxplots provide 25-75% (inner) and 2.5%-97% (outer) ranges and dots for samples outside the 95% range. The vertical dotted line corresponds with zero trend. 169

Figure 5.25: Comparison of initial condition uncertainty (i.e., control simulations with the same atmosphere/ocean parameters but different initial conditions) in 70-year drift (colored) to the full control ensemble of 70-year mean drift for (a) temperature (°C/Century) and (b) precipitation rate ((mm/day)/Century). 173

Figure 6.1: Cross section of the components of the inner structure of a tree that are used for tree ring identification. See text for description (From Fritts (1976).) 179

Figure 6.2: Standardization of tree ring width across three different records. The top panel shows the actual tree ring widths as well as the expected value growth curve. The mean tree ring width is shown at the bottom of the top panel for a straight averaging of the original tree ring widths whereas the bottom panel shows the result of the standardization process. (From Fritts (1971).) 182

Figure 6.3: Varved sediment sample showing annual layers of deposited sediment on a lake bottom. White boxes identify each annual layer while black boxes show sand-layer thickness which has been linked to precipitation in the region. The precipitation dependent sand-layer has been subtracted from the annual layer to provide a proxy data set of varve thickness used in reconstructing temperature variability. (From Thomas and Briner (2009).) 185

Figure 6.4: An example of how temperature is reconstructed from proxy data using linear regression. Circles indicate a hypothetical annual series of proxy data and corresponding instrumental temperature observations over a 100 year calibration period (i.e., 100 circles).

Solid black line is the linear fit to the data and blue lines indicate the 95% prediction intervals. The heavy dashed line and red line indicate potential departures from an assumed linear relationship between the proxy and temperature data. Two examples (A, B) are provided showing the temperature predictions for a given proxy value with corresponding prediction uncertainty ranges (heavy blue vertical lines). (From NAS (2006).) 188

Figure 6.5: Locations of North American proxy-based paleoclimate reconstructions for precipitation (open symbols) and temperature (filled symbols) using proxy data from tree rings (triangles) and varved sediments (squares). The five larger rectangular regions highlight the regions used for calculating climatic information from the CPDN HadCM3L model. 191

Figure 6.6: Annual average temperature anomaly (°C; anomaly from each data set's long-term mean) for (a) SE Alaska summer, (b) NE Canada summer, (c) SW Canada summer, (d) SW USA annual, and (e) E USA spring. 192

Figure 6.7: Annual average precipitation anomaly (mm/day; anomaly from each data set's long-term mean) for (a) S Canada annual, (b) NW USA annual, (c) SW USA annual, (d) Mid USA annual, and (e) SE USA spring. 193

Figure 6.8: Interannual variability (30-yr) for (a) temperature (°C) and (b) precipitation rate (mm/day) for the 1,214 control simulations (five samples per simulation), observational bootstrap distributions (same number of samples) and paleoclimate reconstructions (number of samples vary depending on record length). Boxplots provide 25-75% (inner) and 2.5%-97% (outer) ranges and dots for samples outside the 95% range. 196

Figure 6.9: Decadal variability (100-yr) for (a) temperature (°C) and (b) precipitation rate (mm/day) for the 1,214 control simulations (three samples per simulation), three observational samples for temperature (one per 90-yr data set) and paleoclimate reconstructions (samples vary). Boxplots provide 25-75% (inner) and 2.5%-97% (outer) ranges and dots for samples outside the 95% range. 199

Figure 7.1: Initial ensemble of all transient simulations acquired from CPDN for annual mean (a) temperature (°C) and (b) precipitation rate (mm/day) for the globe and five NA regions. Each plot shows time series for 3,818 individual simulations. Temperature y-axis values are different across regions but all maintain a 30°C range. Precipitation y-axis values are the same. 205

Figure 7.2: Long-term mean drift removal example in annual mean global temperature anomaly output for (a) control and (b) transient simulations having matching atmosphere and ocean parameter values. Original simulations are given in black and those with the control simulation's long-term mean trend from years 21-160 removed in red. Anomalies are relative to a 1941-1970 base period. 209

Figure 7.3: Transient (black) and Transient-Control (red, green) comparisons for those transients having the largest control drift removed for annual mean anomaly of (a) temperature (°C) and (b) precipitation rate (mm/day) for the globe and five NA regions from 1941-2080. Anomalies are relative to a 1941-1970 base period..... 217

Figure 7.4: Annual mean global temperature anomaly for the 1,692 transient simulations (red shading) and three observational data sets (HadCRUT3, NOAA-MLOST, GISTEMP) over the 1941-2010 observational time period. The transient ensemble is shaded according to the

25-75%, 2.5-97.5%, and min-max ranges. Anomaly values are relative to a 1941-1970 base period. 219

Figure 7.5: Comparison of (a) monthly values of the Pacific Decadal Oscillation (PDO) index and (b) the HadCRUT3 temperature anomaly (1961-1990 base period). The 1990-2012 time periods are aligned to allow for comparison. (HadCRUT3 from Met Office Hadley Center, based on Brohan et al. (2006); PDO from the Joint Institute for the Study of the Atmosphere and Ocean, University of Washington, based on Zhang et al. (1997) and Mantua et al. (1997)). 223

Figure 7.6: Same as Figure 7.4 but including regional comparisons for annual mean anomalies of (a) temperature(C) and (b) precipitation rate (mm/day). NARR data are included because it is available at the regional level and the precipitation data sets also include GPCP and NOAA-PREC. Temperature anomalies are relative to a 1941-1970 base period and precipitation anomalies are relative to 1981-2010. 225

Figure 7.7: Annual mean (a) temperature (C/Century) and (b) precipitation rate ((mm/day)/Century) trends for observational periods 1941-2010 (colored) and 1981-2010 (black). Observed trends are plotted using same color scheme. 227

Figure 7.8: Annual mean global temperature anomaly for the 1,692 transient simulations (red shading) and three observational data sets over the 1941-2080 time period. The transient ensemble is shaded according to the 25-75%, 2.5-97.5%, and min-max ranges. Anomalies are relative to a 1941-1970 base period. 230

Figure 7.9: Same as Figure 7.8 but including regional comparisons for annual mean anomalies of (a) temperature(C) and (b) precipitation rate (mm/day). Temperature anomalies are relative to a 1941-1970 base period and precipitation anomalies are relative to 1981-2010. 232

Figure 7.10: Annual mean (a) temperature (C/Century) and (b) precipitation rate ((mm/year)/ Century) trends for past and future transients and controls for 30 year time periods (black) and 70 year periods (colored). Observed trends are plotted using the same color scheme.. 235

Figure 7.11: Comparison of 70 year trends (1941-2010) in annual mean temperature for the globe versus each region. A single point is plotted for each of the 1,692 transient simulations. P-values are all << 0.001. 236

Figure 7.12: Differences in 30 year mean interannual variability and JJA-DJF from 1981-2010 to 2051-2080 for the 1,692 transient simulations (colored) and differences found across five different 30 year periods within all 1,214 control simulations. All values are standardized to the control difference distribution. 243

Figure 7.13: Annual mean temperature (a) 30 year trends, 1981-2010 and (b) 70 year trends, 1941-2010 (°C/Century) over the observational time period for the globe and five NA regions for the 1,692 transient simulations split into distributions corresponding with model parameter values. Actual parameter values are not listed but are arranged in the same order as that given in Table 7.1. Boxplots provide 25-75% (inner) and 2.5%-97% (outer) ranges and dots for samples outside the 95% range. The maximum and minimum range of corresponding observational data sets (including NARR) is shown as a vertical shaded bar. A vertical dotted line identifies zero trend. 247

Figure 7.14: Annual mean precipitation rate (a) 30 year trends, 1981-2010 and (b) 70 year trends, 1941-2010 ((mm/year)/Century) over the observational time period for the globe and five NA regions for the 1,692 transient simulations split into distributions corresponding with model parameter values. Actual parameter values are not listed but are arranged in the same order as that given in Table 7.1. Boxplots provide 25-75% (inner) and 2.5%-97% (outer) ranges and dots for samples outside the 95% range. The maximum and minimum range of corresponding observational data sets (including NARR) is shown as a vertical shaded bar. The observational 70 year trend corresponds with a single data set (NOAA-MPREC) and is a 60 year average corresponding with the data set length. A vertical dotted line identifies zero trend. 248

Figure 7.15: Annual mean temperature (a) 30 year trends, 2051-2080 and (b) 70 year trends, 2011-2010 (°C/Century) for the future time period for the globe and five NA regions for the 1,692 transient simulations split into distributions corresponding with model parameter values. Actual parameter values are not listed but are arranged in the same order as that given in Table 7.1. Boxplots provide 25-75% (inner) and 2.5%-97% (outer) ranges and dots for samples outside the 95% range. A vertical dotted line identifies zero trend. 253

Figure 7.16: Annual mean precipitation rate (a) 30 year trends, 2051-2080 and (b) 70 year trends, 2011-2080 ((mm/year)/Century) for the future time period for the globe and five NA regions for the 1,692 transient simulations split into distributions corresponding with model parameter values. Actual parameter values are not listed but are arranged in the same order as that given in Table 7.1. Boxplots provide 25-75% (inner) and 2.5%-97% (outer) ranges and dots for samples outside the 95% range. 254

Figure 7.17: Annual mean global temperature anomaly for transient ensemble constrained by model performance for 30-year (1981-2010) global temperature trends (red shading; 255 simulations) and the original transient ensemble (black lines; 1,692 simulations). Both ensembles show the 25-75%, 2.5-97.5%, and min-max ranges. Observations are averaged together to give a single estimate. Anomalies are relative to a 1941-1970 base period. 256

Figure 7.18: Same as Figure 7.17 but including regional comparisons for annual mean anomalies of (a) temperature (C) and (b) precipitation rate (mm/day). Temperature anomalies are relative to a 1941-1970 base period and precipitation anomalies are relative to 1981-2010. 257

Figure 7.19: Annual mean global temperature anomaly for transient ensemble constrained by model performance for 70-year (1941-2010) global temperature trends (red shading; 997 simulations) and the original transient ensemble (black lines; 1,692 simulations). Both ensembles show the 25-75%, 2.5-97.5%, and min-max ranges. Observations are averaged together to give a single estimate. Anomalies are relative to a 1941-1970 base period. 259

Figure 7.20: Annual mean global temperature anomaly for transient ensemble constrained by model parameters with greatest sensitivity for 70-year (1941-2010) global temperature trends (red shading; 37 simulations) and the original transient ensemble (black lines; 1,692 simulations). Both ensembles show the 25-75%, 2.5-97.5%, and min-max ranges. Observations are averaged together to give a single estimate. Anomalies are relative to a 1941-1970 base period. 261

Figure 7.21: Same as Figure 7.19 but including regional comparisons for annual mean anomalies of (a) temperature (C) and (b) precipitation rate (mm/day). Temperature anomalies

are relative to a 1941-1970 base period and precipitation anomalies are relative to 1981-2010. 262

Figure 8.1: Annual 30-yr mean (a) temperature (°C) and (b) precipitation rate (mm/day) for the globe and five NA regions from the 1,214 CPDN control simulations (five samples per simulation), CMIP5 control simulations (seven 30-yr samples per simulation for 41 temperature and 37 precipitation simulations), and observational bootstrap distributions (6070 samples). Boxplots provide 25-75% (inner) and 2.5%-97% (outer) ranges and dots for samples outside the 95% range. 269

Figure 8.2: Same as Figure 8.1 but including winter (DJF) and summer (JJA) means. 271

Figure 8.3: Magnitude of the seasonal cycle (JJA-DJF) of temperature for the globe and five NA regions for the 1,214 control simulations (five samples per simulation), CMIP5 control simulations (seven 30-yr samples per simulation for 41 temperature and 37 precipitation simulations), and observational bootstrap distributions (6070 samples). Boxplots provide 25-75% (inner) and 2.5%-97% (outer) ranges and dots for samples outside the 95% range. ... 273

Figure 8.4: Annual 30-yr interannual variability for (a) temperature (°C) and (b) precipitation rate (mm/day) for the globe and five NA regions from the 1,214 control simulations (five samples per simulation), CMIP5 control simulations (seven 30-yr samples per simulation for 41 temperature and 37 precipitation simulations), and observational bootstrap distributions (6070 samples). Boxplots provide 25-75% (inner) and 2.5%-97% (outer) ranges and dots for samples outside the 95% range. 276

Figure 8.5: Same as Figure 8.4 but including winter (DJF) and summer (JJA) interannual variability. 277

Figure 8.6: Annual 100-yr decadal variability for (a) temperature (°C) and (b) precipitation rate (mm/day) for the globe and five NA regions from the 1,214 control simulations (five samples per simulation), CMIP5 control simulations (three 100-yr samples per simulation for 41 temperature and 37 precipitation simulations), and one 90-year sample for each of the temperature observational data sets. Boxplots provide 25-75% (inner) and 2.5%-97% (outer) ranges and dots for samples outside the 95% range. 279

Figure 8.7: Annual mean global temperature anomaly for the 1,692 transient simulations (red shading), three observational data sets (HadCRUT3, NOAA-MLOST, GISTEMP), and (a) 52 CMIP3 and (b) 46 CMIP5 simulations (colored lines) over the 1941-2010 observational time period. The transient ensemble is shaded according to the 25-75%, 2.5-97.5%, and min-max ranges. Anomaly values are relative to a 1941-1970 base period. 282

Figure 8.8: Same as Figure 8.7 but with CMIP3 and CMIP5 ensembles displayed as boxplots representing decadal means values. These boxplots include the 25-75% and 2.5-97.5% ranges. 283

Figure 8.9: Same as Figure 8.8 but includes NA regional results for (a) temperature (°C) and (b) precipitation rate (mm/day). Temperature anomalies are relative to a 1941-1970 base period and precipitation anomalies are relative to 1981-2010. 284

Figure 8.10: Annual mean global temperature anomaly from 1941-2080 for the 1,692 transient simulations (red shading), three observational data sets (HadCRUT3, NOAA-MLOST, GISTEMP), and (a) 52 CMIP3 simulations using SRES A1B and (b) the HadCM3

simulation from CMIP3. The transient ensemble is shaded according to the 25-75%, 2.5-97.5%, and min-max ranges. Anomaly values are relative to a 1941-1970 base period. ... 286

Figure 8.11: Annual mean global temperature anomaly from 1941-2080 for the 1,692 transient simulations (red shading), three observational data sets (HadCRUT3, NOAA-MLOST, GISTEMP), and (a) 46 CMIP5 simulations using RCP 6.0 and (b) four HadGEM2 simulations from CMIP5. The transient ensemble is shaded according to the 25-75%, 2.5-97.5%, and min-max ranges. Anomaly values are relative to a 1941-1970 base period. ... 288

Figure 8.12: Same as Figure 8.11 but with CMIP3 (SRES A1B) and CMIP5 (RCP 6.0) ensembles displayed as boxplots representing decadal means values. These boxplots include the 25-75% and 2.5-97.5% ranges. 290

Figure 8.13: Same as Figure 8.12 but includes NA regional results for (a) temperature (°C) and (b) precipitation rate (mm/day). Temperature anomalies are relative to a 1941-1970 base period and precipitation anomalies are relative to 1981-2010. 291

Figure 8.14: CMIP3 decadal mean global temperature distributions (52 simulations) with annual mean global temperature anomalies for transient ensemble constrained by (a) model performance compared to 30-year (1981-2010) observed trends (red shading; 255 simulations) and (b) model parameters with greatest sensitivity for 70-year (1941-2010) global temperature trends (red shading; 37 simulations) and the original transient ensemble (black lines; 1,692 simulations). Both sets of CPDN ensembles show the 25-75%, 2.5-97.5%, and min-max ranges. CMIP3 shows the 25-75% and 2.5-97.5% ranges and observations are averaged together to give a single estimate (heavy line). Anomalies are relative to a 1941-1970 base period. 293

Figure 8.15: Same as Figure 8.14(a) (i.e., constraining by model performance compared to 30-year (1981-2010) observed trends) but includes NA regional results for (a) temperature (°C) and (b) precipitation rate (mm/day). Temperature anomalies are relative to a 1941-1970 base period and precipitation anomalies are relative to 1981-2010. 296

Figure 8.16: Same as Figure 8.14(b) (i.e., constraining by parameters with greatest impact on 70-year global temperature trends) but includes NA regional results for (a) temperature (°C) and (b) precipitation rate (mm/day). Temperature anomalies are relative to a 1941-1970 base period and precipitation anomalies are relative to 1981-2010. 297

Figure A.1: Comparison of normalized (i.e., mean of distribution subtracted off) long-term mean drift in global mean temperature for all control simulations (black bottom distribution) to anomalies from the average long-term mean drift for each set of control simulations matching one of the transient simulations in the "direct" match cases (top blue distribution) and for four different correlation threshold examples in the "inferred" match cases (four middle red distributions). All distributions are in units of (°C/Century). 344

ABSTRACT

Information on the uncertainties in projections of future climate change from global climate models (GCMs) is vital for their effective use across a wide range of applications, including their increasing role in driving regionally downscaled models for higher resolution output useful to local impacts studies (e.g., hydrologic, ecosystems, agricultural). To better estimate GCM uncertainties, a multi-thousand member perturbed-physics ensemble (PPE) of climate simulations was assessed to quantify uncertainties in future climate change projections for the globe and North American region. The simulations were generated through the distributed computing project Climate*prediction*.net (CPDN), a joint effort between the UK Met Office Hadley Centre and Oxford University, where thousands of simulations were run on PCs across the globe, each running a different version of the Hadley Centre-based HadCM3L coupled atmosphere-ocean GCM with variations to their model physics parameters.

The large PPE was able to model many observed features in the Earth's climate system and climate indices were found to be sensitive to changes in the model's physics parameters with cloud physics parameters being of most importance. The PPE was constrained using observational performance and parameter sensitivity assessments and it was found that the constrained ensembles reduced both the ensemble mean and uncertainty range of the initial ensemble. Results were compared to CMIP3 and CMIP5 ensembles and the CMIP ensembles were found to

underestimate the full range of uncertainties in physics parameters, thus indicating the usefulness of large PPEs to inform users of GCM output of the full range of model parameter and structural uncertainty.

CHAPTER 1

INTRODUCTION

Earth's climate is a highly complex and dynamic system with many interacting components including the atmosphere, hydrosphere, cryosphere, land surface, biosphere, and in more recent times the impacts of human activities (i.e., anthrosphere) (Figure 1.1). Changes amongst these components take place on differing time scales and are driven by a variety of forcing mechanisms (Ruddiman 2007). Over relatively short time periods (i.e., hundreds to a few thousand years) the long-term forcing factors (e.g., solar output changes over millions to billions of years, tectonic activity, and orbital parameter variations) remain essentially constant and therefore have limited impact on climate. The main drivers of century- to millennial-scale changes therefore are short-term solar forcing variations and changes in the composition of the atmosphere (i.e., from anthropogenic effects). On even shorter time scales (e.g., interannual to decadal), Earth's climate can vary due to phenomena such as explosive volcanic eruptions capable of reducing solar radiation reaching Earth's surface or from natural internal variability mechanisms such as coupled atmosphere-ocean variations (e.g., El Niño-Southern Oscillation (ENSO), Artic Oscillation (AO), North Atlantic Oscillation (NAO), Pacific Decadal Oscillation (PDO)) that can exchange and/or redistribute heat and energy between and/or within the atmosphere and ocean systems.

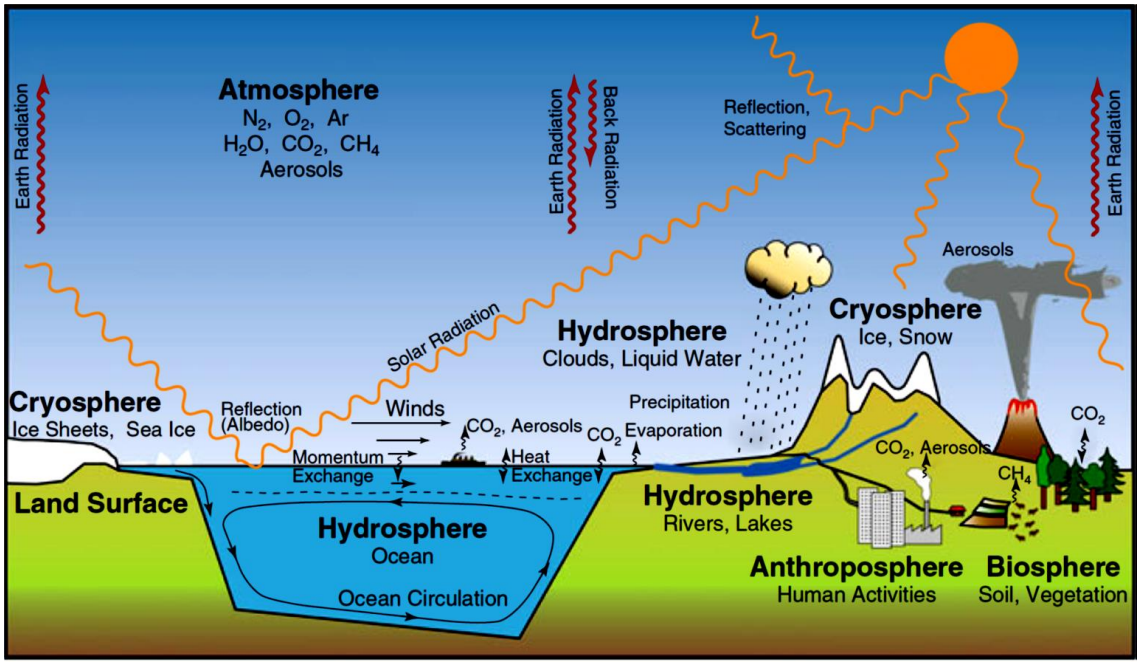


Figure 1.1: Various interacting components making up the Earth's climate system. The most important components include the atmosphere, hydrosphere, cryosphere, land surface, biosphere, and anthrosphere. (From Stocker (2011).)

Acquiring a greater understanding of the driving forces in Earth's climate can better equip us to anticipate how the climate may change in the future and possible impacts these changes could have on natural, managed, and human systems. With that in mind, an extensive amount of research has been conducted over the past decades investigating how Earth's climate system has changed in the past and how it may change in the future. This research has been summarized in a series of reports released every 5-6 years by Working Group I (WGI) of the Intergovernmental Panel on Climate Change (IPCC; IPCC 1990, 1996, 2001, 2007). Each successive report's findings have grown in confidence with the central message being that the Earth's climate is changing, that anthropogenic effects are the dominant cause of these changes since the 1950's and that

the climate will continue to change in the future as anthropogenic effects continue to dominate.

The Summary for Policymakers from WGI's contribution to IPCC's Fifth Assessment Report (AR5) was recently released (Alexander et al. 2013) and affirmed that "Warming of the climate system is unequivocal, and since the 1950's, many of the observed changes are unprecedented over decades to millennia." Figure 1.2 illustrates warming over the past century from three independent global temperature data sets. All three of these data sets show a consistent pattern of warming since the early 1900's with considerable interannual and decadal variability embedded within the trend. This warming trend has been apparent across most of the globe at the regional level as well (Figure 1.3) with the greatest regional surface warming located on continental land masses. This is because a large portion of the surface heating over the ocean is used for evaporating water as well as the fact that the ocean has a greater specific heat than the land surface. It can also transfer surface layer heat to greater depths.

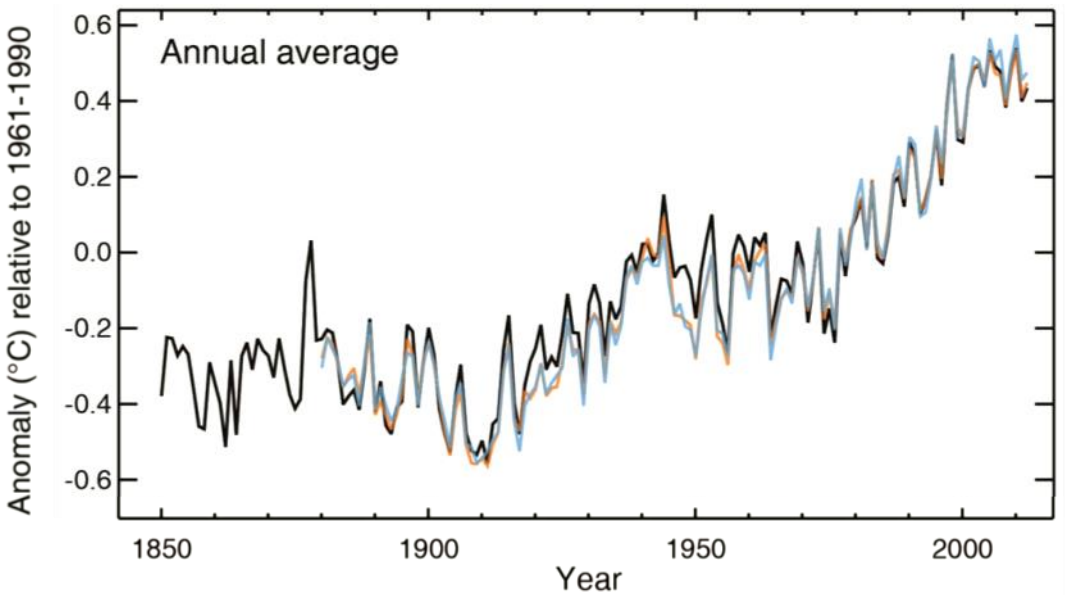


Figure 1.2: Observed annual mean global (land and ocean) temperature anomalies from 1850-2012. Data sets include HacCRUT4 (black; Morice et al. 2012), GISSTEMP (blue; Hansen et al. 2010), and NOAA NCDC MLOST (orange; Vose et al. 2012). Anomalies are from 1961-1990 base period average. (Adapted from Alexander et al. (2013).)

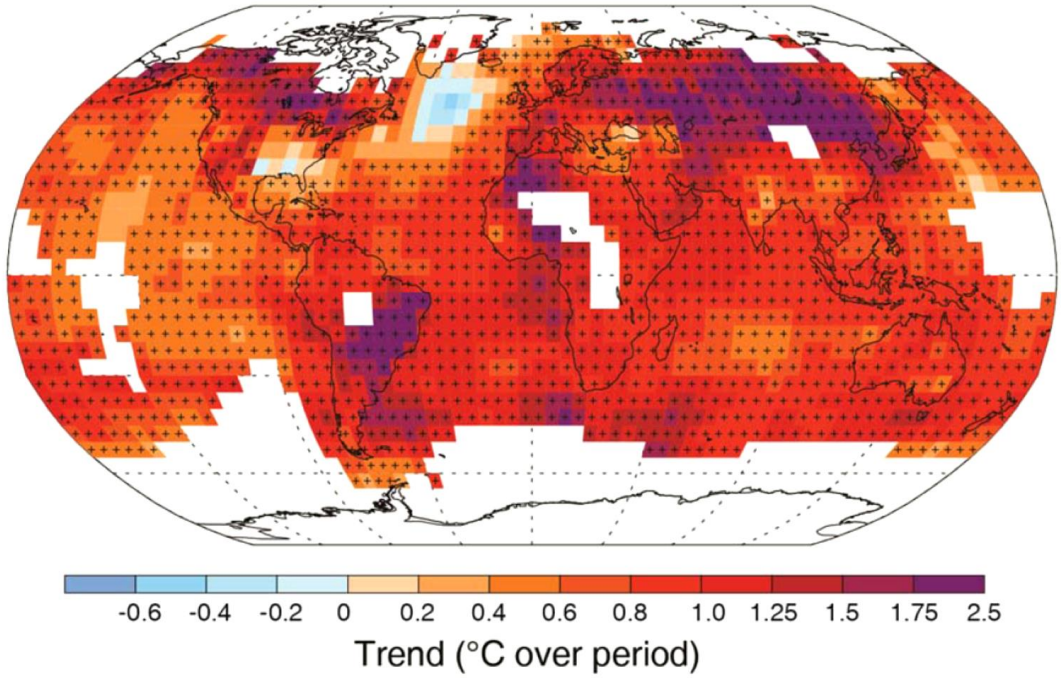


Figure 1.3: Observed surface temperature change from 1901-2012 from NOAA NCDC MLOST (Vose et al. 2012). Trends were calculated for grid cells with greater than 70% complete records and those cells with trends significant at the 10% level contain a "+" sign. (From Alexander et al. (2013).)

While the majority of the globe experienced significant warming over the past century (Figure 1.3) there are two regions of the globe that actually experienced slight cooling. The main region is in the North Atlantic where the relative cooling is thought to be due in part to an influx of cold, fresh (i.e., low density) water from melting glacial ice sheets as well as a relative shift to a more positive phase of the NAO which has a cooling effect on the region (e.g., Bindoff and Willebrand 2007). The second region with slight cooling (or relatively no warming) was in the east-central United States (U.S.) which has been linked to increased cloud cover, precipitation, and soil moisture in the central U.S. due to the linkages between the Great Plains low-level jet and regional precipitation (Pan et al. 2004) as well as increased cloud cover in the southeast U.S. due to interactions between anthropogenic aerosol pollutants and organic aerosols from forest regrowth (Portmann et al. 2009). Increased irrigation across the 20th century also has been identified as a possible cause for some of the cooling (Puma and Cook 2010) as well as multi-decadal variability of sea surface temperatures (SST's) in the tropical Pacific (Robinson et al. 2002; Meehl et al. 2012) with warmer waters corresponding to increased cloud cover over the east-central U.S.

Besides temperature observations there are a number of other recorded indices indicating a warming world over the last century, especially since 1950. Figure 1.4 summarizes some of most important indicators which generally indicate warmer temperatures in the lower troposphere and oceans as well as decreases in Arctic sea ice extent, mountain glaciers and Northern Hemisphere spring snow cover. Additionally there have been increases in sea-level and atmospheric moisture. Precipitation across the globe also has changed over the last century, but with much more regional diversity

(Figure 1.5). In general, dry areas are getting drier and wet areas wetter, especially across the last 60 years, indicating an intensification of the hydrologic cycle. Focusing on the North American (NA) region, the more recent part of the record (i.e., 1979-2010) has shown drier conditions in the west-southwest as well as the southeast and wetter conditions in the central to north-central region.

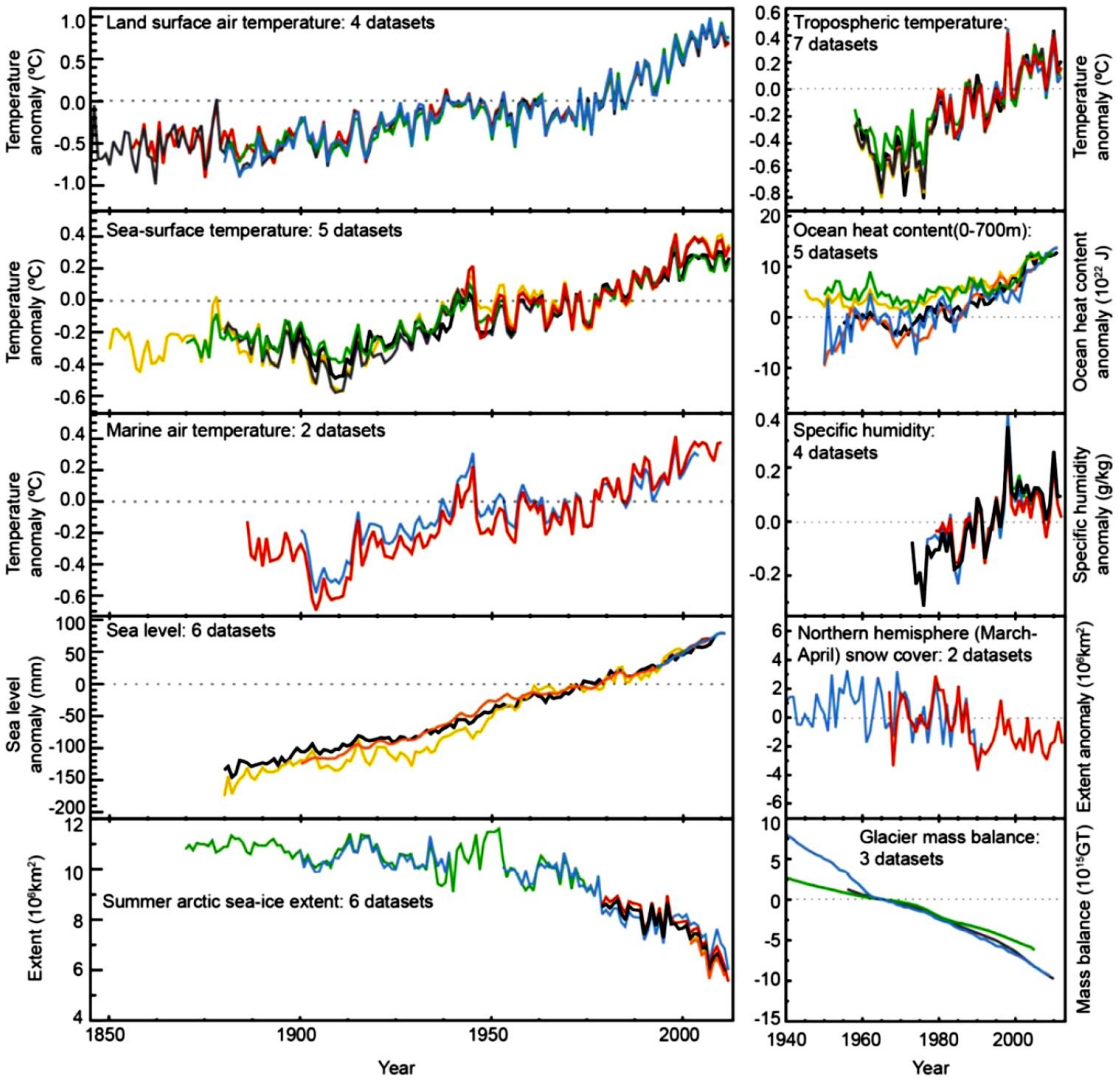


Figure 1.4: A number of indicators of a warming world. See citation for detailed data set information. (From www.ncdc.noaa.gov/bams-state-of-the-climate/; Updated from Arndt et al. (2010).)

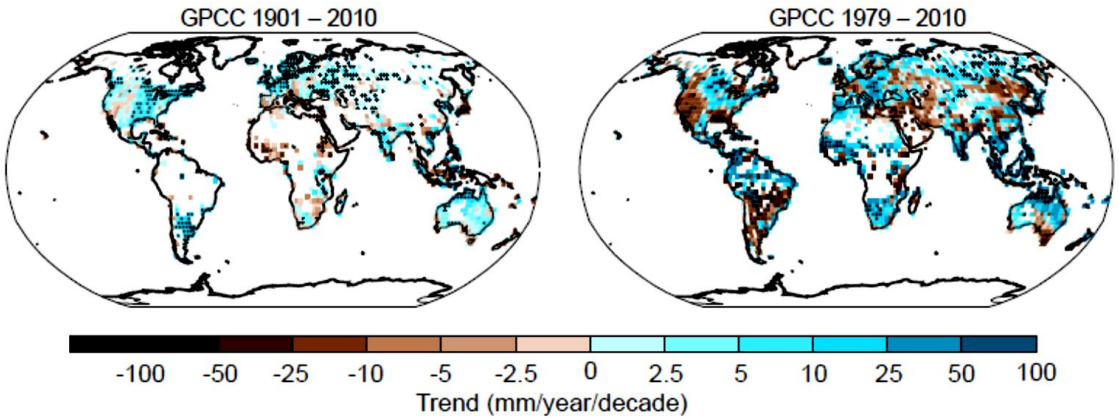


Figure 1.5: Trends in land-based precipitation for 1901-2010 (left) and 1951-2010 (right) from the Global Precipitation Climatology Centre (GPCC) data set (Becker et al. 2013; Schneider et al. 2013). Trends are calculated within grid cells with greater than a70% complete record. White areas (on land) indicate incomplete or missing data. Dark colored individual grid cells indicate cells with significant trends (i.e., zero trend is outside 90% confidence interval. (From IPCC (2013).)

The cause of the late 20th century warming has been attributed to increases in anthropogenic greenhouse gas emissions, particularly CO_2 (IPCC 1990, 1996, 2001, 2007; Alexander et al. 2013). As shown in Figure 1.6, atmospheric CO_2 has increased significantly since the industrial revolution, especially when compared to changes over the past few thousands of years (Figure 1.6(c)), with the majority of the increase coming from the burning of fossil fuels (Figure 1.6(b); Boden et al. 2010). In 2012 atmospheric CO_2 levels reached 392 ppm (Figure 1.6(a)) and concentrations now are higher than anytime in at least the last 800,000 years (see Jansen et al. (2007) and Luthi et al. (2008)). CO_2 and other greenhouse gases such as methane (CH_4) and nitrous oxide (N_2O), which also have increased markedly in the recent past (e.g., Jansen et al. 2007), act to warm the planet by absorbing and reemitting longwave radiation back to the surface thereby keeping a portion of the longwave energy within the climate system that would otherwise have exited out the top of the atmosphere. All greenhouse gases

provide this same general warming effect but CO_2 has been identified as the most "climate-relevant" greenhouse gas because of its relative concentration, rate of increase from anthropogenic sources, and long life span in the atmosphere (Lacis et al. 2010).

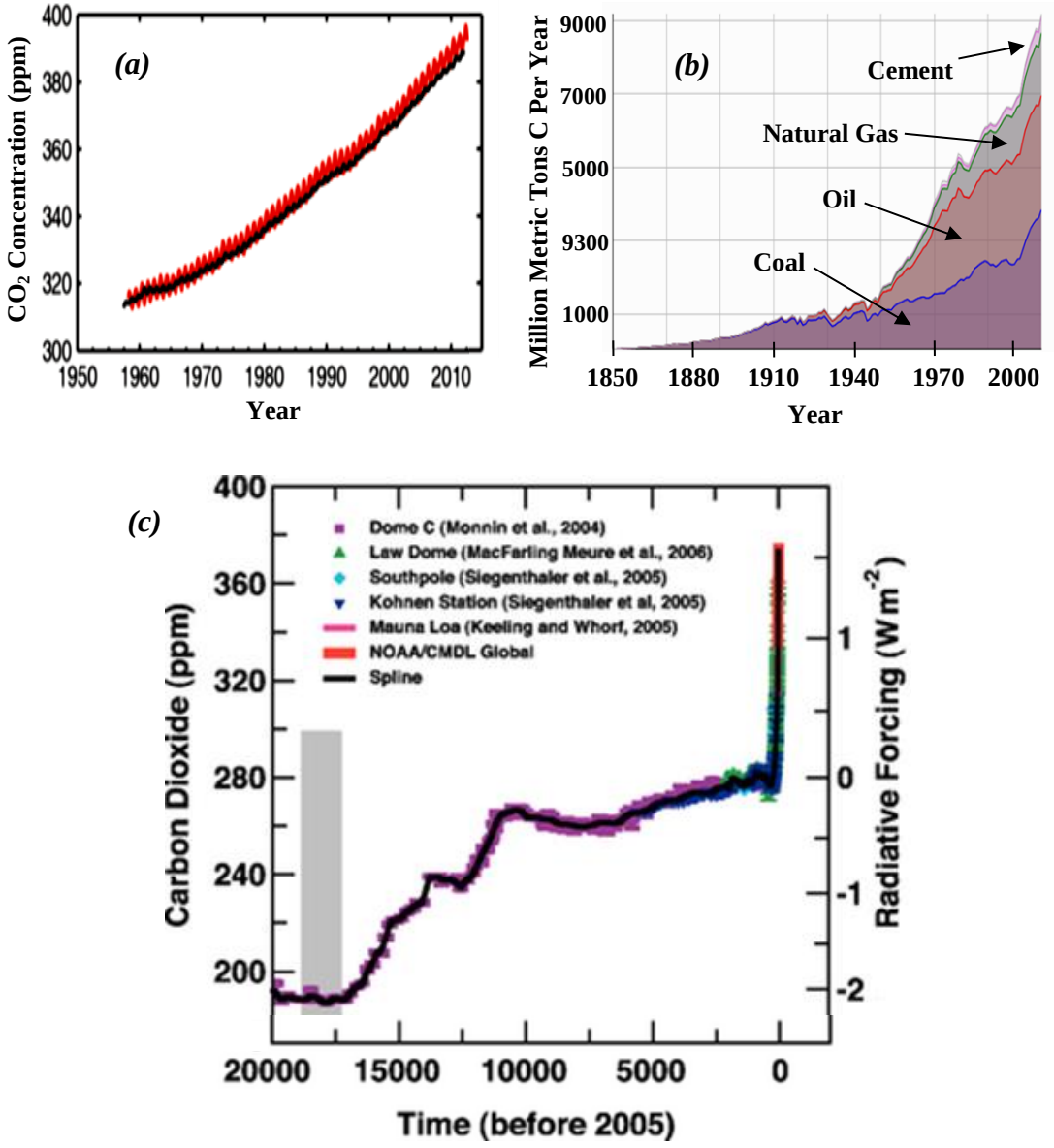


Figure 1.6: Measurements of atmospheric carbon for *(a)* CO_2 concentrations from Mauna Loa, HI (red) and the South Pole (black) from 1958- 2012 (Alexander et al. 2013), *(b)* anthropogenic carbon emissions from burning coal, oil and natural gas and cement production (Boden et al. 2010)), and *(c)* reconstructions of atmospheric CO_2 over the last 20,000 years based on a variety of paleoclimate records combined with current direct measurements (See Figure 6.4 from Jansen et al. (2007) for data set descriptions and references).

Figure 1.7 provides the relative proportion of anthropogenic factors that have acted on Earth's climate system since the year 1750 as well as natural changes from solar forcing. (Note that volcanic forcing was not included because it has only a short-term impact on the climate over the time scale considered.) Changes in the different drivers of climate are given in terms of radiative forcing (RF) which is a measure of the net change in the Earth's energy balance in response to an external perturbation.[1] A positive RF value indicates warming and a negative value cooling of global mean temperatures. As Figure 1.7 illustrates, the net anthropogenic RF (bottom red bars) was positive and significantly larger than the influence of solar irradiance changes. The majority of this forcing came from well mixed greenhouse gases with CO_2 being the largest contributor. The anthropogenic positive forcing has increased rapidly since the 1950's with the total RF relative to 1750 roughly doubling from 1950-1980 and then nearly doubling again from 1980-2010. This illustrates the accelerating influence anthropogenic effects are having on the climate system.

[1] Radiative forcing is defined as "the change in net (down minus up) irradiance (solar plus longwave; in Wm^{-2}) at the tropopause after allowing for stratospheric temperatures to readjust to radiative equilibrium, but with surface and tropospheric temperatures and state held fixed at the unperturbed values" (IPCC 2007). In WGI AR5 (Alexander et al. 2013), rapid adjustments to perturbations were allowed in the RF calculation so as to include faster climate responses from drivers such as aerosols.

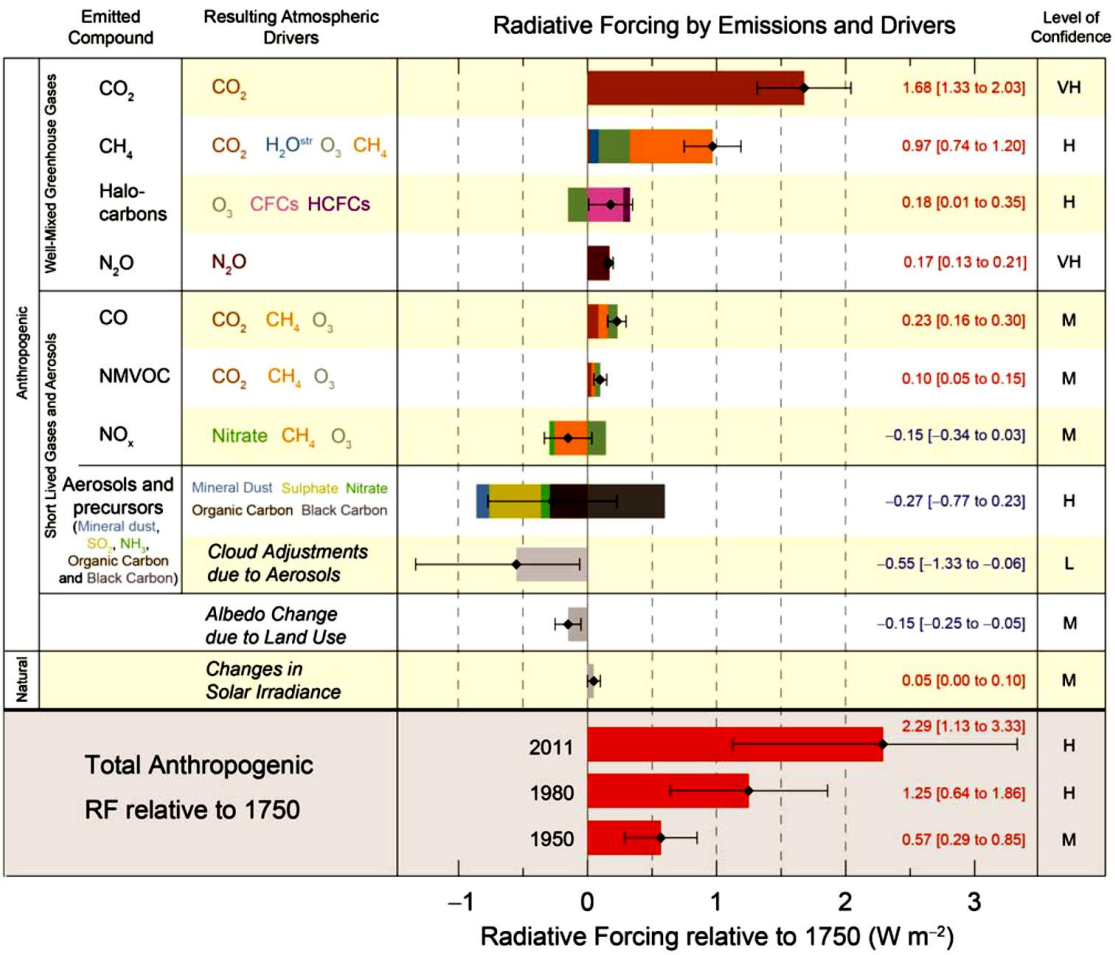


Figure 1.7: Radiative Forcing of various climate drivers from their changes between 1750-2011 in Wm^{-2}. Best estimates are shown as black diamonds and uncertainty ranges as extended lines. Levels of confidence are given on the right hand side as very high (VH), high (H), medium (M), low (L), and very low (VL). See reference for additional details for each individual forcing. (From Alexander et al. (2013).)

With an understanding of the various drivers of Earth's climate system, global climate models, also referred to as general circulation models (GCMs), have been used to simulate past climate conditions across the globe and to make projections of possible future conditions (e.g., Christensen et al. 2007; Hegerl et al. 2007; Meehl et al. 2007b; Randall et al. 2007). (See Chapter 2 for an expanded discussion of climate modeling). One way to test climate models and assess our understanding of climate drivers is to

simulate past conditions and see how well the models agree with observations. When models include both natural and anthropogenic forcings they generally are able to simulate observed trends at both global and regions scales (Figure 1.8). However, when only natural forcings are simulated, models cannot reproduce the warming trend over the latter part of the observational time period (Figure 1.8), further strengthening the evidence for the role anthropogenic effects are having on the climate system.

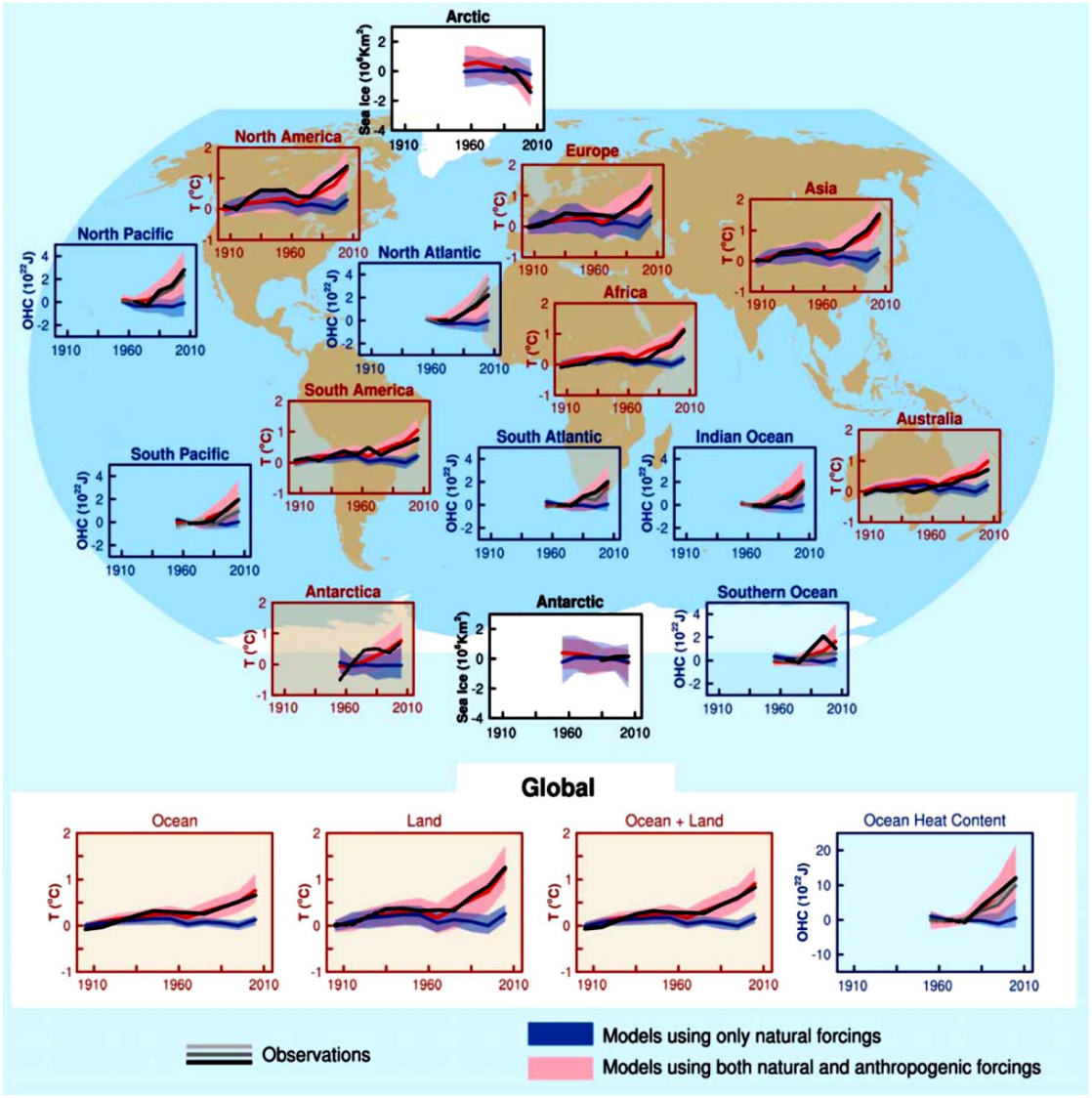


Figure 1.8: Comparison of simulated climate change across the historical time period for simulations CMIP5 simulations that use both natural and anthropogenic forcings (pink) and those that use only natural forcings (blue). Simulated quantities are temperature (light brown backgrounds), ocean heat content (blue backgrounds) and sea ice extent (white background). (From IPCC (2013).)

With increased confidence in the ability of GCMs to reproduce general trends in the past, they have been used to generate projections of future conditions for the planet as a whole and at the regional scale (e.g., Christensen et al. 2007; Meehl et al. 2007b). Figure 1.9 provides annual mean global temperature anomalies as simulated by the most

advanced global climate models in the world (i.e., the World Climate Research Programme's (WCRP's) Coupled Model Intercomparison Projects Phase 5 (CMIP5)). The CMIP5 simulation ensemble is compared with observational estimates from 1950-2004 and then simulates future projections based on a variety of future anthropogenic forcing scenarios called Representative Concentration Pathways (RCP; Vuuren et al. 2011) ranging from a low-emissions scenario (RCP2.6) to a high emissions scenario (RCP8.5). (Refer to Chapter 2 for more details.) It is clear that a relatively large range of uncertainty exists for each individual scenario within the CMIP5 ensemble as well as an even larger uncertainty range based on choice of RCP. Figure 1.10 further emphases the uncertainty in choice of RCP by showing globally gridded model output differences in the low (RCP2.6) and high (RCP) emission scenarios for changes in temperature (Figure 1.10(a)) and precipitation (Figure 1.10(b)) over the next century.

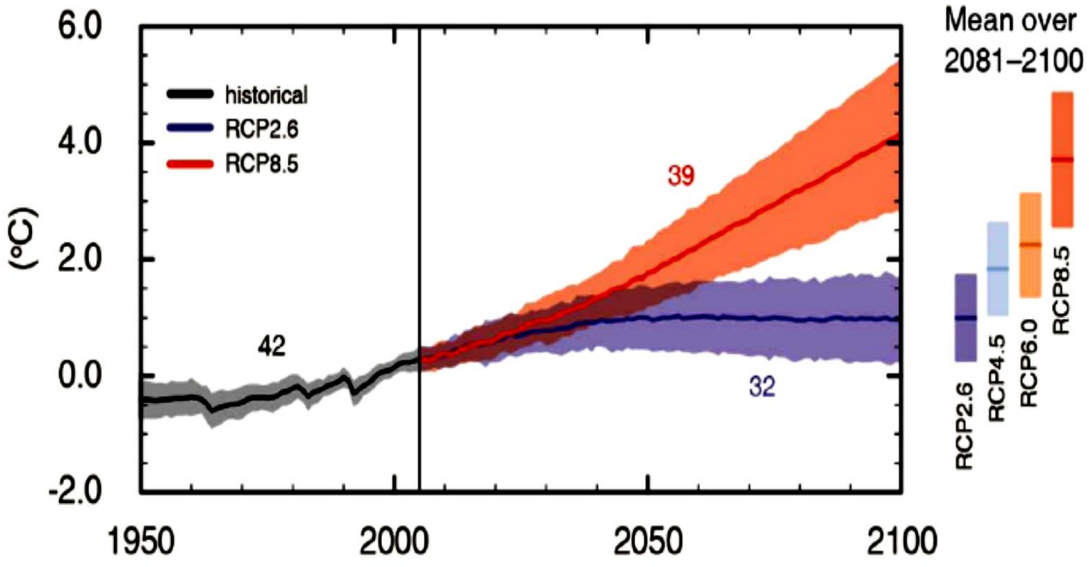


Figure 1.9: CMIP5 ensemble annual mean global surface temperature anomaly time series (from 1986-2005 mean) simulated over the historic period (black) and for two future RCP scenarios with ensemble mean and uncertainty range. The number of models used to calculate the mean is shown for each distribution. Distributions on the right show ensemble mean and uncertainty range for mean temperature from 2081-2100 for the four different RCP scenarios (From Alexander et al. (2013).)

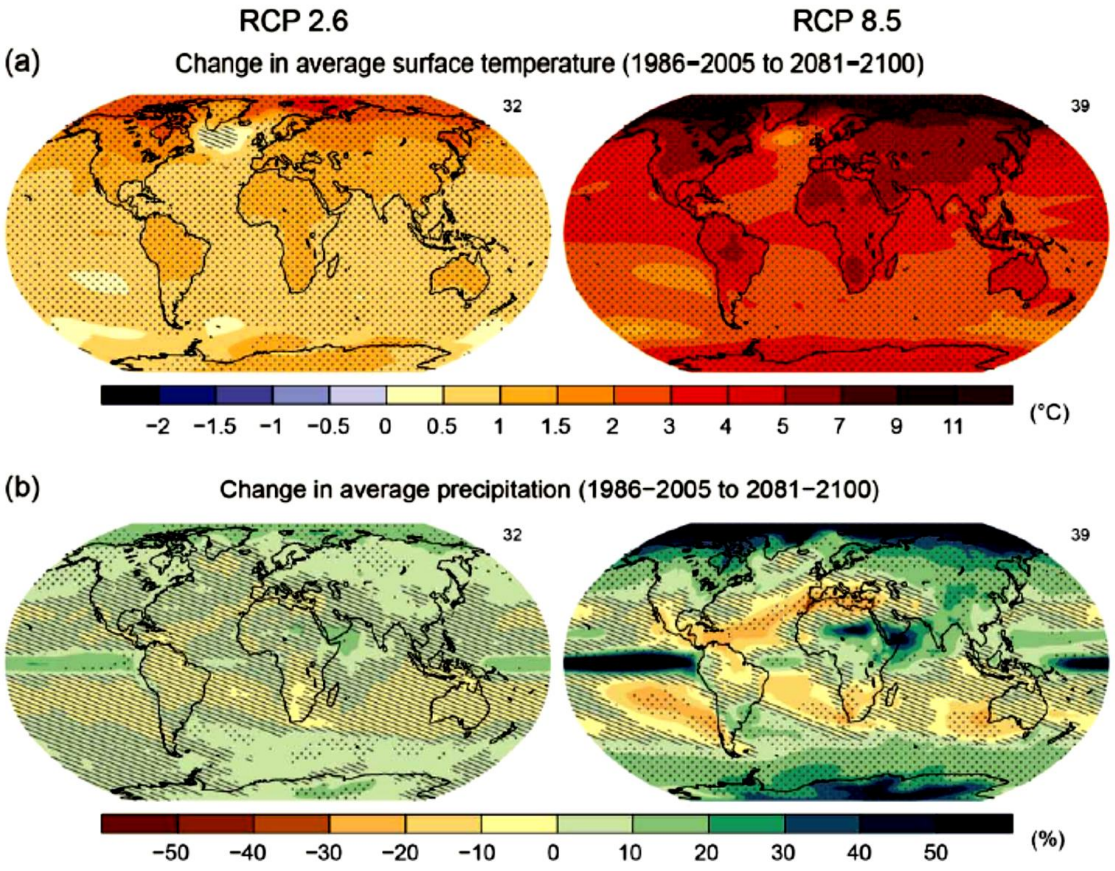


Figure 1.10: Spatial maps of CMIP5 multi-model mean for *(a)* annual mean surface temperature change and *(b)* percent change in annual mean precipitation from 1986-2005 to 2081-2100 for the lower (RCP 2.6) and higher (RCP 8.5) emissions scenarios. Hatching indicates where the multi-model mean change is small compared to internal variability (i.e., change is less than 1 standard deviation of the range of internal variability) and stippling indicates where the change is large compared to internal variability (i.e., change is greater than 2 standard deviations of the range of internal variability). The number of models used to create the mean is shown in upper right corner. (Adapted from Alexander et al. (2013).)

While these global climate model projections provide an extensive amount of information across the globe they are limited in their ability to provide directly applicable information to decision makers at the regional and local level because of the course spatial resolution of GCMs and potential regional and local biases (e.g., Fowler et al. 2007). Therefore, regional downscaling methods have been established to

generate relatively high resolution climate model output that can be incorporated into local scale models such as ecosystems, hydrologic, and agricultural models used in climate change impacts studies. However, these downscaling methods still utilize GCM output to drive their regional models and therefore model uncertainties in the GCM become amplified as they move downstream through regional and local model projections. Thus understanding, quantifying, and constraining uncertainties in GCMs is a fundamental necessity if the scientific community is to provide useful and reliable future projections that can be applicable at the regional and local level. In fact, Racherla et al. (2012) argue that the most important factor in climate change downscaling studies is the skill of the driving global model and that the highest priority should be given to improving GCM long-range climate predictive skill.

Therefore, the background motivation of this dissertation is to provide a better understanding of uncertainties within global and regional climate simulations from a GCM and to identify whether these uncertainties can be quantified and used to constrain future projections. There are three primary sources of uncertainty within GCM climate change predictions (e.g., Tebaldi and Knutti 2007; Hawkins and Sutton 2009): internal variability of the modeled climate system due to changes in the initial state of the climate, model uncertainty based on variations in model development and choice of physics parameters, and uncertainty in the response of the modeled climate due to changes in the external forcings (i.e., anthropogenic emissions scenario and changes to natural forcings). This study will focus on model uncertainties in the first two categories (i.e., internal variability and physics parameter variations) through use of a novel multi-thousand member perturbed physics ensemble (PPE) developed through the

Climate*prediction*.net (CPDN) project (see Chapter 3). This PPE is different than the CMIP Phase 3 (CMIP3) and Phase 5 (CMIP5) multi-model ensembles (MME's) in that it is composed of a large number of simulations generated from a single model with its physics parameters changed across their range of uncertainty. For example, there are 1,214 control simulations (i.e., constant annual but seasonally varying radiative forcing) and 1,692 transient simulations (i.e., includes historic forcings and future emissions scenarios) totaling approximately 170,000 years and 237,000 years of modeled output respectively. (See Chapter 3 for more details). The MME, on the other hand, consists of a relatively limited number of simulations (on the order of 30-50 simulations for control and transient ensembles) generated from different climate modeling groups across the world, each representing climate processes in different ways. (See Chapter 2, Sections 2.2, 2.3 for discussion of MME and PPE respectively.) Therefore the MME represents a collection of simulations considered by each modeling group to be their most probable representation of Earth's climate system (e.g., simulations are adjusted to best fit observational estimates). Thus, the PPE may provide additional information on uncertainties that may not be represented in the MME since the MME simulations are "tuned" to observations and multiple groups sometimes use the same or similar components or parameterizations and therefore they may not span the full range of uncertainties (e.g., Pennell and Reichler 2010; Masson and Knutti 2011). Additionally, the number of simulations in this PPE is significantly larger than most previous PPE analyses (e.g., McSweeney et al. 2012; Sexton et al. 2012) and includes the full coupled model system with atmosphere, ocean, land surface, and sea ice processes represented whereas many previous assessments did not include the fully dynamic coupled model

(e.g., Murphy et al. 2004; Piani et al. 2005; Stainforth et al. 2005; Knutti et al. 2006; Sexton et al. 2012) and therefore offers a more robust assessment of the impact model parameter variations can have on projected future climate.

One of the fundamental questions this study hopes to address is whether a large PPE can provide useful information to complement or improve information provided by MME's. Global and North American regional changes in monthly mean temperature and precipitation rate from 1941-2080 will be assessed to identify whether the PPE can simulate observed mean climate and its natural variability as well as historical changes such as long-term trends and relationships between global and regional changes. The observational analyses can then be used to identify whether some of the simulations produce unrealistic climates. If so, that information can be used to constrain future climate projections based on the model's goodness-of-fit to past performance. The analysis will be limited to monthly mean temperature and precipitation rate because limitations in the saved output (i.e., regional means include ocean grid cells) require observational data sets of sufficient quality over the oceans and because temperature and precipitation are the two main climatic variables assessed in climate change studies.

Additionally, another major question to be addressed in this study is whether climatic indices are sensitive to changes in model physics parameters and if this sensitivity occurs at the global and/or regional level and to what extent. This information can be used to quantify whether certain parameter values lead to unrealistic model climates which can then be used to constrain future projections.

Finally, this study will investigate how the modeled mean, variability, past changes, and future projected changes of the large PPE compares to CMIP MME's, including how any PPE constrained future projections compare to the CMIP MME's and whether the CMIP MME's are covering the full range of possible model uncertainty. Therefore the overall goal of this study is to quantify uncertainties in global and North American regional climate change over the observational and future time period (i.e., 1941-2080) using a multi-thousand member perturbed physics global climate model ensemble in order to provide a better assessment of uncertainties in projections of future climate change.

Chapter 2 provides an overview of climate modeling including the hierarchy of models available and the differences between the global climate model PPE and MME as well as sources of climate model uncertainty. Chapter 3 gives a description of the CPDN project and design of the climate model and experiment used to generate the large PPE in this study. Chapter 4 provides an overview of the observational data sets used for comparing the modeled output to the real Earth system as measured over the historical period. Chapter 5 evaluates the performance of the CPDN PPE model control simulations (i.e., constant annual but seasonally varying radiative forcing) to assess the modeled mean climate and its internal variability compared to the climate system's natural variability from 20th century observational data sets. It also provides an assessment of model sensitivity to parameter variations. Chapter 6 continues the assessment of the CPDN model internal variability but compares it to natural variability in the climate system as estimated from paleoclimate proxy data records from North America across the past few thousand years to provide an alternative measure that is not

limited to the relatively shorter temporal period of the higher resolution instrumental records and satellite data investigated in Chapter 5. Chapter 7 evaluates the performance of the CPDN PPE model transient simulations (i.e., simulations including historic forcings and future emissions scenarios) over the observational time period and assesses the sensitivity of modeled past and future trends to parameter variations. Then future projections are constrained based on observational performance and parameter sensitivity. Chapter 8 provides a comparison between the CPDN PPE control and transient simulation results with the CMIP3 and CMIP5 MME simulations and Chapter 9 summarizes the major results of the study and offers a discussion of the final conclusions and potential for future work.

CHAPTER 2

CLIMATE MODELING OVERVIEW

Understanding the full complexity of Earth's climate system is a difficult task requiring information at high spatial and temporal resolution extending over long periods of time. In an ideal setting, controlled experiments would be performed on the entire Earth system with all interacting processes closely monitored. This type of Earth laboratory does not exist and therefore it is simulated using numerical models with simplified features of the climate system wherein a number of experiments can be run using a variety of boundary conditions, initial conditions, and forcing mechanisms to better quantify how and why the climate has changed in the past and project how it might change in the future. This chapter provides a brief overview of climate modeling with an emphasis on global climate model ensembles because of their use throughout the rest of this study. Section 2.1 reviews the hierarchy of climate models available. Section 2.2 discusses the various uncertainties inherent in these climate models while Sections 2.3 and 2.4 describe global climate model multi-model ensembles and perturbed physics ensembles respectively.

2.1 CLIMATE MODEL HIERARCHY

There are a number of key processes or components that must be considered when constructing a model of the climate system. These include radiation (input, absorption and emission), dynamics (movement of energy), surface processes (changes in albedo, emissivity as well as energy and moisture exchanges), chemistry (chemical

composition and interactions) and resolution (temporal and spatial scales). There are different types of models that have been developed over the years, each varying in complexity and purpose. These can be summarized into four basic groups: lower complexity models, Earth Models of Intermediate Complexity (EMICs), global climate models (GCMs), and regionally downscaled models (e.g., McGuffie and Henderson-Sellers 2005).

2.1.1 Lower Complexity Models

Lower complexity models, sometimes identified as energy balance models (EMBs), are low-order models that may only calculate a global or hemispheric mean and do not provide information at the regional scale. They typically include solving an energy balance equation and may neglect balances of other physical components of the climate system (e.g., mass, momentum, moisture, chemical constituents). They can produce a large ensemble because of their simple computations and therefore can be useful for approximating output of more complex models.

2.1.2 Earth Models of Intermediate Complexity (EMIC)

Earth Models of Intermediate Complexity (EMIC) cover the spectrum from lower complexity EMBs to highly complex global climate models (GCMs) and can include dynamics of the atmospheric and oceanic circulation and representations of biogeochemical cycles. They can include a number of the processes simulated in GCMs but with less detail and coarser resolution. For example, two spatial dimensions

may be used instead of three. Some EMICs include fewer processes and lower detail in order to analyze feedbacks between as many components of the climate system as possible while others limit interactions between the various components in order to look at climate variability in long-term ensemble simulations.

2.1.3 Global Climate Models (GCMs)

The most sophisticated models are the global climate models or general circulation models (GCMs), which simulate a large number of processes and generate a three-dimensional view of the time evolution of the atmospheric and oceanic state. The most comprehensive GCMs are the coupled atmosphere-ocean GCMs which couple interactions between the various climate system components (e.g., atmosphere, ocean, land surface, sea ice, carbon cycle) and provide the most complete assessment of the structure and evolution of the climate system. GCMs solve a series of fundamental equations that involve the conservation of energy, momentum and mass. Their temporal and spatial resolutions continue to change with computational advancements but are roughly tens to hundreds of kilometers in the horizontal direction with approximately 20-40 vertical levels and a time step of around 10-30 minutes.

Due to the still relatively large spatial scales used in GCMs it is not possible to model all aspects of the climate system because some processes take place on the sub-grid scale. Therefore, it is necessary to parameterize these sub-grid processes in order to include their effects on other components of the climate system. Parameterization involves representing important unresolved physical processes in terms of their

relationships to resolved model variables. Parameterization schemes are utilized for a number of processes including radiation, land surface interactions, convection, large-scale precipitation, cloud cover, boundary layer evolution and orographic drag (Stensrud 2007).

The complexity of GCMs has advanced significantly over the past few decades as illustrated in Figure 2.1. With the addition of more processes and their continued improvements, GCMs have been better able to simulate the Earth's climate system. Additionally, computation power has significantly increased, allowing for increased horizontal and vertical resolutions in both the atmosphere and ocean as well as increased storage capacity for the higher resolution output. GCM ensembles and ensemble uncertainty will be discussed further in Sections 2.2, 2.3, and 2.4.

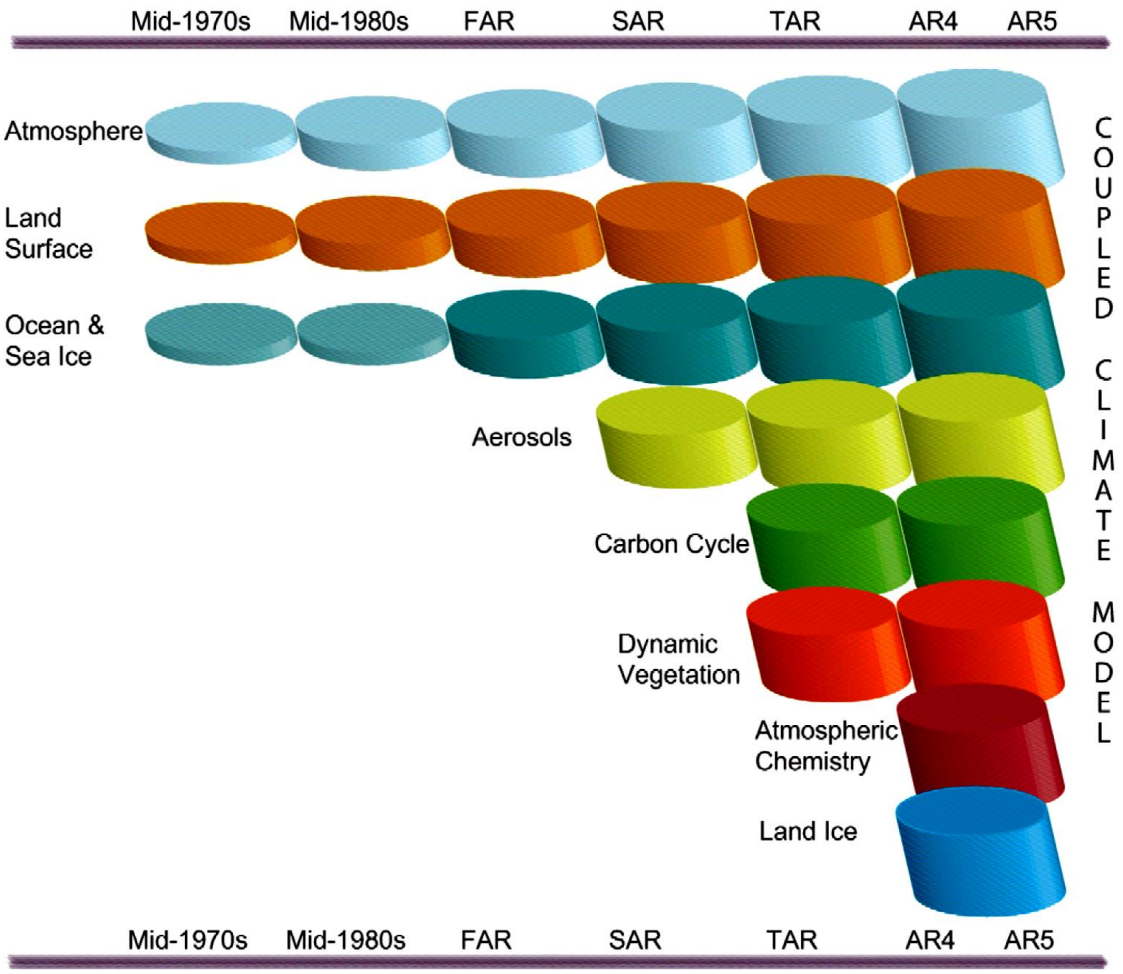


Figure 2.1: Illustration of the development of coupled climate models since the mid-1970's and when various components were introduced into the model. Cylinder height represents the complexity the processes and how it has increased over time. The timing of the five IPCC reports is given along the top. (From IPCC (2013).)

2.1.4 Regional Downscaled Models

Even with the improvements to spatial resolution within GCMs, their horizontal resolution is still only on the order of tens to hundreds of km's and therefore difficult to use for impacts assessments at the local level (e.g., ecosystems, hydrologic, agriculture). For this reason, two main downscaling methods have been developed to obtain more practical regional output. One method is referred to as dynamic downscaling which

uses a high-resolution regional climate model that is driven by boundary conditions set by a GCM. Dynamical downscaling models work much the same way GCMs do only they simulate physical processes at a higher resolution and over a relatively smaller area. The GCM simulates what is occurring around the rest of the world and then their output is incorporated into the boundaries of the regional model. The North American Regional Climate Change Assessment Program (NARCCAP) is one of the main sources for dynamically downscaled products for North America (Mearns et al. 2012; http://www.narccap.ucar.edu/index.html)

The other regional downscaling method is statistical downscaling which utilizes relationships between large-scale atmospheric variables and regional observations to estimate regional changes from GCM output. These statistical models make the assumption that relationships between large-scale features and the local climate will remain constant over time. Recently, a database of over 100 statistically downscaled climate projections from 33 CMIP5 GCMs were generated over the conterminous United States at 800 meter resolution (Thrasher et al. 2013).

2.2 Model Uncertainty in Future Projections

There are three main sources of uncertainty within GCM climate change future projections (e.g., Tebaldi and Knutti 2007; Hawkins and Sutton 2009): internal variability of the modeled climate system due to changes in the initial state of the climate, uncertainty in the response of the modeled climate due to changes in the external forcings (i.e., anthropogenic emissions scenario and changes to natural

forcings), and model uncertainty based on variations in model structural development and choice of physics parameters.

2.2.1 Internal Variability Uncertainty

The internal variability of a climate model refers to the natural variability within the modeled climate system in the absence of any external forcing. This variability can be due to non-linear dynamical processes in any of the components, such as the atmosphere or ocean (e.g., Schneider and Kinter 1994), the transfer of atmospheric variability into the ocean during the atmosphere-ocean coupling process for heat flux forcing (e.g., Dommenget and Latif 2008) and wind-driven fluctuations (e.g., Alexander 2013), or internal ocean variability (e.g., Delworth et al. 1993).

This uncertainty due to internal variability is important over shorter periods of time and over smaller regions. Using a number of different models, Hawkins and Sutton (2009) showed that internal variability played a large role in the uncertainties in projected annual temperature change out to roughly 10 years and were of greater importance at the regional level (Figure 2.2). Model uncertainty (discussed in Section 2.2.3) then took over as being most important out to around 50 years after which time external forcing scenario uncertainty (discussed in section 2.2.2) became dominant. Hawkins and Sutton (2011) found that internal variability was the dominant source of uncertainty for decadal scale changes in regional precipitation out to the first couple decades.

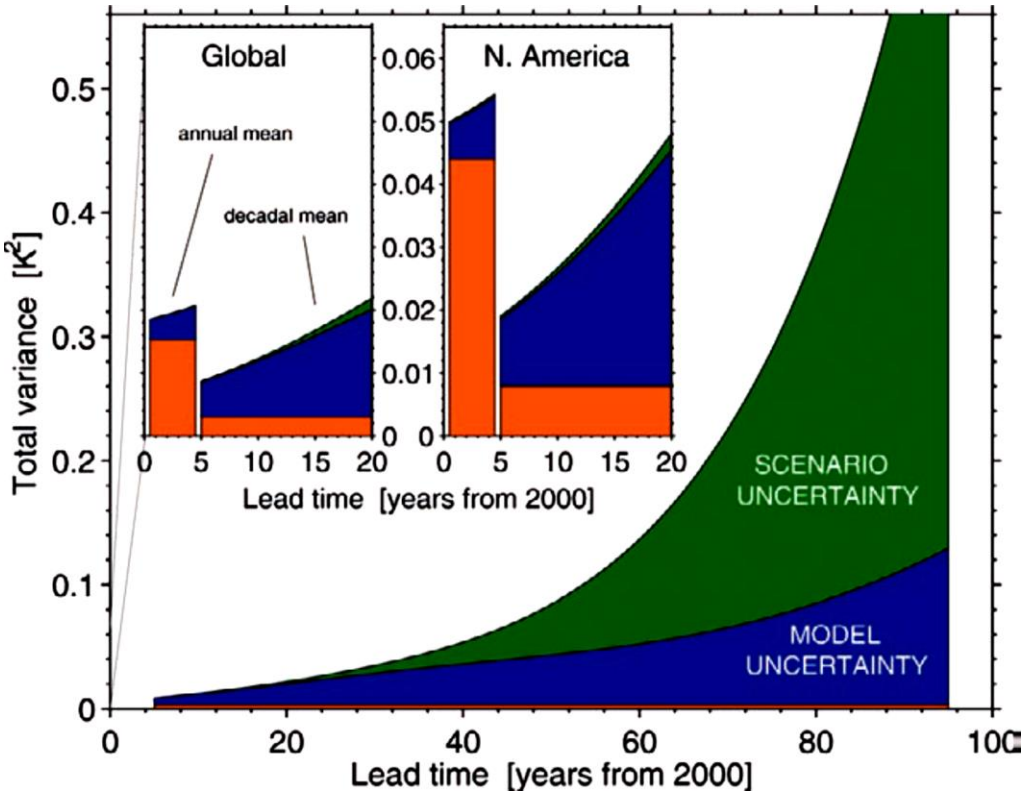


Figure 2.2: Total variance for global mean decadal surface air temperature predictions split into uncertainty in internal variability (orange), model (blue), and forcing scenario (green). Global and North American 20 projections are shown in the two smaller panels with variance in annual mean temperatures over the first five years given as well. (From Hawkins and Sutton (2009).)

Using a single model, Deser et al. (2012) looked at projections of temperature and precipitation trends from 2000-2060 using 40 simulations having the same external forcing (i.e., SRES A1B) but different atmospheric initial conditions. They compared the variation in trends in their initial condition ensemble to the trends found in the CMIP3 multi-model ensemble (see Section 2.2.3 and Section 2.3) under the same forcing scenario but using 21 different models to give an estimate of the variation in model trends due to internal variability. They found that internal variability accounted for approximately 25-50% of the variation in projected temperature trends over most of

the globe and 50-75% of the variation over western NA (Figure 2.3(b)). Additionally, they found that internal variability impacted precipitation more than temperature as is seen in Figure 2.3(a) where a larger percentage of the variation in trends is associated with internal variability, especially across central NA and other regions across the globe.

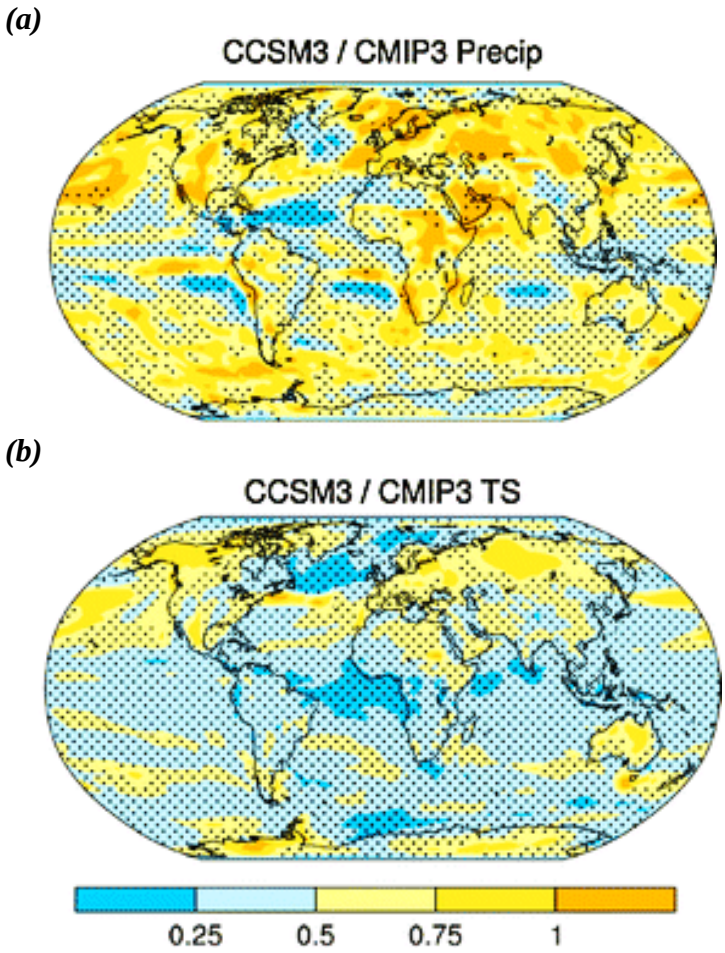


Figure 2.3: Ratio of the variability in trends (2005-2060) between an ensemble varying only its atmospheric initial conditions (i.e., internal variability) and the CMIP3 ensemble for *(a)* precipitation and *(b)* surface temperature. Stippling indicates ratios significantly different than 1 at the 95% confidence level. (Adapted from Deser et al. (2012).)

2.2.2 External Forcing Uncertainty

External forcing uncertainty is associated with a lack of understanding of how certain external factors driving the climate will change in the future. These external factors include changes in natural forcings such as solar output and volcanic activity and anthropogenic effects such as greenhouse gas or pollutant (i.e., aerosol) emissions, land use change, etc., which will be dependent on socioeconomic conditions and technical developments. Figure 2.4 provides possible future scenarios in anthropogenic greenhouse gas emissions (Figure 2.4(b)) based on the primary type of energy that is utilized moving forward across the 21st century (Figure 2.4(a)) as established in the Representative Concentration Pathways (RCPs) from Vuuren et al. (2011). As is evident from the different scenarios, even if a perfect climate model existed that was capable of simulating all of Earth's climate processes at all temporal and spatial resolutions there would still be a large degree of uncertainty in future projections simply based on the uncertainty in how future anthropogenic forcings will change. These external forcing uncertainties linked to future emission scenario differences are investigated using multi-model ensembles which are discussed in Section 2.3.

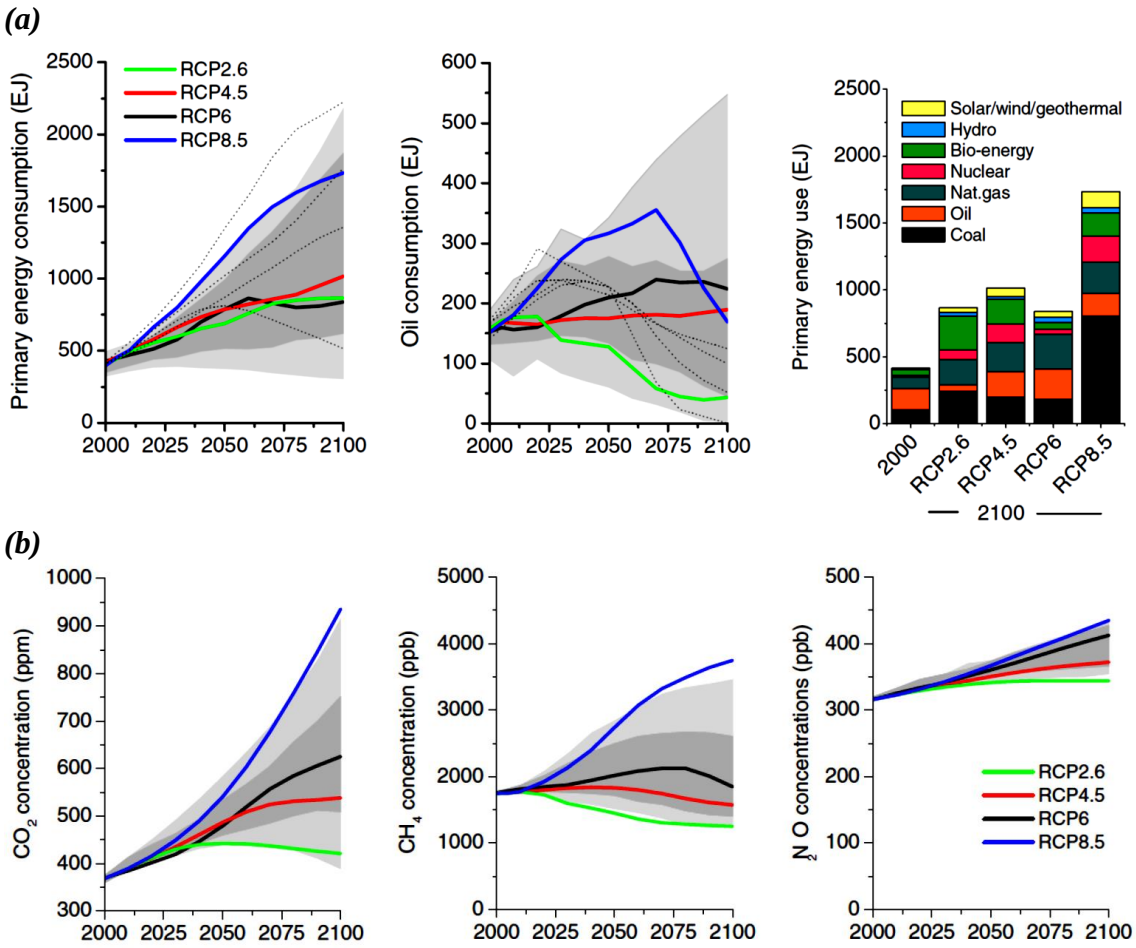


Figure 2.4: Alternative future scenarios from the four Representative Concentration Pathways (RCPs) described in Vuuren et al. (2011). Examples are shown for (a) the primary energy type used across the globe from 2000-2100, including a comparison between the various energy sources between 2000 and 2100 levels for each scenario (right plot) and (b) atmospheric concentrations of the three main anthropogenic greenhouse gases. Dotted lines represent the previous SRES scenarios and gray shading indicates results from other literature sources (see reference for details). (From Vuuren et al. (2011).)

Unknown changes to natural forcings (e.g., solar and volcanic) also create uncertainties in future climate projections but to a much lesser extent than anthropogenic effects. Future projections of climate change typically do not include scenario variations in these natural forcings because their impacts are assumed to be relatively small compared to anthropogenic effects over time periods of roughly a few

hundred years (e.g., solar impact from 1750-2010 shown in Figure 1.7 in Chapter 1) and because of their low predictability, especially volcanos. However, some climate studies are including such natural forcing scenario variations such as the model experiment used in this study (see Chapter 3, Section 3.3.3 and Figure 3.3).

2.2.3 Model Uncertainty

Model uncertainty originates from the fact that different models are constructed in different ways and therefore can produce differing responses when the same external forcings are applied. There are two types of model uncertainty typically classified as distinct from one another. These are model structural uncertainties and model physics parameter uncertainties (e.g., Tebaldi and Knutti 2007). The model structural uncertainties are associated with variations to broad scale components of the model such as type of grid, temporal and horizontal resolution, numerical methods used to solve the equations, parameterization schemes used, or other dynamical components such as those representing the carbon cycle, vegetation, cloud-aerosol interactions, atmospheric chemistry, etc. Multi-Model Ensembles (MMEs) are typically used to assess model structural uncertainties and they are discussed further in Section 2.3.

Model physics parameter uncertainties are associated with the fact that small-scale processes in the model cannot be resolved given the relatively coarse horizontal spatial resolution and therefore must be parameterized using larger-scale variables produced by the model (e.g., Stensrud 2007). In the development of the numerical representation of these processes, there are a number of parameters (i.e., variables in

equations) set to certain values which have their own range of estimated uncertainty. The combination of the uncertainties in all parameter variations makes up a model's overall physics parameter uncertainty. This type of uncertainty is investigated in perturbed physics ensembles (PPEs) which are discussed further in Section 2.4.

2.3 MULTI-MODEL ENSEMBLES

As discussed in Section 2.2.3 there are structural uncertainties inherent in the development of climate models because different modeling groups construct their models in different way. In order to assess these structural uncertainties, model intercomparison studies are typically used in which the model simulations from each of the major climate modeling centers are combined into a larger ensemble called a Multi-Model Ensemble (MME). These intercomparison studies started with the Atmospheric Model Intercomparison Project (AMIP; Gates 1992) which organized standard experimental protocol for atmosphere-only GCMs forced by observed sea surface temperature and sea ice variations, leading to an international framework for model diagnosis, validation, and intercomparison. Following the atmosphere-only model setup came the coupled atmosphere-ocean studies in the Coupled Model Intercomparison Project (CMIP; Meehl et al. 2000). These collections of coupled GCMs have grown in complexity over the years and have been the dominant means for assessing past and future climate change in major assessments such as the CMIP Phase 3 (CMIP3; Meehl et al. 2007a) for the IPCC Fourth Assessment Report (AR4; IPCC 2007) and Phase 5 (CMIP5; Taylor et al. 2011) for the IPCC Fifth Assessment Report (AR5; IPCC 2013).

In providing projections of future climate (e.g., see Chapter 1, Figures 1.9 and 1.10), these MMEs are sometimes weighted according to how well they simulate past metrics such as the climatological mean temperature over a specified region (e.g., Giorgi and Mearns 2002; Tebaldi et al. 2005) or observed trends (e.g., Greene et al. 2006). However, no individual climate model can be identified as the "best" with respect to all variables covering all regions (e.g., Lambert and Boer 2001; Gleckler et al. 2008) and therefore uncertainty remains as to the best metric to use when attempting to weight models (e.g., Tebaldi and Knutti 2007).

It also has been argued that weighting MMEs may not be appropriate given the fact that the models were already calibrated to observations in their development and therefore validating their output based on the same observations may not be that informative (e.g., Weigel et al. 2010). Additionally, it is uncertain whether models performing well in the past will perform well in the future (e.g., model components or parameterizations may not operate the same or follow the same assumptions in a warmer climate). Therefore, a more common method used in assessing MMEs is to give equal weight to all models which often utilizes the assumption that the multi-model mean response to external forcing is a more robust result than any single member of the model (e.g., Tebaldi and Knutti 2007).

Figure 2.5 provides an example of an equally weighted MME reported in IPCC (2007) and the uncertainties inherent when assessing regional-scale changes with such an ensemble. Projected changes across the 21st century are shown for annual and seasonal NA temperature (first row) and precipitation (second row) from the multi-model mean of 21 CMIP3 model simulations. The MME uncertainty is apparent when

looking at the third row which shows the number of models that project increases in precipitation. Therefore across central NA, where a transition zone between increasing and decreasing precipitation exists in the multi-model mean (second row), roughly half the models indicate an increase in precipitation and half a decrease. In terms of using GCMs to inform regional climate change impacts, such as in driving regionally downscaled models, the choice of GCM could have a marked impact on projected regional and local changes.

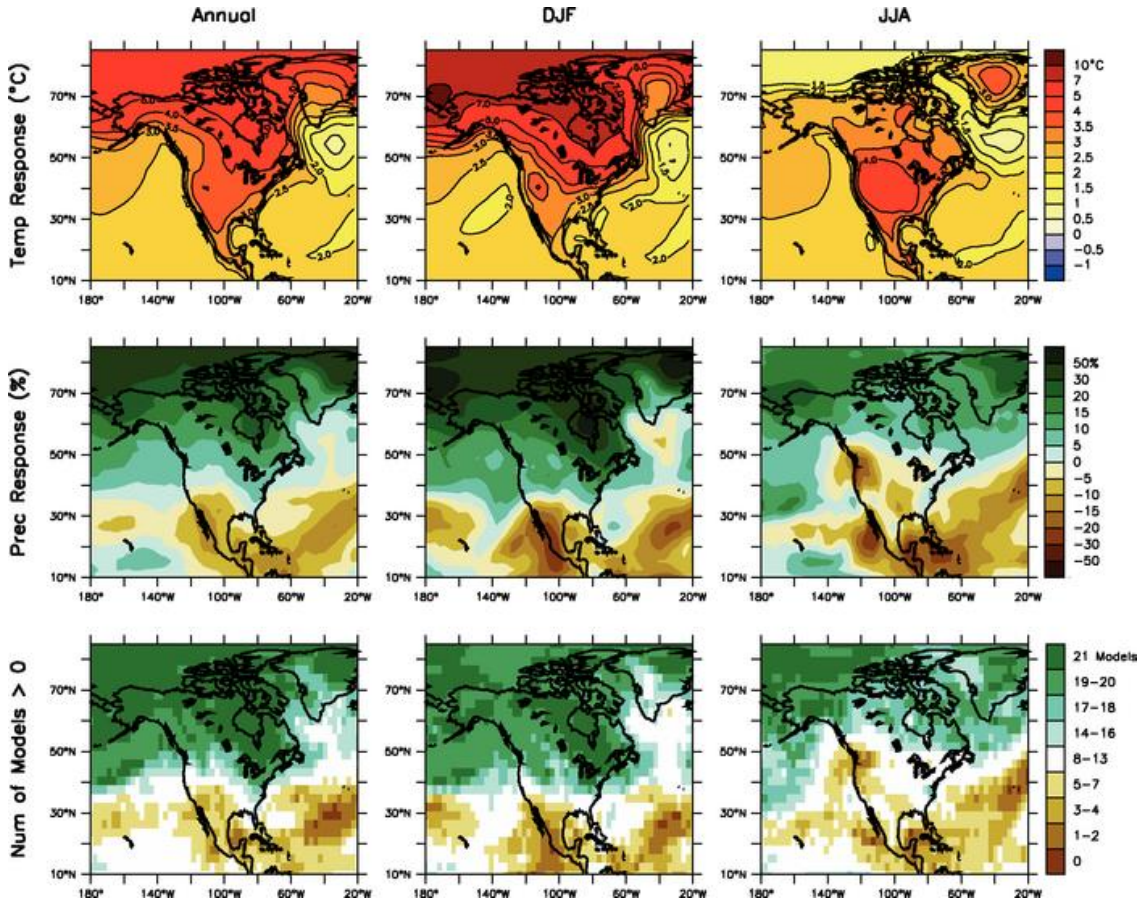


Figure 2.5: MMD multi-model mean temperature and precipitation changes over North America for the A1B scenario. Temperature change (top), fractional change in precipitation (middle) and number of models out of 21 that project increases in precipitation (bottom) for annual mean (left), DJF (center) and JJA (right) mean. Changes are given in terms of difference between 1980-1999 and 2080-2090. (From Christensen et al. (2007).)

The main advantage of MMEs is that the individual models undergo a wide range of development and testing against observed quantities to confirm their credibility (e.g., Gordon et al. 2000; Blackmon et al. 2001; Anderson et al. 2004; Johns et al. 2006). However, a main disadvantage is that they are not designed to sample the full range of model uncertainty as they are in essence an "ensemble of opportunity" assembled from whatever models are made available by the various modeling groups. The ensemble may undersample modeling uncertainties because even though they are produced by independent groups they still contain many similar features such as resolution, parameterizations, types of grids or numerical methods (e.g., Tebaldi et al. 2005; Murphy et al. 2007) and therefore cannot be considered completely independent. Additionally, their sample size is relatively small, around 20-50 simulations, even when multiple simulations are provided by some of the groups.

For that reason it is useful to explore model uncertainty using a different approach such as varying model physics parameters across their range of uncertainty. This approach is discussed in the next section.

2.4 PERTURBED PHYSICS ENSEMBLES

As discussed in Section 2.2.3, model parameter uncertainties are present in the development of climate models when small-scale processes must be parameterized and different parameterization schemes with uncertain parameter values are used to numerically represent processes occurring at the sub-grid scale. To assess these uncertainties, Perturbed Physics Ensembles (PPEs) are generated where a single model

is used to produce a number of simulations with variations to their physics parameters. The range of uncertainty for each parameter is estimated by experts with knowledge of the known physical processes (e.g., Murphy et al. 2004). The most concerted effort in assessing model uncertainty based on PPEs has come from studies based on the Hadley Centre model (e.g., Murphy et al. 2004; Piani et al. 2005; Stainforth et al. 2005; Barnett et al. 2006; Collins et al. 2006; Harris et al. 2006; Knutti et al. 2006; Webb et al. 2006; Collins et al. 2007; Knight et al. 2007; Sanderson et al. 2008a; Sanderson et al. 2008b; Frame et al. 2009; Rougier et al. 2009; Sanderson et al. 2010; Collins et al. 2011; Rowlands et al. 2012). A few other modeling groups also have taken part in GCM PPE assessments (Annan et al. 2005) as well as when using simplified models (e.g., Schneider von Deimling et al. 2006). A brief review is provide below of the series of PPE studies related to the Hadley Centre model that leads up to the model and experiment used in this study (described in Chapter 3).

Murphy et al. (2004) set the stage for this series of Hadley Centre-based PPEs by using the Hadley Centre's atmospheric model (HadAM3; Pope et al. 2000) coupled to a mixed layer slab ocean (i.e., termed HadSM3) to generate 53 simulations with variations to 29 parameters deemed important for controlling key physical characteristics of the sub-grid scale atmospheric and surface processes (e.g., impacting large-scale cloud, convection, radiative transfer, sea ice, surface and boundary layer processes and dynamical transports). These parameters were changed (i.e., perturbed) one at a time and simulations run for present-day and for doubled atmospheric CO_2 to calculate global mean temperature response after doubling CO_2 (i.e., called climate sensitivity). They found a wide range of possible climate sensitivities – of similar

magnitude as found in MME experiments – due to the variation in parameters (i.e., 90% range of 2.4 – 5.4°C). (Note that in all discussions that follow, specific information on each parameter is not given. All relevant parameters are discussed in detail in Chapter 3.)

Stainforth et al. (2005) provided a similar experiment using the same HadSM3 model but focused on a set of six parameters important in cloud and precipitation processes, varying them in a number of different way (i.e., 449 unique combinations) and then applying different initial conditions to produce a set of over 2,500 simulations. This ensemble was produced using the Climate*prediction*.net (CPDN) distributed computing network, as was all of the remaining studies discussed below (See Chapter 3 for description of CPDN). These simulations contained a 15 year calibration phase where heat flux adjustments were calculated to maintain a stable climate when sea surface temperatures (SSTs) were held constant followed by a control phase driven by pre-industrial conditions in which SSTs were allowed to vary and subject to the atmosphere-ocean heat exchange with corrections for the calculated heat flux adjustments and then a doubled CO_2 phase which was the same as the control phase but driven by conditions with double the amount of atmospheric CO_2. They found a very wide range of possible climate sensitivities based on these parameter variations, ranging from around 2-11°C. These initial papers proved that perturbing parameters within a single model could result in an uncertainty range as large or larger than that found in MME studies for assessing large-scale climate system processes.

Following Stainforth et al. (2005), a series of studies continued the investigation of climate sensitivity using the HadSM3 model including Piani et al. (2005) who

provided a best estimate climate sensitivity of 3.3°C with an 90% uncertainty range from roughly 2-6°C and Knutti et al. (2006) who calculated a relationship between climate sensitivity and the magnitude of the seasonal cycle within regions across the globe (i.e., Giorgi and Francisco 2000) where the best estimate climate sensitivity was between 3-3.5°C with a 95% range of 2-5°C and those models with high sensitivities were found to produce seasonal cycles with larger magnitudes compared to observations.

Knight et al. (2007) continued the assessment of climate sensitivity but included a significantly larger number of simulations (i.e., around 57,000) and included variations in computer hardware (i.e., processor, RAM size, and clock speed) and software (i.e., the specific client middleware system used to implement the model on different computer systems) and found that the effect of hardware and software difference were small compared to parameter variation, accounting for less than 1% of climate sensitivity variation. Knight et al. (2007) also found that the entrainment coefficient in clouds was the most important parameter and accounted for 30% of the variation seen in climate sensitivity (refer to Chapter 3, Section 3.3.1 for discussion of parameters and their variations).

Sanderson et al. (2008a) focused on identifying the dominant physical processes responsible for variations in climate sensitivity across a PPE composed of roughly 6,700 model simulations. They found two parameters having the largest impact on climate sensitivity, the entrainment coefficient and ice fall speed. Sanderson et al. (2008b) conducted a similar experiment but used an artificial neural network to interpolate climate sensitivities between the limited number of parameter variations

(e.g., often limited to 2-3 variations) and again found that the most important parameters were entrainment coefficient and ice fall speed with a subset of other parameters also showing degrees of importance when climate sensitivities are exceptionally low or high. These parameters were the empirically adjusted cloud fraction and critical relative humidity.

Ackerley et al. (2009) used a smaller set of simulations in a PPE (i.e., 243) but introduced a sulfur cycle parameterization scheme into the HadSM3 model and varied a set of parameters within that scheme. They found that none of the parameters in the sulfur cycle scheme had much of an impact on climate sensitivity but the more important aspect was that they produced a realistic sulfur cycle that was included in all future versions of the CPDN model.

Following these climate sensitivity experiments with the simplified HadSM3 model, a new set of PPEs were generated using a fully coupled atmosphere and fully dynamic ocean GCM which was termed HadCM3L (Frame et al. 2009), a version of the coupled Hadley Centre model HadCM3 (Gordon et al. 2000; Collins et al. 2001) only with slightly lower ocean resolution (see Chapter 3 for details). Sanderson et al. (2010) used the HadCM3L model with roughly 1,600 simulations varying 24 independent parameters from the atmospheric and oceanic models as well as the sulfur cycle. Model simulations were run from 1850-2000 using observed forcings and then from 2001-2060 using SRES scenario A1B including a number of alternative scenarios for solar and volcanic past and future forcing (see reference for more details). They found that parameters governing cloud formation, convection strength, and ice fall speed were the

most significant in altering climate feedbacks. Perturbations of oceanic and sulfur cycle parameters had relatively little effect on the atmospheric feedbacks.

The HadCM3L model was then used in a concerted effort to generate a large PPE under the British Broadcasting Corporation (BBC) Climate Change Experiment (CCE), also known as the Transient Coupled Model Experiment (Frame et al. 2009; http://www.bbc.co.uk/sn/climateexperiment) which consists of simulations covering the period 1920-2080 using historic forcings and the SRES A1B scenario. (The BBC CCE is explained in detail in Chapter 3, Section 3.3.) Fowler et al. (2010) used 304 simulations from the HadCM3L BBC CCE to assess projected changes in extreme precipitation over the United Kingdom (UK) and found that detectable changes in extreme winter precipitation may be detectable by the simulated year 2010 and that changes in extreme summer precipitation was not detectable through the entire simulation (i.e., out to 2080). They also found that the entrainment coefficient and ice fall speed were important parameters for governing changes in summer precipitation and that the accretion constant and scaling factor for anthropogenic sulfur aerosol emissions also were found to have a significant impact on the time of detectable change. Their results suggested that increased precipitation efficiency, through changes in the entrainment coefficient, have an important effect on heavy precipitation generation in climate models.

Finally, Rowlands et al. (2012), used 2,752 simulations from the HadCM3L BBC CCE to observationally constrain future projections of global temperature. They created a goodness-of-fit statistic based on spatio-temporal patterns of surface temperatures around the globe from 1961-2010 to identify simulations performing

better over the observational period. They found that the original PPE extended to larger global temperatures compared to the constrained ensemble which indicated temperature increases between 1.4-3.0°C by 2050, relative to the 1961-1990 mean (Figure 2.6). The current study builds on Rowlands et al. (2012) by investigating similar HadCM3L simulations across both the globe and North American regions. The next chapter describes in detail the HadCM3L BBC CCE simulations used in this study as well as all parameter variations.

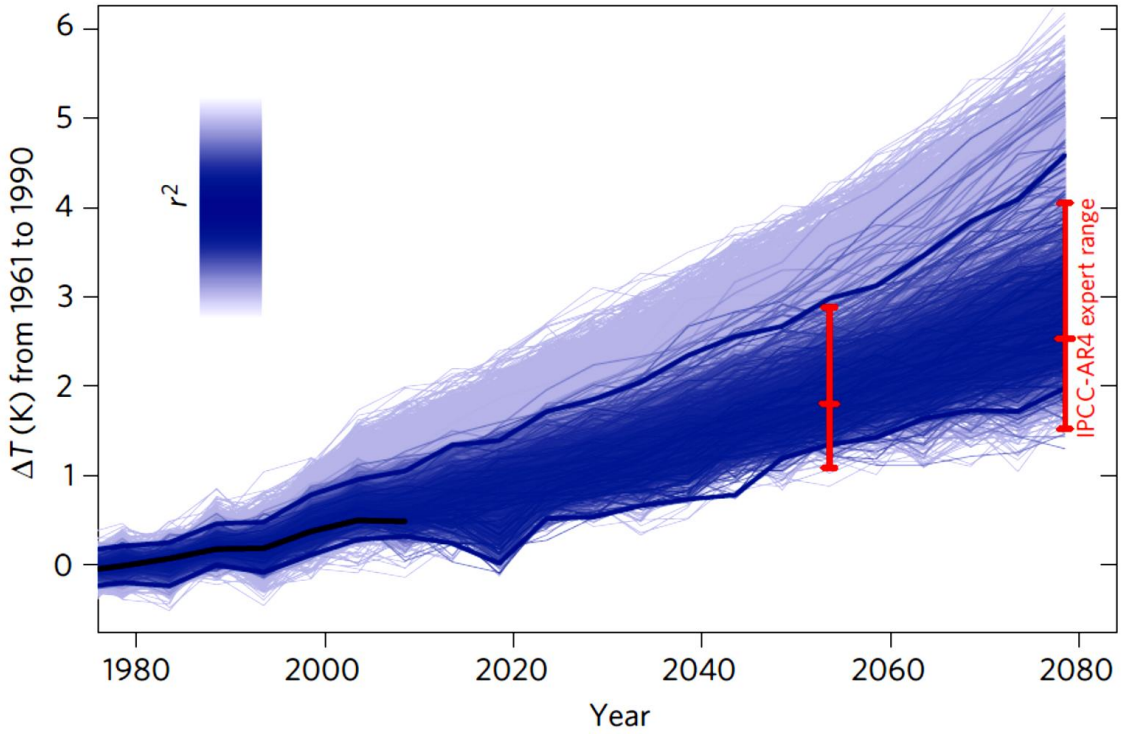


Figure 2.6: Global mean temperature anomalies (from 1961-1990 mean) for 2,752 simulation from the HadCM3L BBC CCE. Blue shading indicates a calculated goodness-of-fit metric (r^2) with dark blue lines indicating the 66% confidence range. Global mean observations are shown as the thick black line and red bars indicate the CMIP3 ensemble likely range and multi-model mean (center red dash). (From Rowlands et al. (2012).)

CHAPTER 3

CLIMATE*PREDICTION*.NET CLIMATE MODEL AND EXPERIMENT DESIGN

This chapter contains a description of the climate model and experiment developed by the Climate*prediction*.net (CPDN) project that is used in this study. Section 1 provides background information on the design and goals of the CPDN project. Section 2 describes the HadCM3L global climate model and Section 3 describes the accompanying BBC Climate Change Experiment (CCE), the output of which is used in this study.

3.1 Climate*prediction*.net

3.1.1 CPDN Project Design

Climate*prediction*.net (CPDN) is a distributed computing project operated out of Oxford University designed to investigate climate modeling uncertainties by generating a large number of climate model simulations, each containing slight variations to their model physics parameters, forcings, and initial conditions in an effort to assess how these variations impact the resulting modeled climate and how such information can be used when modeling future climate projections (Allen 1999; Stainforth et al. 2002; Stainforth et al. 2004; Massey et al. 2006). While typical climate model simulations require the use of large supercomputers, CPDN utilizes the processing power of thousands of personal computers whose idle time has been voluntarily donated by participants from the general public. This is accomplished through use of the Berkeley

Open Infrastructure for Network Computing (BOINC) software platform hosted out of the Space Sciences Laboratory at the University of California, Berkeley (http://boincstats.com). BOINC was originally designed for the Search for Extra-Terrestrial Intelligence (SETI@home) project (Reichhardt 1999; Korpela et al. 2001) which created the distributed computing network concept for analyzing narrow-bandwidth radio telescope signals from space in an effort to detect signals from extra-terrestrial intelligent life. For these distributed computing network projects, participants download programs and input files to their personal computers which run the applications during idle processing time and then, when complete, upload the computed output files back to the CPDN main servers.

The processing power from a distributed computing network can rival or surpass that of a supercomputer with the added benefit of not having to share central processing unit (CPU) time with jobs from other projects, as is common with most supercomputers. CPDN currently has over 260,000 participants (around 18,000 active at any given time) from over 20 different countries providing over 530,000 host computers (around 25,000 active). This corresponds to an average performance of roughly 32 trillion Floating-point Operations Per Second (FLOPS) or 32 TeraFLOPS.[2] (Refer to http://boincstats.com/en/stats/2/project/detail for the most up-to-date performance statistics.) Figure 3.1 shows the processing power of the world's top supercomputers over time. While performance of the top supercomputers has risen above the 32

[2] By comparison, the more established SETI@home project has nearly 1.4 million users (approximately 150,000 active) and over 3.3 million host computers (220,000 active) across 233 countries resulting in around 640 TeraFLOPS.

TeraFLOPS mark in recent years, the distributed computing network still holds the advantage of being able to dedicate all processing power to its own specified projects.

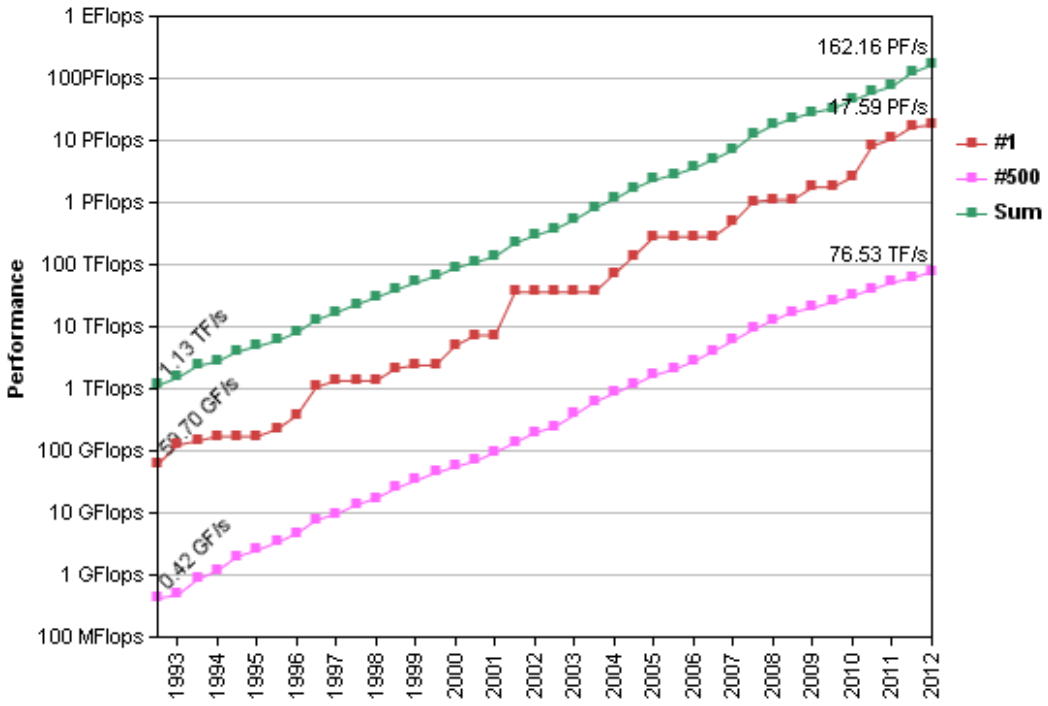


Figure 3.1: Supercomputer Performance over time. Performance is calculated in terms of Floating-point Operations Per Second (FLOPS) and shown for the top performer for a given year (red), 500th top performer (pink) and the sum FLOPS over all 500 top supercomputers (green). (From top500.org.)

3.1.2 Overview of CPDN Experiments

Here a brief review is presented of the progression of experiments launched by CPDN. Refer to the perturbed physics ensemble section in Chapter 2 for a discussion of any pertinent results that have come out of CPDN research.

CPDN was officially launched in 2003 using the UK Met Office Hadley Centre Slab Model version 3 (HadSM3), a global climate model containing an atmospheric

model (HadAM3) and simplified single layer "slab" ocean. The corresponding initial experiment run by each participant was comprised of three, 15-year phases: a calibration phase to calculate heat flux adjustments required to maintain a stable climate when sea surface temperatures (SSTs) were held constant (i.e., fluxes representing heat transport by ocean currents which were not included in the model), a control phase driven by pre-industrial conditions in which SSTs were allowed to vary and subject to the atmosphere-ocean heat exchange with corrections for the calculated heat flux adjustments, and a doubled CO_2 phase which was the same as the control phase but driven by conditions with double the amount of atmospheric CO_2.

In 2004 a thermohaline circulation experiment was launched which used the same HadSM3 model and three phases from the initial experiment but included a fourth 15-year phase where SSTs in the North Atlantic were adjusted to resemble the impacts of a 50% slowdown in the thermohaline circulation (i.e., the meridional overturning circulation in the north Atlantic).

In 2006 the fully coupled atmosphere-ocean general circulation model (AO-GCM) HadCM3L was released to participants under what was identified as the BBC Climate Change Experiment (CCE). The model is sometimes referred to as the transient coupled model because climate forcings are allowed to vary with time in the experiment, generating a hindcast covering 1921-2000 and a forecast from 2001-2080. This model and experiment are used in this study and therefore a more detailed description is provided in Section 3.2 for the HadCM3L model and Section 3.3 for the BBC CCE.

In 2008 a geo-engineering experiment was developed to investigate global climate impacts that would result from humans injecting aerosol particles into the stratosphere. The HadCM3L model was used and simulations generated from 2000-2080 with and without the inclusion of various amounts of aerosols to quantify its impacts.

And in 2010 a paleoclimate experiment was initiated called the millennium experiment that investigated climate across the past millennium by running simulations from 800 AD to 1900 AD with a variety of perturbed model physics parameters and natural forcing scenarios. Also in 2010 a regional climate modeling experiment was launched called weather@home which ran regional climate models in the distributed computing network platform to generate higher resolution climate change results. The regions of the world modeled in this experiment were Europe, Western United States, and Southern Africa.

3.2 HadCM3L Model Design

HadCM3L (Jones and Palmer 1998) is a coupled atmosphere-ocean general circulation model (AO-GCM) based on the UK Met Office Hadley Centre Coupled Model version 3 (HadCM3; Gordon et al. 2000; Collins et al. 2001) which is the successor of model version 2, (HadCM2; Johns et al. 1997), and the original Hadley Centre coupled model (Murphy 1995a, 1995b; Murphy and Mitchell 1995) and is run under the UK Met Office Unified Model (MetUM) system (Cullen 1993; Brown et al. 2012). Table 3.1 highlights the key components in the HadCM3L atmospheric and

ocean model design. These are discussed further in the next two subsections. The atmosphere-ocean coupling strategy and flux adjustments are unique to the specific climate change experiment used (i.e., BBC-CCE) and therefore will be described in that section (Section 3.3.2).

Table 3.1: Summary of key components in the HadCM3L model design.

Atmosphere	
Horizontal Grid	Arakawa-B Grid [Arakawa and Lamb 1977]
Horizontal Resolution	2.5° latitude by 3.75° longitude
Vertical Grid	Lorenz Grid [Lorenz 1960; Holdaway et al. 2012]
Vertical Resolution	19 levels; hybrid coordinate [Simmons and Burridge 1981]
Dynamics	Eularian advection; split-explicit time integration [Cullen and Davies 1991; Cullen 1993]
Integration Time Step	30 minutes
Radiation	[Edwards and Slingo 1996; Cusack et al. 1998; Cusack et al. 1999]
Clouds	[Smith 1990; Martin et al. 1994; Gregory and Morris 1996]
Precipitation (Large Scale)	[Senior and Mitchell 1993; Gregory 1995]
Convection	[Gregory and Rowntree 1990; Gregory and Allen 1991; Gregory et al. 1997]
Boundary Layer	[Smith 1990, 1993]
Land Surface	[Cox et al. 1999]
Gravity Wave Drag	[Gregory et al. 1998]
Sulfur Cycle	[Ackerley et al. 2009]
Ocean	
Horizontal Resolution	2.5° lat by 3.75° long
Vertical Resolution	20 levels; higher resolution near surface
Bathymetry	[ETOPO5 1988; Gordon et al. 2000]; Iceland removed; Denmark Straits deepened
Dynamical Equations	Primitive equations; rigid-lid [Bryan 1969b; Cox 1984]
Integration Time Step	60 minutes
Vertical Mixing (momentum)	Mixed layer: K-Theory [Large et al. 1994] Below mixed layer: K-Theory [Pacanowski and Philander 1981]
Vertical Mixing (tracers)	Mixed layer: hybrid scheme [Large et al. 1994; Kraus and Turner 1967] Below mixed layer: K-Theory [Pacanowski and Philander 1981]
Eddy Mixing	[Gent and McWilliams 1990); Visbeck et al. 1997; Griffies et al. 1998]
Topographically-Based Mixing	Straits of Gibraltar scheme; Greenland-Iceland ridge overflow scheme [Gerdes et al. 1991; Roether et al. 1994]
Sea Ice	[Crossley and Roberts 1995]
Radiation Absorption	Solar double exponential decay [Paulson and Simpson 1977]

3.2.1 Atmospheric Model

The atmospheric component of HadCM3L is the same atmospheric model used in its parent model HadCM3 (Johns et al. 1997). It has a horizontal resolution of 2.5° latitude (lat) by 3.75° longitude (long), corresponding to a global grid 96 cells north/south by 72 cells east/west with cells approximately 417 km in the north/south direction by 278 km in the east/west direction at the Equator and 295 km north/south by 278 km east/west at 45° of latitude[3]. An Arakawa-B staggered grid is used (Arakawa and Lamb 1977) with wind components calculated at grid cell boundaries and all other variables calculated at a cell's center.

The vertical grid consists of 19 layers following a sigma (σ)-p hybrid coordinate (Simmons and Burridge 1981) with increasing resolution towards the surface and layers that transition from a σ coordinate[4] (i.e., terrain-following) in the lowest four layers to pure pressure layers in the three layers nearest the upper boundary at around 30 km altitude (i.e., approximately 10 mb atmospheric pressure near the center of the stratosphere). Table 3.2 shows the σ-p hybrid coordinate used in the vertical grid and Figure 3.2 shows a general representation of the vertical layers. A Lorenz vertical grid is applied (e.g., Lorenz 1960; Holdaway et al. 2012) where the vertical component of the wind is calculated at the layer boundaries while all other variables are calculated in between the layers.

---

[3] Latitudinal distances for each degree of change remain relatively constant at approximately 111 km (only minor discrepancies caused by changes in Earth's not quite spherical, ellipsoidal, shape) and therefore grid cells maintain a 278 km latitudinal cell size while longitudinal distances for each degree of change varies from near 111 km near the equator to zero at the poles. Therefore the longitudinal cell size at locations of interest over North America are roughly 361 km at 30°N, 268 km at 50°N, and 143 km at 70°N while latitudinal cell size remain a constant 278 km for each.

[4] The σ coordinate is defined as the pressure at a given level divided by the surface pressure. This allows vertical levels in the σ coordinate system to follow orography.

Table 3.2: The σ-p hybrid vertical grid of Simmons and Burridge (1981) used to generate the HadCM3L atmospheric model's vertical structure. The hybrid coordinate (H) is calculated using the equation $H = (A/10^5\ Pa) + B$. (From Johns et al. (1997).)

Layer	A (Pa) layer centre	A (Pa) layer boundary	B layer centre	B layer boundary	Hybrid coordinate
		0.005×10^4		0.000	0.0005
19	0.046×10^4		0.000		0.005
		0.100×10^4		0.000	0.010
18	0.148×10^4		0.000		0.015
		0.200×10^4		0.000	0.020
17	0.296×10^4		0.000		0.030
		0.400×10^4		0.000	0.040
16	0.553×10^4		0.002		0.057
		0.718×10^4		0.003	0.075
15	0.886×10^4		0.011		0.100
		1.065×10^4		0.018	0.125
14	1.180×10^4		0.031		0.149
		1.300×10^4		0.045	0.175
13	1.366×10^4		0.063		0.200
		1.434×10^4		0.082	0.225
12	1.458×10^4		0.104		0.250
		1.482×10^4		0.127	0.275
11	1.469×10^4		0.153		0.300
		1.456×10^4		0.179	0.325
10	1.401×10^4		0.215		0.355
		1.345×10^4		0.251	0.385
9	1.232×10^4		0.299		0.422
		1.118×10^4		0.348	0.460
8	0.947×10^4		0.410		0.505
		0.773×10^4		0.473	0.550
7	0.581×10^4		0.541		0.599
		0.385×10^4		0.611	0.650
6	0.241×10^4		0.675		0.699
		0.094×10^4		0.741	0.750
5	0.047×10^4		0.788		0.793
		0.000×10^4		0.835	0.835
4	0.000×10^4		0.870		0.870
		0.000×10^4		0.905	0.905
3	0.000×10^4		0.930		0.930
		0.000×10^4		0.956	0.956
2	0.000×10^4		0.975		0.975
		0.000×10^4		0.994	0.994
1	0.000×10^4		0.997		0.997
		0.000×10^4		1.000	1.000

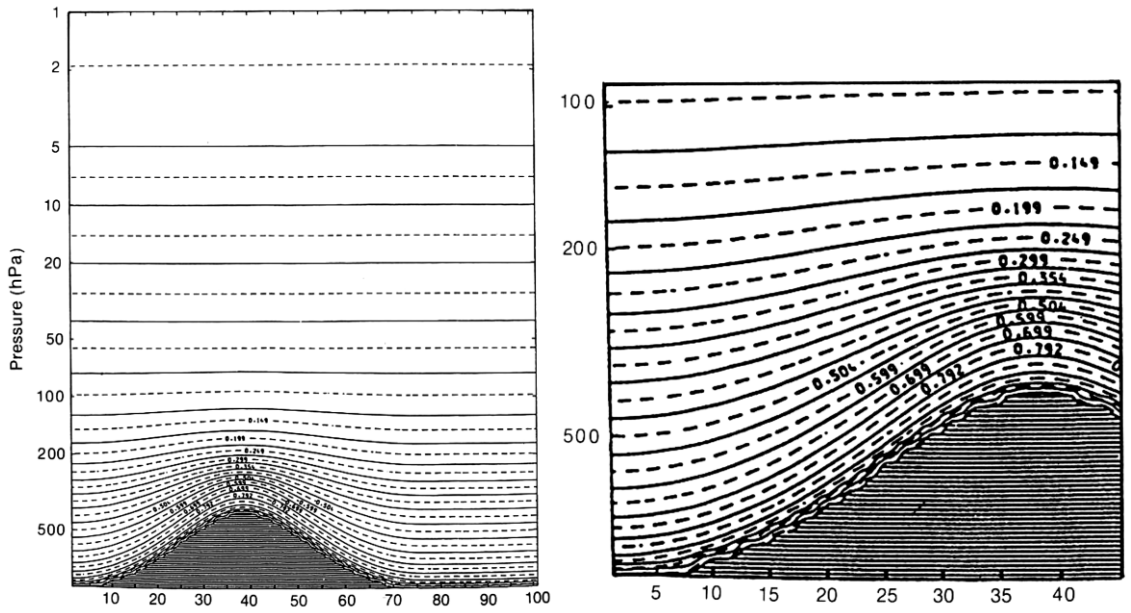


Figure 3.2: Illustration of the HadCM3L atmospheric model's σ-p hybrid coordinate vertical structure (left) with an enlarged view of the lowest 100 mb (right). Vertical layers transition from σ (i.e., terrain-following) layers near surface to pure pressure layers at the top boundary with higher resolution near the surface. Hybrid coordinate values are provided at the layer centers across the lowest 100 mb (refer to Table 3.2). (From Cullen (1993).)

The dynamical equations used are quasi-hydrostatic versions of the primitive equations developed to conserve energy, mass, momentum, angular momentum, and total water with full representation of the Coriolis force (Cullen and Davies 1991; Cullen 1993). A Eularian advection scheme is used with split-explicit time integration (Cullen and Davies 1991) and a dynamical time step of 30 minutes. The derived model variables include temperature, pressure, horizontal wind components, liquid water potential temperature, and total water mixing ratio.

A number of complex processes take place on the sub-grid scale and therefore must be parameterized in order for their effects to be included in the model. The parameterization schemes used in the atmospheric model are summarized below. They

are run every three hours and include schemes for radiation, clouds, large scale precipitation, convection, boundary layer, land surface, gravity wave drag, and the sulfur cycle. (See Section 3.3.1 for parameterization scheme parameter perturbations included in the climate change experiment for this study.)

RADIATION: The radiation scheme is from Edwards and Slingo (1996) and includes modifications from Cusack et al. (1999). This scheme incorporates six shortwave and eight longwave bands and includes the effects of CO_2, H_2O, and O_3 as well as the minor trace gases O_2, N_2O, CH_4, CFC11, and CFC12. Aerosol effects also are included (Cusack et al. 1998).

CLOUDS: The cloud scheme is from Smith (1990) with modifications from Gregory and Morris (1996) and Martin et al. (1994). The scheme generates cloud ice, cloud water, and cloud amount from model variables of total moisture and liquid water potential temperature. Mixed phase, liquid and ice, clouds are allowed in the scheme. In general, clouds form in the model when a critical relative humidity value is reached within a given grid cell. Cloud-radiation feedbacks are included as well as interactions with the other parameterization schemes.

PRECIPITATION (LARGE-SCALE): Large-scale precipitation is parameterized using Senior and Mitchell (1993) which converts cloud liquid and ice into precipitation based on a total water and total ice content threshold. Phase changes between cloud water and ice are represented, and precipitation rates can be enhanced through the process of seeding from layers above as precipitation is allowed to fall from one layer to another. Also, the evaporation of falling rain and snow based on Gregory (1995) is included.

CONVECTION: Convection (moist and dry) is parameterized using the mass flux scheme of Gregory and Rowntree (1990) with the inclusion of downdrafts (Gregory and Allen 1991) and representation of convective momentum transport (Gregory et al. 1997). Shallow, deep, and mid-level convection are included. Convective parcels are allowed to mix with the environmental air surrounding it and evaporation occurs with falling precipitation. Forced entrainment and detrainment also are included.

BOUNDARY LAYER: The boundary layer scheme (Smith 1990, 1993) is a first order turbulent mixing scheme that mixes heat, moisture, and momentum into the vertical within the lowest 1-2 km atmospheric model layers which can be influenced by the modeled Earth's surface (i.e., boundary layer). A key component of the scheme is use of a vertical mixing coefficient that depends on various factors that can influence the strength of turbulent motions within the boundary layer, factors such as wind shear and atmospheric stability.

LAND SURFACE: The land surface is parameterized using the Met Office Surface Exchange Scheme (MOSES) from Cox et al. (1999). This scheme calculates surface to atmosphere water and energy fluxes from associated surface and subsurface (four soil layers) model variables. It also calculates vegetation to atmosphere fluxes of CO_2, incorporating both photosynthesis and stomatal conductance (i.e., exchange of CO_2 and water vapor through plant stomata). Additionally, freezing and melting is represented in the sub-surface soil layers, and surface and subsurface basin-wide river catchment runoff is instantaneously transported to the respective costal outflow location.

GRAVITY WAVE / OROGRAPHIC DRAG: The generation and breaking of sub-grid scale orographically forced atmospheric gravity waves are represented using Gregory et al. (1998) which is an advancement of Palmer et al. (1986). The scheme includes representation of anisotropic orography (i.e., orography that is non-circular in its horizontal structure), low-level wave breaking of trapped waves along the lee side of orography, flow blocking, and the hydraulic jump phenomena (i.e., higher velocity flow building up after encountering lower velocity flow).

SULFUR CYCLE: The atmospheric model contains an interactive sulfur cycle parameterization that converts sulfur dioxide (SO_2, e.g., from anthropogenic and volcanic sources) and dimethyl sulphide (DMS, e.g., from volcanic sources and ocean phytoplankton) into sulfate aerosols (Ackerley et al. 2009). The direct effects (e.g., aerosol scattering and absorption of solar radiation) and indirect effects (e.g., altering cloud albedo and precipitation efficiency) of the resulting sulfate aerosols are represented in the model.

3.2.2 Ocean Model

The ocean component of the HadCM3L model is similar to the ocean model of its parent model HadCM3, but is adjusted in a few areas to increase the computational efficiency for use in the distributed computing network. (See Gordon et al. (2000) for a detailed description of the ocean model in the HadCM3 parent model.) The horizontal resolution of HadCM3L is the same as the atmosphere, 2.5° lat by 3.75° long, which is courser than its parent model's resolution of 1.25° lat by 1.25° long but is the same as

the second generation model, HadCM2. The vertical grid has 20 levels that transition from higher resolution near the ocean surface (10 m thickness) to a lower resolution at the ocean bottom (616 m thickness; See Table 3.3). The higher resolution near the surface allows the mixed layer to be resolved.

Table 3.3: Vertical levels in the HadCM3L ocean model as well as background vertical diffusivity of tracers between a given level and the level directly above it. (From Johns et al. (1997).)

Level	Depth (m)	Thickness (m)	Vertical diffusivity (10^{-5} m^2/s)
1	5.0	10.0	–
2	15.0	10.0	1.03
3	25.0	10.0	1.06
4	35.1	10.2	1.08
5	47.9	15.3	1.11
6	67.0	23.0	1.16
7	95.8	34.5	1.22
8	138.9	51.8	1.32
9	203.7	77.8	1.46
10	301.0	116.8	1.68
11	447.1	175.3	2.01
12	666.3	263.2	2.50
13	995.6	395.3	3.23
14	1501.0	615.0	4.34
15	2116.0	615.0	6.06
16	2731.0	615.0	7.79
17	3347.0	615.0	9.51
18	3962.0	615.0	11.23
19	4577.0	616.0	12.95
20	5193.0	616.0	14.68

Ocean bathymetry (i.e., ocean bottom topography) is constructed from the 5 arc-minute (1/12° lat by 1/12° long) global land and ocean relief gridded data set (ETOPO5) from the National Geophysical Data Center (ETOPO5 1988; Gordon et al.

2000). Iceland is removed and the Denmark Straits (i.e., between Iceland and Greenland) deepened in HadCM3L compared to HadCM3 due to the fact that the distance across the Denmark Straits in the lower resolution HadCM3L is less than the size of a single grid cell. Making this adjustment allows for a more realistic North Atlantic circulation through an improved northward heat transport into the North Atlantic and Nordic Sea region (Jones 2003).

The dynamical equations used are based on the primitive equations model with a "rigid-lid" approximation[5] (Bryan 1969b; Cox 1984). A one hour integration time step is used and the derived model variables include potential temperature and salinity (referred to as tracers) and horizontal velocity (i.e., momentum). The remainder of this section provides information on the important components and parameterization schemes of the ocean model. These are summarized in Table 3.1.

VERTICAL MIXING: Vertical mixing of momentum is parameterized in the mixed layer[6] using a K-Theory scheme based on Large et al. (1994) and below the mixed layer a K-Theory scheme based on Pacanowski and Philander (1981) is applied. K-Theory schemes contain prognostic equations for their first order moments but then parameterize the higher-order moments, utilizing a vertical diffusion coefficient. This coefficient is based on both local properties and a background vertical diffusivity value which is held constant across the entire depth of the ocean.

[5] A "rigid-lid" approximation sets vertical motions to zero at the ocean surface which eliminates fast moving surface gravity waves. This allows for a longer integration timestep to be used and therefore permits longer simulations due to the improved computational efficiency.
[6] The mixed layer is a portion of the uppermost ocean containing relatively homogenous properties (e.g., temperature and salinity) due predominantly to turbulent mixing.

Vertical mixing of tracers (i.e., potential temperature and salinity) below the mixed layer is parameterized using Pacanowski and Philander (1981) while in the mixed layer a hybrid mixing scheme is used. In this hybrid scheme, a K-Theory diffusive mixing scheme is used (Large et al. 1994) as well as a mixed layer energy balance model based on Kraus and Turner (1967) that provides the input of turbulent kinetic energy from the wind available for mixing temperature and salinity in the mixed layer. When negative surface buoyancy fluxes are present at the ocean's surface, a convective adjustment is applied to mix the fluxes down to a level of neutral buoyancy. For the vertical mixing of tracers, a background vertical diffusivity value at each layer varies with depth and is shown on the right hand column of Table 3.3. (See Appendix A in Gordon et al. (2000) for a more detailed description of the vertical mixing parameterizations.)

EDDY MIXING: Ocean eddies are circulations in the water that can cause mixing to occur but are typically smaller than the ocean model grid cell and therefore must be parameterized. The parameterization scheme used for eddy mixing of tracers is the Visbeck et al. (1997) version of the Gent and McWilliams (1990) scheme. Potential energy is removed adiabatically by diffusion of isopycnal (i.e., constant density) layer thickness with a thickness diffusion coefficient established locally (Visbeck et al. 1997). Additionally, the Griffies et al. (1998) form of the Redi (1982) isopycnal mixing scheme is used to diffuse tracers along isopycnal surfaces. And a latitude dependent horizontal mixing of momentum (viscocity) formulation is used to adequately resolve subtropical western boundary currents while also maintaining numerical stability in the

diffusion equation at high latitudes where grid cell lines converge. (See Appendix A in Gordon et al. (2000) for a more detailed description of the eddy mixing scheme.)

TOPOGRAPHICALLY-BASED MIXING: The Straits of Gibraltar, connecting the Mediterranean Sea and Atlantic Ocean, cannot be resolved within the model's topography/bathymetry and therefore a mixing parameterization is included to simulate the outflow of water from the Mediterranean into the Atlantic (e.g., Manabe and Stouffer 1988). The temperature and salinity are completely mixed between the westernmost grid cell of the Mediterranean and corresponding easternmost grid cell in the Atlantic with the mixing taking place within the top 13 ocean layers (i.e., 1200 m), the depth over which water is expected to sink after entering the Atlantic.

Also, two simplified sill (i.e., raised ridge on the ocean bottom) overflow parameterization schemes were included for the Greenland-Iceland-Scotland ridge (Gerdes et al. 1991; Roether et al. 1994). These schemes allow for more realistic mixing near the ocean bottom ridge. For example, dense water at the top of a ridge is allowed to flow down the sloped surface as a boundary current as opposed to being mixed out with the underlying water.

SEA ICE: The sea ice model of Crossley and Roberts (1995) is built directly into the ocean model. Its thermodynamics are from Semtner (1976) and includes representations of ice concentration (Hibler 1979), the amount of ice below the water line based on the weight above it (Ledley 1985), sea ice leads (i.e, an ice-free fracture in the sea ice), and ice formation and melting, including its impact on ocean salinity. Sea ice dynamics are parameterized using Bryan (1969a) which allows advection of ice thickness, ice concentration, and snow depth. Ocean heat fluxes are computed from the

ocean water into the bottom of the ice with surface fluxes from the ice or leads into the atmosphere calculated in the atmospheric model. Energy is mixed vertically down into the open water of leads from the atmospheric wind above and surface albedo is parameterized to account for differences in sea ice surfaces (e.g., bare ice, snow of different ages, or the presence of melt ponds). Sea ice rheology (e.g., Feltham 2008) is represented by inhibiting sea ice convergence after the ice depth reaches 4 m (Steele et al. 1997). However, ice is allowed to continue growing thicker with continued freezing.

SOLAR RADIATION ABSORPTION: The upper ocean is designed to selectively absorb shortwave solar radiation with depth using the double exponential decay function created by Paulson and Simpson (1977) based on observations which assumes an ocean water clarity of Type 1B (Jerlov 1968).

3.3 BBC Climate Change Experiment

The HadCM3L output utilized in this study was generated as part of the climate*predicion*.net British Broadcasting Corporation (BBC) climate change experiment (CCE), also known as the Transient Coupled Model Experiment (Frame et al. 2009; http://www.bbc.co.uk/sn/climateexperiment). In this experiment, a large number of climate simulations were generated with variations to their atmosphere and ocean model physics parameters, past and future forcings, and initial conditions to investigate how these changes can impact the resulting modeled climate. In the first sub-section the perturbed physics parameters will be described. The atmosphere-ocean coupling process and flux adjustment procedure will be provided in the second sub-section followed by a description of the control and transient simulations in the third

sub-section. The fourth sub-section reviews available model output from this experiment.

3.3.1 Physics Parameter Perturbations

A number of physics parameters in the atmosphere and ocean model components of HadCM3L were varied (i.e., perturbed) across their current range of uncertainty through expert elicitation (Murphy et al. 2004). These perturbed parameters are discussed below for the atmospheric parameters and then for the ocean parameters. An initial condition parameter also was perturbed and will be discussed at the end of this sub-section. All parameters are summarized in Table 3.4.

Table 3.4: CPDN perturbed parameters, associated parameterization schemes and perturbation values. Default parameter values are highlighted in bold.

Parameter	Description	Perturbed Values
ATMOSPHERE		
ALPHAM	Albedo at melting point of ice	**0.5**, 0.57, 0.65
ANTHSCA	Scaling factor for anthropogenic sulfates	0.5, 0.8, **1.0**, 1.2, 1.5
CLOUDTAU	Time a circulating air parcel remains in cloud (s)	3.6, **10.8**, 32.4 [x 10^3]
CT	Accretion constant (s^{-1})	0.5, **1**, 4 [x 10^{-4}]
CW_LAND [a]	Precipitation threshold over land (kg m^{-3})	1, **2**, 20[x 10^{-4}]
CW_SEA [a]	Precipitation threshold over sea (kg m^{-3})	2, **5**, 50 [x 10^{-5}]
DTICE	Temperature range of ice albedo variation	2, 5, **10**
EACF	Empirically adjusted cloud fraction	**0.5**, 0.63, 0.67 [**]
ENTCOEF	Entrainment coefficient	0.6, 1.0, **3.0**, 9.0
I_CNV_ICE_LW [b]	Type of convective cloud ice crystal used in longwave radiation	**1**, 7
I_CNV_ICE_SW [b]	Type of convective cloud ice crystal used in shortwave radiation	**3**, 7
I_ST_ICE_LW [b]	Type of stratiform cloud ice crystal used in longwave radiation	**1**, 7
I_ST_ICE_SW [b]	Type of stratiform cloud ice crystal used in shortwave radiation	**2**, 7
ICE_SIZE	Ice crystal size (m)	2.5, **3.0**, 4.0 [x 10^{-4}]
L0 [c]	Sulfate mass scavenging parameter L0 (s^{-1})	2.17, **6.5**, 19.5 [x 10^{-5}]
L1 [c]	Sulfate mass scavenging parameter L1 (s^{-1})	0.99, **2.96**, 8.86 [x 10^{-5}]
NUM_STAR	Condensation threshold for accumulation	0.1, **1.0**, 10 [x 10^6]
RHCRIT	Critical relative humidity	0.65, **0.73**, 0.9 [**]
SO2_HIGH_LEVEL	Sulfur cycle: model level for SO2 (high level) emissions	1, **3**, 5
VF1	Ice fall speed (m s^{-2})	0.5, **1.0**, 2.0
VOLSCA	Sulfur cycle: scaling factor for emission from natural (volcanic) emissions	1, **2**, 3
OCEAN		
HANEY	Haney heat forcing coefficient ($Wm^{-2}K^{-1}$)	**81.88**, 163.76
HANEYSFACT	Haney salinity forcing factor	**0.25**, 1.0
ISOPYC	Isopycnal diffusion of tracers (m^2s^{-1})	0.2, **1**, 2 [x 10^3]
MLLAM	Wind mixing energy scaling factor (m^2 s)	0.3, **0.7**
VDIFFDEPTH [d]	Ocean: increase of background vertical mixing of tracer with depth (ms^{-1})	0.7, **2.8**, 9.6 [x 10^{-8}]
VDIFFSURF [d]	Ocean: background vertical mixing of tracer (diffusion) at surface (m^2s^{-1})	0.5, **1**, 2 [x 10^{-5}]
VERTVISC	Ocean: background vertical mixing of momentum (viscocity) (m^2s^{-1})	0.5, **1.0** [x10^{-5}]
INITIAL CONDITIONS		
DTHETA	Initial condition potential temperature perturbation applied to atmosphere (°C)	**0**, 0.01, 0.02, 0.03, 0.04, 0.05, 0.06 0.07, 0.08, 0.09

a, **b**, **c**, **d** Individual groups of parameters perturbed together

** Parameter values represent mean over 19 model levels (variations occur at each level)

The following perturbed parameters are associated with the HadCM3L atmospheric model, which includes components of the sulfur cycle

ALPHAM (Albedo at the melting point of ice is): The albedo (i.e., reflectivity) of sea ice can vary depending on temperature and therefore parameter ALPHAM allows for different albedos to be set at the melting point of ice. The perturbed values are (**0.5**, 0.57, 0.65). (Note that default parameters will be highlighted in bold throughout these discussions.) Also see parameter DTICE, which is related to ALPHAM.

ANTHSCA (Scaling factor for anthropogenic sulfates): There is uncertainty in the exact anthropogenic SO_2 emissions that have occurred in the past or will occur in the future. Therefore parameter ANTHSCA is used to scale historical and future SO_2 emissions estimates to generate a range of possible scenarios. These SO_2 emission are important in the model because they can be oxidized in the atmosphere and thereupon be converted to atmospheric sulfate aerosols which scatter/absorb solar radiation (direct effects) and alter cloud albedo and precipitation efficiency (indirect effects). (Refer to Ackerley et al. (2009) for further discussion on the model's sulfur cycle processes.) The parameter values are [0.5, 0.8, **1.0**, 1.2, 1.5] and correspond to multipliers used to scale the estimated past and future time series (see Figure 3.3c).

CLOUDTAU (Time a circulating air parcel remains in a cloud): This parameter is in the sulfur cycle parameterization scheme and represents the amount of time an air parcel takes to transit through a cloud which affects how much anthropogenic SO_2 is oxidized while passing through it. The oxidation process removes SO_2 from the cloud and converts it to atmospheric sulfate aerosols which scatter/absorb solar radiation (direct effects) and alter cloud albedo and precipitation efficiency (indirect effects).

CLOUDTAU is directly related to the oxidation rate so that as CLOUDTAU increases (decreases) the oxidation rate and therefore amount of sulfate aerosols in the atmosphere increases (decreases). (Refer to Ackerley et al. (2009) for further discussion on CLOUDTAU, see their Eq. (2), and the model's sulfur cycle processes.) The parameter variations are [3.6, **10.8**, 32.4 ($x10^3$ s)] which represent minimum, best guess, and maximum value estimates (Ackerley et al. 2009).

CT (Accretion constant): This parameter establishes the cloud droplet to rain conversion or accretion rate (i.e., the time it takes to convert cloud droplets to rain). (See Gregory and Morris (1996) and Smith et al. (1998)) CT has been found to impact cloud, water vapor, and lapse rate feedbacks with a decreased parameter value found to reduce the rate of cloud water accreted onto falling precipitation thereby increasing the amount of clouds for a given temperature and humidity (Sanderson et al. 2010). A different way to explain it is that an increase in CT allows more cloud droplets to be removed by falling rain which reduces the overall cloud coverage. CT was found to increase extreme precipitation as the parameter value is increased (Fowler et al. 2010). The parameter values are [0.5, **1**, 4 ($x10^{-4}$ s^{-1})].

CW_LAND; **CW_SEA** (Precipitation threshold over land and sea): This parameter controls the rate at which cloud liquid water is converted to large-scale precipitation. Different values are used over land (CW_LAND) and over sea (CW_LAND) because of the variation in cloud condensation nuclei (CCN) residing over each (e.g., a greater number of CCN are present over land). These two parameters have been found to have a large impact on shortwave cloud, water vapor, and lapse rate feedbacks (Sanderson et al. 2010). Lower parameter values result in clouds precipitating with greater efficiency,

resulting in reduced cloud coverage. Sanderson et al. (2010) showed that when the parameter values were increased it resulted in a positive humidity feedback because larger humidities could remain in the atmosphere without initiating precipitation. They also showed that an increase in the parameter values caused an increase in shortwave cloud feedback in the tropics and decrease at high latitudes. (See Gregory and Morris (1996) and Smith et al. (1998) for further details.) The parameter values for CW_LAND are [1, **2**, 20 ($x10^{-4}$ kg m^{-3})] and for CW_SEA are [2, **5**, 50 ($x10^{-5}$ kg m^{-3})] and they are perturbed together (i.e., when one is at its lowest, middle, or highest value the other is as well).

DTICE (Temperature range of ice albedo variation): The albedo (i.e., reflectivity) of sea ice can vary depending on temperature and parameter DTICE sets the temperature range below the melting-point in which sea-ice varies linearly between the melting albedo and the cold ice albedo. The perturbed values are [2, 5, **10** (°C)].

EACF (Empirically adjusted cloud fraction): This parameter identifies how much cloud cover there will be when the specific humidity within a grid cell equals the saturation value (i.e., the air is saturated) and therefore is a scaling factor for cloudiness for a given temperature and humidity profile. (See Smith et al. (1998) for further details.) It has been found that an increase in EACF results in an increase in the amount of clouds present for a given value of temperature and humidity and therefore acts to amplify boundary layer cloud over the oceans and decrease them over landmasses (Sanderson et al. 2010). EACF values can vary with height across the 19 model vertical layers. There are three perturbed parameter options and these are distinguished by the single values [**0.5**, 0.63, 0.67] representing the average value across all 19 levels. Table

3.5 lists the exact EACF values at each atmospheric level for the three options and it is apparent that the perturbations allow for increased cloud coverage for a given temperature and humidity, especially in the lowest model levels.

Table 3.5: Empirically adjusted cloud fraction (EACF) parameter perturbation values, which vary with height. The EACF parameter perturbation value identifier is the average of all values across the 19 vertical layers in the atmosphere.

Vertical Level	EACF = 0.5 (default)	EACF = 0.63	EACF = 0.67
19	0.50	0.60	0.65
18	0.50	0.60	0.65
17	0.50	0.60	0.65
16	0.50	0.60	0.65
15	0.50	0.60	0.65
14	0.50	0.60	0.65
13	0.50	0.60	0.65
12	0.50	0.60	0.65
11	0.50	0.60	0.65
10	0.50	0.60	0.65
9	0.50	0.60	0.65
8	0.50	0.60	0.65
7	0.50	0.60	0.65
6	0.50	0.633	0.70
5	0.50	0.666	0.75
4	0.50	0.70	0.80
3	0.50	0.70	0.80
2	0.50	0.70	0.80
1	0.50	0.70	0.80

ENTCOEF (Entrainment coefficient): This parameter sets the rate at which convective clouds mix with their surrounding environmental air. In previous studies it was found that variations to ENCOEF played a significant role in altering modeled climate characteristics (e.g., Knight et al. 2007; Sanderson et al. 2008a; Fowler et al. 2010;

Sanderson et al. 2010). In the convection parameterization scheme (Gregory and Rowntree 1990) a proportion of the rising air within an unstable grid cell (i.e., having positive buoyancy[7] when lifted to the next vertical layer) across each vertical layer is allowed to mix a portion of the surrounding air into the rising air (called entrainment) as well as mix a portion of the rising air into the surrounding air (called detrainment). The rate of these two processes is proportional to the value set for the parameter ENTCOEF. The parameter values are [0.6, 1.0, **3.0**, 9.0].

When ENTCOEF is set to lower values, rising convective air is less diluted by the environmental air surrounding it and therefore maintains greater buoyancy and can rise to higher altitudes before reaching a level of zero buoyancy. The result is an increased depth of convection and greater transport of moisture to higher levels. When ENTCOEF is set to higher values more mixing occurs resulting in weaker convective activity and greater moisture in the mid-troposphere.

Sanderson et al. (2008a) found that decreasing ENTCOEF resulted in a moistening of the upper troposphere and lower stratosphere and a drying of the lower troposphere across the tropics. The greater mid- to upper level moisture was found to increase clear-sky absorption of longwave radiation but at the same time produce a compensating effect by increasing reflection of shortwave radiation through greater albedo from an increase in high-level cloud formation. The difference in these two compensating effects impacts a model's climate sensitivity (i.e., the global mean temperature response to a doubling of atmospheric CO_2) and it was found that this

[7] While the exact definition of buoyancy can vary (e.g., see discussion in Doswell and Markowski (2004)), it is generally understood to be the density difference between a fluid parcel and its surrounding environmental fluid. Therefore, if a rising parcel of air has lower density than the air surrounding it; it will have positive buoyancy and continue to rise until it reaches a level where its density is equal to that of the air surrounding it (i.e., level of zero buoyancy).

difference can be dependent on other model parameter settings. For example, Knight et al. (2007) found that ENTCOEF was responsible for 30% of the variation in climate sensitivity with lower ENTCOEF values tending to correspond with higher climate sensitivity but this relationship was modulated by parameters RHCRIT, CT and VF1. Cloud formation was suppressed when values of RHCRIT were higher, CT lower, and VF1 lower which resulted in less reflection of solar radiation while the lower ENTCOEF maintained greater clear-sky absorption of longwaver radiation, thus leading to greater climate sensitivity.

Additionally, Fowler et al. (2010) found that variations to ENTCOEF impacted precipitation efficiency and lead to changes to heavy precipitation. This was due to the fact that ENTCOEF partially controls the amount of convective activity simulated in a model (Gregory and Rowntree 1990) which is responsible for the majority of heavy precipitation.

I_CNV_ICE_LW; I_CNV_ICE_SW; I_ST_ICE_LW; I_ST_ICE_SW (Type of convective/stratiform cloud ice crystal used in longwave/shortwave radiation): These parameters allow for non-spherical ice particles in the radiation scheme. Their parameter values are I_CNV_ICE_LW [**1**, 7], I_CNV_ICE_SW [**3**, 7], I_ST_ICE_LW [**1**, 7], I_ST_ICE_SW [**2**, 7] and they are perturbed together (i.e., when one is at its default value or secondary value the others are as well). The default values assume spherical ice particles while the non-default value (i.e., 7) allows for non-spherical ice particles in the radiation scheme (Edwards and Slingo 1996) and is associated with an alteration to the expressions for cloud optical depth, single scatter albedo, and scattering

direction which are functions of cloud water content and effective ice particle size (Slingo 1989; Ingram 1990).

ICE_SIZE (Ice crystal size in radiation): This parameter gives the effective radius for ice crystals in clouds (i.e., radius the ice would have if it were perfectly spherical) and is used in the radiation scheme (Edwards and Slingo 1996) for calculating how reflection takes place for incoming and outgoing radiation. The parameter values are [2.5, **3.0**, 4.0 ($x10^{-4}$m)[8]].

L0; L1 (Sulfate mass scavenging parameters): These two parameters are in the sulfur cycle parameterization scheme and are scavenging coefficients for the removal (i.e., scavenging) of SO_2 from the atmosphere by precipitation falling below a cloud. These two parameters increase or decrease by the same factor and their relation is given in Eq. 3.4 below along with the other scavenging parameterization scheme equations of Woodage et al. (2003) and Ackerley et al. (2009),

$$\frac{dS}{dT} = -\lambda(R,S)S \tag{3.1}$$

$$\lambda(R,S) = L_0 R^{2/3} \qquad for\ S \leq S_0 \tag{3.2}$$

$$\lambda(R,S) = L_0 \left(\frac{R}{S}\right)^{2/3} \quad for\ S > S_0 \tag{3.3}$$

$$L_0 = L_1 {S_0}^{-2/3} \tag{3.4}$$

where S is SO_2 concentration (ppbv), T is time, R is rainfall rate (mm h^{-1}), and S_0 is a SO_2 threshold concentration. (Refer to Ackerley et al. (2009), see their Eqs. (3-5), for further discussion on L0 and L1 and the model's sulfur cycle processes.) The parameter

[8] Note a possible error in the literature for this parameter. All but one of the CPDN articles say units are "m" which is obviously incorrect and Sanderson et al. (2010) says they are [2.5, 3.0, 4.0 ($x10^{-5}$m)] but it is probably [2.5, 3.0, 4.0 ($x10^{-4}$m)] because in Heymsfield (1977), which is used for calculating ice fall speed, they show average ice crystal lengths of between roughly 0.3-0.5 mm with minimum length around 0.1mm and max length around 0.5mm. These are on the order of ($x10^{-4}$m) not ($x10^{-5}$m).

values are [2.17, **6.5**, 19.5 ($x10^{-5}$ s^{-1})] for L0 and [0.99, **2.96**, 8.86 ($x10^{-5}$ s^{-1})] for L1 which represent minimum, best guess, and maximum value estimates (Ackerley et al. 2009).

NUM_STAR (Condensation threshold for accumulation): This parameter is in the sulfur cycle parameterization scheme and is the aerosol concentration threshold for identifying when new particle formation is stopped and condensation onto accumulation mode particles begins. (Refer to Ackerley et al. (2009) for further discussion on NUM_START and the model's sulfur cycle processes.) The parameter values are [0.1, **1.0**, 10 ($x10^{6}$)] and represent minimum, best guess, and maximum value estimates (Ackerley et al. 2009).

RHCRIT (Critical relative humidity): This parameter relates the atmospheric humidity in a grid cell to the amount of cloud within the grid cell. Because the size of a grid cell is significantly larger than individual clouds the model cannot simply wait for an entire grid cell to become saturated before initiating cloud formation but rather must set a threshold for when to parameterize cloud initiation at the sub-grid scale. RHCRIT defines this threshold and it corresponds to the critical relative humidity[9] at which point cloud water vapor is initiated within a grid cell (Smith 1990). An increase in RHCRIT reduces the overall water cloud coverage for a given relative humidity because a greater amount of moisture is required to initiate clouds. Alternatively a decrease in RHCRIT was found not only to increase the amount of water cloud but also to decrease the amount of ice cloud (e.g., Pope et al. 2000).

[9] Relative humidity is defined as the ratio of the partial pressure of water vapor to the saturated vapor pressure of water at a given temperature. Therefore it varies with temperature

Sanderson et al. (2010) showed that the shortwave cloud feedback is positive when RHCRIT is increased because the corresponding reduction in boundary layer clouds increased the amount of shortwave solar radiation reaching the surface. They also found, contrary to what might be expected, that the longwave cloud feedback was positive as well because there was an increase in high-level clouds due to the increase in available moisture (from less boundary layer cloud amount) even though a greater relative humidity was required to form the clouds. Therefore, the increase in high-level clouds increased longwave absorption and reemission back to the surface. These shortwave and longwave feedbacks were generally found across the global average but were especially evident near the equator.

RHCRIT values can vary with height across the 19 model vertical layers and therefore the perturbed variations also can vary with height. There are three perturbed parameter options. These will be distinguished by the single values [0.65, **0.73**, 0.9] representing the average value across all 19 levels (see Table 3.6).

Table 3.6: Critical relative humidity (RHCRIT) parameter perturbation values, which vary with height. The RHCRIT parameter perturbation value identifier is the average of all values across the 19 vertical layers in the atmosphere.

Vertical Level	RHCRIT = 0.65	RHCRIT = 0.73	RHCRIT = 0.90
19	0.60	0.70	0.90
18	0.60	0.70	0.90
17	0.60	0.70	0.90
16	0.60	0.70	0.90
15	0.60	0.70	0.90
14	0.60	0.70	0.90
13	0.60	0.70	0.90
12	0.60	0.70	0.90
11	0.60	0.70	0.90
10	0.60	0.70	0.90
9	0.60	0.70	0.90
8	0.60	0.70	0.90
7	0.60	0.70	0.90
6	0.60	0.70	0.90
5	0.60	0.70	0.90
4	0.60	0.70	0.90
3	0.85	0.85	0.90
2	0.90	0.90	0.90
1	0.95	0.95	0.95

SO2_HIGH_LEVEL (Model level for high level SO_2 emissions): This parameter represents the highest atmospheric model level at which anthropogenic emissions are released. In the model there are two levels from which anthropogenic emissions are released. One is at the surface level and the other is at a higher model level to represent emissions coming from industrial plant chimney stacks. The parameter values are [1, **3**, 5].

VF1 (Ice fall speed coefficient): This parameter scales the fall speed of cloud ice particles in the cloud parameterization scheme (Gregory and Morris 1996). It is within

the formula for parameterizing ice fall speed based on the observational study of Heymsfield (1977)

$$V_F = V_{F1}\left(\frac{\rho q_c / C}{c_F}\right)^{0.17} \tag{3.5}$$

where V_F is the fall velocity of ice from within a cloud, V_{F1} is the ice fall speed coefficient, ρ the density of water, q_c the total cloud condensed water content, C the fractional cloud area in a grid cell, and c_F a set parameter equal to 1.01086×10^{-3} kg m^{-3}. The expression ($\rho q_c/C$) is defined as the incloud condensed water density.

When cloud water condenses onto ice nuclei to form ice crystals of sufficient size they begin to fall out of a cloud. The speed at which the ice crystals fall is defined as V_F in Eq. 3.5, which is partly governed by the ice fall speed coefficient VF1. Larger values of VF1 allow for faster fallout of cloud ice which leads to larger particle sizes and increased precipitation amount.

Consistent results for climatic effects of VF1 variations have been found in previous CPDN studies (e.g., Sanderson et al. 2008a; Sanderson et al. 2008b; Sanderson et al. 2010) as well as other non-CPDN studies (Grabowski 2000; Wu 2002). Lower values of VF1 resulted in a warmer, cloudier, more moist lower troposphere with reduced precipitation. The greater moisture increased the clear-sky longwave absorption as did the increase in low-level cloudiness, both resulting a positive feedback on warming. However there was a compensating effect due to increased shortwave solar radiation reflection from increased cloud cover. Sanderson et al. (2008a) also found a reduced latent heat flux at the surface which they deduced as a result of lower surface insolation due to increased cloudiness. And Fowler et al. (2010) showed that a reduction in VF1 could lead to an increase in extreme precipitation in summer at the

regional scale (e.g., over the United Kingdom) due to the increased available moisture, which is contrary to the general global results as stated above. The VF1 parameter values are [0.5, **1.0**, 2.0 (m s^{-2})].

VOLSCA (Scaling factor for emissions from volcanic emissions): This parameter is from the sulfur cycle parameterization scheme and is a scaling factor on estimated sulfur emissions from volcanic sources that are continually erupting as opposed to the single event explosive eruptions. (Refer to Ackerley et al. (2009) for further discussion on VOLSCA and the model's sulfur cycle processes.) While the scaling factor is unitless it corresponds to a scaled change from an approximated continuous volcanic emissions value of 15 teragrams of sulfur per year ($Tg(S)a^{-1}$) which is defined as having a VOLSCA value of 2. Two additional values are used, one corresponding with 50% less annual emission (7.5 $Tg(S)a^{-1}$) defined as VOLSCA equals 1, and the other with 50% more annual emissions (22.5 $Tg(S)a^{-1}$) defined as VOLSCA equals 3. These three emissions values were chosen because they cover the range of uncertainty defined by Houghton et al. (2001). Therefore the parameter values are [1, **2**, 3] and represent minimum, best guess, and maximum value estimates (Ackerley et al. 2009).

The following perturbed parameters are associated with the HadCM3L ocean model.

HANEY (Haney heat forcing coefficient): This parameter introduces a time lag for the correction of model generated sea surface temperatures (SSTs) to observed SSTs (Haney 1971; Jones and Palmer 1998) when spinning up the ocean model. The parameter values are [**81.88**, 163.76 ($Wm^{-2}K^{-1}$)]

HANEYSFACT (Haney salinity forcing factor): This parameter introduces a time lag for the correction of model generated sea surface salinities (SSSs) to observed SSSs (Haney 1971; Jones and Palmer 1998) when spinning up the ocean model. The parameter values are [**0.25**, 1.0].

ISOPYC (Isopycnal diffusion of tracers): This parameter is associated with the mixing of tracers (i.e., temperature and salinity) along surfaces of constant density (i.e., isopycnal) in the ocean and are from the Griffies et al. (1998) parameterization scheme. The parameter values are [0.2, **1**, 2 ($x10^3 m^2 s^{-1}$)].

MLLAM (Wind mixing energy scaling factor): This parameter comes from the vertical mixing parameterization of mixed layer energetics (Gordon and Bottomley 1985) based on Kraus and Turner (1967) which provides input from wind mixing energy (i.e., energy from the atmospheric wind that is available for mixing into the ocean). As described in Gordon et al. (2000), the wind mixing energy is parameterized using $\lambda \rho_o u^*$ where λ is the wind mixing energy scaling factor MLLAM, ρ_o is a reference sea water density, and u^* is the friction velocity. This turbulent energy is mixed down into the ocean using the exponential decay function $\exp(-z/\delta)$ where z is ocean depth from the surface and δ is the decay scaling factor, that represents the depth to which the available turbulent energy is decreased to 1/e (i.e., approximately 0.37) of its initial value.

VDIFFSURF; **VDIFFDEPTH** (Background vertical mixing of tracer at surface/with depth): These parameters correspond with the depth dependent background vertical mixing of tracers (i.e., diffusion) below the ocean mixed layer in the Pacanowski and Philander (1981) vertical mixing parameterization scheme by defining a surface value

(VDIFFSURF) and then how the surface value varies with depth (VDIFFDEPTH). The parameter values for VDIFFSURF are [0.5, **1**, 2 ($x10^{-5}$ m^2s^{-1})] and for VDIFFDEPTH are [0.7, **2.8**, 9.6 ($x\ 10^{-8}$ ms^{-1})]. The default values are shown in Table 3.3.

VERTVISC (Background vertical mixing of momentum): This parameter represents the background value of vertical mixing of momentum (i.e., viscosity) below the ocean mixed layer in the Pacanowski and Philander (1981) vertical mixing parameterization scheme. The total vertical mixing of momentum below the mixed layer is parameterized based on the local gradient in the Richardson number, which relates vertical stability and shear and indicates when convective overturning may occur, and this VERTVISC value (Gordon et al. 2000). The parameter values are [0.5, **1.0** ($x10^{-5}$ m^2s^{-1})].

The following perturbed parameters are associated with the initial conditions in the HadCM3L model.

DTHETA (Initial condition): To include the uncertainty relating to different initial condition in the model, a temperature perturbation was introduced in the atmosphere during its spinup phase. This parameter indicates the temperature perturbations used which are [**0**, 0.01, 0.02, 0.03, 0.04, 0.05, 0.06 0.07, 0.08, 0.09 (°C)]

3.3.2 Atmosphere-Ocean Coupling and Flux Adjustments

Based on all of the individual perturbed parameter variations, there are 153 different atmospheric parameter configurations (i.e., different atmospheres) and 10 different ocean parameter configurations. Therefore a combined 1,530 different combinations are possible when the atmosphere and ocean model components of

HadCM3L are coupled together. (These combinations will interchangeably be referred to as different model versions.)[10]

Typically, the coupling process requires a simulation spin up period from hundreds to thousands of years to bring the two models into a state of equilibrium and may require flux adjustments to remove any anomalous fluxes at the interface of the two models. Any anomalous fluxes present could lead to drifts in climate variables. With the large number of simulations planned in their project, CPDN developed an alternate spin up and flux adjustment procedure to reduce the amount of time required in the coupling process (Frame et al. 2009). In this process the atmosphere and ocean components were spun up separately, using simpler model versions of their counterpart, and then were combined after flux adjustments were calculated based on the simpler models. The 153 atmospheres were coupled to a simple slab ocean and spun up for 15 years while the 10 oceans were coupled to a standard atmosphere (i.e., generalized vertical structure of temperature, pressure, and density) for a 200 year period. A longer spin up period was required for the ocean because of the longer response time of the fully dynamic ocean. Climatic conditions in the spin up process corresponded approximately to those in the year 1920. Once the flux adjustments were calculated for each of the fully dynamic atmospheres and oceans separately they were then coupled to one another and each of their flux adjustments combined to create a single flux adjustment.

[10] Not all of the atmosphere/ocean combinations are available for analysis. This is because a number of simulations were removed due to a variety of model output file errors (see the first section in both Chapter 5 and Chapter 7) and because a large number of initial simulations were generated using an incorrect parameter setting for the amount of sulphate aerosols in the atmosphere which led to unrealistic modeled climates (Myles Allen and Dan Rowlands, 2010, Personal Communication).

Since this coupling process does not officially spin up and apply flux adjustments with the two fully dynamic models, it is possible that the resulting modeled climate may not be in complete balance. This is investigated further in the control simulation analysis (See Chapter 5, Section 5.2).

3.3.3 Control and Transient Simulations

Two different types of simulations were run for each HadCM3L coupled model version. The first is a 160 year control simulation that maintains constant forcings representative of average conditions of roughly 1880-1920. Solar radiation was allowed to vary across the typical annual solar cycle but is the same for each year in the 160 year simulation. This control simulation allows for investigation of the model's mean climate and variability due to internal chaotic processes in the climate system. See Chapter 5 for the analysis of the control simulations.

The second type of simulation is a 160 year transient simulation with forcings that vary with time, corresponding to the time period 1921-2080. A variety of natural and anthropogenic forcings were introduced to the different HadCM3L model versions, thereby allowing investigation of another level of uncertainty in modeling the climate. Atmospheric concentrations of well mixed greenhouse gases (GHGs), ozone, and SO_2 vary according to historically observed values over the period 1921-2000 and use the Special Report on Emissions Scenarios (SRES) A1B scenario (Nakićenović and Swart 2000), a mid-range emissions scenario, for 2001-2080 future variations. The scenario results in an atmospheric CO_2 concentration reaching 720 ppm in 2100. The emission

scenarios from SRES have recently been updated (Vuuren et al. 2011) and the A1B scenario is qualitatively similar to the new mid-range Representative Concentration Pathway (RCP) 6.0 although they do contain differences resulting in less warming near the end of the future projection period in RCP 6.0.

Figure 3.3a shows radiative forcing estimates for well mixed greenhouse gases covering both the historical and future time period. Because there is uncertainty in the anthropogenic SO_2 emissions that have occurred in the past and will occur in the future, the emissions estimated over the historical period and those identified in SRES A1B have been scaled to different magnitudes using the parameter "anthsca" to account for that uncertainty (Figure 3.3c).

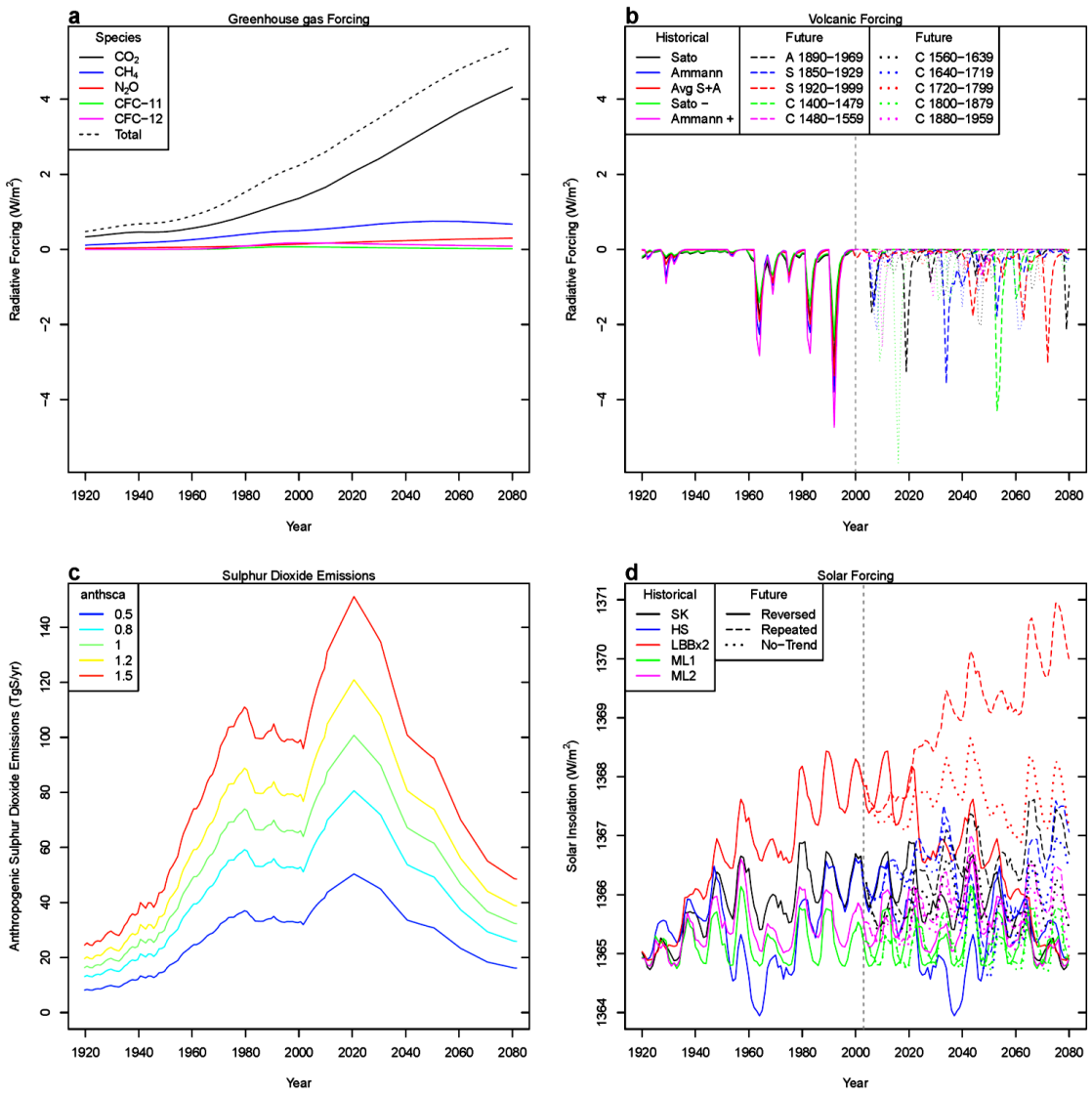


Figure 3.3: Natural and anthropogenic forcing and SO_2 emissions scenarios applied to the BBC-CCE HadCM3L transient simulations. (a) Radiative forcing due to well mixed greenhouse gases using 1921-2000 historical values and the 2001-2080 SRES A1B future scenario. (b) Radiative forcing from volcanic sulphate aerosol emissions. Five historical scenarios are included based on Sato et al. (1993) (S), Ammann et al. (2003) (A), a logarithmic average of the two (Avg S+A), lower magnitude version (Sato-), and higher magnitude version (Ammonn+). Ten future volcanic emission scenarios are created based on the same two data sets (S,A) as well as Crowley (2000) (C). The time periods used from each data set are listed in the legend. (c) Five versions of historical and SRES A1B annual average global anthropogenic SO_2 emissions scaled by parameter "anthsca." (d) Five historical solar forcing scenarios from 1920-2003 are included based on Hoyt and Schatten (1993) (HS), Lean et al. (1995) (LBBx2), Solanki and Krivova (2003) (SK) and the other two based on expert elicitation (ML1, ML2), (see Frame et al. 2009). Fifteen future scenarios are created based on three versions of each of the historical five; a continuation of the historical trend (Repeated), a reversal of the historical trend (Reversed), and zero trend (No-Trend). (From Rowlands et al. 2012, Supplementary Information.)

Multiple realizations of past and future volcanic and solar forcings also were applied to the HadCM3L model versions (Figure 3.3b,d). Five different versions of volcanic forcings were included for the 1921-2000 historical period, all based on observational data sets of volcanic aerosols in the stratosphere (Figure 3.3b). One of the five is based on Sato et al. (1993) and another on Ammann et al. (2003) with the other three being a logarithmic average of the two, lower magnitude version of Sato et al. (1993), and higher magnitude version of Ammann et al. (2003). Ten future volcanic forcings, 2001-2080, were created based on various segments of each of the two data sets as well as from segments of an additional longer data set from Crowley (2000). (See Figure 3.3 caption for full description of each of these.)

Five different versions of solar forcing were included for the 1921-2003 historical period (Figure 3.3d). Three of these were based on published observational data sets (Hoyt and Schatten 1993; Lean et al. 1995; Solanki and Krivova 2003) and two others were constructed based on expert elicitation (see Frame et al. 2009). Fifteen future scenarios, 2004-2080, were created based on the five historical period versions; a continuation of the historical trend, a reversal of the historical trend, and zero trend. (See Chapter 7 for the full transient simulation analysis.)

3.3.4 Model Output

The HadCM3L model generates two sets of output for both the control and transient simulations. The first set is area-averaged monthly mean time-series for the globe and 51 regions representing various land regions, ocean basins and other relevant

locations such as those associated with the El Nino Southern Oscillation (ENSO) and the North Atlantic Oscillation (NAO). These regions are based on the so called Giorgi regions (i.e., Giorgi and Francisco 2000) commonly used in climate modeling studies. Table 3.5 provides their boundaries for the North American regions investigated in this study and Figure 3.4 provides a visual representation. Table 3.6 lists some of the main variables available for the globe and over North America in the area-averaged monthly mean time-series output. This study will focus on surface air temperature and total precipitation rate output because of their importance in the Earth's climate and because the regional averages include ocean grid cells and therefore would be difficult to find relevant observational data sets to make a comparison with (e.g., maximum and minimum temperature).

Table 3.7: Boundaries used in the area-averaged monthly mean time series output for the CPDN North American regions.

Name	**Label**	**Min Lat** (°N)	**Max Lat** (°N)	**Min Long** (°E)	**Max Long** (°E)
Alaska, NW Canada	ALA	60	72.5	-170	-103
E Canada, etc.	CGI	50	75	-103	-10
Western NA	WNA	30	60	-130	-103
Central NA	CNA	30	50	-103	-85
Eastern NA	ENA	25	50	-85	-50

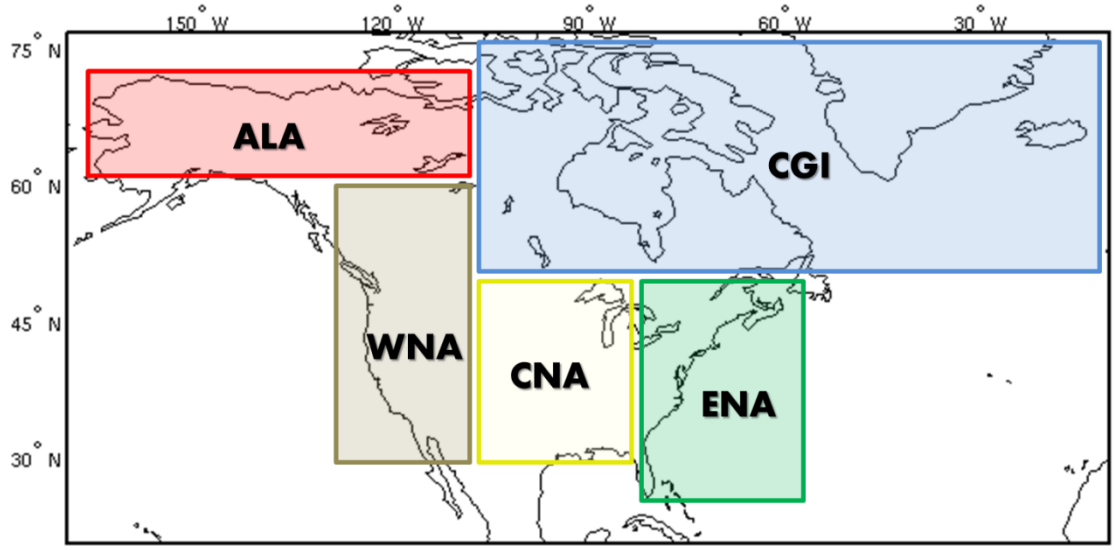


Figure 3.4: North American regions investigated containing area-averaged monthly mean time-series output.

Table 3.8: Model output variables available for the globe and over North America for the HadCM3L area-averaged monthly mean time series.

HadCM3L Output Variables	
surface (1.5 m) air temperature total precipitation rate surface (1.5 m) relative humidity at 1.5 m surface (1.5 m) daily minimum temperature surface (1.5 m) daily maximum temperature	mean sea level pressure u component of wind v component of wind convective cloud amount

The other set of available HadCM3L model output available for both the control and transient simulations is globally gridded (2.5° lat x 3.75° long) decadal mean quantities. This output will not be investigated in the present study but will be the focus of future research.

CHAPTER 4

OBSERVATIONAL DATA SETS

A number of observational data sets were used to assess the climate model performance throughout this study. This chapter provides a review of the datasets used for temperature, precipitation rate and a reanalysis product (i.e., the North American Regional Reanalysis). Table 4.1 at the end summarizes the key features of each.

4.1 TEMPERATURE

Observational temperature data sets were acquired from three independent groups that have been the standard datasets used for observational assessments around the globe (e.g., IPCC 2001, 2007). They have a variety of similarities and differences discussed below but the main feature of each is that they utilize observations from both the land and ocean to generate a globally gridded data set over both land and ocean. This was a necessity because the CPDN HadCM3L model output included both land and ocean grid cells in their regional mean values.

4.1.1 HadCRUT3

The first temperature data set is the third version of the Met Office Hadley Centre and Climate Research Unit (CRU) at the University of East Anglia HadCRUT3 (Brohan et al. 2006) acquired from CRU (www.cru.uea.ac.uk). Its gridded land component is constructed based on approximately 4,500 land station data measurements around the globe from the Global Historical Climatology Network (GHCN; Peterson and Vose 1997), U.S. Historical Climate Network (USHCN;

http://cdiac.ornl.gov/epubs/ndp/ushcn/ushcn.html), and Antarctic Scientific Committee on Antarctic Research (SCAR; http://www.scar.org/). The gridded ocean air temperature component is approximated using sea surface temperature (SST) data from ships and buoys as organized in the International Comprehensive Ocean-Atmosphere Data Set (ICOADS; Woodruff et al. 1998).

Homogeneity adjustments are made to account for possible variations in recording methods such as changes in station site, measurement time, or instrumentation for land-based stations and changes in buckets used to sample ocean water in the early 20th century. Nearest neighbor comparisons are made as well as other manual quality control measures. Monthly mean temperature anomalies of individual observations from the 1961-1990 long-term mean (LTM) are averaged across 5° latitude (lat) by 5° longitude (long) grid cells with minimum data record requirements and other quality control measures applied. Anomalies are used because of the large uncertainties associated with absolute values as they can vary markedly from one location to another within a specified region (e.g., especially across varying topography) making it difficult to obtain a truly accurate observational estimate, especially when large quantities of data are missing between official measurement stations. Anomaly estimates, however, have been shown to be strongly correlated between recording stations out to roughly 1,200 km (Hansen and Lebedeff 1987).

Grid cells containing no data are left as such with no attempt made to interpolate the temperature of the cell from surrounding data. This is the major difference between the HadCRUT3 data set and the other two temperature data sets which both use some type of interpolation method to infill grid cells containing no recorded observations.

Therefore in locations where there are minimal to no observations, such as polar regions, HadCRUT3 has empty grid cells with no data. This must be taken into account when calculating global averages or averages near the poles as the relatively colder grid cell samples will not be included in an average. Temperature data from HadCRUT3 are available from 1850-present with obvious increases in uncertainties in the earlier part of the record due to reduced measurement station coverage. A new version of HadCRUT3 came out (i.e., HadCRUT4) but was not used because it only recently became available.

4.1.2 NOAA-MLOST

The second temperature data set is the NOAA Merged Land-Ocean Surface Temperature analysis (NOAA-MLOST) version 3.5.1 (Smith and Reynolds 2005; Smith et al. 2008), acquired through NOAA/OAR/ESRL PSD, Boulder, Colorado, USA (http://www.esrl.noaa.gov/psd/). Its gridded land component is constructed based on approximately 4,400 land station data measurements from GHCN and USHCN and its gridded ocean air temperature is constructed from ship and buoy data from ICOADS. Homogeneity adjustments are made as well as a variety of quality control to remove non-climatic variations in the data record. Monthly mean temperature anomalies of individual observations from the 1971-2000 long-term mean (LTM) are averaged across 5° lat by 5° long grid cells with minimum data record requirements and other quality control measures applied. When grid cells contain no data it is interpolated using characteristics of the larger surrounding region (i.e., 25° lat by 25° long). Temperature data from NOAA-MLOST is available from 1880-present.

4.1.3 NASA-GISTEMP

The third temperature data set is the NASA Goddard Institute for Space Studies (GISS) Surface Temperature analysis (GISTEMP; Hansen et al. 1999; Hansen et al. 2001) acquired through NOAA/OAR/ESRL PSD, Boulder, Colorado, USA (http://www.esrl.noaa.gov/psd/). Its gridded land component is constructed based on approximately 6,300 land station data measurements from GHCN, USHCN and Antarctic SCAR. Its gridded ocean component comes from the Hadley Centre Sea Ice and Sea Surface Temperature data set (HadISST; Rayner et al. 2003) and an updated data set from Reynolds et al. (2002). Homogeneity adjustments are made as well as a variety of quality control measures to remove non-climatic variations in the data record. Monthly mean temperature anomalies of individual observations from the 1951-1980 long-term mean (LTM) are averaged across 2° lat by 2° long grid cells with minimum data record requirements and other quality control measures applied. When grid cells contain no data, interpolation is used to fill in the gaps by combining station data out to 1,200 km from the grid box center as anomalies were shown to have high correlation out to this range (Hansen and Lebedeff 1987). Temperature data from GISTEMP is available from 1880-present.

4.2 PRECIPITATION RATE

Observational precipitation data sets were acquired from two independent groups. As with temperature, these data sets covered both land and ocean regions.

4.2.1 GPCP

The first precipitation data set is the Global Precipitation Climatology Project (GPCP version 2.1 (Huffman et al. 1997; Adler et al. 2003; Huffman et al. 2009) established by the World Climate Research Program (WCRP). The data was acquired through NOAA/OAR/ESRL PSD, Boulder, Colorado, USA (http://www.esrl.noaa.gov/psd/). The GPCP data set is constructed based on a complex merged analysis of thousands of rain gauge stations and low-orbit satellite microwave data and geosynchronous-orbit satellite infrared data. Relationships between the satellite data and surface precipitation were established using knowledge that microwave brightness temperatures observed from space are dependent on the modification of the emitted surface microwave radiation by hydrometeors in the atmosphere and infrared data are used to relate precipitation with cold cloud top areas. Monthly mean precipitation rate is calculated over 2.5° lat by 2.5° long grid cells from 1979-present.

4.2.2 NOAA-PREC

The second precipitation data set is the NOAA Precipitation Reconstruction (NOAA-PREC; Chen et al. 2002; Chen et al. 2003) acquired through NOAA/OAR/ESRL PSD, Boulder, Colorado, USA (http://www.esrl.noaa.gov/psd/). It is constructed in a similar manner as GPCP with rain gauge and satellite data except an attempt is made to estimate precipitation over the oceans in the pre-satellite era and therefore provide a longer data set. They utilize information from satellites and rain gauge observations over islands and land areas during the satellite era to establish

broad-scale variations that could have occurred over the oceans using the same gauges in the pre-satellite era. Therefore, precipitation estimates over the oceans prior to 1979 contain significantly greater uncertainty than estimates post-1979. The PREC data set contains monthly mean precipitation rate anomalies from 1951-present with anomalies over land based on the 1951-1990 LTM and over the ocean based on the 1979-1998 LTM.

4.3 NORTH AMERICAN REGIONAL REANALYSIS (NARR)

One regional reanalysis was also included for comparison. This was the North American Regional Reanalysis (NARR; Mesinger et al. 2006) acquired through NOAA/OAR/ESRL PSD, Boulder, Colorado, USA (http://www.esrl.noaa.gov/psd/). NARR is a reanalysis which means it generates climate variables using a dynamical model (e.g., including parameterization schemes, as used in climate models) instead of simply averaging/interpolating observed variables as purely observational data sets do. NARR runs the National Centers for Environmental Prediction (NCEP) Eta Model over the North American region using boundary conditions from its global reanalysis counterpart, the NCEP – Department of Energy (DOE) Global reanalysis model, and assimilates into the model a number of observed fields to help drive the simulated climate. These assimilated variables include quantities such as temperature, wind precipitation, moisture, pressure, snow depth, etc. coming from a variety of sources (e.g., surface measurements, rawinsondes, dropsondes, aircraft, satellites). The main advantage of NARR compared to conventional observational data sets is that it provides

a number of output variables (i.e., similar to those from a climate model) at high temporal (3 hourly) and spatial resolutions (32 km horizontal resolution with 45 vertical atmospheric layers). Pertinent to this study, monthly mean values of both temperature are precipitation are available from 1979-present over the North American region. There are some issues with NARR precipitation in that it does not handle precipitation outside the contiguous U.S. well because precipitation data is utilized in the reanalysis process and therefore in data sparse regions (e.g., Mexico, Canada, or over the ocean) the resulting precipitation output is less trustworthy and tends to be smaller than actual values (e.g., Bukovsky and Karoly 2007; Mo et al. 2005; Mesinger et al. 2006).

Table 4.1: Observational data sets and one reanalysis (i.e., NARR) used in this study.

Data Set	Variable	Resolution	Begins	Reference
HadCRUT3	T_{mean} (C)	5°, monthly, globe	1850	Brohan et al. 2006
NOAA-MLOST	T_{mean} (C)	5°, monthly, globe	1880	Smith et al. 2008
NASA-GISTEMP	T_{mean} (C)	2°, monthly, globe	1880	Hansen et al. 2001
GPCP	P_{mean} (mm/day)	2.5°, monthly, globe	1979	Huffman et al. 2009
NOAA-PREC	P_{mean} (mm/day)	2.5°, monthly, globe	1948	Chen et al. 2002
NARR	T_{mean} (C) P_{mean} (mm/day)	32 km , monthly, North America	1979	Mesinger et al. 2006

CHAPTER 5

CONTROL SIMULATION ANALYSIS

The goal of this chapter is to evaluate the performance of the HadCM3L control simulations from the climate*prediction*.net (CPDN) British Broadcasting Corporation (BBC) Climate Change Experiment (CCE) compared to detrended observational data. The control simulations maintain a constant annual but seasonally varying radiative forcing (refer to discussion in Chapter 3, Section 3.3.3) and therefore are compared to detrended observations to assess the modeled mean climate and its variability due to internal chaotic processes in the simulated climate system, including coupling between the atmosphere, ocean, land surface, and sea ice.

Section 5.1 provides the quality control measures applied to the CPDN BBC CCE output and Section 5.2 assesses both the initial adjustment period when the atmosphere and ocean model components were coupled together as well as long-term model drift caused by surface flux imbalances. Sections 5.3, 5.4, and 5.5 provide analyses of the modeled climate mean, seasonal cycle, and variability respectively to assess how well the model simulated the natural climate system and Section 5.6 investigates relationships between the climate indices within and across regions as well as to teleconnection indices. Section 5.7 evaluates the sensitivity of climate indices and model drift to variations in model physics parameters and Section 5.8 investigates initial conditions uncertainty. Section 5.9 summarizes the key findings of this chapter.

5.1 Quality Control of Control Simulation Ensemble

The initial control simulation output acquired from CPDN was examined to assure the quality of the simulations utilized throughout the rest of this study. Each simulation's Network Common Data Form (NetCDF) files were checked for errors and the surface air temperature at 1.5 m (hereafter temperature) and total precipitation rate (hereafter precipitation) values were evaluated over the globe and five North American (NA) regions to search for errors, outliers, or duplicates.

5.1.1 NetCDF File Errors

A total of 1,236 initial control simulations were downloaded from the CPDN servers, nine of which were immediately discarded due to NetCDF file generation errors in the CPDN archiving process. Of the remaining 1,227 simulations, 12 were missing at least one monthly output value within one of their annual NetCDF files and 11 of these were discarded. The 12th simulation was left in the official ensemble because it was missing a monthly value within the first 20 years of the simulation, a period that is not used in analyses because the model's atmosphere and ocean are still in the adjustment period of the coupling process (see Section 5.2).

Within the remaining 1,216 simulations, a search was conducted for the presence of any non-meteorological values (e.g., NaN, Inf, zero) which were identified in previous versions of the CPDN output. No instances of these values were found and therefore all 1,216 control simulations were verified as having a complete set of available model output.

5.1.2 Erroneous Outliers

Figure 5.1 displays the absolute temperature and precipitation over the globe and NA regions for all available control simulations. An obvious outlier can be seen within most of the ensembles around simulation year 120. Stainforth et al. (2005) identified a small number of CPDN simulations containing "sudden jumps" in the output values from the order of 10^2 up to 10^8, which they concluded were a result from the loss of information during either PC shut-down at a critical processing point or from running a computer system at a faster speed than rated by its manufacturer (i.e., 'overclocking'). This outlier appears to be an example of one of the "sudden jumps" they describe. To systematically identify this outlier and any others hidden within the ensemble, an anomaly test was conducted on output values for each region. Monthly and annual anomaly values were calculated from the long-term mean for each simulation as well as month-to-month and year-to-year difference anomalies. These anomalies were standardized with respect to the full distribution of anomaly values across all simulations (i.e., divided by the standard deviation of all anomalies for a specific region/quantity) and then sorted to identify simulations with the largest anomalies.

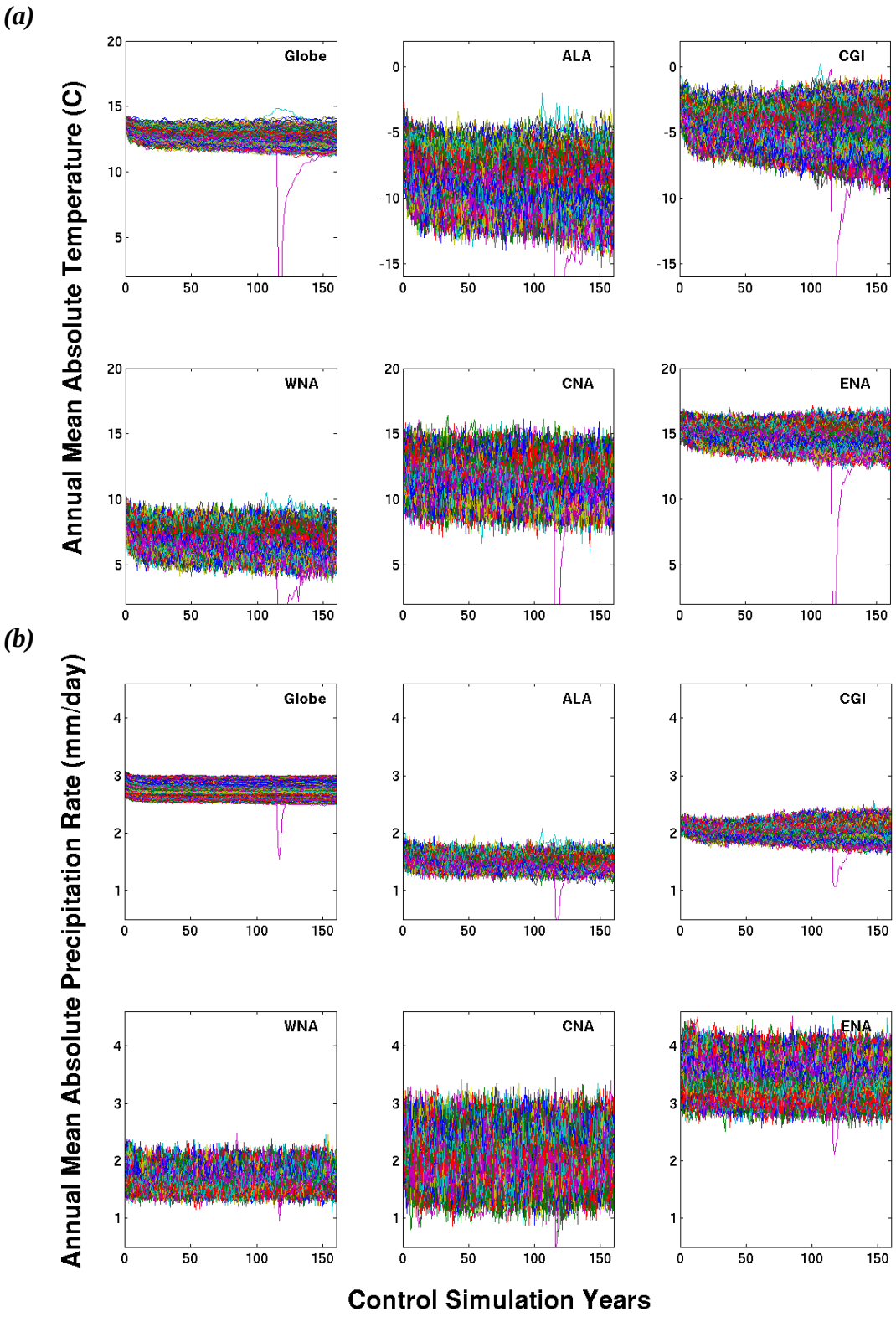


Figure 5.1: Initial ensemble of all control simulations acquired from CPDN for annual mean absolute *(a)* temperature (°C) and *(b)* precipitation rate (mm/day) for the globe and five NA regions. Each plot shows time series for 1,216 individual simulations.

Each anomaly test identified a similar but not always consistent set of simulations containing the largest anomalies for a given variable/region and therefore these higher anomalies were assessed individually to determine if they were caused by an error within the model or if they were simply larger natural fluctuations within the modeled climate. Two simulations were determined to contain non-climatic outliers and the metric accurately distinguishing them was global mean annual average temperature anomalies greater than six standard deviations. There were some instances with similar six standard deviation anomalies or slightly higher anomalies that did not correspond with an actual error in the output. This can still be expected given the sheer number of samples assessed. For example, in the annual average tests, the number of samples expected to be outside the range of 1, 2, 3, 4, and 5 standard deviations under a normal distribution for 170,240 samples (e.g., 1,216 simulations x 140 years) is 54,476 (32%), 7,831 (4.6%), 459 (0.27%), 10 (0.0063%) and 0.1 (0.000057%) samples respectively. Therefore we would expect some anomalies to reach the 4-5 standard deviation range and since the distributions were not completely Gaussian in nature, this could result in even a few larger anomalies, as was found.

Figure 5.2 shows the two outlier simulation cases removed from the official control ensemble. A "typical" control simulation also is plotted for comparison purposes. An abrupt change can be seen in most regions for the two outlier simulations. However, in specific regions there are instances where the anomalous jump was similar in magnitude to the natural variability found in that region. This helps explain why the global average turned out to be the more useful quantity to identify the outliers.

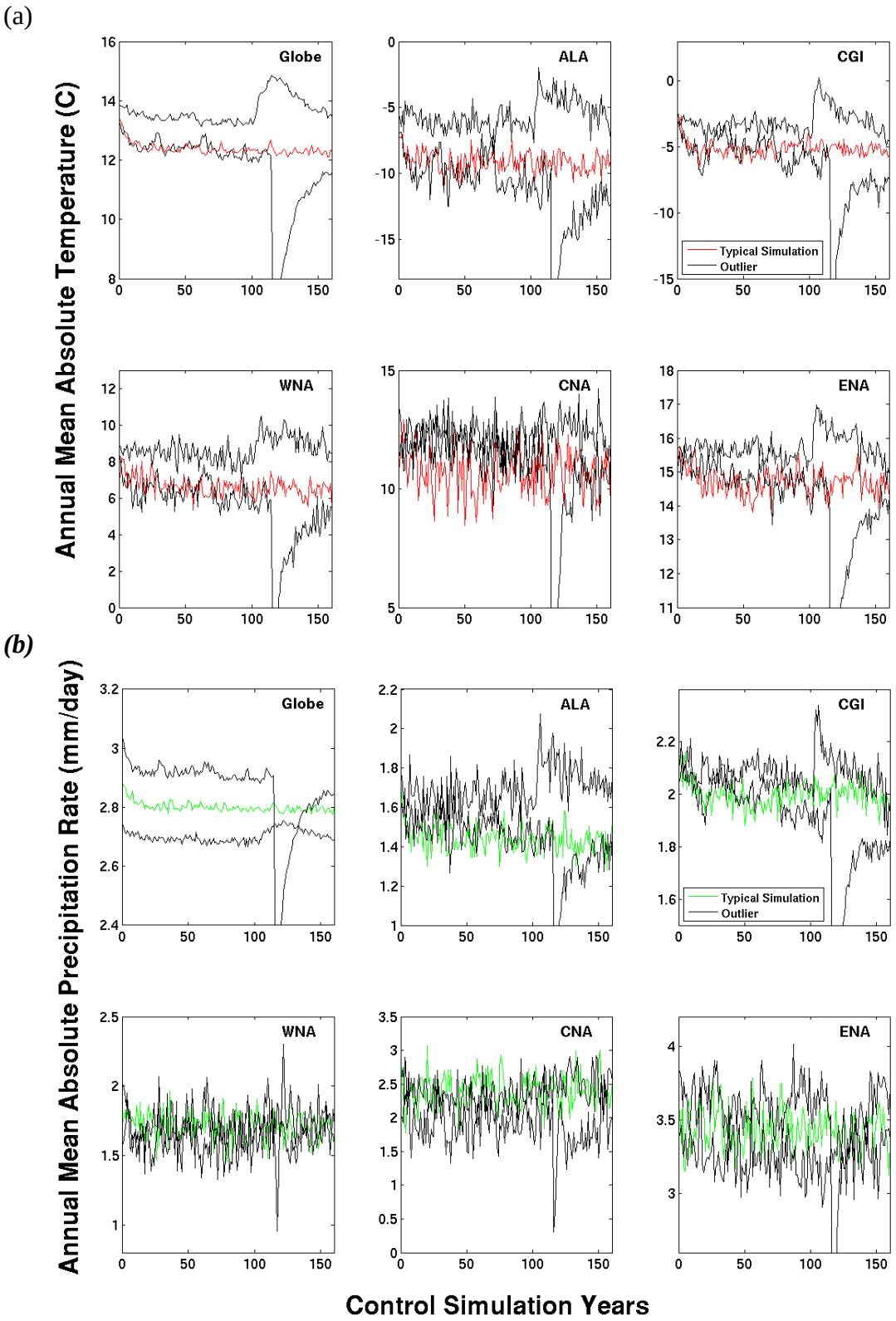


Figure 5.2: Two simulations containing outliers (black) and a typical simulation (red, green) for annual mean absolute *(a)* temperature (°C) and *(b)* precipitation rate (mm/day) for the globe and five NA regions.

5.1.3 Duplicates

After the two outlier simulations were removed, the remaining 1,214 control simulations were searched for any duplicate simulations, another feature identified in previous versions of the CPDN output. Within the control simulation ensemble, there were combinations of 138 atmospheres, ten oceans, and eight initial conditions. An assessment of the parameter variations indicated 187 simulations having one or more simulations with matching atmosphere, ocean, and initial conditions[11]. While we would expect these simulations to have the same output as well, the actual output did not match exactly in any of the cases. As is illustrated in a representative example in Figure 5.3, the output in these instances closely resemble one another but were not an exact match. All such instances were kept in the final control ensemble because their output differences were found to be caused by inconsistencies in the initial condition parameter (DTHETA) and deemed appropriate to retain in the ensemble as discussed below.

[11] Many of the 187 simulations had more than one exact match and therefore the total number of duplicate simulations actually totaled 213.

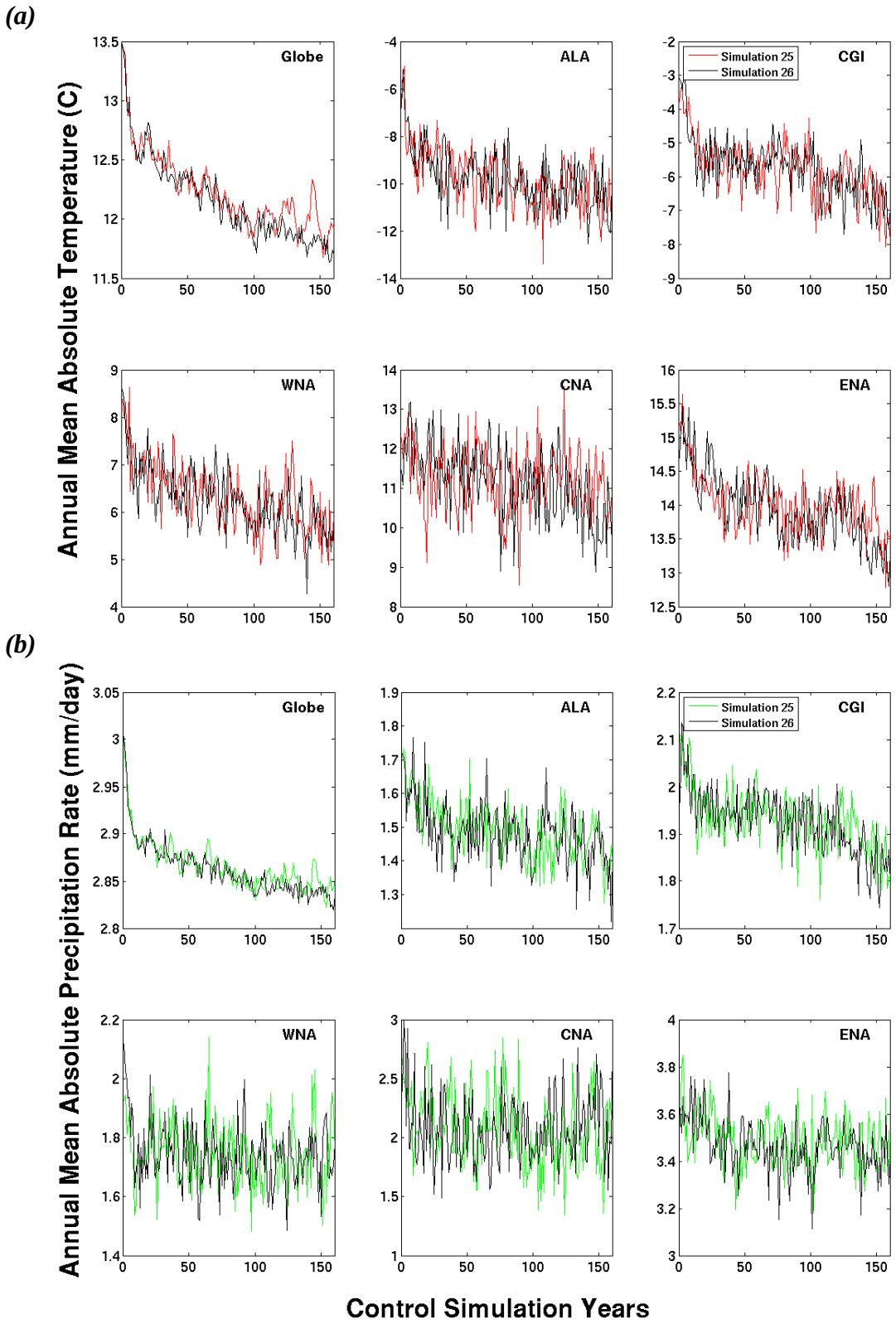


Figure 5.3: Two simulations with identical model parameters but with different output for annual average absolute *(a)* temperature (°C) and *(b)* precipitation rate (mm/day) for the globe and five NA regions.

To better understand the cause of the output variation within parameter duplicates, the ensemble was searched for any instances when two or more simulations contained identical output for three different time periods: the entire 160 year period, the first 20 years of the simulation, and the first 12 months of the simulation. Simulations with duplicate output were found but only for portions of certain simulations. No simulations had completely identical output for the entire 160 year period. There were 148 simulations having identical output with at least one other simulation (197 matches total) over the first 12 months of a simulation with only five of those remaining identical through at least the first 20 years of the simulation. All simulations with the same first year had an identical atmosphere and ocean but were labeled as having different DTHETA values.

Of the five duplicates over the first 20 year period, four had a matching atmosphere and ocean and one had a complete match of all parameters (e.g., DTHETA match as well). Figure 5.4 shows two simulations having identical output through the first 20 years of a simulation, after which time the output diverged into different but still similar values. These initially identical simulations indicate that the two simulations must have started out with identical parameter settings (e.g., atmosphere, ocean, and DTHETA) and therefore the DTHETA parameter setting must have been mislabeled in the NetCDF files[12]. That, however, does not explain why the two simulations eventually diverge. There are a few possibilities for explaining this. The first is that the computer within the distributed computing network running one of the simulations may

[12] The exact DTHETA value cannot be officially confirmed by the CPDN group because their archived NetCDF files are the same used in this study and therefore the only way to identify the true value is for the original simulations to be rerun with a variety of DTHETA values applied which is not computationally feasible.

have encountered a restart or similar disruption in the middle of the simulation as described by Stainforth et al. (2005). Such a restart may have caused the parameters to be reset, resulting in the initiation of a new initial condition temperature perturbation (e.g., established by the DTHETA parameter value) which would act to slightly alter the climate output indices. Another possibility is that the variety of computers generating output could have slightly different architectures (i.e., different Intel processors) that may have resulted in slightly different model output.

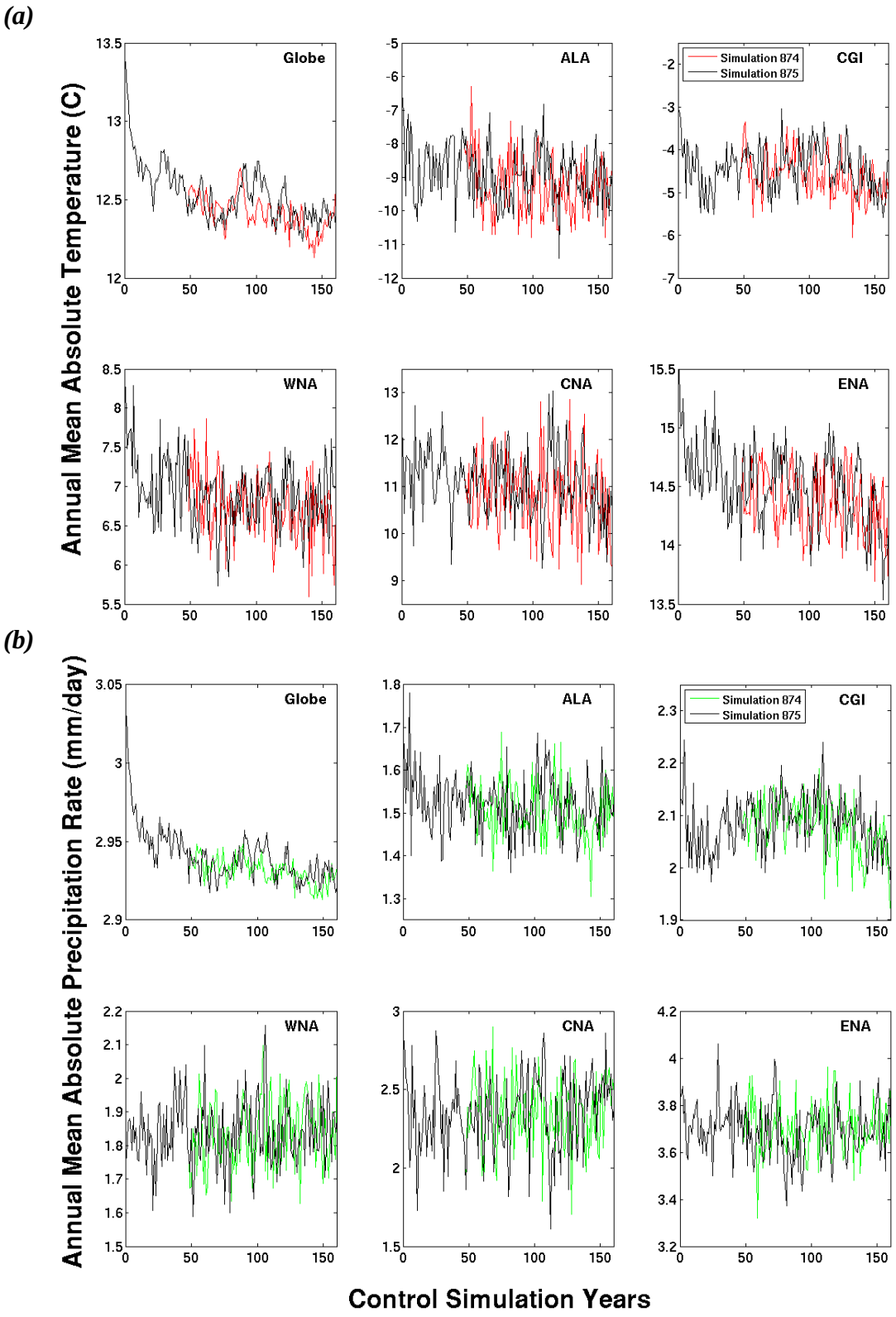


Figure 5.4: Two simulations that have identical output initially but then subsequently diverge for annual mean *(a)* temperature (°C) and *(b)* precipitation rate (mm/day) for the globe and five NA regions.

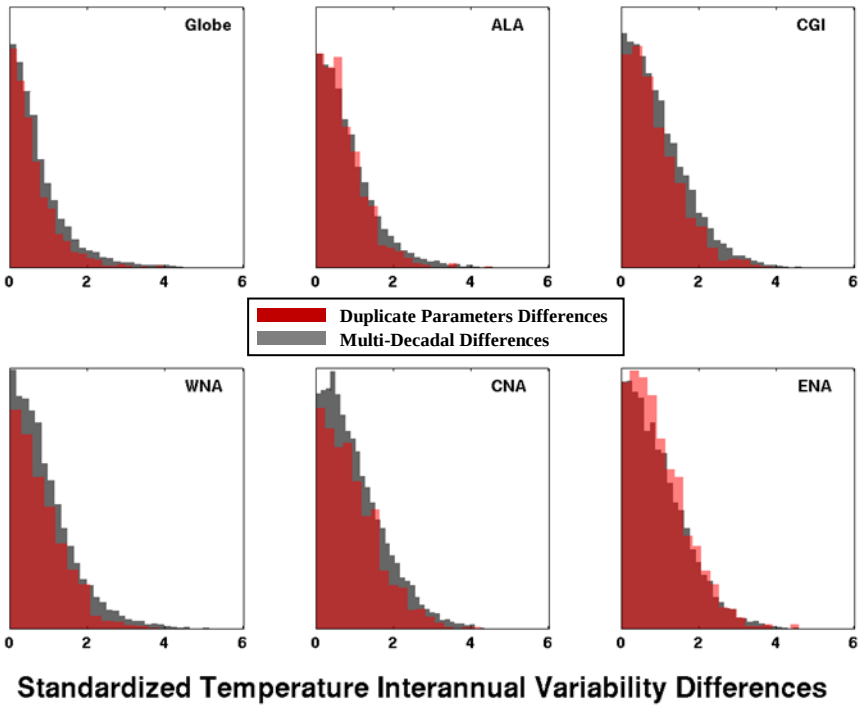
Assuming the duplicate parameter and output discrepancies can be attributed to one of the aforementioned issues, its significance must be assessed and a decision made on how to handle such simulations. While the simulations generally are quite similar, there are some instances when the climate statistics appear to have noticeable differences. For example, the global temperature output for the two simulations in Figure 5.3(a), which have seemingly identical parameter settings, show a marked difference in their variability over the final 50 years of the simulations. To investigate this further, the mean, magnitude of the seasonal cycle, and interannual variability were calculated for corresponding 30-year time periods across simulations with duplicate parameters[13] and then the magnitude of their differences compared against the range of actual values across of the full control ensemble. The differences for the mean and the magnitude of the seasonal cycle were small compared to the full ensemble distribution (not shown). Most of these differences fell within half a standard deviation of the full distribution range with a few reaching near one standard deviation.

Differences in interannual variability, on the other hand, were relatively larger with differences on the order of 1-2 standard deviations of the full distribution and reaching up to four in some cases. These differences, however, were found to be of similar magnitude as multi-decadal differences of interannual variability within a single control simulation (Figure 5.5). Figure 5.5 shows the distribution of interannual variability differences for the 213 simulations having identical parameters as well as the multi-decadal variations from all control simulations. The two distributions were standardized by the full distribution of all 30-year interannual variability values across all controls, and since the multi-decadal analysis distribution has an order of magnitude

[13] The five 30 year periods were 1941-1970, 1961-1990, 1991-2020, 2021-2050, and 2051-2080.

more samples, it was rescaled in the y-direction for better comparison. It is evident from the two distributions that the interannual variability differences between simulations with matching parameters but differing output is nearly identical in magnitude to the multi-decadal variations that can be expected within a control simulation. This further supports the conclusion of an initial condition restart issue as the cause of output differences in simulations with identical parameter settings. If at some point in time within a simulation the initial condition temperature perturbation is reintroduced, it could cause the interannual variability to change to a slightly different state which could lead to the two simulations having different interannual variability characteristics within any given 30-year period, but this difference would still be within the normal multi-decadal variability.

(a)



(b)

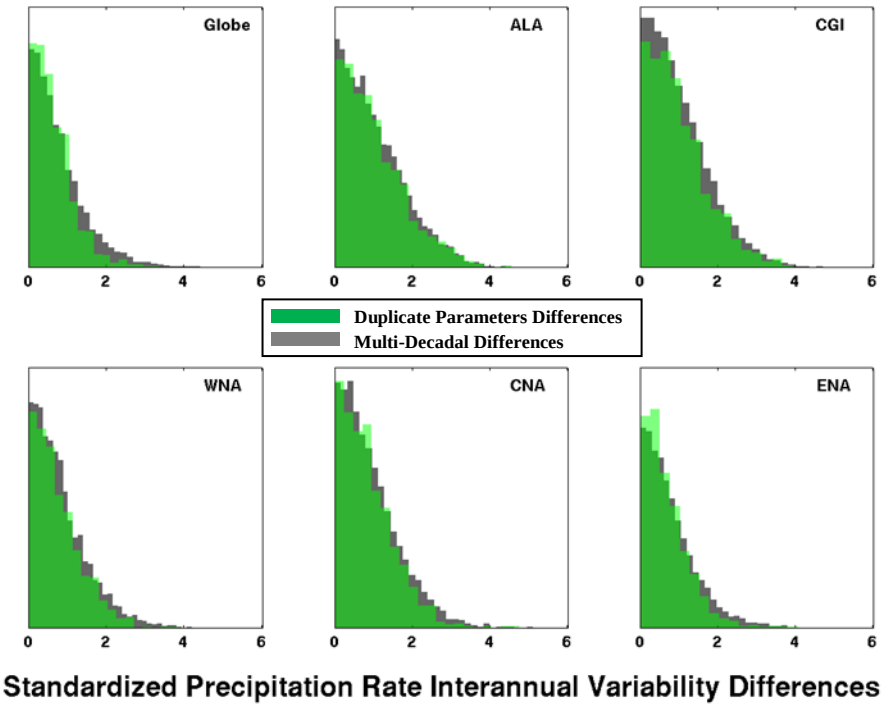


Figure 5.5: Standardized differences between interannual variability within corresponding 30-year periods in simulation pairs having identical parameters (red, green) compared to multi-decadal differences within all control simulations (gray) for *(a)* temperature (°C) and *(b)* precipitation rate (mm/day). Distributions are standardized by the distribution of 30-year interannual variability values from all control simulations and the two distributions are rescaled on the y-axis because of the sample size difference (1,065 duplicate; 12,140 multi-decadal).

In conclusion, it was determined that both the simulations with partially duplicated output and those with listed duplicates in their parameter variations but with output variations would be kept in the ensemble and treated as simulations with either initial condition variations or computer architecture differences. There would be no skill in attempting to remove any one of these duplicate pairs due to the fact that there was no way to identify the "correct" simulation for that set of parameter variations without having CPDN carefully rerun all of the simulations in a highly controlled environment, which is not feasible.

Also, this duplicate issue was discovered only because some of the simulations actually had duplicates generated. The large number of other control simulations with no matched pairs may be subject to the same initial condition or computer architecture issues but there is no matched pair available for comparison. In summary, this issue will, in effect, add noise to the analyses and will be noted as an additional source of uncertainty, particularly to the parameter sensitivity analysis for interannual variability as there will be multiple factors influencing the spread in its distribution, not just the known parameter variations.

5.1.4 Final Ensemble

The final set of 1,214 control simulations was comprised of 138 atmospheres, ten oceans and eight initial conditions. From these there are 642 simulations having a unique atmosphere/ocean combination with the remaining 572 containing a duplicate atmosphere/ocean combination with a variation to the initial conditions. Table 5.1 lists the number of control simulations having each particular parameter value.

Table 5.1: CPDN perturbed parameters and the number of control simulations out of 1,214 that have a particular parameter value. Atmosphere and ocean parameters are grouped separately and the initial condition parameter is given at the end. Default parameter values are highlighted in bold.

Parameter	Description	Values	Control Simulations
ATMOSPHERE			
ALPHAM	Albedo at melting point of ice	**0.5**	**231**
		0.57	462
		0.65	521
ANTHSCA	Scaling factor for anthropogenic sulfates	0.5	0
		0.8	0
		1.0	**1,214**
		1.2	0
		1.5	0
CLOUDTAU	Time a circulating air parcel remains in cloud (s) [x 10^3]	3.6	278
		10.8	**581**
		32.4	355
CT	Accretion constant (s^{-1}) [x 10^{-4}]	0.5	345
		1	**404**
		4	465
CW_LAND [a]	Precipitation threshold over land (kg m^{-3}) [x 10^{-4}]	1	474
		2	**400**
		20	340
CW_SEA [a]	Precipitation threshold over sea (kg m^{-3}) [x 10^{-5}]	2	474
		5	**400**
		50	340
DTICE	Temperature range of ice albedo variation	2	521
		5	462
		10	**231**
EACF	Empirically adjusted cloud fraction **	**0.5**	**512**
		0.63	278
		0.67	424
ENTCOEF	Entrainment coefficient	0.6	377
		1.0	403
		3.0	**338**
		9.0	96

a, **b**, **c**, **d** Individual groups of parameters perturbed together

** Parameter values represent mean over 19 model levels (variations occur at each level)

Table 5.1: Continued.

Parameter	Description	Values	Control Simulations
I_CNV_ICE_LW [b]	Type of convective cloud ice crystal used in longwave radiation	**1**	**1034**
		7	180
I_CNV_ICE_SW [b]	Type of convective cloud ice crystal used in shortwave radiation	**3**	**1034**
		7	180
I_ST_ICE_LW [b]	Type of stratiform cloud ice crystal used in longwave radiation	**1**	**1034**
		7	180
I_ST_ICE_SW [b]	Type of stratiform cloud ice crystal used in shortwave radiation	**2**	**1034**
		7	180
ICE_SIZE	Ice crystal size (m) [x 10^{-4}]	2.5	381
		3.0	**471**
		4.0	362
L0 [c]	Sulfate mass scavenging parameter L0 (s^{-1}) [x 10^{-5}]	2.17	293
		6.5	**506**
		19.5	415
L1 [c]	Sulfate mass scavenging parameter L1 (s^{-1}) [x 10^{-5}]	0.99	293
		2.96	**506**
		8.86	415
NUM_STAR	Condensation threshold for accumulation [x 10^{6}]	0.1	405
		1.0	**595**
		10	214
RHCRIT	Critical relative humidity [**]	0.65	526
		0.73	317
		0.9	371
SO2_HIGH_LEVEL	Sulfur cycle: model level for SO_2 (high level) emissions	1	163
		3	**809**
		5	242
VF1	Ice fall speed (m s^{-2})	0.5	301
		1.0	**425**
		2.0	488
VOLSCA	Sulfur cycle: scaling factor for emission from natural (volcanic) emissions	1	669
		2	**352**
		3	193

a, **b**, **c**, **d** Individual groups of parameters perturbed together

** Parameter values represent mean over 19 model levels (variations occur at each level)

Table 5.1: Continued.

Parameter	Description	Values	Control Simulations
OCEAN			
HANEY	Haney heat forcing coefficient ($Wm^{-2}K^{-1}$)	**81.88**	**1082**
		163.76	132
HANEYSFACT	Haney salinity forcing factor	**0.25**	**885**
		1.0	329
ISOPYC	Isopycnal diffusion of tracers (m^2s^{-1}) [x 10^3]	0.2	130
		1	**867**
		2	217
MLLAM	Wind mixing energy scaling factor (m^2 s)	0.3	253
		0.7	**961**
VDIFFDEPTH [d]	Ocean: increase of background vertical mixing of tracer with depth (ms^{-1}) [x 10^{-8}]	0.7	265
		2.8	**581**
		9.6	368
VDIFFSURF [d]	Ocean: background vertical mixing of tracer (diffusion) at surface (m^2s^{-1}) [x 10^{-5}]	0.5	265
		1	**581**
		2	368
VERTVISC	Ocean: background vertical mixing of momentum (viscocity) (m^2s^{-1}) [x10^{-5}]	0.5	245
		1.0	**969**
INITIAL CONDITIONS			
DTHETA	Initial condition potential temperature perturbation applied to atmosphere (°C)	**0**	**3**
		0.01	3
		0.02	2
		0.03	4
		0.04	311
		0.05	300
		0.06	287
		0.07	304
		0.08	0
		0.09	0

a, **b**, **c**, **d** Individual groups of parameters perturbed together

****** Parameter values represent mean over 19 model levels (variations occur at each level)

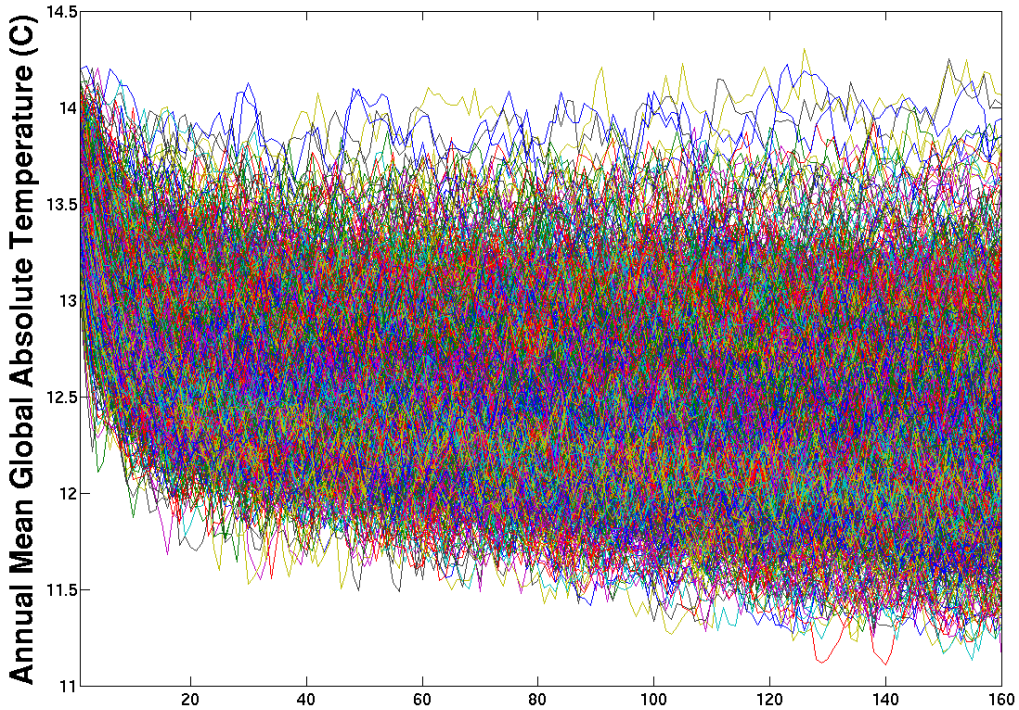
5.2 MODEL DRIFT

5.2.1 Drift Due to Initial Model Coupling Adjustment

When the atmosphere and ocean models were coupled together (see Chapter 3, Section 3.3.2) there was a period of time at the beginning of each simulation when the two model components were transitioning into the final coupled system. During this adjustment phase, climatic indices contained a large amount of drift until the system came into a state of equilibrium or, as will be discussed more in Section 5.2.2, a quasi-equilibrium state where the climate system still retained a certain degree of drift.

The initial adjustment period of drift is highlighted in Figure 5.6 where annual mean global absolute temperatures are shown for all simulations over the full 160 year time period (Figure 5.6(a)) as well as a closer look at the first 30-years (Figure 5.6(b)). A relatively large trend can be seen in the first five to ten years of the simulations followed by a transition into a more stable, yet sometimes still drifting, climate starting around 20 years into the simulation. This same general characteristic can be found throughout all NA regions for both temperature and precipitation as shown in Figure 5.7 which shows only the first 30 years of the control ensemble.

(a)



(b)

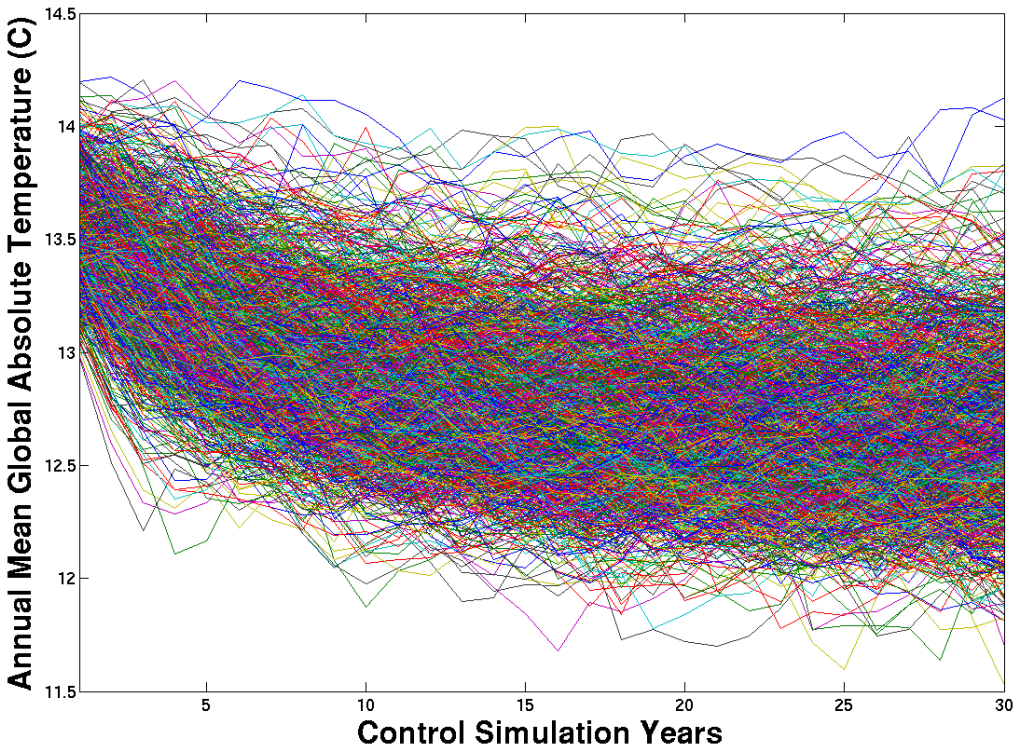


Figure 5.6: Control simulation 1,214 member ensemble of annual mean global absolute temperature (°C) for *(a)* the full 160 year period and *(b)* the initial 30-year period.

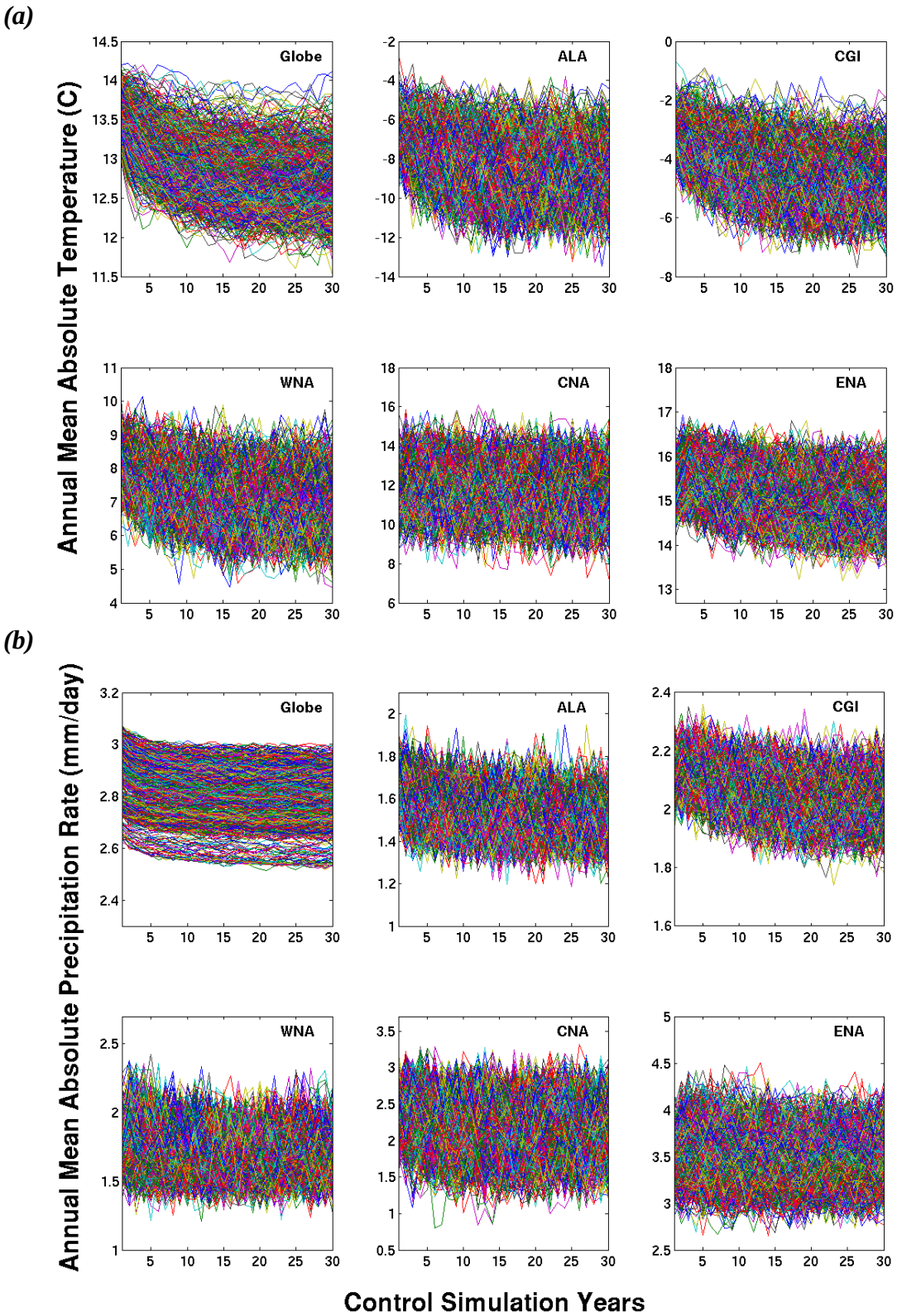


Figure 5.7: Control simulation 1,214 member ensemble of the initial 30-year period for annual mean absolute *(a)* temperature (°C) and *(b)* precipitation rate (mm/day) for the globe and five NA regions.

The initial period of drift at the beginning of the simulations will affect any climate analyses and therefore must be discarded. To identify the optimum year to begin analyses, distributions of trends within each of the 16 decades over all control simulations for global mean temperature were calculated and are given in Figure 5.8. The decadal distributions clearly show relatively larger trends within the first two decades, after which time the trends appear similar for the remaining decades. A similar result can be found in the NA regions and for precipitation (Figure 5.9). Therefore, the first 20 year period was not used in control analyses and all subsequent discussions of the control simulations will be based on a time period of model years 21-160.[14]

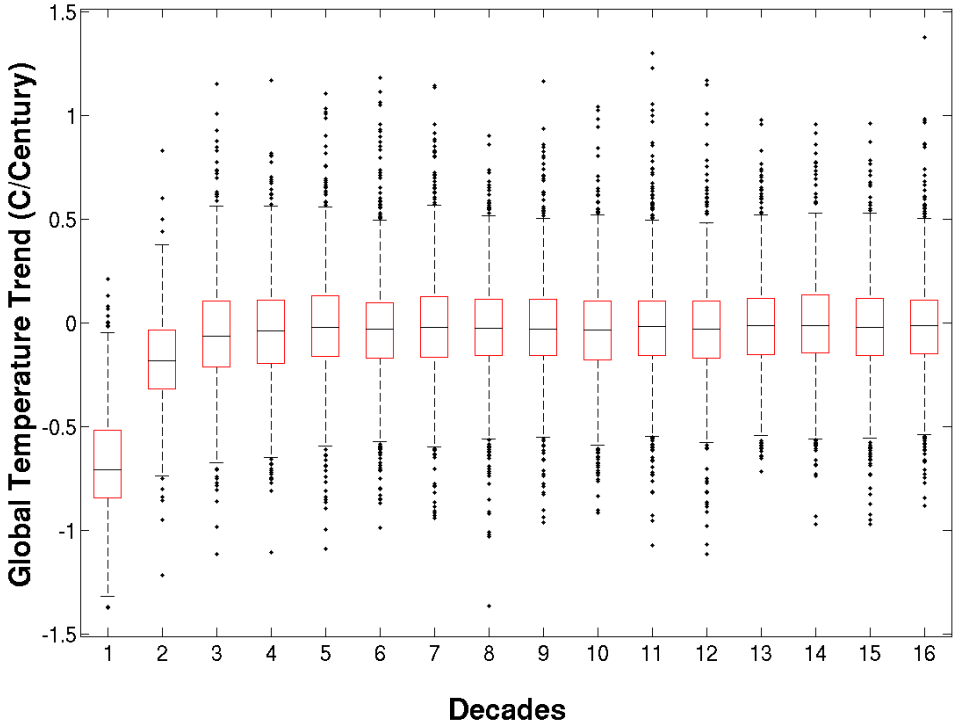


Figure 5.8: Trends per decade for the 1,214 control simulation's global mean annual mean temperature (°C/century). The boxplots indicate the mean and 25%-75% range within the box with whiskers out to the 95% range and subsequent trends in the outer 5% as black dots.

[14] Control simulation years 21-160 correspond to transient years 1941-2080 (see Chapter 7)

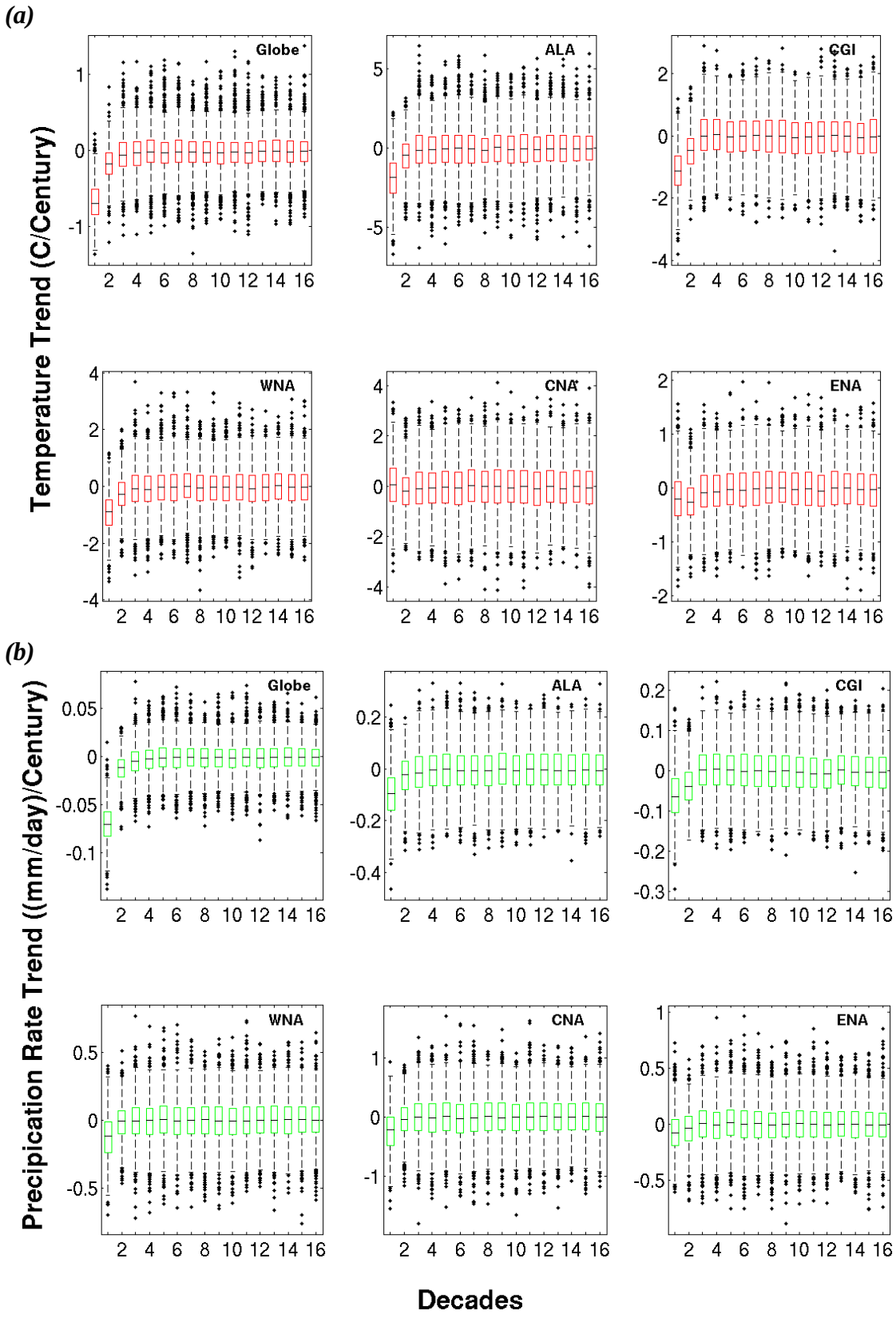


Figure 5.9: Same as Figure 5.8 but including the NA regions for *(a)* temperature (°C/century) and *(b)* precipitation ((mm/day)/century).

5.2.2. Long-Term Mean Drift

Within the established control analysis period (years 21-160), Figures 5.6(a), 5.8, and 5.9 still indicate that many of the simulations maintain a long-term mean trend throughout the rest of the simulation even though flux adjustments were applied in the atmosphere/ocean coupling process. As discussed in Chapter 3 (Section 3.3.2), a more generalized flux adjustment procedure was employed in the CPDN project in which the flux adjustments were established based on couplings between the separated fully dynamic atmosphere and ocean models with simpler versions of their counterparts in order to accommodate the large quantity of simulations to be generated. Therefore when the two fully dynamic components were coupled together, additional flux inequalities were evidently present which were not represented by the simple model coupling process, thus resulting in a long-term mean drift.

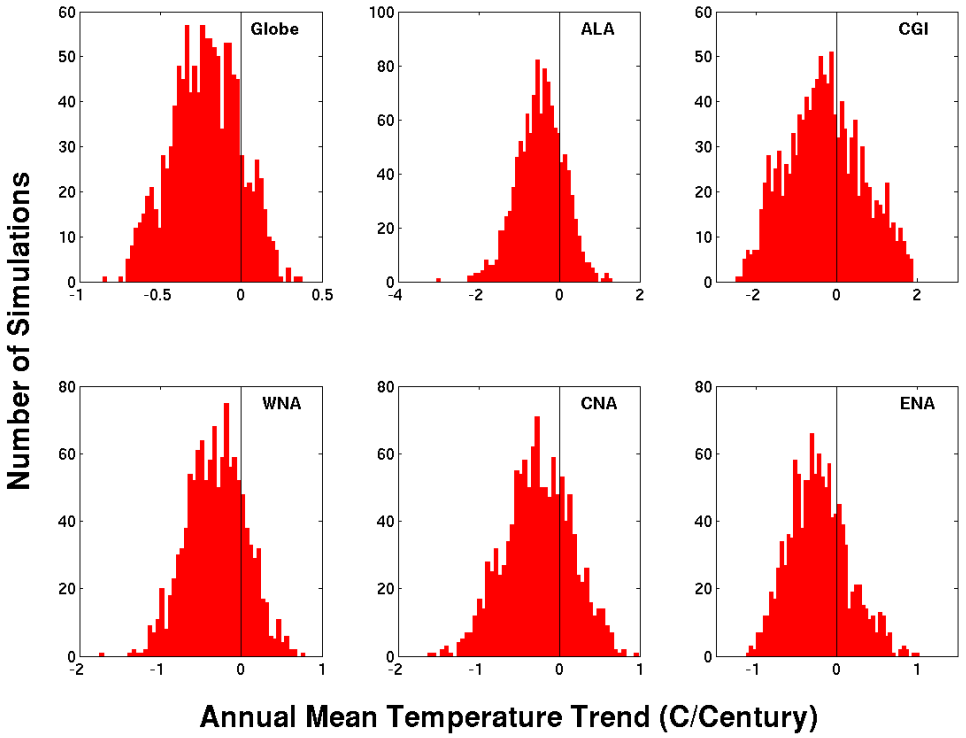
Because the goal of a control simulation is to establish a stable climate from which various forcings can be applied and model responses established (i.e., generating transient simulations), if the supposedly stable control simulation contains a component of drift then that drift also will be present in the corresponding transient simulation and the climatic response will be a combination of the drift and forced response. Therefore, the long-term drift must be accounted for and removed in order to isolate the forced response. For that reason, when assessing transient simulations in Chapter 7, the long-term mean drift of each transient's matching control simulation (i.e., with matching atmosphere and ocean parameters) was removed prior to any analysis (see Chapter 7, Section 7.2 for the drift removal process).

Figure 5.10 provides the distributions for long-term trends in annual mean temperature and precipitation for all control simulations and Table 5.2 lists the 95% range of these trends along with observed trends in three observational data sets (see Chapter 4). The main point is that long-term mean drift in the model's unforced control climate could be of the same magnitude or greater than trends found in the observed climate over the past 30-90 years. This highlights the significance of the drift and confirms the necessity to remove it from the transient simulations prior to any analysis. The long-term mean drift sensitivity to variations in model parameters is discussed in Section 5.7.2 and the actual transient drift removal process described in Chapter 7, Section 7.2.

Table 5.2: The 95% range of control simulation 140 year trends in annual mean temperature (°C/century) and precipitation rate ((mm/day)/century) for the globe and NA regions. All three observational temperature data set trends are from 1921-2010 and precipitation rate trends are from 1981-2010 for GPCP and 1951-2010 for NOAA-PREC. Refer to Chapter 4 for further discussion of the observational data sets.

	Globe	ALA	CGI	WNA	CNA	ENA
Temperature						
CPDN 95%	-0.6, 0.17	-1.7, 0.6	-1.9, 1.6	-1.02, 0.4	-1.08, 0.54	-0.88, 0.58
HadCRUT3	0.73	1.47	0.46	0.74	-0.10	0.27
NOAA-MLOST	0.79	1.46	0.39	0.84	0.13	0.26
GISTEMP	0.68	1.61	0.75	0.88	0.21	0.46
Precipitation						
CPDN 95%	-0.04, 0.001	-0.1, 0.04	-0.16, 0.15	-0.07, 0.06	-0.18, 0.11	-0.11, 0.07
GPCP	0.01	0.12	-0.76	-0.56	0.05	-1.05
NOAA-PREC	-0.06	-0.02	0.002	-0.003	0.35	0.11

(a)



(b)

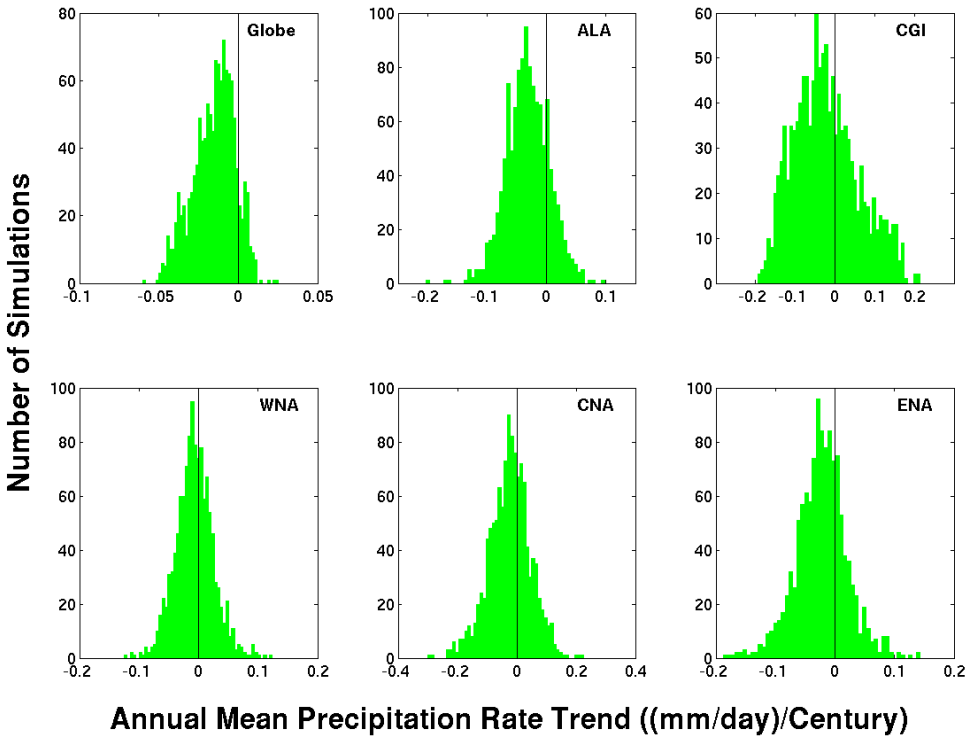


Figure 5.10: Control simulation long-term mean trends from years 21-160 in annual mean *(a)* temperature (°C/century) and *(b)* precipitation rate ((mm/day)/century) for the globe and NA regions. There is one drift value for each of the 1,214 simulations.

5.3 MEAN

5.3.1 Annual Mean

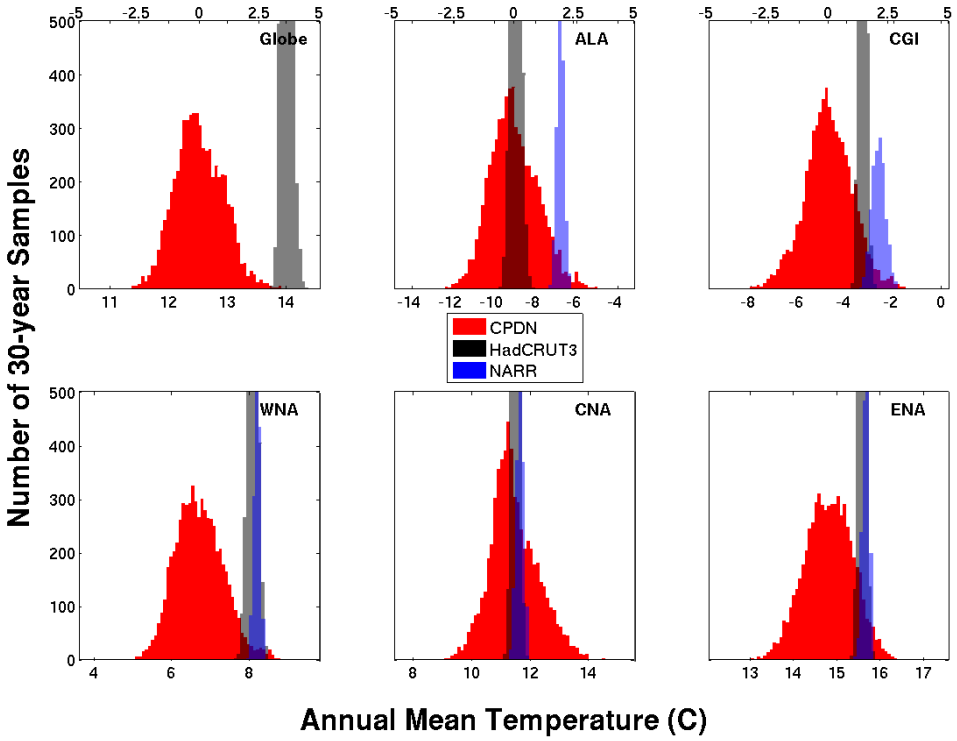
To assess the performance of the mean climate of the control simulations, each simulation was split into five 30-year samples (i.e., model years 21-50, 41-70[15], 71-100, 101-130, 131-160) and the annual mean temperature and precipitation calculated for the globe and five NA regions. Splitting simulations into 30-year samples when assessing climatic indices was preferred to calculating a single average for each simulation because the five samples can represent multi-decadal variations that may be present in the simulations and also because observational data sets have lengths of up to only 30-90 years for comparison and therefore 30 years allows for a common time period of averaging. Also, using a 30-year mean is widely recognized as an appropriate standard period for calculating climatic averages because it adequately removes most short-term variability (WMO 1983, 1988). Figure 5.11 provides the resulting 6,070 CPDN samples (e.g., five samples from each of the 1,214 simulations) along with observational (HadCRUT3, GPCP) and reanalysis (NARR) 30-year mean bootstrap distributions for comparison.[16] Bootstrap distributions were calculated by splitting the observational data sets into 5-year blocks and then creating 30-year samples by randomly selecting blocks, allowing them to be resampled in the random selection

[15] The 30 year sample covering model years 41-70 overlaps with the sample from 21-50 in order to gain 30-year samples across the entire 140 years of each simulation. The overlapping sample could have been taken from any time period within the simulation but starting the second sample 20 years after the official start of the control simulation analysis (e.g., 41) is a logical choice because the early portions of the first sample (years 21-50) is the only location that could still be slightly impacted by the initial readjustment period model drift over the first 20 years of simulation (Section 5.2.1) and therefore the overlapped sample could provide a more accurate representation of the early portion of each simulation.

[16] Neither the long-term mean trend in the CPDN simulations nor the 20th century trend in observational data were removed prior to calculating 30-year mean samples because the trends are small compared to the absolute values being compared. Also, if the trends were removed then we would be required to set an arbitrary mean to anchor the detrended data to (e.g., mean of the entire time series) which would add its own degree of uncertainty that may be of the same order of magnitude as that added when leaving the trends in.

process. The total number of samples generated was equal the number of CPDN samples (i.e., 6,070) and the relative proportion of samples coming from each data set was set to match the relative differences in the length of their records (e.g., 90 years versus 30 years).

(a)



(b)

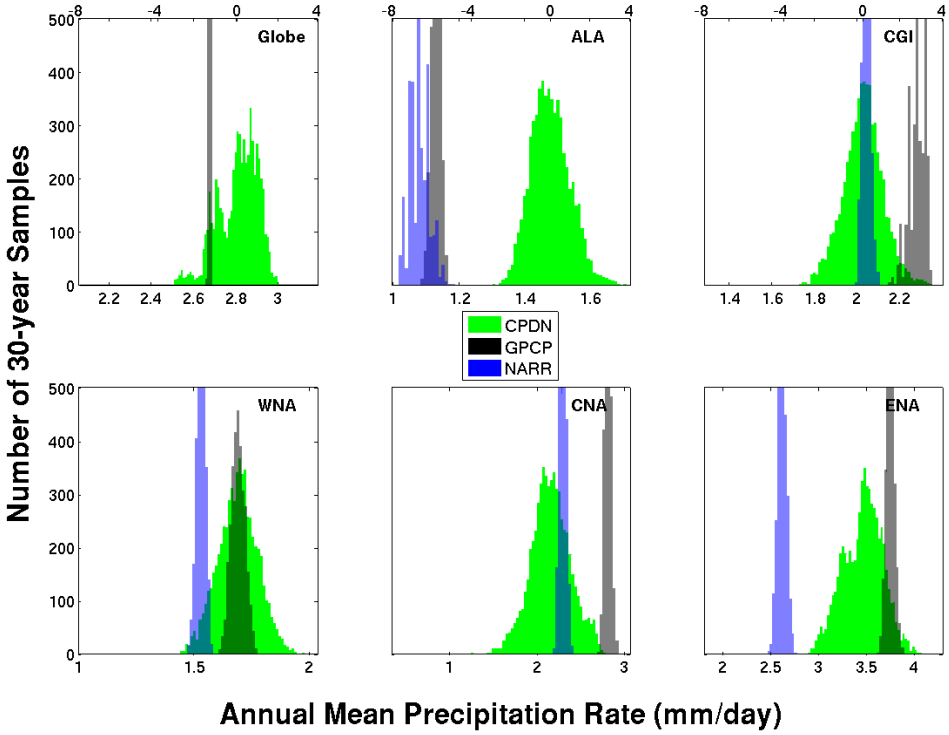


Figure 5.11: Annual 30-yr mean *(a)* temperature (°C) and *(b)* precipitation rate (mm/day) for the globe and five NA regions from the 1,214 control simulations (five samples per simulation) and observational bootstrap distributions (same number of overall samples). The upper x-axis in each region is standardized values based on the CPDN distribution in that region. The y-axis is set to highlight the CPDN distributions (i.e., observations can be cut off).

The CPDN distributions in Figure 5.11 are much broader than the corresponding observational distributions (i.e., contain a greater range of simulated mean temperature and precipitation). This can be attributed to the large number of climate model parameter variations used and the resulting wide range of simulated climates. While this may imply that many of the simulated climates contain biases and are unrealistic, another possibility is that the observational distributions are erroneously too narrow. Recall that the bootstrap method used to generate these distributions was based on relatively short time periods, 30-90 years, and therefore such a short time span may not fully represent the entire range of possible climatic states of the recent past.

From Figure 5.11 it also is evident that CPDN and observational distributions do not show consistent characteristics across regions. While the distributions of annual mean temperature in CNA each have a similar mean and some of the other regions have either the observational or reanalysis distribution aligned with CPDN, most regions contain varying degrees of misalignment. This may imply that parameter variations affect climatic indices differently across different regions causing variation in model biases (investigated further in Section 5.7). Or it may suggest that observational estimates are not properly representing the actual climate in certain regions. (For a number of instances the observational and reanalysis data sets do not even align.) These observational inadequacies could be caused by, for example, insufficient temporal or spatial data coverage or uncertainties in the methods used to construct the data sets themselves. One aspect of potential significance is that the CPDN NA regional averages contain both land and ocean grid cells and therefore the observational

averages also were calculated based on both land and ocean data which incorporated the added uncertainties associated with limited ocean observations.

Additionally, the annual mean quantities assessed here are absolute values, which can vary markedly from location to location within a specified region making it difficult to obtain a truly accurate observational estimate when large quantities of data are missing between official measurement stations. It is for this reason that anomaly values are typically used instead of absolute values because the biases are removed and additionally because there is a strong correlation between anomaly estimates across relatively large distances (on the order of 1,200 km), which reduces the impact of missing data (Hansen and Lebedeff 1987). Absolute values, however, were used when analyzing the climate mean here and seasonal cycle in Section 5.3.2 because the biases themselves are the important aspects to be investigated in these two indices.

With that said, some possible explanations for various features found in Figure 5.11 can be given. The first feature to note is the distributional differences found in the global temperatures in Figure 5.11(a). The observational means come from the HadCRUT3 data set which is missing data from around the polar regions (refer to Chapter 4 for all observational data set references) and therefore a calculation of global mean in this instance will be missing relatively colder data points, the net result being a warmer global mean than the actual average. Therefore the difference is associated with a bias in the observations. It should be noted that the NARR data set is not shown in any global average because it contains reanalysis data only over the NA region. An additional note is that only one observational data set is given for temperature and precipitation, besides the reanalysis data set, because the other available data sets

discussed in Chapter 4 did not provide absolute value versions of their data, only anomalies from a long-term mean which was not provided.

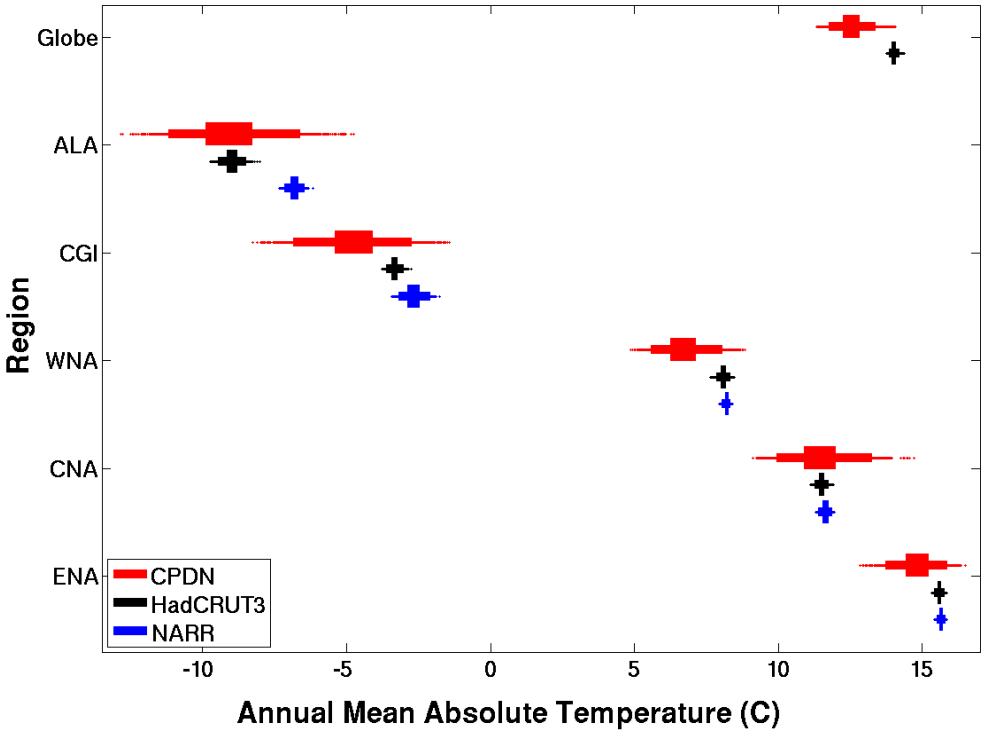
Another feature that stands out is that CGI, WNA, and ENA temperatures for the majority of CPDN samples are cooler than observations. This could be because the model has poor representation of topography, due to its course horizontal resolution, and/or snow and ice processes. Also, a significant fraction of these regions are comprised of ocean and therefore the observations may not be representing the true average value within the land/ocean region because of observational limitations across the ocean. This seems probable given the fact that the observations of the two land locked regions (ALA, CNA) align relatively well with CPDN (except for NARR in ALA).

With the precipitation distributions, the observations are even more varied compared to CPDN than what is seen in the temperature distributions. Given the aforementioned issues with calculating observational regional absolute means it is difficult to identify the specific causes of the discrepancies. One feature that can be explained further is the fact that NARR estimates are generally smaller than GPCP observed estimates. It has been found that NARR does not handle precipitation outside the contiguous U.S. well because precipitation data is utilized in the reanalysis process and therefore in data sparse regions (e.g., Mexico, Canada, or over the ocean) the resulting precipitation output is less trustworthy and tends to be smaller than actual values (e.g., Bukovsky and Karoly 2007; Mo et al. 2005; Mesinger et al. 2006). While we might anticipate this effect to be slightly less for landlocked CNA, that region still includes overlap into Canada and Mexico which may be one of the reasons causing the

difference between it and CPCP. Even though NARR is close to the CPDN distribution mean, GPCP may be closer to the actual value since an underestimation in modeled precipitation over that region may be anticipated due to difficulty in modeling convective activity across this region, especially nocturnal summertime mesoscale convective systems (e.g., Davis et al. 2003).

Figure 5.12 provides the same information as Figure 5.11, but displays the distributions in box and whiskers form across the entire temperature and precipitation range to illustrate differences in the relative magnitudes of annual mean values across regions. These types of boxplots, showing the 25%-75% (inner larger box), 2.5%-95% (outer skinnier box), and all samples outside the 2.5%-95% range (small dots of same color) will be used throughout the remainder of this study when comparing distributions. The 25%-75% can be referred to as the 50% range and the 2.5%-95% referred to as the 95% range.

(a)



(b)

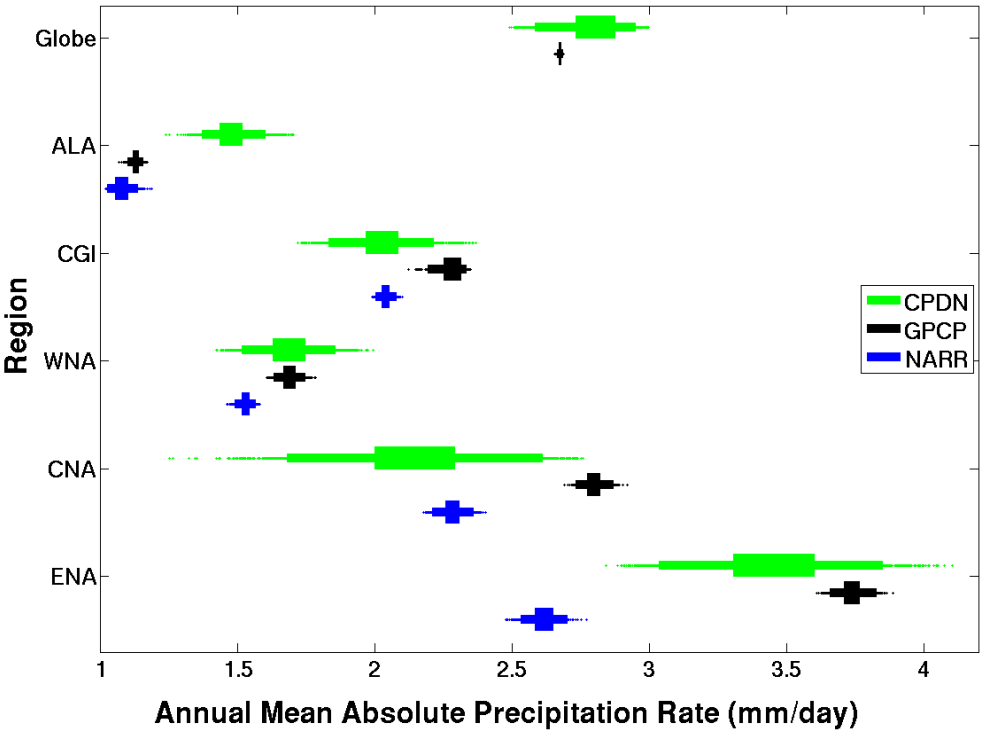


Figure 5.12: Annual 30-yr mean *(a)* temperature (°C) and *(b)* precipitation rate (mm/day) for the globe and five NA regions from the 1,214 control simulations (five samples per simulation) and observational bootstrap distributions (same number of samples). Boxplots provide 25-75% (inner) and 2.5%-97% (outer) ranges and dots for samples outside the 95% range.

In general, the relative magnitudes of CPDN temperature distributions across the different regions were consistent with those found in the observational data (Figure 5.12(a)). The north to south temperature gradient was found across the NA regions with the northern regions cooler than the southern regions. The colder temperatures in ALA versus CGI can be explained by the fact that CGI contains greater ocean area than ALA as well as the fact that CGI could be influenced by the northward transport of heat from North Atlantic Ocean currents. WNA, CNA, and ENA get slightly warmer respectively from west to east which can be expected given that WNA reaches farther north than the other two regions and ENA reaches slightly farther south. Also, WNA includes Pacific Ocean waters with currents flowing from north to south bringing with it cooler temperatures while ENA includes the warmer Gulf Stream waters flowing up from the south.

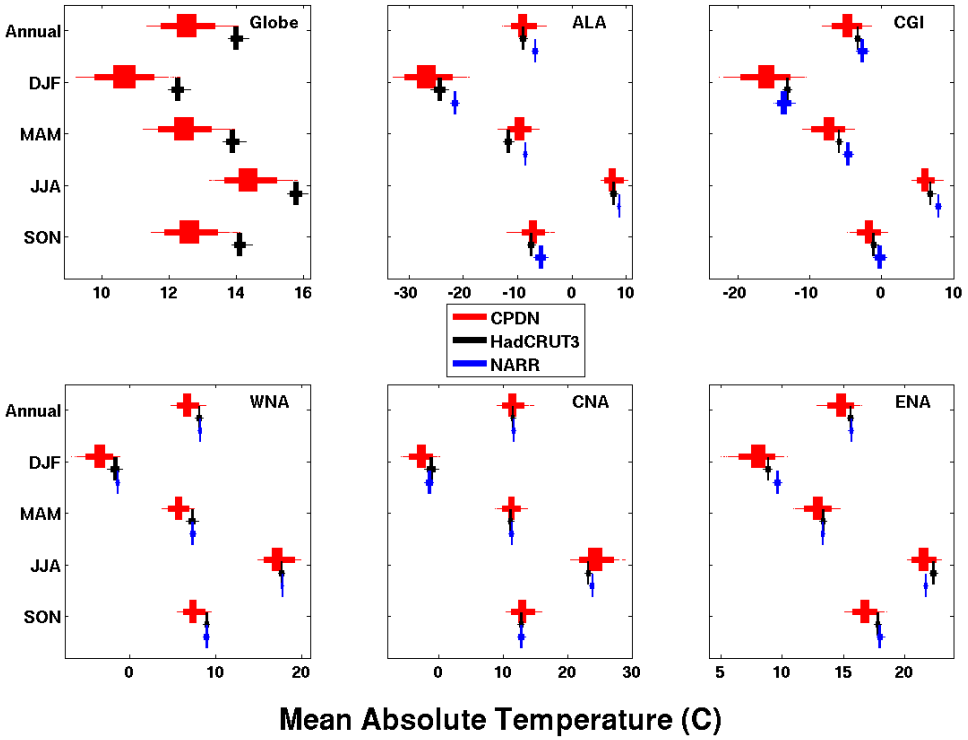
In Figure 5.12(b) the CPDN distribution relative magnitudes for precipitation across different regions also were generally consistent with those found in observational data with a few discrepancies between the GPCP and NARR data sets as already discussed. The drier to wetter transition from west to east was found going from WNA to CNA to ENA. And to the north, CGI correctly simulated larger precipitation than ALA because of its warmer temperatures and influence of the North Atlantic Ocean heat and moisture transport. One feature that stands out is the much broader CPDN distribution range found in CNA precipitation (and somewhat in ENA as well) compared to the other regions. This shows that parameter variations have a greater impact on annual mean precipitation in these regions. (Parameter sensitivity will be explored more in Section 5.7.) The region generating the largest amount of

precipitation is ENA because a large portion of its area resides in or near warm tropical waters. The warmer temperatures allow for greater moisture availability and the region can include precipitation from tropical convective storm activity.

5.3.2 Seasonal Means

Next, the seasonal means in temperature and precipitation were assessed. Figure 5.13 displays the seasonal mean distributions which exhibited similar characteristics as the annual mean distributions (also shown) from Figure 5.12, most notably the same broader distribution compared to observations. Note that the x-axis range for each region can vary due to the differing regional magnitudes. The CPDN seasonal temperatures in Figure 5.13(a) appear to have performed well, having a distinct seasonal cycle matching that of observations.

(a)



(b)

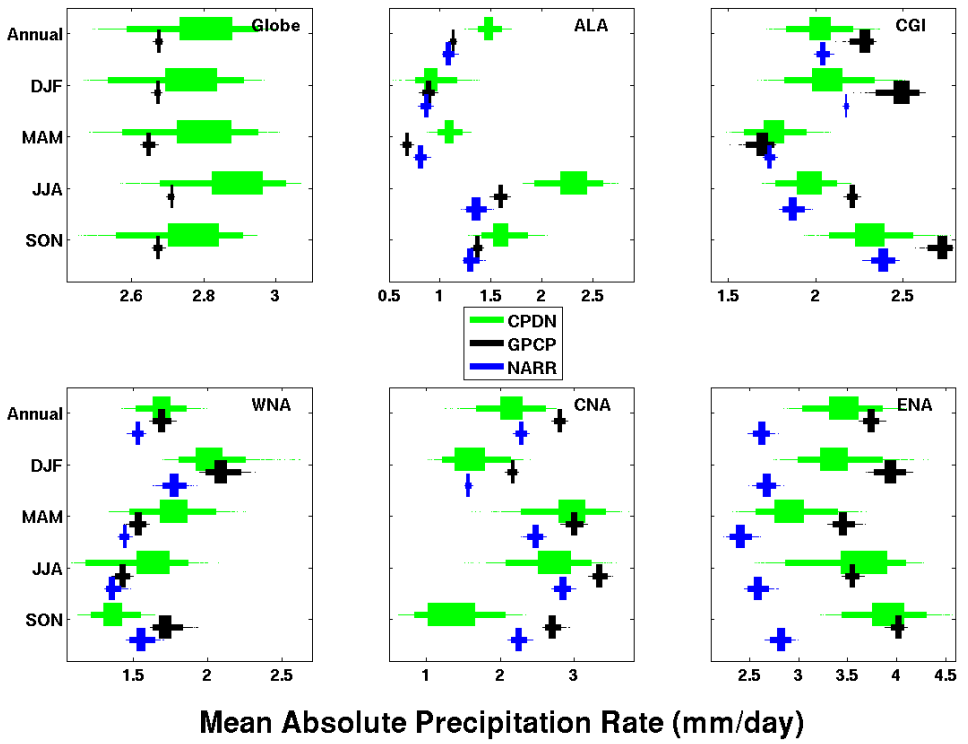


Figure 5.13: Same as Figure 5.12 but including seasonal 30-yr means for (*a)* temperature (°C) and *(b)* precipitation rate (mm/day).

The seasonal precipitation shown in Figure 5.13(b) had more disparity than that found in temperature with only a modest seasonal cycle apparent in some of the regions. At a very general level the magnitude variations between seasons of CPDN appear to match that of observations with a few exceptions. One thing that stands out is that CNA was quite a bit drier in SON than what observations might suggest. If this is a model bias then a potential reason could be that the model may not be fully capturing the fall season convective activity. The excessive SON drying is a reason for CNA having a relatively wide annual average distribution compared to other region (Figure 5.12(b)).

Another feature that stands out is CPDN ALA precipitation in JJA which is appreciably greater than observations. This could be caused by an error in the observations due to poor observational density in that region because the CPDN ALA JJA temperatures do not reveal any anomalous warmth, which could have increased moisture available to that region. However, the additional precipitation could be the result of some kind of anomalous transport of moisture to the region either through atmospheric circulation or warm ocean current inaccuracies.

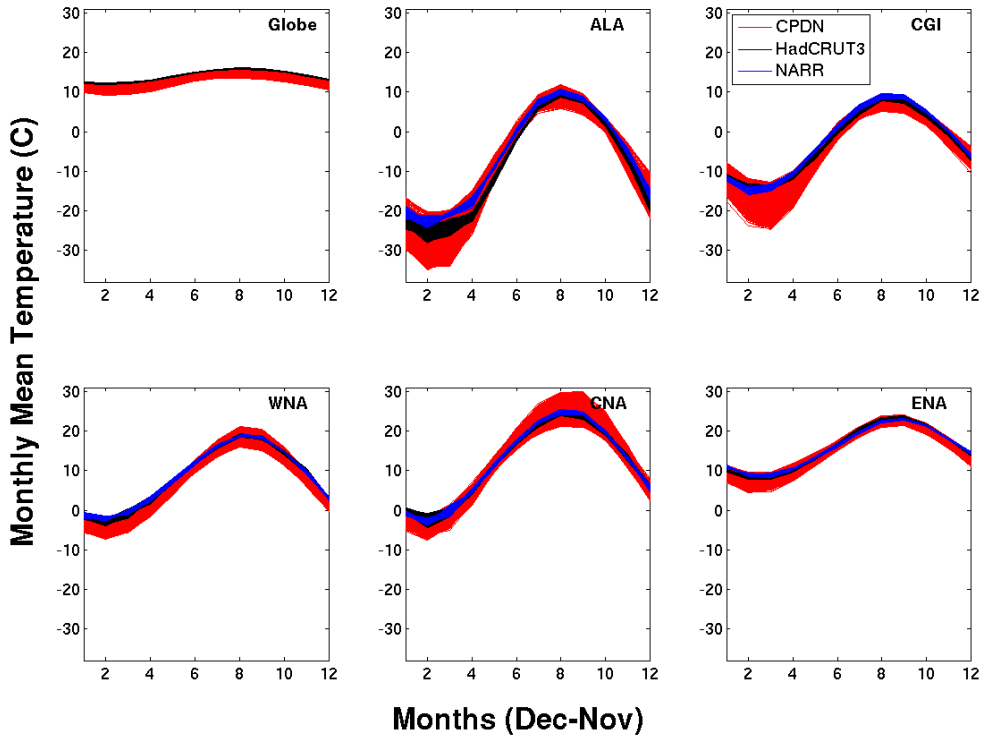
5.4 SEASONAL CYCLE

This section assesses the seasonal cycle of temperature and precipitation in the CPDN simulations. The first subsection evaluates the mean seasonal cycle and the second the magnitude of the seasonal cycle in terms of the difference between northern hemisphere (NH) summer and winter (JJA-DJF).

5.4.1. Mean Seasonal Cycle

The monthly mean values in temperature and precipitation for 30-year samples is shown in Figure 5.14 for all CPDN simulations along with observational data set bootstrap samples. Both CPDN simulations and observational data sets were detrended and centered on their absolute means prior to the analysis to remove any long-term drift in the simulations or greenhouse gas forced trends in the observations (i.e., only looking at natural variability). The CPDN temperature monthly averages in Figure 5.14(a) have a distinct seasonal cycle in good agreement with observations. This was anticipated as the seasonal cycle in temperature is predominantly controlled by solar radiation changes across the seasons. Comparing across regions, the general temperature seasonal cycle magnitudes appear to match observational magnitude differences well (all y-axes are the same). Two areas to point out in Figure 5.14(a) are the larger temperature ranges seen in CPDN for ALA and CGI winter which may be related to a greater sensitivity of winter temperatures in these regions to changes in model parameter values. Alternatively since both of these are northern regions there may be some missing observational grid points or measurements in the extreme northern portion of the regions causing the temperatures to be too warm.

(a)



(b)

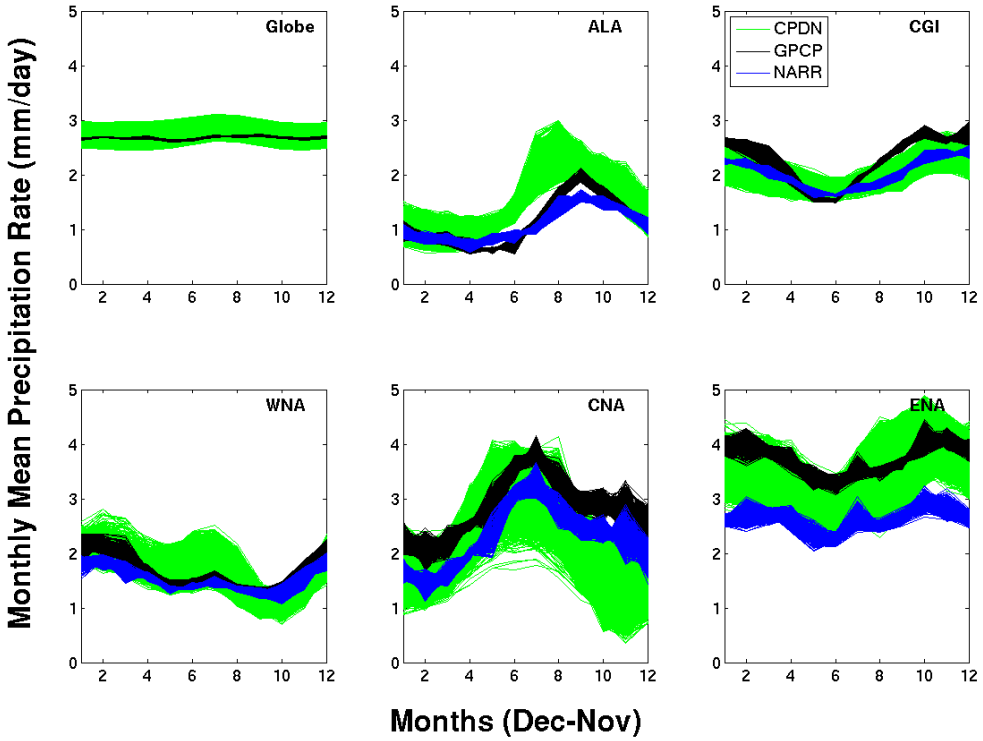


Figure 5.14: Mean seasonal cycle 30-yr averages for *(a)* temperature (°C) and *(b)* precipitation rate (mm/day) for the globe and five NA regions for the 1,214 control simulations (five samples per simulation) and observational bootstrap distributions (same number of samples). The y-axis is the same in all regions for a given variable.

The precipitation seasonal cycles for CPDN and observations show more variability than temperature (Figure 5.14(b)), a characteristic also anticipated since precipitation is dependent on a number of variables (e.g., moisture fluxes/availability, geographical distributions, large scale general circulation patterns, storm tracks, etc., as well as the size and location of the region in which the average is being computed). Even with this complexity, the cycle in which precipitation varies in the observations can generally be seen in CPDN simulations. The general magnitudes looking across regions generally match the observations and within an individual region the wet and dry periods for the most part line up. A few obvious exceptions are the drier CPDN fall and wetter ALA summer (as discussed in Section 5.3.2). The wet bias in ALA appears to be due to the fact that the increase in precipitation in the models begins earlier than what is implied by the observations. Again it is uncertain whether this is an actual bias or an artifact of limited observational coverage in the region.

5.4.2 Magnitude of the Seasonal Cycle (JJA-DJF)

To assess the magnitude of the seasonal cycle a simple measure of NH summer minus winter (JJA-DJF) was calculated. Only temperature is discussed here because, as was shown in the previous subsection, precipitation does not necessarily have a straight forward seasonal cycle and does not always have its maximum and minimum occurring in summer or winter. Using this measure provides a single value that can be used to assess the model's response to solar forcing and will be useful for investigating parameter variation sensitivity (Section 5.7). Also, the magnitude of the seasonal cycle in temperature can be a useful indicator for assessing a model's global temperature response to changes in CO_2 (also called climate sensitivity), because the changes in solar forcing have similar feedback mechanisms as those associated with changes in greenhouse gas forcing (e.g., feedbacks in water vapor, ice albedo).

Figure 5.15 provides the magnitude in seasonal cycle of temperature for CPDN and observations which generally align. Any differences between the two tend to be a somewhat larger range of higher magnitudes in seasonal cycle for CPDN. This can subtly be seen in Figure 5.14 as well and from that figure it appears that one of the dominant factors is the cooler winters in the CPDN models, especially seen in ALA and CGI. With the greater range of JJA-DJF, the CPDN model parameter variations may alter various feedback processes (e.g., water vapor, albedo, cloud) and result in a greater range of climate sensitivities than found in the observed climate (see Section 5.7 for further discussion).

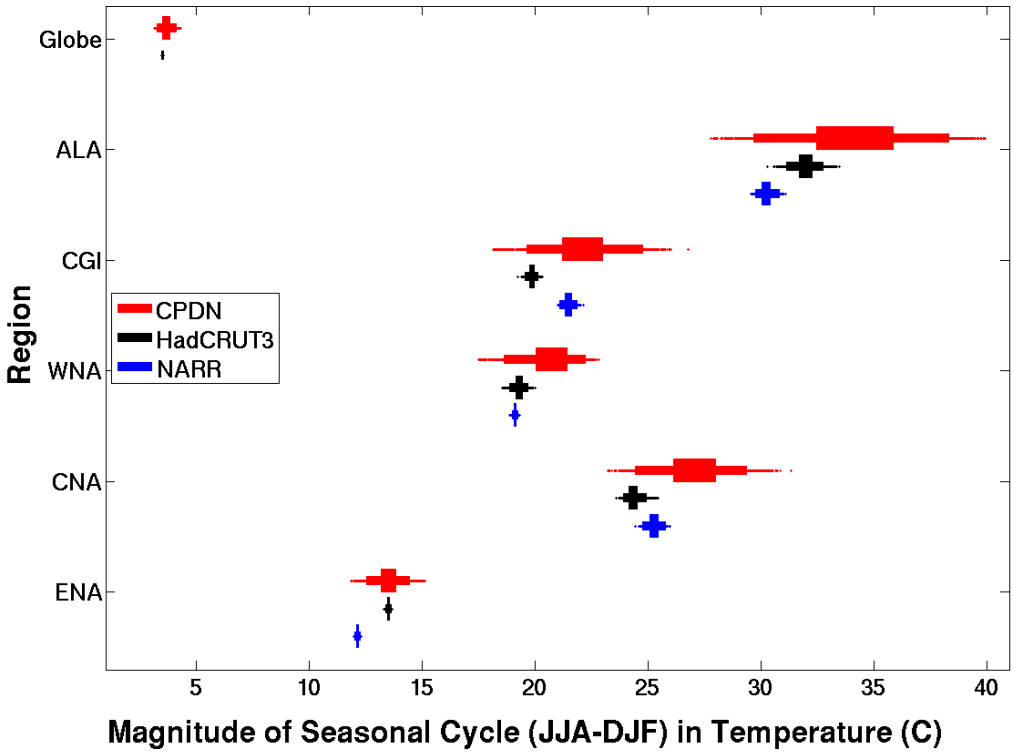


Figure 5.15: Magnitude of the seasonal cycle (JJA-DJF) of temperature for the globe and five NA regions for the 1,214 control simulations (five samples per simulation) and observational bootstrap distributions (same number of samples). Boxplots provide 25-75% (inner) and 2.5%-97% (outer) ranges and dots for samples outside the 95% range.

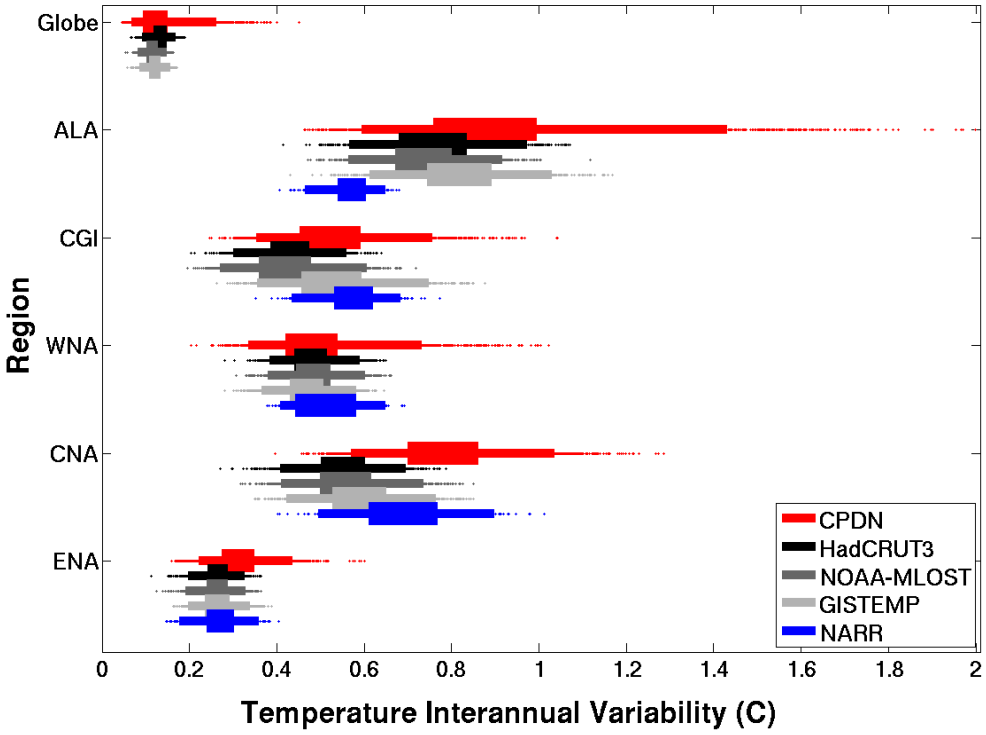
5.5 VARIABILITY

This section investigates the variability of temperature and precipitation in the CPDN simulations. The first subsection evaluates year-to-year variability (interannual variability) for annual and seasonal averages and the second section investigates the interannual variability of individual months. Interannual variability will be defined as the standard deviation of temperature or precipitation within a defined time period (e.g., 30 years).

5.5.1 Interannual Variability

The interannual variability in annual mean temperature is shown in Figure 5.16(a) along with observational bootstrap distributions made up of three different observational data sets (HadCRUT3, NOAA-MLOST, GISTEMP) and one reanalysis data set (NARR). The precipitation comparison is shown in Figure 5.16(b) with observational data sets (GPCP, NOAA-PREC) and the same reanalysis (NARR). Additional observational data sets were available for this variability analysis compared to the mean and seasonal cycle analysis because here anomaly values can be used (which were the only data provided for some observational data sets) since the magnitude of the absolute values do not impact calculations of year-to-year variability. Both the CPDN simulations and observational data sets were detrended prior to the analysis to remove any long-term drift in the simulations or greenhouse gas forced trends in the observations (i.e., only looking at natural, unforced variability).

(a)



(b)

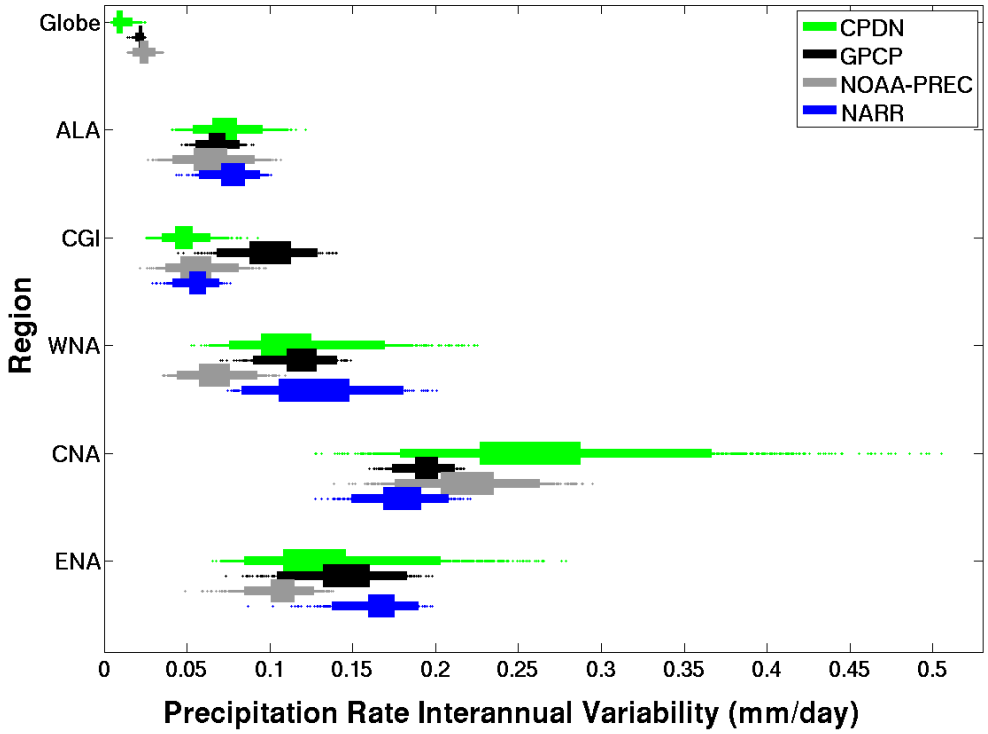


Figure 5.16: Annual 30-yr interannual variability for *(a)* temperature (°C) and *(b)* precipitation rate (mm/day) for the globe and five NA regions from the 1,214 control simulations (five samples per simulation) and observational bootstrap distributions (same number of samples). Boxplots provide 25-75% (inner) and 2.5%-97% (outer) ranges and dots for samples outside the 95% range.

The interannual variability for both CPDN temperature and precipitation were generally in good agreement with observations for the majority of their distributions with a few exceptions. A common feature found in annual temperature variability (Figure 5.16(a)) was a number of samples in each region with larger variability compared to observations, especially ALA. A closer look at the interannual variability within individual seasons (Figure 5.17(a)) provides some insight into which part of the year this greater variability originated from. This information will be useful when assessing parameter variations and identifying possible modeled process changes responsible for the larger variability (see Section 5.7.1 for physical explanations of the characteristics discussed here based on the parameter sensitivity analysis). Relatively larger values of global interannual variability were found across all seasons while the ALA, CGI, WNA, and ENA had most of their increased variability in DJF with additional samples coming from MAM. CNA had a large amount of its increased variability coming from JJA with all other seasons also having slightly larger values.

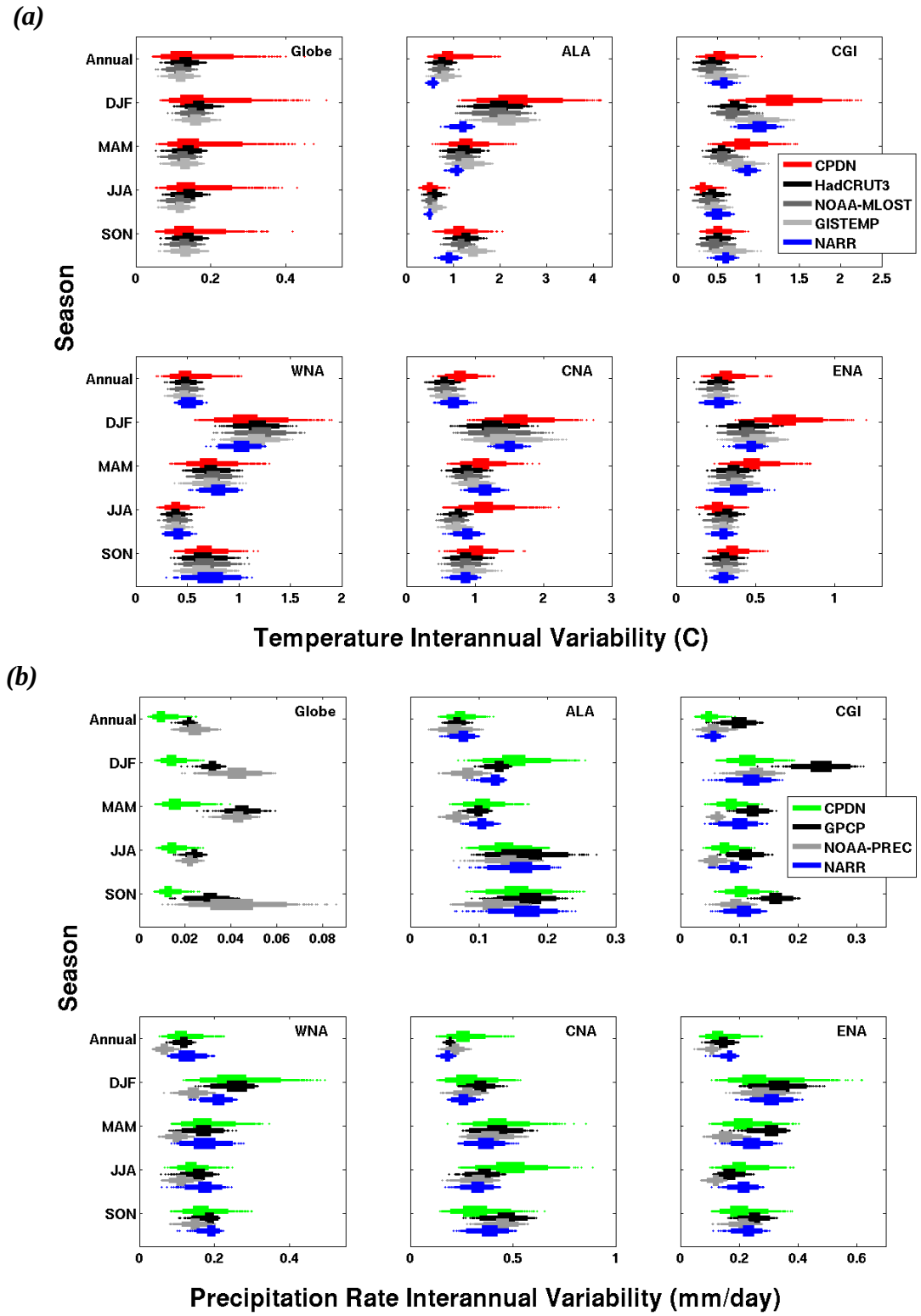


Figure 5.17: Same as Figure 5.16 but including both annual and seasonal 30-yr interannual variability for *(a)* temperature (°C) and *(b)* precipitation rate (mm/day).

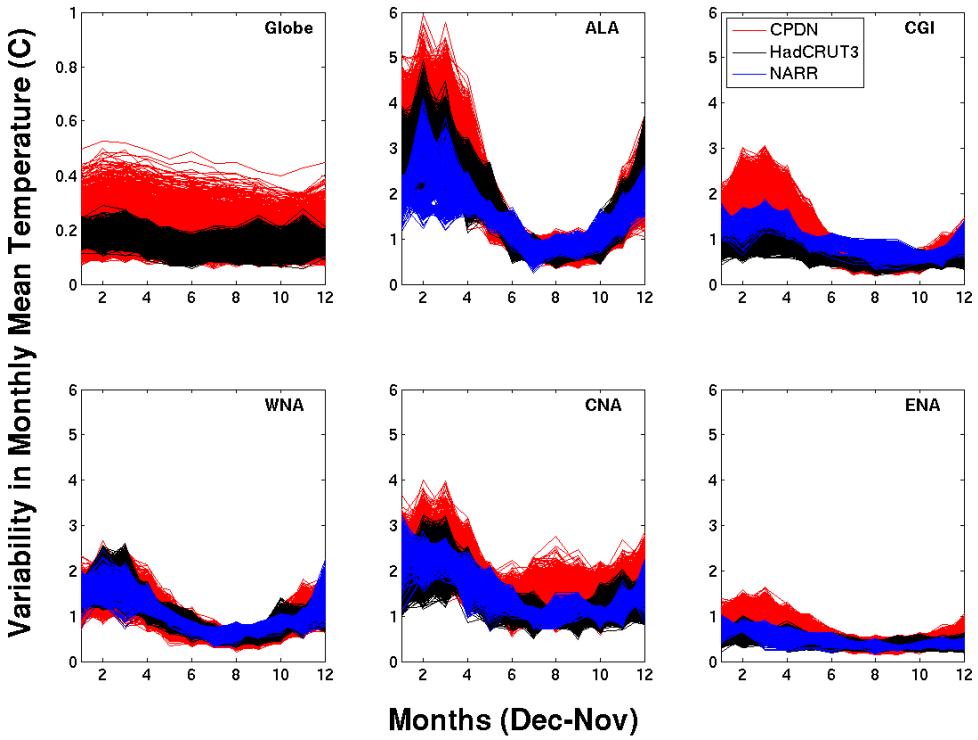
The simulated annual precipitation variability (Figure 5.16(b)) had a few aspects worth pointing out. The main point was the extension of the CNA precipitation distribution to much larger values of interannual variability. From the seasonal distributions (Figure 5.17(b)) it is apparent that this increased variability predominantly came from JJA and somewhat from MAM. Again, this will be discussed further in Section 5.7.1 when the specific parameter variations responsible for the increased variability are identified.

Another aspect to point out is shift in the entire distribution of CGI precipitation from the observational data set GPCP (Figure 5.16(b)), which is originating almost entirely from DJF (Figure 5.17(b)). This is almost certainly an issue with the GPCP data set when attempting to properly estimate precipitation over a region with limited observational measurement sites. Recall that while all three of the precipitation data sets displayed a general decrease in precipitation in CGI over the final decade of the observational period CGI showed a more significant drop (Chapter 4, Section 4.2)) which would explain this increase in variability.

5.5.2 Monthly Interannual Variability

Instead of looking at year-to-year variations at an annual or seasonal scale, individual months also can be assessed. Figure 5.18 shows the monthly interannual variability over the same 30-year time periods for CPDN and observations. This simply illustrates how much the temperature or precipitation in a given month can vary within a 30-year time period (e.g., standard deviation of 30 years of December temperatures).

(a)



(b)

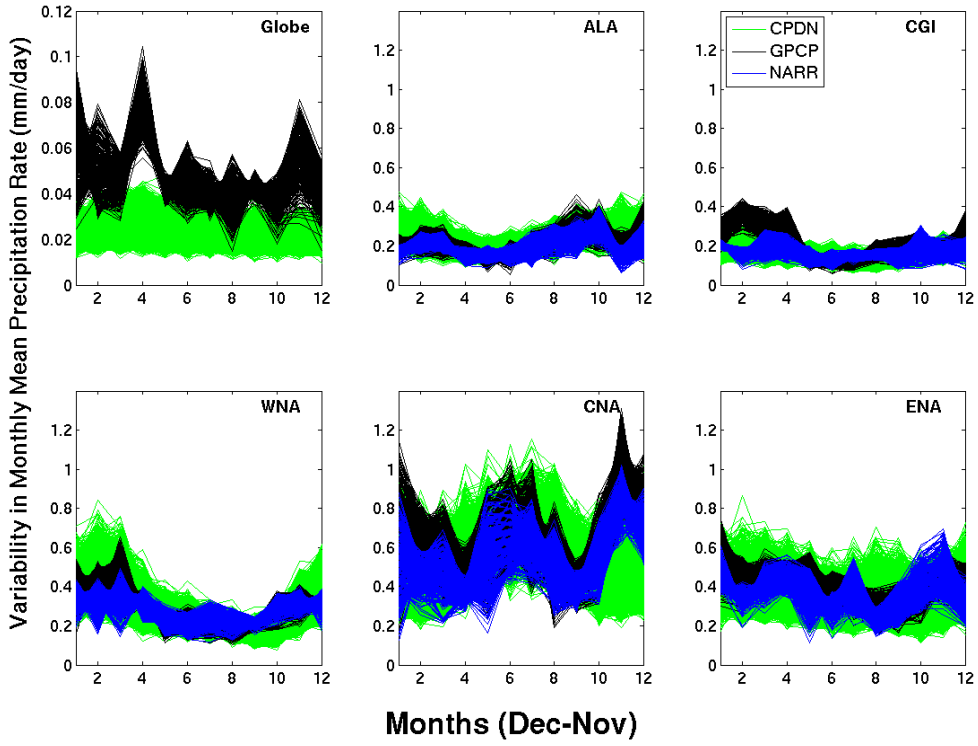


Figure 5.18: Monthly interannual variability 30-yr averages for *(a)* temperature (°C) and *(b)* precipitation rate (mm/day) of the globe and five NA regions for the 1,214 control simulations (five samples per simulation) and observational bootstrap distributions (same number of samples). The y-axis for the global plots differs from the regional plots.

In general, CPDN temperature and precipitation follow the relative magnitudes of observed monthly variability. And it is clear from Figure 5.18(a) that CPDN winter temperatures tend to have greater variability than summer temperatures, especially visible in ALA, which is a feature also found in observations. This is the result of a greater temperature difference between mid-latitudes and polar regions during northern hemisphere winter and the arctic frontal passages that traverse the region during that time period. The magnitude of this difference decreases as more ocean water is included in a region, which tends to limit variability because of the greater amount of energy required to change the ocean surface temperature compared to land (seen when comparing WNA and ENA to CNA and CGI to ALA). Additionally, CPDN winter temperatures in CGI appear to have some samples with greater variability, as does ALA to some extent (a feature also found in seasonal interannual variability in Figure 5.17(a)). And the major aspect to note in monthly variability in precipitation (Figure 5.18(b)) is the greater variability seen in CNA compared to the other regions, which also was found in seasonal interannual variability in Figure 5.17(b). This cause and explanation for this greater range in variability is explored further in the parameter sensitivity analysis of Section 5.7.1.

5.6 REGIONAL AND VARIABLE RELATIONSHIPS

Next a variety of temperature and precipitation relationships were investigated. The first sub-section describes relationships between temperature and precipitation within each individual region while the second sub-section explores relationships across regions. The third sub-section addresses relationships associated with the El-Niño Southern Oscillation (ENSO) and North Atlantic Oscillation (NAO) teleconnection patterns.

5.6.1 Temperature and Precipitation Relationships within the same Regions

The correlation between interannual variations of temperature and precipitation in each 140-year simulation was calculated for each NA region and the globe for all 1,214 CPDN control simulations as well as for the various combinations of temperature and precipitation observational data sets. The CPDN correlations were calculated across the entire 140 year simulation after the non-climatic long-term mean drift was removed (Section 5.2.2) and the long-term mean trends, associated with the response to increasing greenhouse gas forcing, were removed from observations so as to not influence the natural variability comparisons. It should be noted that these observational data set correlations are calculated over shorter time spans (30-90 years) than the CPDN simulations.

Table 5.3 summarizes the correlation results. The CPDN results are shaded and list the mean temperature and precipitation correlation of all 1,214 simulations followed by the 2.5%-97.5% range in brackets. The observational results are listed below the CPDN results and represent the mean correlation followed by the minimum and

maximum in parentheses covering combinations from the four temperature and three precipitation data sets (with NARR included). Across the regional results, an asterisk identifies the largest mean correlation magnitude for both CPDN and observations within a specific season and yellow shading identifies the largest mean correlation magnitude within a specific region.

Table 5.3: Temperature (C) and precipitation rate (mm/day) correlations for a given region and time period. CPDN correlations are shaded and contain the mean and 2.5%-97.5% range of the distribution of correlations from each simulation (i.e., 140-year comparison) in brackets with observational data set correlations directly beneath them with their mean and minimum and maximum values from the correlation calculated within each data set in parentheses. Asterisks (*) mark the largest mean correlation magnitude for both CPDN and observations within each given season and yellow shading identifies the mean largest correlation magnitude for both CPDN and observations within each given region (both for NA regions only).

CPDN Observations	Annual	DJF	MAM	JJA	SON
Globe	0.66 [0.22, 0.9]	0.45 [0.14, 0.76]	0.63 [0.28, 0.88]	0.46 [0.14, 0.72]	0.24 [-0.2, 0.7]
	0.15 (-0.07, 0.37)	0.08 (0.05, 0.13)	0.24 (0.09, 0.39)	0.25 (0.08, 0.46)	- 0.14 (-0.32, 0.07)
ALA	0.37 [0.14, 0.56]	* 0.50 [0.22, 0.68]	* 0.32 [0.14, 0.49]	- 0.13 [-0.36, 0.1]	0.30 [0.08, 0.48]
	0.09 (-0.07, 0.16)	* 0.27 (0.16, 0.54)	- 0.05 (-0.26, 0.25)	- 0.18 (-0.36, -0.01)	0.10 (-0.03, 0.27)
CGI	0.00 [-0.25, 0.37]	- 0.35 [-0.56, 0.03]	- 0.15 [-0.34, 0.12]	0.14 [-0.04, 0.34]	- 0.18 [-0.38, 0.07]
	- 0.24 (-0.34, -0.15)	- 0.27 (-0.46, -0.09)	- 0.25 (-0.62, 0.12)	0.00 (-0.24, 0.3)	- 0.14 (-0.28, -0.01)
WNA	0.22 [-0.08, 0.59]	0.35 [0.16, 0.58]	0.31 [0.0, 0.66]	- 0.50 [-0.65, -0.29]	0.11 [-0.11, 0.31]
	0.17 (0.11, 0.24)	0.26 (0.08, 0.39)	0.15 (0.08, 0.26)	- 0.45 (-0.63, -0.14)	*- 0.28 (-0.48, -0.11)
CNA	*- 0.56 [-0.71, -0.18]	0.01 [-0.25, 0.31]	- 0.17 [-0.41, 0.16]	*- 0.88 [-0.93, -0.5]	*- 0.34 [-0.5, -0.1]
	*- 0.31 (-0.39, -0.23)	0.08 (0.02, 0.13)	- 0.14 (-0.22, 0.0)	*- 0.51 (-0.62, -0.41)	- 0.11 (-0.2, -0.04)
ENA	0.16 [-0.33, 0.55]	- 0.13 [-0.47, 0.31]	0.07 [-0.28, 0.41]	0.13 [-0.26, 0.37]	0.08 [-0.17, 0.3]
	- 0.05 (-0.24, 0.17)	0.00 (-0.16, 0.07)	*- 0.26 (-0.48, 0.03)	- 0.19 (-0.31, -0.04)	- 0.07 (-0.28, 0.21)

It is apparent from Table 5.3 that the correlation found in both control simulations and the observations cover a very wide range. Therefore, it will be more useful to focus more on the distribution means when making comparisons. An initial note to make that has already been discussed previously is on the difficulty in estimating a realistic global precipitation value from observational data and therefore the global temperature and precipitation correlations are of lesser importance. However, we do see that the global relationship in the models is relatively large owing to the fact that global precipitation variations are related to temperature variations, especially through altered tropical convection and moisture availability at higher latitudes.

Therefore, focusing on NA regional temperature and precipitation correlations, the strongest seasonal relationships found in each individual region was the same for both the control simulations and observations (yellow shading in Table 5.3), except for ENA where the correlations were generally smaller than those found in the other regions. The weaker relationships across ENA could be attributed to the large amount of ocean grid cells within that region which may offset some of the impacts changing temperatures might have due to heat transfer with the ocean.

The major features are similar when looking at the strongest relationships between temperature and precipitation both across regions within an individual season (asterisk in Table 5.3) and across seasons within an individual region (yellow shading). These are mainly found within DJF and JJA seasons. The strongest relationships found in DJF was in ALA. This was a positive correlation because temperature directly impacts the amount of atmospheric moisture available in that region. Therefore, larger

temperatures mean more moisture available for generating precipitation. WNA also had a similar, but slightly smaller positive correlation in DJF which makes sense as that region encompasses higher latitudes than the other three lower NA regions and is adjacent to the ALA region. Also, WNA contains relatively higher topography and therefore a similar effect of moisture availability at higher altitudes depending on temperature, also could be involved.

Interestingly, the other high-latitude region (CGI) has relatively larger relationships in both its control simulations and observations for DJF but unlike the positive relationship found in ALA, this relationship is negative. This can be explained by the fact that this region is impacted by variations in the semi-permanent Icelandic Low and Azores High in the North Atlantic, fluctuations typically quantified by the North Atlantic Oscillation (NAO) Index (see Chapter 4, Section 4.4 for NAO discussion as well as Section 5.6.3 below). In the Northern Hemisphere winter, when the Icelandic Low is stronger (i.e., positive NAO phase) the CGI region experiences lower temperatures because the stronger low is associated with stronger northerly (i.e., colder) winds on the western side of the low over northeastern Canada and Greenland as well as greater precipitation because of an increase in storm activity with the strengthened low. When the low is weaker (i.e., negative NAO phase) CGI experiences the opposite effects of relatively higher temperatures and lower precipitation. This negative relationship between temperature and precipitation during CGI winter is properly simulated in the model. Section 5.6.3 provides further NAO relationship information across the NA regions.

In JJA, the largest relationships were in CNA and WNA which were both negative correlations indicating larger drying (e.g., evaporation and evapotranspiration) with increased summer temperatures. This effect seemed apparent in CNA for both control simulations and observations for MAM and SON as well which is why it ended up with the strongest correlation between annual temperature and precipitation among NA regions.

5.6.2 Relationships between Regions

Next correlations of temperature and precipitation were calculated across NA regions and the globe in a variety of combinations (Tables 5.4 – 5.7). The tables are set up with the same control simulations and observational distinctions shown in Table 5.3 (e.g., shading and distribution representation). Any tables showing precipitation correlations include an additional row/column giving the regional correlations to global temperature. Again, control simulation correlations are for the entire 140 year simulation and observational correlations cover between 30-90 years depending on the data set.

Table 5.4 and 5.5 provide annual mean temperature and precipitation correlations across regions respectively. In general, CPDN had a wide range of correlation values for most combinations while the observational range was typically much smaller, probably due to the difference in the number of samples between the two sets. Looking at the mean temperature correlations (Table 5.4), CPDN indicated a greater relationship between the globe and both ALA and WNA which also was found in the observations. However, CPDN did not show the same higher correlations

between the globe and the other regions. The range of parameter values used therefore may be impacting the global to regional relationships in these instances. Cases when both CPDN and the observations had relatively higher regional correlations in temperature were typically found when region were next to one another. For precipitation correlations (Table 5.5) there were not any significant features that stood out except for possibly the higher relationship between global temperature and global precipitation that was not identified in the observations. As a higher correlation may be expected because of global temperature's impact on rainfall in the tropics, this may be indicative of poor observational estimates of precipitation.

Table 5.6 and 5.7 provide DJF and JJA means for temperature and precipitation correlations across regions respectively. DJF mean correlations are given in the lower left corner while JJA mean correlations are given in the upper right corner. As with the annual temperature relationships in Table 5.4, observations typically had higher mean correlations between the globe and each region while CPDN did not. And again regions aligned next to one another generally had higher correlations in both CPDN and observations, more so in DJF. And for precipitation (Table 5.7), again CPDN global precipitation had a higher correlation than observations. Other than that, the main feature that stood out was the larger negative correlation between WNA and ALA precipitation. This may have to do with the large scale circulation where higher pressure and therefore less precipitation situated over one region indicates lower pressure over the other.

Table 5.4: Regional annual mean temperature (°C) correlations of annual means for CPDN gray shading; mean [2.5%, 97.5%]) and observations (second line, white; mean (min, max)). Yellow shading indicates a mean correlation magnitude ≥ 0.3.

	Globe (Temp)	ALA (Temp)	CGI (Temp)	WNA (Temp)	CNA (Temp)	ENA (Temp)
Globe (Temp)	CPDN-Annual	0.40 [0.09, 0.77]	0.15 [-0.15, 0.47]	0.42 [-0.05, 0.77]	-0.11 [-0.42, 0.16]	0.16 [-0.29, 0.54]
	Observations-Annual	0.65 (0.63, 0.68)	0.56 (0.54, 0.59)	0.56 (0.55, 0.58)	0.47 (0.46, 0.48)	0.48 (0.46, 0.51)
ALA (Temp)			0.33 [0.13, 0.54]	0.31 [0.08, 0.68]	-0.27 [-0.48, -0.03]	-0.03 [-0.25, 0.33]
			0.45 (0.37, 0.51)	0.55 (0.43, 0.6)	0.27 (0.2, 0.36)	0.16 (0.12, 0.23)
CGI (Temp)				0.11 [-0.13, 0.42]	-0.13 [-0.37, 0.16]	-0.06 [-0.3, 0.26]
				0.33 (0.3, 0.35)	0.44 (0.37, 0.59)	0.48 (0.44, 0.52)
WNA (Temp)					0.19 [-0.12, 0.42]	0.05 [-0.21, 0.34]
					0.56 (0.47, 0.71)	0.15 (0.06, 0.23)
CNA (Temp)						0.51 [0.27, 0.71]
						0.63 (0.58, 0.69)
ENA (Temp)						

Table 5.5: Same as Table 5.4 but for precipitation rate (mm/day). Global temperature correlations per region also are included.

	Globe (Temp)	Globe (Precip)	ALA (Precip)	CGI (Precip)	WNA (Precip)	CNA (Precip)	ENA (Precip)
Globe (Temp)	CPDN-Annual	0.66 [0.22, 0.9]	0.18 [-0.06, 0.37]	0.10 [-0.11, 0.39]	0.34 [0.05, 0.7]	0.32 [0.02, 0.71]	0.28 [0.01, 0.68]
	Observations-Annual	0.15 (-0.07, 0.37)	-0.01 (-0.08, 0.06)	-0.01 (-0.18, 0.19)	0.13 (0.02, 0.24)	-0.10 (-0.16, -0.04)	0.10 (-0.07, 0.28)
Globe (Precip)			0.17 [-0.09, 0.36]	0.07 [-0.14, 0.33]	0.32 [0.03, 0.63]	0.38 [0.06, 0.7]	0.15 [-0.11, 0.51]
			0.05 (-0.08, 0.17)	0.46 (0.31, 0.61)	0.16 (0.04, 0.29)	0.08 (-0.21, 0.36)	0.31 (0.30, 0.32)
ALA (Precip)				-0.02 [-0.21, 0.17]	-0.32 [-0.51, -0.09]	0.06 [-0.17, 0.28]	0.07 [-0.13, 0.26]
				0.26 (0.15, 0.46)	-0.17 (-0.37, 0.17)	-0.09 (-0.17, -0.04)	-0.21 (-0.35, -0.1)
CGI (Precip)					-0.03 [-0.21, 0.17]	-0.05 [-0.23, 0.16]	-0.10 [-0.3, 0.18]
					0.31 (0.11, 0.49)	0.33 (0.17, 0.50)	0.12 (-0.34, 0.48)
WNA (Precip)						0.27 [0.03, 0.64]	0.04 [-0.2, 0.47]
						0.12 (0.09, 0.14)	0.35 (0.22, 0.58)
CNA (Precip)							0.09 [-0.23, 0.50]
							0.17 (0.04, 0.42)
ENA (Precip)							

Table 5.6: Regional temperature (°C) correlations of JJA means (upper-right) and DJF means (lower-left) for CPDN (shaded: mean [2.5%, 97.5%]) and observations (second line, white; mean (min, max)). Yellow shading indicates a mean correlation magnitude ≥ 0.3.

	Globe (Temp)	ALA (Temp)	CGI (Temp)	WNA (Temp)	CNA (Temp)	ENA (Temp)
Globe (Temp)	CPDN-JJA	0.22 [0.00, 0.55]	0.05 [-0.19, 0.31]	0.15 [-0.14, 0.41]	-0.12 [-0.5, 0.14]	0.13 [-0.13, 0.39]
	Observations-JJA	0.31 (0.21, 0.44)	0.58 (0.55, 0.62)	0.40 (0.38, 0.43)	0.38 (0.37, 0.38)	0.58 (0.57, 0.58)
ALA (Temp)	0.35 [0.06, 0.68]	CPDN-DJF	0.03 [-0.18, 0.24]	-0.04 [-0.29, 0.20]	-0.21 [-0.47, 0.00]	-0.12 [-0.34, 0.11]
	0.50 (0.49, 0.53)	Observations-DJF	0.21 (0.14, 0.32)	0.26 (0.20, 0.34)	0.07 (-0.01, 0.14)	0.09 (-0.05, 0.24)
CGI (Temp)	0.20 [-0.09, 0.45]	0.33 [0.13, 0.5]		0.05 [-0.15, 0.26]	0.02 [-0.19, 0.22]	0.21 [-0.03, 0.44]
	0.35 (0.31, 0.40)	0.40 (0.32, 0.5)		0.22 (0.17, 0.3)	0.53 (0.41, 0.81)	0.60 (0.57, 0.64)
WNA (Temp)	0.34 [-0.05, 0.66]	0.19 [-0.02, 0.48]	0.18 [-0.07, 0.44]		0.23 [-0.01, 0.41]	0.20 [-0.09, 0.42]
	0.51 (0.50, 0.53)	0.43 (0.23, 0.52)	0.36 (0.31, 0.41)		0.26 (0.17, 0.3)	0.22 (0.13, 0.35)
CNA (Temp)	0.01 [-0.28, 0.22]	-0.29 [-0.47, -0.03]	-0.14 [-0.36, 0.15]	0.31 [0.1, 0.52]		0.26 [0.02, 0.47]
	0.38 (0.35, 0.41)	-0.02 (-0.12, 0.04)	0.04 (-0.02, 0.07)	0.53 (0.46, 0.7)		0.62 (0.56, 0.68)
ENA (Temp)	0.05 [-0.33, 0.42]	-0.13 [-0.35 [0.16]	-0.11 [-0.33, 0.2]	-0.02 [-0.27, 0.27]	0.65 [0.51, 0.78]	
	0.19 (0.18, 0.2)	-0.16 (-0.22, -0.13)	0.07 (-0.01, 0.17)	-0.02 (-0.14, 0.24)	0.59 (0.56, 0.62)	

Table 5.7: Same as Table 5.6 but for precipitation rate (mm/day). Global temperature correlations per region also are included.

	Globe (Temp)	Globe (Precip)	ALA (Precip)	CGI (Precip)	WNA (Precip)	CNA (Precip)	ENA (Precip)
Globe (Temp)	CPDN-JJA	0.46 [0.14, 0.72]	0.05 [-0.13, 0.24]	-0.01 [-0.19, 0.19]	0.14 [-0.1, 0.42]	0.12 [-0.11, 0.44]	0.07 [-0.14, 0.25]
	Observations-JJA	0.26 (0.08, 0.46)	0.21 (0.12, 0.31)	-0.07 (-0.25, 0.15)	-0.03 (-0.13, 0.06)	-0.18 (-0.37, 0.03)	-0.07 (-0.19, 0.05)
Globe (Precip)	0.45 [0.14, 0.76]	CPDN-DJF	0.05 [-0.13, 0.22]	0.04 [-0.13, 0.22]	0.25 [0.03, 0.47]	0.32 [0.06, 0.54]	-0.02 [-0.22, 0.2]
	0.09 (0.05, 0.13)	Observations-DJF	0.14 (0.07, 0.2)	0.33 (0.25, 0.4)	-0.08 (-0.1, -0.06)	-0.26 (-0.6, 0.09)	0.14 (0.11, 0.18)
ALA (Precip)	0.14 [-0.11, 0.35]	0.17 [-0.1, 0.36]		-0.01 [-0.2, 0.18]	-0.13 [-0.36, 0.06]	-0.02 [-0.25, 0.19]	-0.02 [-0.22, 0.16]
	-0.16 (-0.27, -0.04)	0.01 (-0.18, 0.19)		0.08 (-0.02, 0.24)	-0.06 (-0.29, 0.24)	-0.24 (-0.33, -0.09)	-0.13 (-0.16, -0.09)
CGI (Precip)	0.05 [-0.13, 0.31]	0.06 [-0.13, 0.25]	-0.01 [-0.19, 0.17]		-0.08 [-0.25, 0.1]	-0.06 [-0.27, 0.17]	-0.05 [-0.27, 0.14]
	0.00 (-0.08, 0.08)	0.28 (0.26, 0.29)	0.19 (0.17, 0.21)		0.29 (0.2, 0.48)	0.03 (-0.22, 0.22)	0.04 (-0.1, 0.17)
WNA (Precip)	0.18 [-0.07, 0.54]	0.08 [-0.15, 0.36]	-0.63 [-0.74, -0.47]	-0.02 [-0.22, 0.16]		0.20 [-0.06, 0.42]	-0.21 [-0.4, -0.02]
	0.32 (0.17, 0.44)	0.06 (-0.06, 0.18)	-0.45 (-0.5, -0.38)	0.18 (-0.02, 0.36)		0.04 (-0.07, 0.11)	-0.13 (-0.23, -0.03)
CNA (Precip)	0.22 [-0.06, 0.67]	0.22 [-0.01, 0.55]	-0.05 [-0.27, 0.16]	-0.11 [-0.33, 0.16]	0.23 [0.01, 0.59]		-0.17 [-0.42, 0.3]
	0.00 (-0.14, 0.12)	0.19 (0.14, 0.23)	-0.02 (-0.08, 0.04)	0.09 (0.05, 0.11)	0.21 (0.14, 0.26)		-0.06 (-0.24, 0.16)
ENA (Precip)	0.28 [-0.04, 0.71]	0.15 [-0.09, 0.51]	-0.01 [-0.23, 0.18]	-0.28 [-0.45, -0.07]	0.08 [-0.16, 0.47]	0.18 [-0.44, 0.59]	
	0.20 (0.08, 0.3)	0.45 (0.20, 0.71)	-0.22 (-0.51, 0.15)	0.02 (-0.39, 0.38)	0.38 (0.21, 0.58)	0.27 (0.21, 0.35)	

5.6.3 NAO and ENSO Teleconnections

Next, relationships in the model associated with the North Atlantic Oscillation (NAO) and El Niño-Southern Oscillation (ENSO) are explored. The CPDN simulations contained monthly mean sea level pressure (MSLP) output for the grid cell nearest Stykkisholmur/Reykjavik, Iceland and Ponta Delgada, Azores. Meteorological measurement stations at these two sites (or alternative nearby locations) have been used to calculate an NAO index, typically defined as the normalized pressure difference between the two stations which reside near the semi-permanent Icelandic Low and Azores High in the North Atlantic and provides a measure of the fluctuating strength of the two pressure systems (e.g., Rogers 1984; Hurrell 1995; Jones et al. 1997; Hurrell et al. 2013) which can greatly impact global weather, especially continental regions surrounding the North Atlantic.

Therefore the normalized pressure difference between Iceland and Azores was calculated for both the observed data (acquired from NOAA's Climate Prediction Center (CPC)) and simulated output. (The normalization process involved dividing a location's data/output by its own standard deviation prior to calculating the difference in order to minimize the impact of the larger variability in the more northern measurement (i.e., Iceland).) To see whether the model was properly simulating the variability of the NAO, a comparison was made of seasonal interannual variability between it and observations. The calculated NAO index from observations had data from 1921-2001 and therefore it was split up into 30 year periods using 10-year overlapping (i.e., 6 samples). The CPDN control simulations had calculated NAO index values for years

21-160 and therefore were split up into five 30-year periods for all 1,214 simulations (i.e., 6070 samples). Figure 5.19 provides the resulting CPDN distributions and 6 observational samples and it is clear that the NAO variability in the model closely resembles the range of the observations.

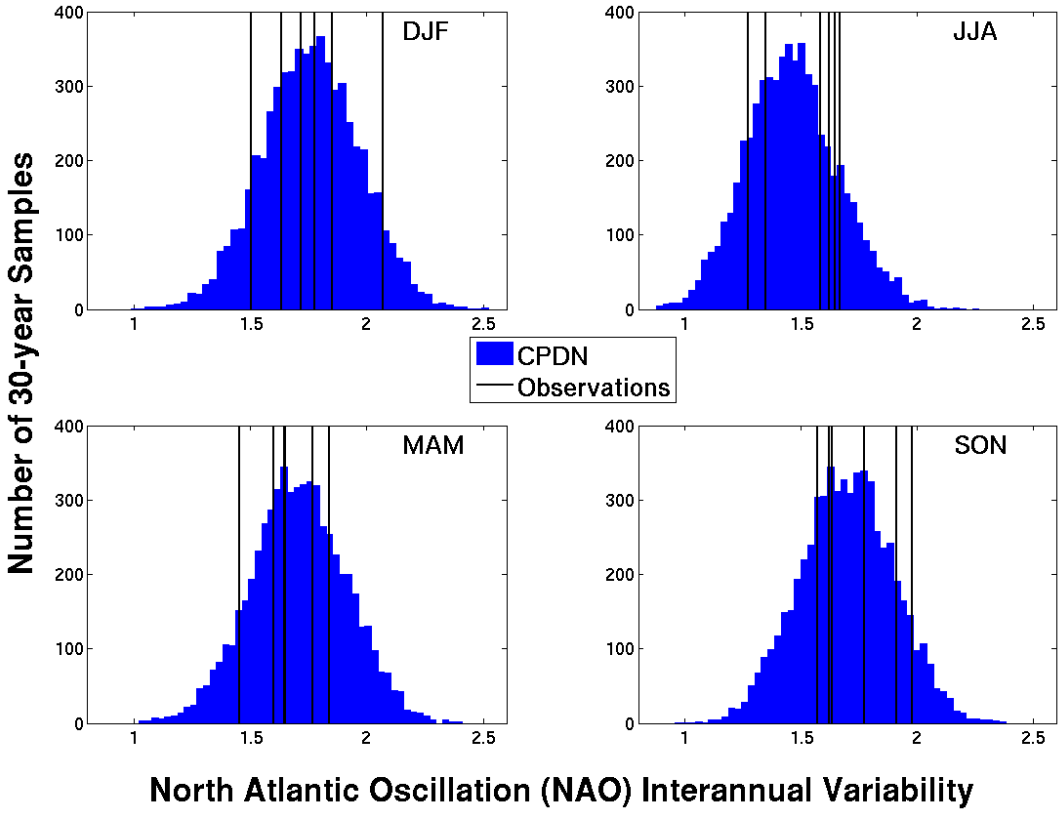


Figure 5.19: Interannual variability in NAO calculated for CPDN control simulations (five 30-year samples per simulation) and observations (six 30-year samples; 10 year overlapping blocks from 80 years of data).

Next relationships were investigated between the NAO index value and annual and seasonal global and regional temperature and precipitation for both the CPDN model simulations and observations. Table 5.8 and 5.9 list the resulting correlations in

both the observations and control simulations. Note that each CPDN control simulation contained a corresponding correlation (i.e., 1,214 correlations) and therefore the tables display the mean followed by the 2.5% and 97.5% values in the range of all correlations. The observations, however, came from each data set (i.e., between 2-4 correlations) and therefore the tables display their mean followed by the minimum and maximum correlations found.

The model appeared to get the main NAO teleconnection features correct, with the largest impacts occurring across eastern NA during DJF. The strongly negative relationship between NAO and temperature in the CGI region for DJF was properly simulated as well as the general negative relationship that occurs throughout the entire year in that region. When NAO is in a positive phase, the Icelandic Low and Azores high are relatively stronger resulting in the jet stream and storm track remaining farther to the north across NA and the North Atlantic which keeps colder air held in place at higher latitudes (i.e., the CGI region). The opposite is true for CNA and ENA during a positive phase of the NAO as the more northerly jet allows warmer southerly air to penetrate into their regions. This positive correlation was correctly modeled (Table 5.8)

The most dominant feature typically found in precipitation associated with a positive NAO phase is increased precipitation in the North Atlantic/Greenland area. This positive correlation was properly modeled as seen in Table 5.9. Also, another NA feature with positive phase NAO has been a decrease in spring precipitation across ENA and this negative correlation was somewhat found in the models, but small for both observations and simulations.

Table 5.8: Correlations between NAO and global and NA regional temperatures across seasons for 1,214 control simulations (shaded; mean[2.5%,97.5%]) and observations (directly beneath; mean[min,max]). Correlation magnitudes ≥0.3 are highlighted yellow.

CPDN/Obs	Annual	DJF	MAM	JJA	SON
Globe	-0.02 [-0.24,0.18]	-0.07 [-0.25,0.13]	0.08 [-0.14,0.28]	0.00 [-0.16,0.19]	-0.01 [-0.21,0.16]
	-0.03 [-0.05,-0.02]	0.17 [0.16,0.20]	-0.28 [-0.3,-0.27]	0.04 [0.03,0.06]	-0.09 [-0.11,-0.06]
ALA	-0.14 [-0.33,0.05]	-0.17 [-0.37,0.01]	-0.08 [-0.26,0.12]	-0.03 [-0.23,0.17]	-0.09 [-0.27,0.13]
	-0.03 [-0.05,-0.01]	-0.04 [-0.06,-0.04]	-0.16 [-0.19,-0.13]	0.15 [0.10,0.30]	0.06 [-0.19,0.16]
CGI	-0.49 [-0.65,-0.28]	-0.60 [-0.73,-0.35]	-0.36 [-0.52,-0.19]	-0.14 [-0.31,0.05]	-0.44 [-0.57,-0.27]
	-0.44 [-0.48,-0.38]	-0.52 [-0.59,-0.41]	-0.53 [-0.58,-0.40]	-0.04 [-0.2,0.04]	-0.24 [-0.41,-0.17]
WNA	0.08 [-0.16,0.34]	-0.02 [-0.25,0.33]	0.18 [-0.01,0.36]	0.14 [-0.03,0.33]	0.11 [-0.09,0.31]
	0.11 [0.08,0.18]	0.11 [0.10,0.14]	0.19 [0.17,0.22]	0.30 [0.24,0.44]	0.09 [-0.14,0.17]
CNA	0.39 [0.23,0.55]	0.44 [0.26,0.59]	0.38 [0.19,0.54]	0.13 [-0.07,0.36]	0.28 [0.08,0.46]
	0.14 [0.13,0.19]	0.42 [0.32,0.47]	0.17 [0.14,0.24]	-0.09 [-0.12,-0.04]	0.04 [-0.02,0.06]
ENA	0.44 [0.26,0.58]	0.45 [0.26,0.58]	0.35 [0.18,0.52]	0.02 [-0.19,0.27]	0.36 [0.14,0.52]
	0.24 [0.22,0.28]	0.36 [0.23,0.43]	-0.06 [-0.14,0.11]	0.02 [-0.02,0.06]	0.06 [-0.11,0.14]

Table 5.9: Same as Table 5.8 but for correlations between NAO and precipitation.

CPDN/Obs	Annual	DJF	MAM	JJA	SON
Globe	-0.07 [-0.26,0.14]	0.00 [-0.19,0.20]	0.08 [-0.13,0.29]	0.08 [-0.1,0.28]	0.07 [-0.12,0.25]
	-0.06 [-0.31,0.2]	0.12 [0.11,0.13]	-0.06 [-0.09,-0.03]	0.21 [0.15,0.27]	0.06 [-0.16,0.29]
ALA	0.00 [-0.19,0.19]	-0.04 [-0.24,0.17]	0.07 [-0.11,0.23]	-0.03 [-0.25,0.16]	0.03 [-0.15,0.20]
	0.08 [-0.09,0.17]	0.02 [-0.03,0.06]	0.38 [0.34,0.41]	0.16 [0.05,0.24]	0.02 [-0.02,0.10]
CGI	0.43 [0.24,0.59]	0.64 [0.43,0.78]	0.55 [0.39,0.69]	0.10 [-0.13,0.37]	0.45 [0.25,0.59]
	0.34 [0.31,0.37]	0.35 [0.19,0.60]	0.27 [-0.04,0.69]	-0.21 [-0.34,-0.04]	0.12 [-0.18,0.36]
WNA	-0.09 [-0.29,0.10]	-0.03 [-0.25,0.17]	0.00 [-0.20,0.20]	-0.03 [-0.20,0.16]	0.01 [-0.16,0.2]
	-0.06 [-0.13,0.01]	-0.02 [-0.1,0.02]	-0.27 [-0.34,-0.22]	-0.25 [-0.35,-0.2]	-0.03 [-0.11,0.03]
CNA	-0.11 [-0.28,0.08]	-0.06 [-0.26,0.16]	-0.04 [-0.23,0.16]	-0.12 [-0.31,0.07]	-0.13 [-0.3,0.06]
	0.01 [-0.02,0.08]	0.00 [-0.08,0.16]	-0.01 [-0.12,0.06]	-0.03 [-0.06,-0.02]	0.10 [-0.03,0.18]
ENA	0.03 [-0.28,0.32]	-0.22 [-0.41,0.01]	-0.08 [-0.31,0.15]	0.20 [-0.13,0.41]	-0.05 [-0.23,0.13]
	0.13 [0.06,0.22]	0.09 [-0.02,0.19]	-0.10 [-0.16,-0.02]	0.08 [0.03,0.17]	0.03 [-0.05,0.16]

Next, relationships in the model associated with the El Niño-Southern Oscillation (ENSO) were explored. ENSO is associated with the cycle of anomalously warm and cool ocean water temperatures in the eastern equatorial Pacific Ocean which also affects air surface pressure in the tropical western Pacific. These variations can have broad climatic impacts across the entire globe. The CPDN simulations contained monthly mean air temperatures over the Niño 3.4 region, a region across the central Pacific used to generate an index for the phase of El Niño. Therefore variations in temperatures across this region were compared to the observed sea surface temperatures (SSTs) used to create the El Niño index (i.e., the ERSST.V3B SST data set from NOAA CPC). Granted this comparison is between air temperature and SST but the two are roughly correlated when interested in assessing changes in temperature across the region. Note that the observed SST data set was detrended to remove any impact of warming ocean waters over the past century.

Figure 5.20 shows the comparison of seasonal interannual variability between the CPDN and observed Niño 3.4 temperatures for 30-year time periods similar to the comparison for NAO in Figure 5.19. The observations had data from 1951-2010 and therefore were split up into four 30-year periods with 10-year overlapping. Again, the CPDN control simulations were split up into five 30-year periods for all 1,214 simulations. The variability distributions for CPDN appear to be skewed towards larger variability with the distribution mean (i.e., black diamond in Figure 5.20) close to the four observed variability estimates. The reasoning for the skewed CPDN is not completely apparent but may have to do with the fact that the ocean model has a fairly

course resolution that may not be able to accurately represent ocean processes important for ENSO.

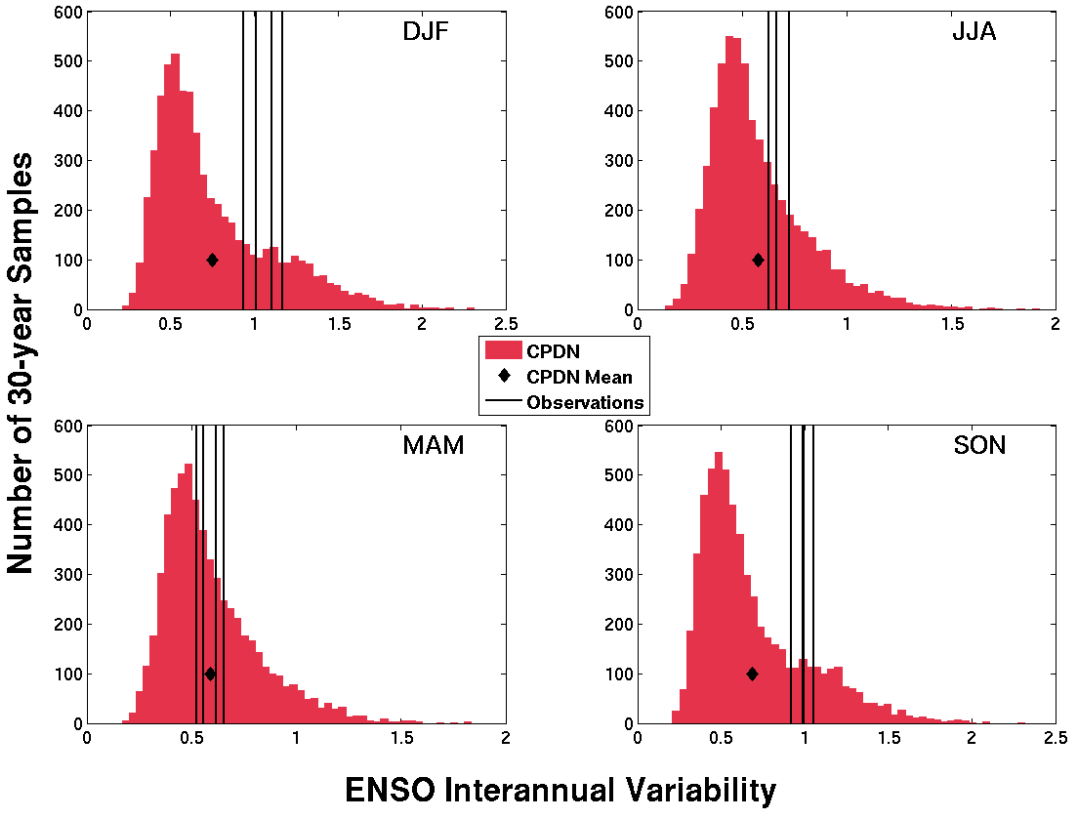


Figure 5.20: Interannual variability in Niño 3.4 SST anomalies calculated for CPDN control simulations (five 30-year samples per simulation) and observations (four 30-year samples; 10 year overlapping blocks from 60 years of data).

Next relationships were investigated between the Niño 3.4 temperatures (i.e., ENSO) and annual and seasonal global and regional temperature and precipitation for both the CPDN model simulations and observations. Table 5.10 and 5.11 show the resulting correlations and were constructed in the same manner as the NAO correlation tables. The first feature that stands out in the correlations between ENSO and

temperature (Table 5.10) was the high correlation found throughout all seasons for the globe. This aligns with the slight warming/cooling that occurs at the global scale with phase changes in ENSO due to the large region across the Central Pacific that experiences a relatively significant warming/cooling with each phase change. Another major feature of a positive ENSO phase is a general warming of west-northwest United States and western Canada/Alaska in winter/spring. This was modeled well in the controls simulations as is seen in Table 5.10 with larger positive correlations for ALA and WNA in DJF and MAM. Additionally, a negative phase ENSO is typically associated with warmer summer temperatures across the south-central United States which also was modeled well as CNA had a larger negative correlation in JJA (Table 5.10).

With precipitation relationships to ENSO (Table 5.11), again the model performed well. The positive phase of ENSO typically corresponds with wetter conditions in DJF for WNA, CNA, and ENA which was found in the respective correlations.

Table 5.10: Correlations between Niño 3.4 temperatures and global and NA regional temperatures across seasons for 1,214 control simulations (shaded; mean[2.5%,97.5%]) and observations (directly beneath; mean[min,max]). Correlation magnitudes ≥0.3 are highlighted yellow.

CPDN/Obs	Annual	DJF	MAM	JJA	SON
Globe	0.73 [0.51,0.90]	0.66 [0.42,0.87]	0.65 [0.4,0.85]	0.59 [0.34,0.83]	0.63 [0.39,0.84]
	0.32 [0.32,0.32]	0.53 [0.52,0.55]	0.40 [0.38,0.41]	0.23 [0.22,0.25]	0.28 [0.26,0.30]
ALA	0.32 [0.01,0.71]	0.28 [-0.07,0.64]	0.27 [-0.03,0.6]	0.18 [-0.06,0.52]	0.22 [-0.01,0.54]
	0.21 [0.14,0.25]	0.15 [-0.12,0.26]	0.27 [0.26,0.3]	0.02 [-0.04,0.07]	0.16 [0.14,0.18]
CGI	0.01 [-0.27,0.31]	0.08 [-0.24,0.36]	0.00 [-0.21,0.22]	-0.10 [-0.3,0.12]	0.03 [-0.18,0.28]
	-0.11 [-0.15,-0.08]	0.12 [0.09,0.20]	-0.05 [-0.19,0.01]	-0.23 [-0.27,-0.19]	-0.24 [-0.26,-0.22]
WNA	0.32 [-0.17,0.68]	0.28 [-0.24,0.6]	0.32 [-0.04,0.65]	0.00 [-0.3,0.26]	0.17 [-0.12,0.48]
	0.24 [0.21,0.27]	0.31 [0.27,0.43]	0.27 [0.15,0.33]	0.03 [-0.04,0.09]	0.05 [-0.01,0.08]
CNA	-0.26 [-0.52,-0.01]	-0.11 [-0.45,0.14]	-0.11 [-0.36,0.13]	-0.32 [-0.59,-0.08]	-0.10 [-0.33,0.09]
	-0.02 [-0.05,0.03]	0.11 [0.04,0.27]	-0.11 [-0.14,-0.1]	-0.29 [-0.33,-0.27]	-0.24 [-0.25,-0.24]
ENA	0.01 [-0.42,0.46]	-0.03 [-0.49,0.41]	0.08 [-0.35,0.5]	-0.06 [-0.31,0.22]	0.05 [-0.20,0.25]
	-0.13 [-0.22,-0.09]	-0.06 [-0.1,-0.04]	-0.09 [-0.19,-0.04]	-0.30 [-0.42,-0.25]	-0.19 [-0.22,-0.15]

Table 5.11: Same as Table 5.10 but for correlations between Niño 3.4 temperatures and precipitation.

CPDN/Obs	Annual	DJF	MAM	JJA	SON
Globe	0.53 [-0.02,0.83]	0.39 [0.00,0.70]	0.54 [0.11,0.82]	0.40 [0.02,0.65]	0.11 [-0.38,0.65]
	0.06 [0.05,0.07]	0.21 [0.05,0.37]	0.18 [0.18,0.19]	-0.15 [-0.18,-0.12]	-0.28 [-0.41,-0.16]
ALA	0.12 [-0.12,0.33]	0.11 [-0.19,0.33]	0.13 [-0.08,0.31]	-0.01 [-0.21,0.18]	0.04 [-0.13,0.22]
	-0.00 [-0.16,0.08]	-0.14 [-0.25,-0.03]	0.02 [-0.07,0.16]	-0.25 [-0.31,-0.18]	0.29 [0.09,0.41]
CGI	-0.01 [-0.21,0.21]	-0.04 [-0.21,0.15]	0.05 [-0.21,0.28]	-0.06 [-0.26,0.13]	0.02 [-0.19,0.20]
	0.10 [0.04,0.21]	-0.11 [-0.17,-0.01]	0.20 [0.06,0.31]	-0.13 [-0.23,0.00]	-0.12 [-0.24,-0.02]
WNA	0.39 [0.04,0.7]	0.20 [-0.18,0.57]	0.40 [0.04,0.71]	0.22 [-0.02,0.51]	0.14 [-0.06,0.38]
	0.21 [0.15,0.29]	0.39 [0.37,0.45]	0.11 [0.06,0.21]	0.15 [0.07,0.24]	0.01 [-0.02,0.04]
CNA	0.45 [0.17,0.76]	0.31 [-0.07,0.73]	0.37 [0.06,0.68]	0.25 [0.02,0.50]	0.34 [0.10,0.60]
	0.19 [0.1,0.24]	0.32 [0.18,0.42]	0.01 [0.01,0.02]	0.14 [0.12,0.17]	0.08 [0.06,0.10]
ENA	0.33 [0.02,0.65]	0.41 [0.12,0.78]	0.15 [-0.17,0.49]	0.05 [-0.17,0.26]	0.13 [-0.07,0.39]
	0.42 [0.41,0.43]	0.60 [0.44,0.74]	0.40 [0.34,0.49]	0.04 [-0.02,0.15]	0.29 [0.13,0.57]

5.7 SENSITIVITY TO PHYSICAL PARAMETER VALUES

The parameter perturbations applied to CPDN control simulations are assessed to evaluate uncertainties in climate indices based on variations in these parameters. (For parameter perturbation discussions refer to Section 5.1.4 or Chapter 3, Section 3.3.1) Section 5.7.1 assesses the sensitivity of simulated mean, interannual variability, and magnitude of the seasonal cycle to variations of each model parameter and Section 5.7.2 assesses sensitivity of long-term model drift to variations in model parameters.

5.7.1 Mean, Variability, and Seasonal Cycle

A sensitivity analysis was performed to identify the correlation between CPDN model parameter variations and control simulation mean and interannual variability of temperature and precipitation and magnitude of the seasonal cycle (JJA-DJF) of temperature over the globe and NA regions. Five 30-year samples of each of these indices were calculated for each control simulation and then linked with the appropriate parameter values for that particular simulation. Each parameter varies in a sequential low-to-high manner and therefore correlations were calculated between the parameter values and climate indice values from all samples over all control simulations. Table 5.12 gives the results for those parameter values having climate indice correlation magnitudes greater than or equal to (≥) 0.4. The parameters are listed in order of importance with the most influential parameters listed on top. Higher correlation magnitudes imply that varying the parameter's value has a larger impact on the resulting simulated climate indice value.

Table 5.12: Model physics parameters with correlation magnitude ≥ to 0.4 between their variations and climate indices over a defined region. The climate indice information is provided showing the variable of either temperature (T) or precipitation rate (P); the indice of either mean, interannual variability (Int Var), or magnitude of seasonal cycle (JJA-DJF); and the time period of either annual or one of the four seasons. Correlations are listed with magnitudes ≥ to 0.5 (yellow) and 0.7 (red) highlighted. Parameters are listed in order of generally higher sensitivity to lower. All correlations shown have p<<0.00001.

Parameter	Globe	ALA	CGI	WNA	CNA	ENA
VF1	P:Mean (An) [0.80] P:Mean (DJF) [0.80] P:Mean (MAM) [0.80] P:Mean (JJA) [0.79] P:Mean (SON) [0.79] T:Mean (JJA) [-0.51] T:Mean (SON) [-0.51] T:Mean (An) [-0.49] T:Mean (DJF) [-0.47] T:Mean (MAM) [-0.45]	P:Mean (DJF)[-0.52] P:Mean (SON) [-0.51] T:JJA-DJF [0.51] T:Mean (DJF) [-0.49]	T:Mean (DJF)[-0.42] T:Mean (An) [-0.41] T:Mean (SON) [-0.40] T:JJA-DJF [0.40]	P:Mean (JJA)[0.62] P:Mean (MAM) [0.61] P:Mean (An) [0.55] T:Mean (JJA) [-0.55] T:Mean (An) [-0.51] T:Mean (SON) [-0.43] T:Mean (DJF) [-0.42]	T:Mean (JJA)[-0.68] P:Mean (JJA) [0.61] P:Mean (MAM) [0.55] T:Mean (An) [-0.55] T:JJA-DJF [-0.50] T:Mean (SON) [-0.40]	P:Mean (JJA) [0.75] P:Mean (SON) [0.71] P:Mean (An) [0.69] T:Mean (JJA) [-0.54] T:Mean (SON) [-0.46] T:Mean (An) [-0.43]
ENTCOEF		T:Mean (JJA) [0.63] T:Mean (An) [0.58] P:Mean (SON) [0.54] T:Mean (DJF) [0.53] T:Mean (MAM) [0.49] P:Mean (JJA) [-0.49] P:Mean (DJF) [0.47] T:Int Var (DJF) [-0.42]	P:Mean (JJA) [0.62]	P:Mean (JJA) [-0.69] P:Int Var (SON) [0.59] P:Mean (SON) [0.55] P:Mean (DJF) [0.44] T:Mean (JJA) [0.43] P:Int Var (DJF) [0.42] T:Mean (An) [0.41]	P:Mean (SON) [0.79] P:Mean (DJF) [0.78] P:Int Var (SON) [0.65] P:Mean (An) [0.57] P:Int Var (DJF) [0.45] T:Int Var (JJA) [-0.43]	P:Int Var (JJA) [0.63] P:Int Var (SON) [0.54] P:Int Var (MAM) [0.49] P:Mean (MAM) [0.48] P:Mean (JJA) [-0.47]
EACF			P:Mean (SON) [0.49] P:Mean (MAM) [0.48] P:Mean (An) [0.46] P:Mean (DJF) [0.45]	T:JJA-DJF [-0.46]	T:Mean (DJF) [0.50] T:JJA-DJF [-0.48]	

Table 5.12: Continued

Parameter	Globe	ALA	CGI	WNA	CNA	ENA
VDIFFDEPTH, VDIFFSURF	T:Mean (MAM) [0.45] T:Mean (DJF) [0.44] T:Mean (An) [0.42]	P:Mean (MAM) [0.41]	P:Mean (DJF) [0.44] P:Mean (MAM) [0.44] P:Mean (An) [0.41]	T:Mean (MAM) [0.52] T:Mean (DJF) [0.43] T:Mean (An) [0.42] T:Mean (SON) [0.40]		
CW_LAND, CW_SEA		T:Mean (JJA) [-0.50] P:Mean (JJA) [-0.40]		T:JJA-DJF [-0.42]		
CT	T:Int Var (MAM) [-0.40] T:Int Var (DJF) [-0.41]	T:Mean (JJA) [0.40]				
HANEYSFACT			T:Mean (JJA) [-0.41] T:Mean (MAM) [-0.41] T:Mean (An) [-0.40]			

Seven parameters were identified as being more important than the others in influencing climate model output with two of those (VFI and ENTCOEFF) having the most significance (Table 5.12). These two parameters have been identified in previous studies as being important as well (refer back to Chapter 3, Section 3.3.1). To gain a better perspective on what these correlations imply, Figures 5.21, 5.22, 5.23 provide distributions for temperature and precipitation annual mean and interannual variability and magnitude of the seasonal cycle in temperature respectively for variations in each parameter listed in Table 5.12. A characteristic found in all of these examples was that while some of the distributions display marked shifts in climate indice values when changing a parameter value, the majority of distributions across the various regions show little to no change when varying these "important" parameters. Additionally, there are instances when only a single region may be impacted while the other regions show relatively no change (e.g., impact of varying ENTCOEF for CNA mean precipitation, Figure 5.21(b)). Therefore, it appears that parameter variations identified as being most influential to changes in the natural variability of modeled climate typically do not impact all regions the same. This fact will be explored further below.

First, looking at annual mean temperature (Figure 5.21(a)), only the top two parameters (VFI and ENTCOEFF) had a consistent change in temperature with parameter variation across nearly all regions. (Note that actual parameter values are not listed in these figures but the ordering corresponds with Table 5.1 in which values are listed smallest to largest from top to bottom and therefore the first distribution shown in Figure 5.21 for each parameter represents that parameter's smallest value and the last distribution represents the parameter's highest value.)

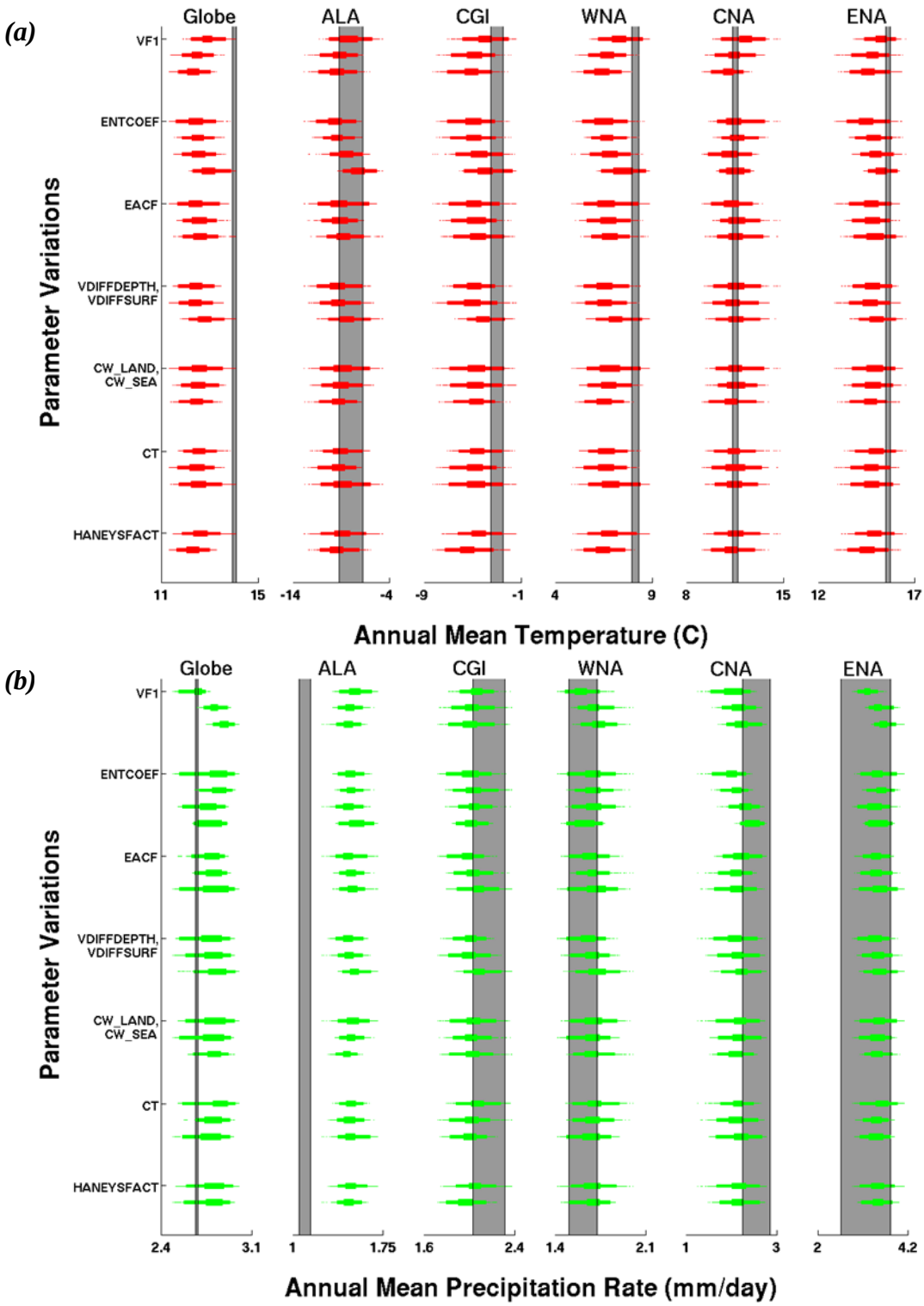


Figure 5.21: Annual mean *(a)* temperature (°C) and *(b)* precipitation rate (mm/day) of the globe and five NA regions for the 1,214 control simulations (five 30-yr samples per simulation) split into distributions corresponding with model parameter values. Actual parameter values are not listed but are arranged in the same order as that given in Table 5.1. Boxplots provide 25-75% (inner) and 2.5%-97% (outer) ranges and dots for samples outside the 95% range. The 95% range of observational (plus NARR) bootstrap distributions is shown as a vertical gray bar.

The parameter VFI is the ice fall speed coefficient which scales the speed at which cloud ice particles fall out of the sky (refer back to Chapter 3, Section 3.3.1 for all parameter full discussions). Figure 5.21(a) shows that lower values of VFI had higher mean annual temperatures across all regions (i.e., the first/top distribution had warmer temperatures and the last/bottom distribution had cooler temperatures). The reasoning for this is that when VFI is lower, there is slower fallout of cloud ice which, compared to higher VFI values, increases low-level cloudiness and reduces the rate at which cloud water is condensing onto ice nuclei leaving the atmosphere with greater moisture. The net result is warming due to greater longwave absorption from both low-level clouds and clear skies with greater moisture. While there also would be an increase in reflection in shortwave solar radiation from increased cloud cover (a cooling effect), the previous warming effects must have outweighed this effect, which also was found in previous studies (see Chapter 3, Section 3.3.1).

Parameter VFI also was important for variations in annual mean precipitation (Figure 5.21(b). The globe, WNA, CNA, and ENA all had relatively higher mean precipitation when VFI was at larger values. Larger VFI corresponds with faster fallout of cloud ice which increases overall precipitation amount. This relationship was not found in ALA or CGI where there was no change or even a slight distribution shift in the opposite direction (i.e., lower VFI equaled more precipitation). This inevitably must have been caused by the colder air temperatures in those regions. While lower VFI values reduced the cloud ice fallout speed, which resulted in less precipitation in the warmer regions, it also increased moisture, which has greater importance for precipitation at higher latitudes where temperatures are colder and there is less moisture

available. The two effects therefore resulted in roughly no net change in precipitation distributions with VFI variations in ALA and CGI.

The other parameter found most important for annual mean temperature and precipitation differences (Figure 5.21) was ENTCOEF. This is the entrainment coefficient which sets the rate at which convective clouds mix with their surrounding environmental air. For annual mean temperature (Figure 5.21(a)) all regions had an increase in temperature with increasing values of ENTCOEF, except for CNA which had relatively no change. Higher values of ENTCOEF means more mixing occurs between convective clouds and their surrounding air which weakens convection and results in greater moisture in the low- to mid-troposphere, compared to lower values of ENTCOEF which reduces mixing and allows stronger convection and greater transport of moisture to higher levels in the troposphere. Therefore the greater moisture at higher levels in the troposphere with lower ENTCOEF allow for increased high-level cloud formation which increases the reflection of shortwave solar radiation and results in a cooling of the lower troposphere and surface, as was found in the distributions of Figure 5.21(a).

CNA, however, did not exhibit this same characteristic. It had relatively no change in mean temperature with ENTCOEF variations. This is likely attributed to an offset of the previously mentioned effects by variations to the attributes of convective activity over this region, a region containing greater amounts of convective activity than other regions. With the other regions, a decrease in ENTCOEF resulted in a net cooling effect but decreased ENTCOEF also means stronger convection which could result in an alteration of the cloud cover that increases absorption of longwave radiation thus

increasing the warming effect. Additionally, stronger convection may generate cloud tops at higher altitudes which emit longwave radiation away from Earth's surface at a cooler temperature thereby increasing the amount of longwave radiation remaining in the system.

For annual mean precipitation (Figure 5.21(b)) the only notable feature found when changing ENTCOEF was found in CNA where decreasing ENTCOEF values aligned with decreasing precipitation. Again, the reasons for CNA being different than the other regions for this parameter can be tied to the fact that CNA contains a relatively large amount of convective activity. When ENTCOEF is smaller there are relatively smaller regions of stronger convection versus when ENTCOEF is larger and there are larger regions of weaker convection. This is because more near-surface moisture is being transported to the upper troposphere with stronger convection, leaving less moisture available at the surface for additional storms to form in nearby model grid cells (i.e., lower moisture reduces number of times convection is triggered in model's convection scheme). Additionally, when the moisture is transported into the upper troposphere it then can be transported out of the region by upper level winds, reducing regional moisture and overall precipitation.

Next, Figure 5.22 shows variations of interannual variability to changes in the top parameter values from Table 5.12. It is evident that parameter variations have minimal impact on interannual variability in either temperature or precipitation. The only variations tend to be in the ranges of some of the distribution (e.g., global temperature variations with changes to ENTCOEF). This figure is shown simply to point out the fact parameter variations have limited effects on interannual variability.

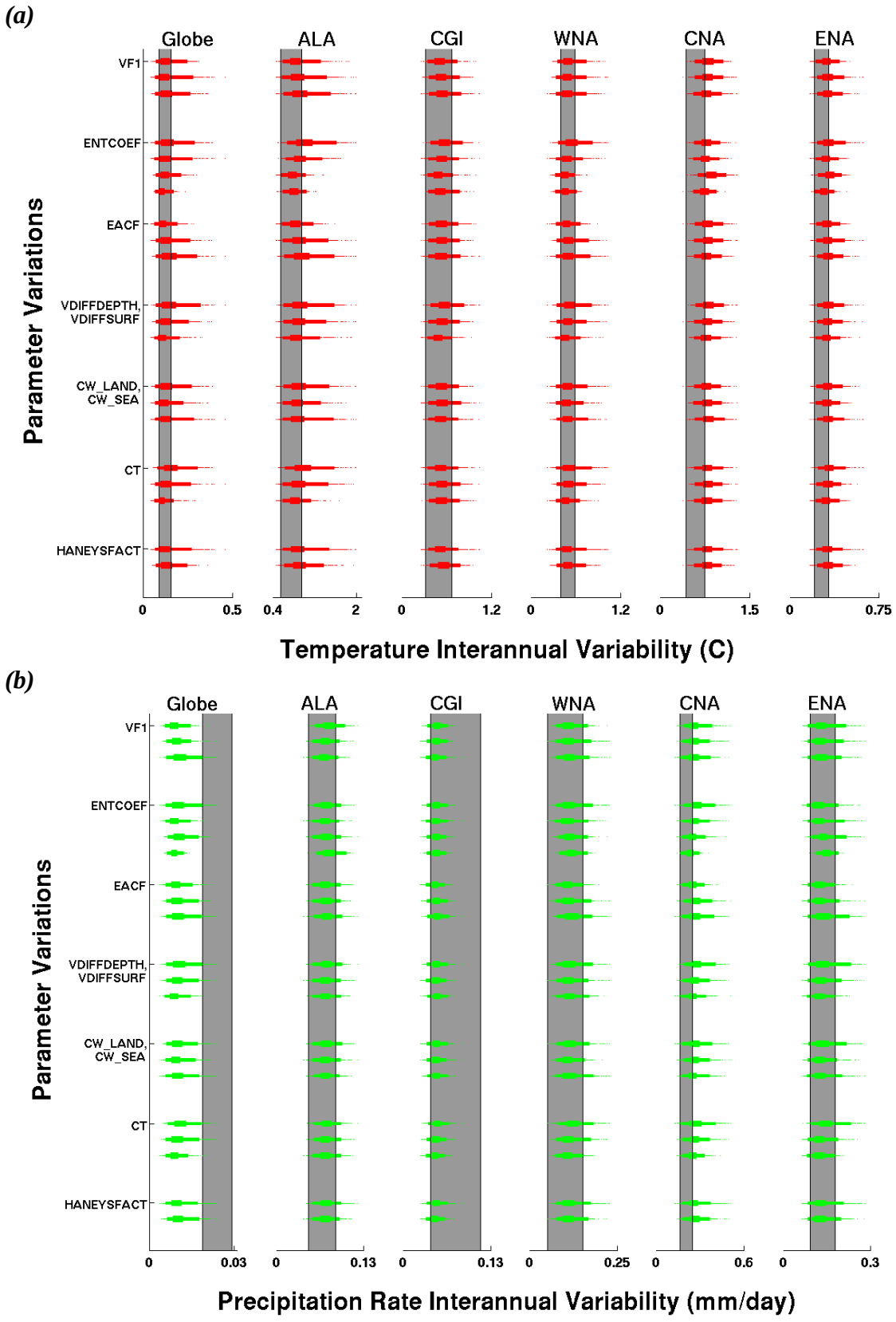


Figure 5.22: Same as Figure 5.21 but for interannual variability.

Finally, Figure 5.23 provides the variations of the magnitude of the seasonal cycle (JJA-DJF) to changes in the top parameter values from Table 5.12. Again the impacts of parameter variations are minimal for most cases. One interesting feature is that JJA-DJF in ALA and CGI decreased as VFI decreased while in CNA the opposite relationship is found. In Figure 5.21(a) it was shown that a decrease in VFI resulted in warmer annual temperatures for all three of these regions. Therefore, the higher temperatures for ALA and CGI (higher latitude regions) with decreased VFI went into warming the winter period (DJF), while the warming in CNA went into warming the summer period (JJF).

A similar opposing shift of JJA-DJF between these regions also can be found with changes in the parameter ENTCOEF (Figure 5.23). The regions ALA and CGI both had slight decreases in JJA-DJF with increases in ENTCOEF which align with the greater mean temperatures found with increases in ENTCOEF (Figure 5.21(a)), and probable DJF warming. However, variations in the ENTCOEF caused virtually no change in CNA annual mean temperature (Figure 5.21(a)). The increase in JJA-DJF with increasing ENTCOEF was probably still caused by an increase in JJA temperatures but it is assumed that warmer and cooler seasons within the annual average resulted in a net zero change for the entire year with changing ENTCOEF.

A final note is that the third most influential parameter from Table 5.12, EACF, appears to show slight decreases in JJA-DJF across all regions with increasing values (Figure 5.23). EACF is the empirically adjusted cloud fraction (Chapter 3, Section 3.3.1) and it defines the amount of cloud cover there will be for a given amount of moisture within a grid cell. Larger values of EACF result in a general increase in

cloudiness and therefore the decrease in JJA-DJF with increasing EACF could be explained by greater reflection of solar radiation by clouds in JJA (relative to DJF) causing cooler summer temperatures.

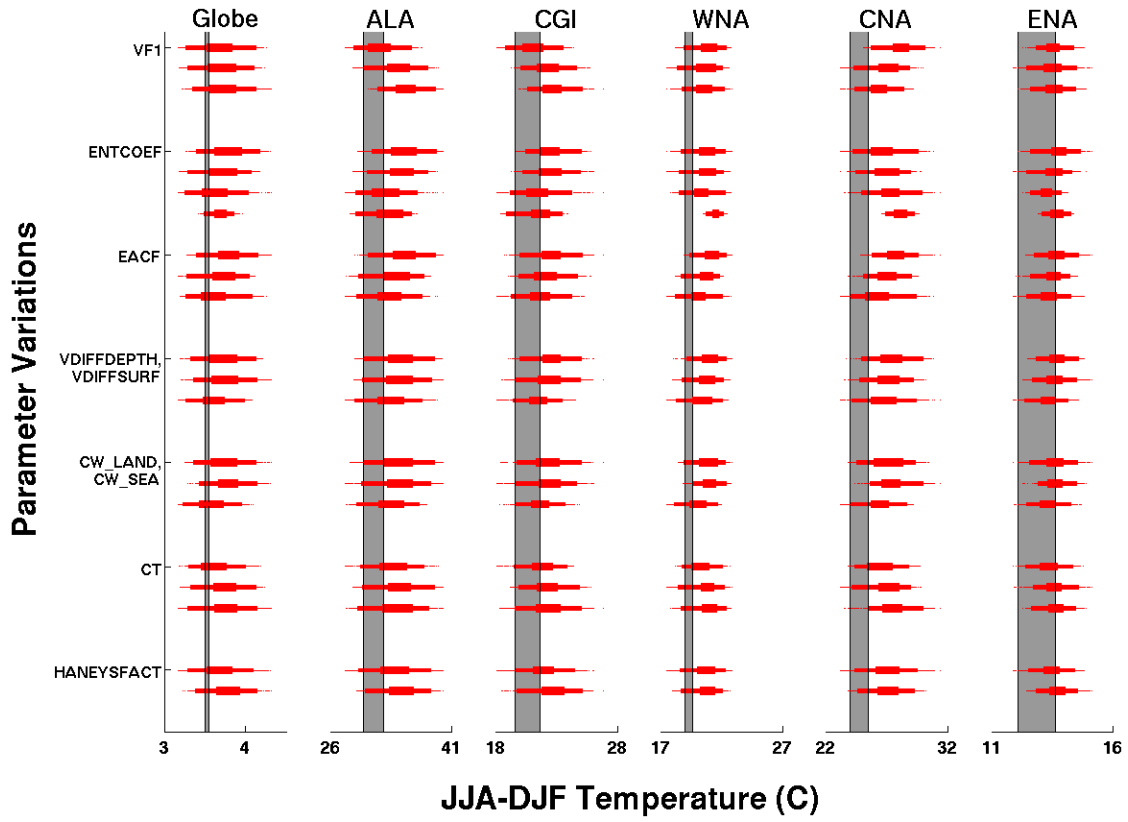


Figure 5.23: Same as Figure 5.21 but for the magnitude of the seasonal cycle (JJA-DJF) of temperature (°C).

5.7.2 Long-term Mean Drift

As discussed in Section 5.2.2, a component of long-term mean drift may be present in many of the control simulations. A sensitivity analysis was conducted to assess the impact model parameter variations have on this long-term mean drift. Table 5.13 provides the parameters having a correlation magnitude between its parameter

values and long-term mean drift ≥ 0.2[17]. It is evident from the relatively lower correlation values and fewer parameters, compared to the previous parameter sensitivity analysis, that individual parameter variations do not have a large impact on long-term mean drift. Figure 5.24 illustrates this by showing long-term mean drift distributions for parameter variations of some of the more sensitive parameters. Since precipitation long-term mean drift tended to be minimal and followed the same characteristics changes in long-term mean temperature drift, only temperature distribution changes are shown in Figure 5.24 and briefly discussed below.

Table 5.13: Model physics parameters with correlation magnitude ≥ to 0.2 between their variations and climate long-term mean drift of temperature (Temp) or precipitation (Precip) over a defined region. Correlations with magnitudes greater than 0.4 are highlighted yellow. Parameters are listed in order of generally higher sensitivity to lower. All correlations shown have p<<0.00001.

Parameter	Globe	ALA	CGI	WNA	CNA	ENA
VDIFFDEPTH, VDIFFSURF	Temp [0.42] Precip [0.37]	Temp [0.48] Precip [0.42]	Precip [0.36] Temp [0.34]	Temp [0.46]	Temp [0.35]	Temp [0.38]
HANEYSFACT	Precip [-0.38] Temp [-0.38]	Precip [-0.34] Temp [-0.31]	Temp [-0.47] Precip [-0.42]	Temp [-0.43]	Temp [-0.34]	Temp [-0.39]
ISOPYC	Precip [-0.33] Temp [-0.30]	Temp [-0.26] Precip [-0.25]	Temp [-0.30] Precip [-0.26]	Temp [-0.34]	Temp [-0.24]	Temp [-0.28]
ENTCOEF	Temp [0.32] Precip [0.32]		Precip [0.20]	Precip [-0.22]	Temp [0.25]	Temp [0.26]
HANEY	Precip [-0.31] Temp [-0.29]	Precip [-0.23] Temp [-0.21]	Temp [-0.31] Precip [-0.28]	Temp [-0.29]	Temp [-0.23]	Temp [-0.27]
VF1	Precip [-0.23]					

[17] While a correlation magnitude of 0.2 is quite small it is shown here because the resulting parameters are utilized in Appendix A when creating "inferred" control matches to transient simulations.

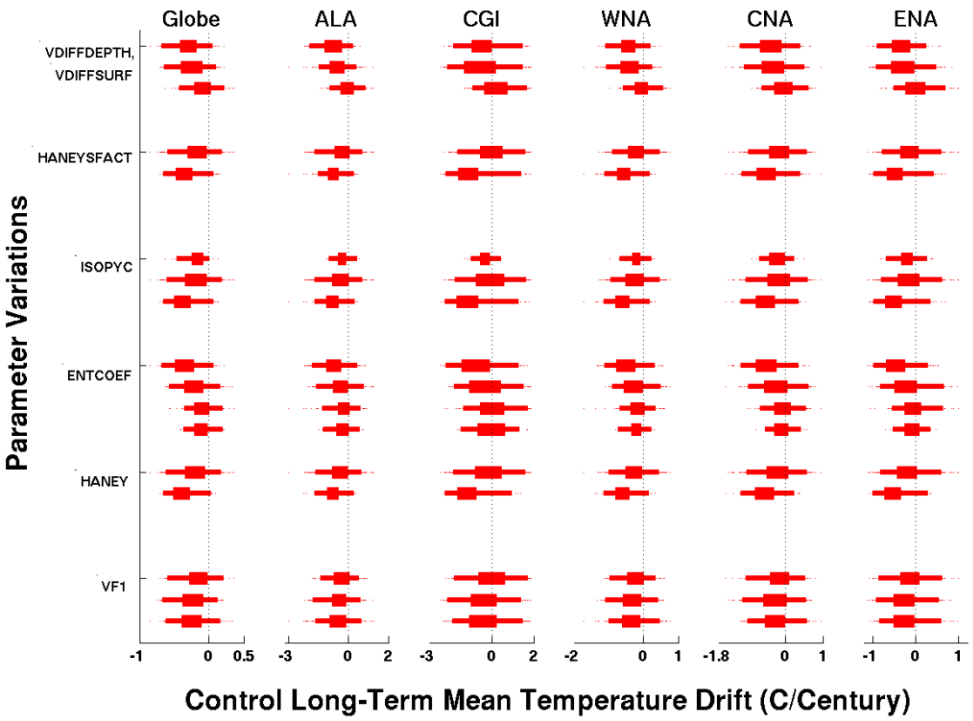


Figure 5.24: Long-term mean drift in temperature (°C/Century) for the globe and five NA regions for the 1,214 control simulations split into distributions corresponding with model parameter values. Actual parameter values are not listed but are arranged in the same order as that given in Table 5.1. Boxplots provide 25-75% (inner) and 2.5%-97% (outer) ranges and dots for samples outside the 95% range. The vertical dotted line corresponds with zero trend.

An initial thing to point out in Figure 5.24 is that all regions tend to shift in the same direction with varying parameter values for all parameters. Parameters VDIFFDEPTH and VDIFFSURF vary together and correspond to the background vertical mixing of ocean temperature and salinity by defining the rate at which vertical mixing changes with depth (VDIFFDEPTH) and a surface value of vertical mixing to start with (VDIFFSURF). Increasing these parameters (i.e., vertical mixing) increases the transport of heat away from the surface layers and therefore reduced any imbalance of heat built up at the atmosphere/ocean interface, thus reducing long-term mean drift which is what Figure 5.24 shows (i.e., distributions move closer to zero drift line).

Parameter HANEYSFACT sets the time lag for the correction of model generated sea surface salinities (SSSs) to observed SSSs in the spin up phase of the model. This process attempts to reduce drift in the model and therefore it is understandable that varying it alters the long term mean model drift.

Parameter ENTCOEF has already been discussed above and was found to increase annual mean temperatures in the atmosphere as its values increased. It was found in Figure 5.24 that as ENTCOEF increased long-term mean drift went from a larger negative drift to a smaller trend. Therefore the increased temperature assisted in offsetting the atmosphere/ocean imbalance that was causing a cooling trend (i.e., drift went from negative trend to less negative trend).

Parameter HANEY is the Haney heat forcing coefficient and it sets the time lag for the correction of modeled sea surface temperature. Therefore a larger HANEY value corresponds to a longer lag time which can allow for greater buildup of heat imbalances, which is seen in Figure 5.24 as the temperature drift becomes a larger negative value with increasing HANEY value.

5.8 Initial Conditions Uncertainty

As discussed in Chapter 2, Section 2.2.1 one of the three main types of climate model uncertainty comes from uncertainty in the internal variability in the modeled climate system. The control simulation ensemble discussed in this chapter provides an opportunity to assess this internal variability uncertainty because a number of the control simulations containing the same atmosphere and ocean parameters were run

with differing initial conditions (i.e., DTHETA from Table 5.1). Therefore an analysis was conducted on sets of control simulations differing only by their initial condition parameter (i.e., all atmosphere and ocean parameters were the same) with the stipulation that they must be comprised of at least three simulations with differing initial conditions in order to get a more representative sample of possible variations. All such control sets were identified and the 70-year drift (i.e., control simulation years 21-90) calculated for each initial condition variation member. The mean 70-year drift of all members in a set was then calculated and anomalies established from this mean for each member. The anomalies across all initial condition variation control sets were then combined into a single distribution for temperature and precipitation in each region and compared to the full distribution of 70-year drift from all controls. This provides a relative estimate of the influence initial condition variations and therefore internal variability can have on climate model assessments. Granted assessing control simulation trends is a rather crude method for assessing the impact of internal variability on climate model results but the transient simulation analysis in Chapter 7 did not offer a useful alternative due to the fact that solar, volcanic, and anthropogenic scaling factor parameters were varied alongside initial conditions and therefore the initial condition parameter alone could not be isolated to quantify its impact on transient climate changes such as forced trends over the historic or future projection period.

Figure 5.25 provides the results of the initial condition uncertainty assessment where the anomaly distributions of initial condition variations in 70-year drift are compared to the full control ensemble of 70-year mean drift. Table 5.14 quantifies the ratios of the 50% and 95% distribution differences shown in Figure 5.25. The

uncertainty in internal variability accounted for roughly half of the 50% uncertainty range in global 70-year control drift in both temperature and precipitation and a bit more than half for the 95% range. For regional temperatures this percentage stayed roughly the same but for regional precipitation the internal variability uncertainty accounted for approximately 80-90% of the total uncertainty in most regions.

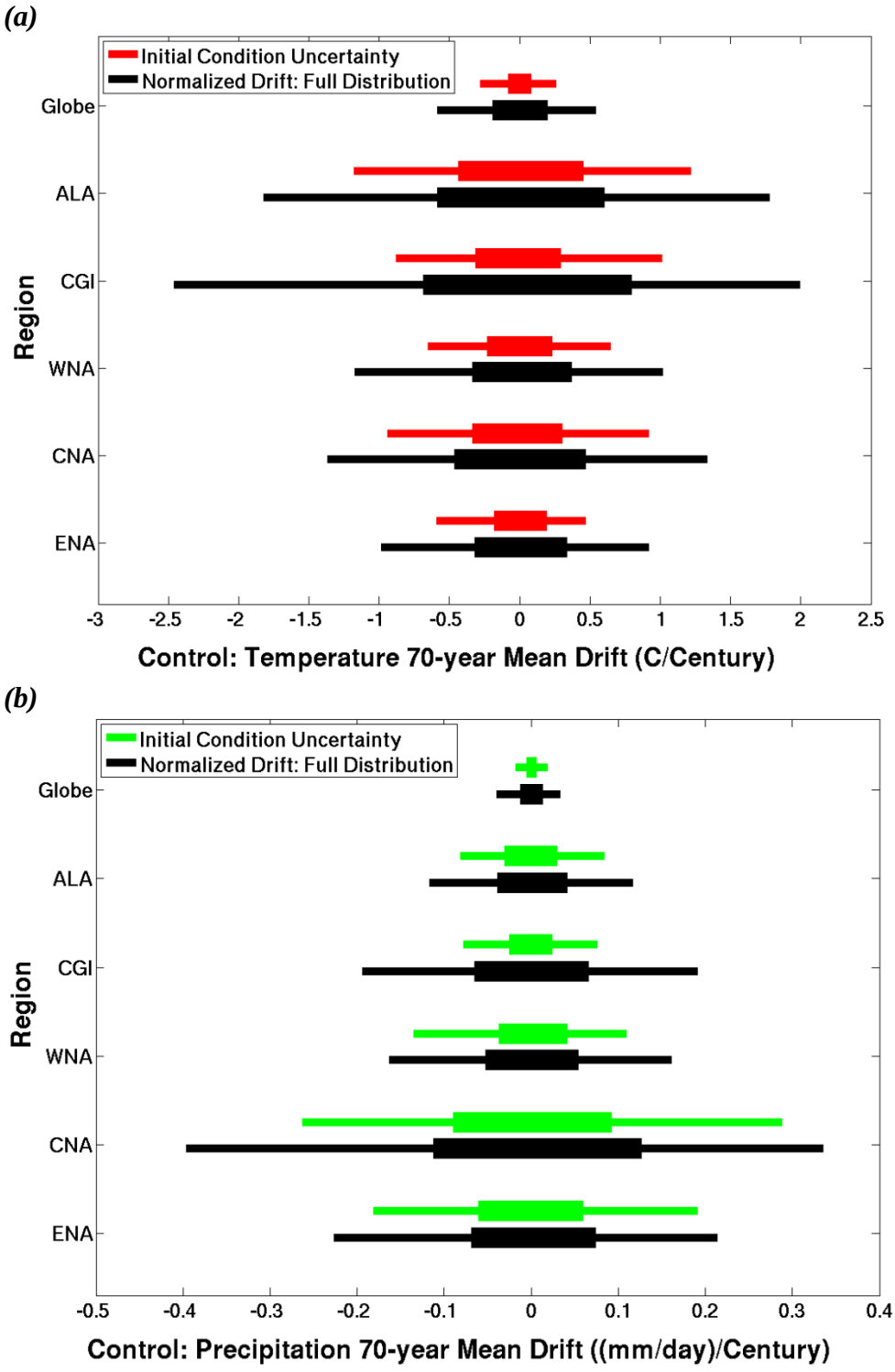


Figure 5.25: Comparison of initial condition uncertainty (i.e., control simulations with the same atmosphere/ocean parameters but different initial conditions) in 70-year drift (colored) to the full control ensemble of 70-year mean drift for (a) temperature (°C/Century) and (b) precipitation rate ((mm/day)/Century).

Table 5.14: Ratios of initial condition uncertainty in 70-year control drift compared to the full range of 70 year drift for the 50% and 95% range. Larger ratio values indicate an increased influence of the initial conditions variations (i.e., internal variability) to the 70-year trends.

	Temperature		Precipitation	
	50% Range	95% Range	50% Range	95% Range
Globe	0.56	0.69	0.50	0.62
ALA	0.74	0.63	0.84	0.74
CGI	0.41	0.50	0.45	0.49
WNA	0.65	0.70	0.82	0.88
CNA	0.62	0.76	0.88	0.80
ENA	0.70	0.64	0.89	0.82

5.9 SUMMARY

This chapter provided an evaluation of the performance of the CPDN HadCM3L control simulations across the globe and NA regions compared to observational data sets. The control simulations maintained a constant annual but seasonally varying radiative forcing and therefore were compared to detrended observations to assess the modeled mean climate and its variability due to internal chaotic processes in the simulated climate system, including coupling between the atmosphere, ocean, land surface, and sea ice.

There were a total of 1,214 simulations comprised of 138 atmospheres, ten oceans and eight initial condition variations resulting in 642 unique atmosphere/ocean combinations with the remaining 572 containing duplicates atmosphere/ocean combinations with variations to initial conditions. The controls contained relatively large drift in the first 20 years of their simulations due to atmosphere/ocean adjustments

associated with the coupling process and therefore these initial 20 years were not used in any analysis (i.e., including the corresponding transient simulation years of 1921-1940). Control simulations also contained long-term mean drift from flux inequalities not removed by the flux adjustment process. This drift had to be removed from the corresponding transient simulations having the same atmosphere and ocean parameter values because a similar drift would exist in those forced simulations.

The absolute mean temperatures of the control simulations were generally aligned or slightly cooler than observational estimates due to possibly poor representation of topography due to the models relatively coarse resolution. Additionally the observational estimates of absolute mean values may not have been representing the true value due to the difficulties in establishing absolute values compared to anomalies and because of limitations in ocean observations. The magnitude of the seasonal cycle in temperature in the simulations aligned generally well with observations but with the range of CPDN distributions being significantly larger than the ranges of observations and extending to slightly larger magnitudes.

The interannual variability of the majority of the simulations and observations agreed well, with a general tendency in the model to extend to larger magnitudes of variability. However, with only 30-90 years of observational data to compare to, the full range of the climate system's natural variability may not be represented in the existing observational data sets.

Parameter variations in the control simulations did not always impact all regions or both temperature and precipitation in the same way and therefore a universal

parameter value or set of parameter values could not be isolated and used to remove model simulations based on performance compared to observations.

Most of the model parameter uncertainty was found to be associated with two cloud physics parameters: the ice fall speed (VFI) which impacts cloudiness (and therefore solar radiation and surface temperature) and precipitation by scaling the speed at which cloud ice particles fall out of the sky and the entrainment coefficient (ENTCOEF) which sets the rate at which convective clouds mix with their surrounding environmental air and impact the transport of moisture to higher levels in the troposphere. These two parameters have been found important in previous studies as well (e.g., Knight et al. 2007; Sanderson et al. 2008a; Sanderson et al. 2008b; Sanderson et al. 2010).

The uncertainty in internal variability was found to account for roughly half of the 50% uncertainty range in global 70-year control drift in both temperature and precipitation and a bit more than half for the 95% range. For regional temperatures this percentage stayed roughly the same but for regional precipitation the internal variability uncertainty accounted for approximately 80-90% of the total uncertainty in most regions.

CHAPTER 6

NORTH AMERICAN PALEOCLIMATE COMPARISON

The observational datasets used to assess natural variability in the HadCM3L control simulations in Chapter 5 were relatively short in duration (e.g., 30-100 years) due to the limited length of higher resolution instrumental records and satellite data (Chapter 4). Therefore these near-term observations may not represent the full range of variability in the climate system. One method used to extend the climate record further back in time, on the centennial to millennial scale, to get a better sense of past variability is the use of paleoclimate proxy data from sources such as tree rings, corals, ice cores, or sediments (e.g., see reviews in Jones and Mann 2004; NAS 2006; Mann 2007). When these proxy sources are sensitive to changes in their surrounding climate, they can be used to reconstruct climate variables such as temperature and precipitation.

In this chapter, proxy data sets from across North America (NA) are utilized to compare climate variability of the more distant past (i.e., during the last 2,000 years) to variability found in the modern observational period and in the CPDN control simulations. Section 6.1 provides an overview of the two types of proxy data sources used in this analysis (tree rings and varved lake and ocean sediments), and Section 6.2 describes the climate reconstruction process. Section 6.3 reviews the various NA proxy data sets used and Section 6.4 gives the resulting interannual and decadal variability comparisons to the more recent observational data sets and HadCM3L control simulations.

6.1 PROXY DATA SOURCES

6.1.1 Tree Rings

Using tree ring characteristics to study climate (termed dendroclimatology) is one of the most widely used methods for reconstructing past climates at an annually resolved scale. This is in part due to the fact that tree ring data provide some of the strongest statistical relationships with instrumental climate records, the biophysical relationships between temperature and rainfall variations and tree growth, and their relatively widespread distribution around the globe compared to other annually resolved proxy data sources (e.g., Bradley 1999; Jones and Mann 2004). A large collection of worldwide tree ring data has been collected and made available for the wider scientific community with a number of the records extending back 1-2 thousand years (Grissino-Mayer and Fritts 1997).

The basic structure of a tree is shown in Figure 6.1. Just inside of the bark layer is the vascular cambium which produce phloem cells (adjacent to the bark), responsible for the transport of sugars and photosynthetic material, and the xylem cells (adjacent to the phloem cells), responsible for transporting water from the roots to the rest of the tree. Over time the phloem cells are compressed and become part of the bark and the xylem cells become rigid wood. At the beginning of the growing season the xylem material is thin walled and low in density giving it a lighter color. This region of growth is called the earlywood. Near the end of the growing season, tree growth slows and the xylem material is thinker walled and higher in density which gives it a darker color. This region of growth is called the latewood. The combined earlywood and latewood comprise a single annual ring (i.e., tree ring) and therefore the transition from

one year to the next can be identified by the light to dark color transitions, or the corresponding density differences.

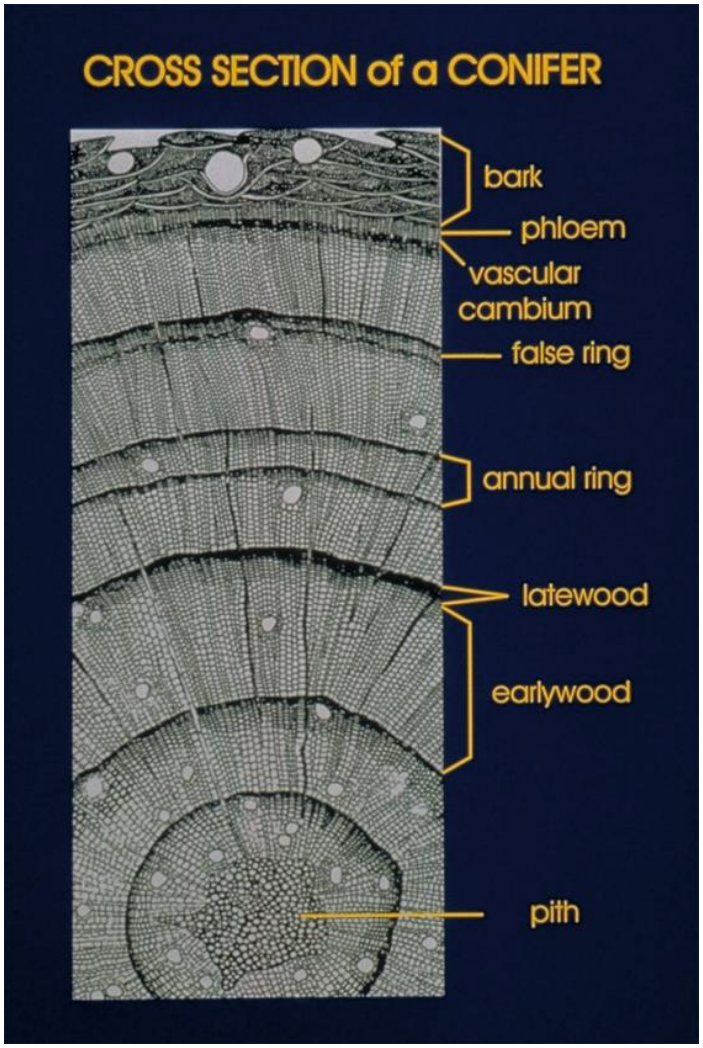


Figure 6.1: Cross section of the components of the inner structure of a tree that are used for tree ring identification. See text for description (From Fritts (1976).)

Information on the climate in which a tree has grown can be acquired from analyzing characteristics of its tree rings such as ring width, density and chemical composition. Many factors can influence these tree ring characteristics including climatic factors such as temperature, precipitation, sunshine, humidity and non-climatic

factors such as tree species, tree age, soil nutrients and tree nutrient storage (Bradley 1999). It is therefore necessary to identify the desired climate signal from amongst all of these competing factors which is done by choosing site locations where trees are growing under climatic stress (i.e., where temperature or precipitation are the limiting factors) such as near the limit of their ecological range. In these locations, variations in the climate signal of interest cause significant changes in tree growth. For example, trees growing in semiarid regions such as the southwest United States are often limited by water availability and therefore tree ring characteristics may reflect changes in precipitation (e.g., Salzer and Kipfmueller 2005). Trees growing at the latitudinal or altitudinal boundaries may be limited by temperature and therefore reflect temperature variations (e.g., Davi et al. 2003).

In order to create long-term tree ring records, multiple trees across a number of time periods are combined to create a single master chronology. To accomplish this, tree ring sequences are aligned so their corresponding growth patterns match one another within overlapping periods. This often includes the incorporation of dead trees to the chronology, which can even originate from beams or logs used to build structures over the last few thousand years (e.g., Robinson 1976).

Prior to combining the individual tree ring records into a long master chronology, the individual records must be standardized to account for each tree's mean growth rate (e.g., Fritts 1971, 1976). For example, tree rings are generally wider during a tree's early stages of life and then become narrower with age. These effects have nothing to do with changes in climate and therefore must be removed. One method used to account for this is termed Regional Curve Standardization (RCS). In this

method, the expected value of the tree ring characteristic or parameter (e.g., ring width or density) is calculated as a function of the tree's age. Then the actual parameter is divided by the expected value at any given year in the sequence, thereby standardizing the record. Once the various records have all been standardized for growth rate, they can be combined to form a single master chronology for that specific site or region. Figure 6.2 provides an example of this process and shows how non-climatic variability can be produced in the master chronology if the standardization process is not applied (i.e., compare the fourth time series, which is the combined record, for the top and bottom panels).

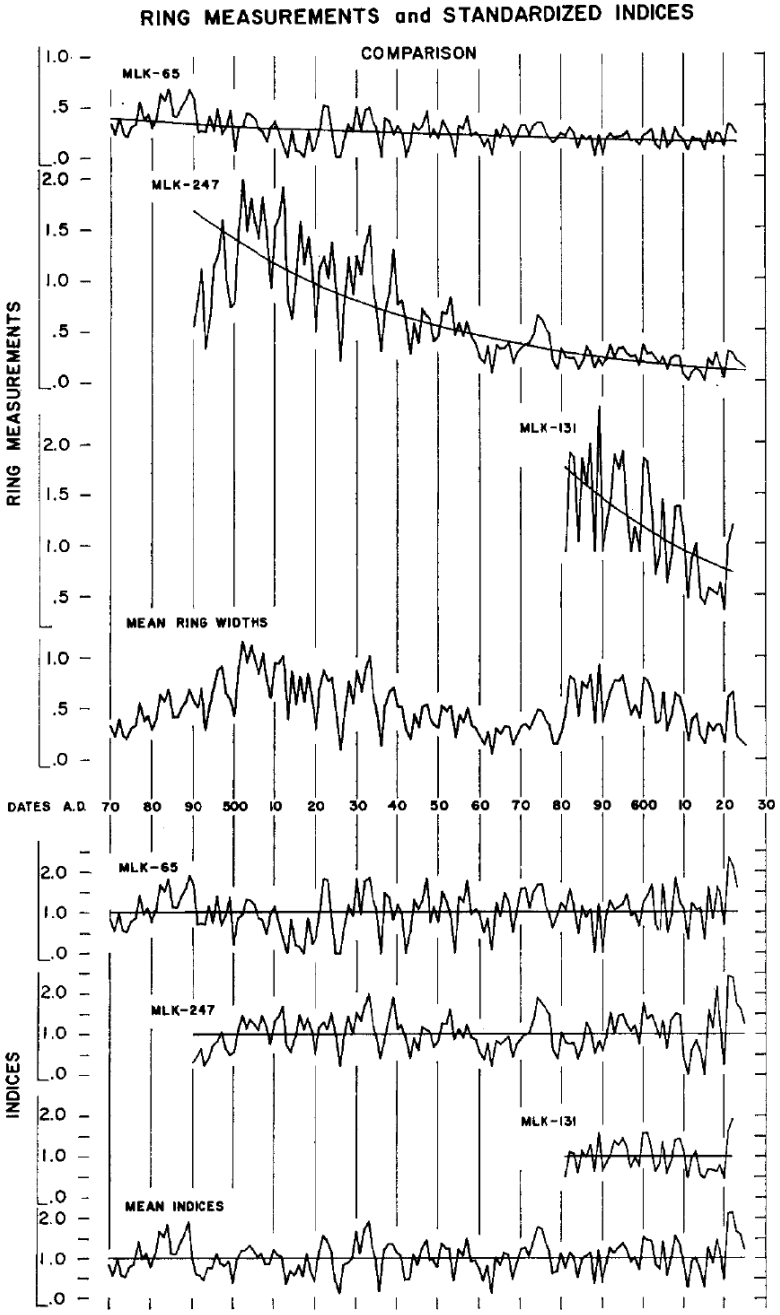


Figure 6.2: Standardization of tree ring width across three different records. The top panel shows the actual tree ring widths as well as the expected value growth curve. The mean tree ring width is shown at the bottom of the top panel for a straight averaging of the original tree ring widths whereas the bottom panel shows the result of the standardization process. (From Fritts (1971).)

There are a number of limitations when using tree-ring records as proxy data. These include the limited areal coverage available where trees are found to be sensitive to either temperature or precipitation. In many instances, tree growth is dependent on both of these climate indices and therefore their effects cannot be separated. Further, there are a number of non-climatic factors that can influence tree growth and these are not always known across the record. Additionally, studies looking at the recent chronologies of tree ring characteristics point to a possible change in the response of these indicators to climatic changes over the 20th century (Briffa et al. 1998) with a suggested cause being enhanced tree growth due to higher CO_2 concentrations (Graybill and Idso 1993). This response change must be taken into account, if present, when attempting to find relationships between modern instrumental data and temperature or precipitation (see Section 6.2).

The final steps in using tree ring data to reconstruct paleoclimates is the calibration of the master chronology with overlapping instrumental data, verification of that reconstruction with instrumental data not used in the calibration phase, and then the application of the proxy/temperature relationship across the chronology record prior to the instrumental data. These steps are also used in the other proxy data reconstructions and therefore will be discussed in general in Section 6.2.

6.1.2 Varved Lake and Ocean Sediments

When sediments are deposited into distinct annual layers at the bottom of a water body they are called laminated or varved sediments. Variations in the characteristics of these varved sediments through time can indicate changes to the climatic conditions in the surrounding region. In closed-basin glacial lakes, inorganic sediments are deposited on the lake bottom according to the meltwater discharge into the lake. During the warm season, glacial ice melt increases which increases the flow of meltwater into the lake. These higher energy conditions allow larger grained sediments (e.g., silt and fine sand) to be brought into the lake and deposited on the lakebed. During winter, the ice melt is significantly reduced which decreases the meltwater and limits the flow of sediment into the lake to only the very small variety (e.g., clay-sized). Therefore, annual layers can be identified.

As with tree rings, both precipitation and temperature can influence the characteristics of the varved sediments and therefore sites are selected where the meltwater into the lake is highly sensitive to one of the variables. Examples can be found in Arctic Canadian lakes where summertime meltwater flux into the lakes are highly temperature sensitive (e.g., Lamoureux and Bradley 1996; Thomas and Briner 2009). In some varved sediments the effects of temperature and precipitation can be separated. Figure 6 shows a core taken from a varved sediment in which the varve thickness has been identified as sensitive to temperature but, additionally, small sand layers within each annual layer can be linked to precipitation. Therefore, the two can be separated when attempting to reconstruct climate conditions in the area.

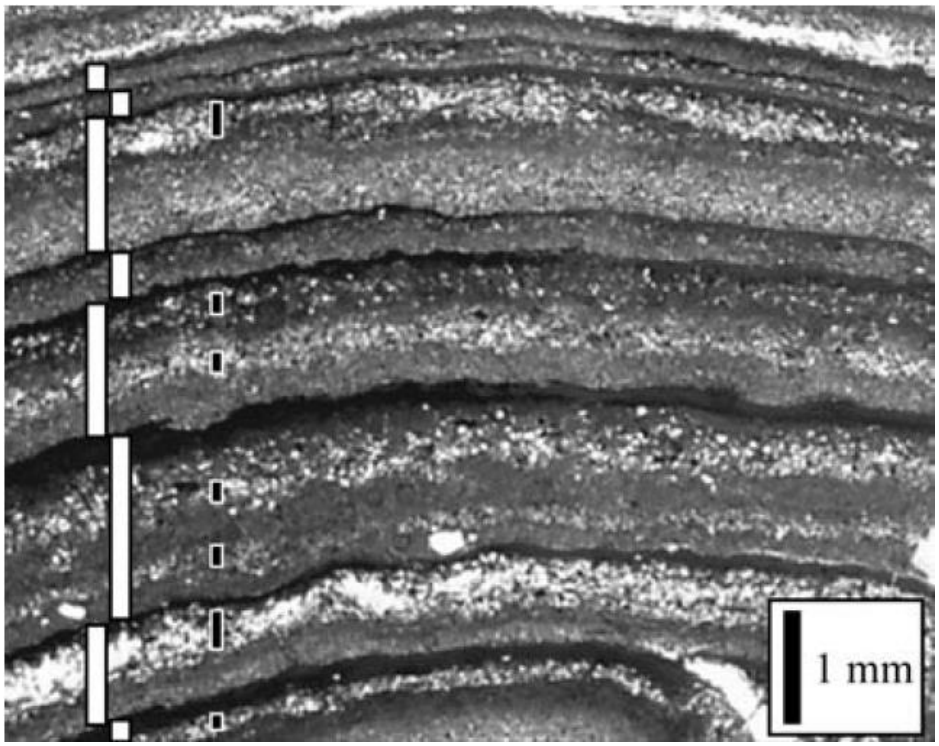


Figure 6.3: Varved sediment sample showing annual layers of deposited sediment on a lake bottom. White boxes identify each annual layer while black boxes show sand-layer thickness which has been linked to precipitation in the region. The precipitation dependent sand-layer has been subtracted from the annual layer to provide a proxy data set of varve thickness used in reconstructing temperature variability. (From Thomas and Briner (2009).)

A complicating factor with these types of glacial lake sediments is that the glacier location relative to the lake can impact the sedimentation rate. Since the glacier moves closer or farther away from the lake depending on the climatic conditions as well, this can impact interpretations of sedimentation rate variability (e.g., Leonard 1997). Other factors such as hillslope activity, sediment release upstream of the lake and transport of sediment by lake ice also can influence the varved sediment record in unpredictable ways that cannot be interpreted from the proxy record (Thomas and Briner 2009).

Occasionally, varved sediments can be formed along ocean coastlines or within estuaries when sedimentation takes place at fast enough rates. Climate sensitive indicators within each layer can be analyzed such as temperature dependent magnesium/calcium ratios inferred from deposited shells (e.g., Cronin et al. 2003). The temperature of the water in which these shelled organisms lived can be determined and then related to local surface temperatures. These varved sediment records, however, are formed in open bodies of water connected to the ocean which complicates the background conditions impacting sediment accumulation each year. Additionally, organisms in the sediment accumulation regions may mix the sediments and alter the characteristics of the original layers (Turekian 1978). An influx of pollution, especially in recent decades, also can complicate the record and influence the calibration process (e.g., NAS 2006).

6.2 PALEOCLIMATE RECONSTRUCTION METHOD

The general method used to reconstruct past climates is similar for both the tree ring and varved sediment proxies described in the previous section. This method consists of three main steps: comparing the proxy data with the overlapping instrumental record to determine an empirical relationship with the climate variable of interest, validating the relationship over a separate time period, and using the relationship to reconstruct the climate variable throughout the rest of the proxy record.

The first step in this process involves calibrating the proxy record against the instrumental climate data, typically using the statistical technique of linear regression (Figure 6.4). Once the proxy record and instrumental record have been aligned over the same time period, proxy values and their corresponding observational values are identified (e.g., open circles in Figure 6.4). Once all of these pairs are identified a linear least squares line is established which forms the basis for the relationship between the proxy and observational values used to reconstruct past values of the climate variable. For example, if a proxy value had a magnitude of B in Figure 6.4 sometime in the distant past then the reconstructed value would be T_B. While the blue lines in the figure show the 95% prediction interval, it is clear that a reconstructed climate variable at a proxy value of A will have more uncertainty than at B since A is outside the range used to generate the proxy/climate variable linear relationship (i.e., no samples extend out to A).

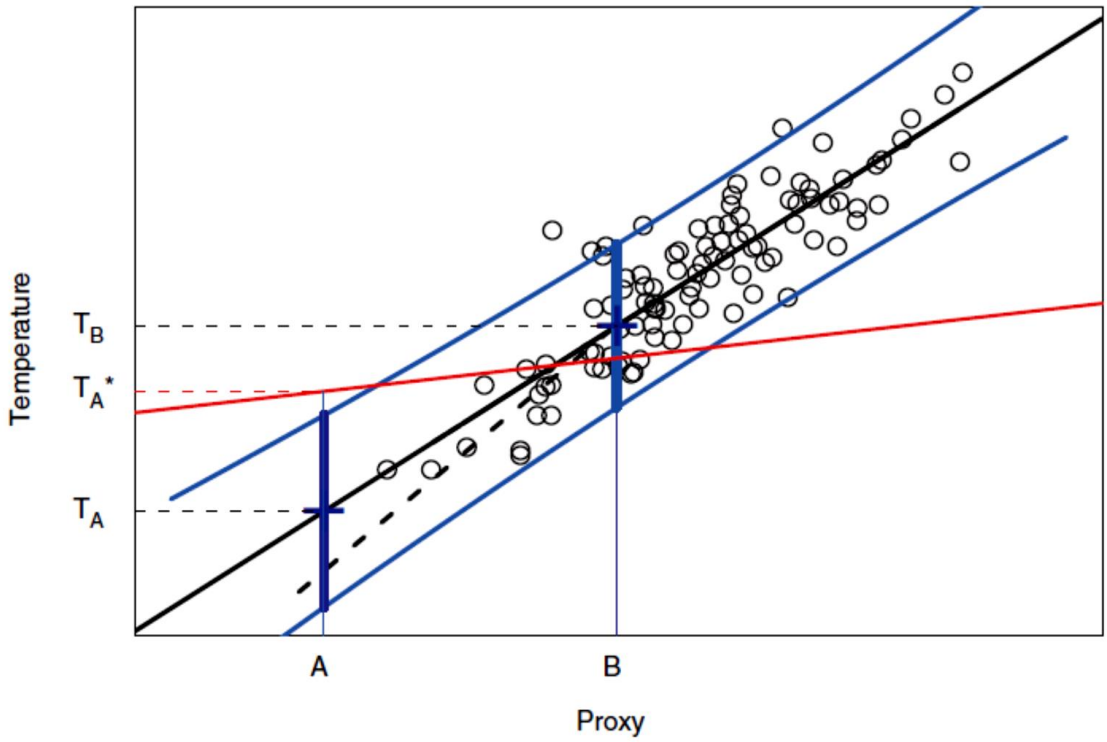


Figure 6.4: An example of how temperature is reconstructed from proxy data using linear regression. Circles indicate a hypothetical annual series of proxy data and corresponding instrumental temperature observations over a 100 year calibration period (i.e., 100 circles). Solid black line is the linear fit to the data and blue lines indicate the 95% prediction intervals. The heavy dashed line and red line indicate potential departures from an assumed linear relationship between the proxy and temperature data. Two examples (A, B) are provided showing the temperature predictions for a given proxy value with corresponding prediction uncertainty ranges (heavy blue vertical lines). (From NAS (2006).)

Once the empirical relationship is calculated it is tested over a part of the instrumental record that was not used in the calibration process. Climate variables are reconstructed from the proxy record during this period and the results compared to observations using any number of metrics to assess the measureable skill in the predicted variable. If the relationship is found to have predictive skill then it is used to reconstruct the climate variable over the rest of the entire proxy record.

This linear regression method assumes that a linear statistical relationship exists between the proxy data and the value of the climate variable. The derived relationship

would not produce reliable reconstructions if there were portions of the proxy/climate variable relationship that were not linearly related. This is illustrated in Figure 6.4 with the heavy dashed black line. If the relationship in the upper portion of the proxy record were different then the lower portion then the linearity assumption would be violated and a more complex relationship would have to be established.

Additionally, the statistical relationship is assumed to be maintained throughout the entire calibration, validation and reconstruction period (called the stationarity assumption). If it varies with different time periods then the calibrated relationship would not accurately reconstruct the actual climate variable. This is illustrated by the red line in Figure 6.4 which could represent the actual proxy/climate variable relationship at a time in the distant past. Since this relationship differs from the one established in the calibration phase, the reconstructed values would not reflect the actual variability of the climate variable (e.g., see the difference in reconstructed temperatures at proxy value A).

One thing to note with regard to this linear regression method is that the reconstructed climate variable can potentially have less variability than what is found in the instrumental data. This is because only a single value is assigned to a given proxy reading whereas there may be a range of potential values that could represent the proxy data. For example, see the multiple temperature/proxy pairs near proxy value B (i.e., multiple circles). The reconstruction assigns a temperature value of T_B for this proxy reading while the actual pairings over the calibration period indicated a number of potential temperature values. Therefore a reduction in variability can be expected when analyzing paleoclimate reconstructions.

6.3 NORTH AMERICAN PALEOCLIMATE RECONSTRUCTIONS

A number of proxy-based paleoclimate reconstructions were available across North America from the National Climatic Data Center's (NCDC's) World Data Center for Paleoclimatology (http://www.ncdc.noaa.gov/paleo/recons.html), the world's largest archive of paleoclimatic data. These reconstructions varied in their location, temporal resolution and length of record. Since the goal of this assessment was to compare interannual and decadal variability estimates from these paleoclimate reconstructions to the more recent relatively high resolution observations and the control simulations, only data sets with annual temporal resolution were utilized. This requirement narrowed the data sets to mainly tree rings and varved sediment records.

The geographic location of each data set is shown in Figure 6.5 and labeled according to its proxy data type (symbol shape) and climatic variable (solid or light colored fill for temperature and precipitation respectively). More detailed information on each data set is given in Table 6.1 including the time period covered, season, and relevant references. The actual reconstructed temperature and precipitation anomaly data sets are shown in Figure 6.6 and 6.7 respectively. Each proxy-based dataset followed a similar climate reconstruction procedure as discussed in the previous section and therefore specific details on each will not be given here but can be found in the corresponding references (Table 6.1). Some general information on the data sets is discussed below, including some of the more important details that could impact the resulting variability analysis that is provided in the next section.

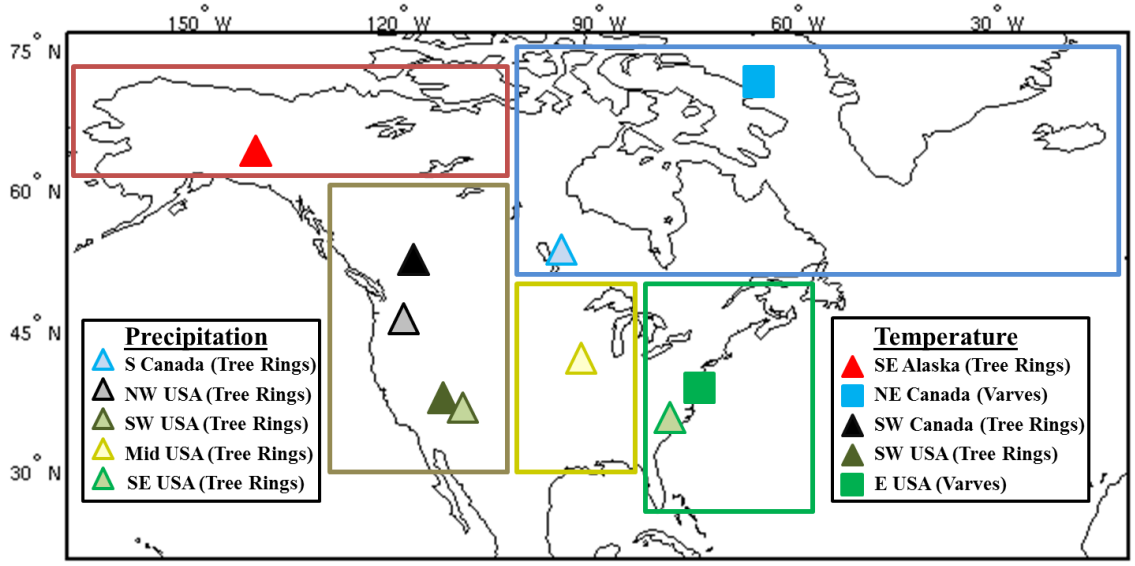


Figure 6.5: Locations of North American proxy-based paleoclimate reconstructions for precipitation (open symbols) and temperature (filled symbols) using proxy data from tree rings (triangles) and varved sediments (squares). The five larger rectangular regions highlight the regions used for calculating climatic information from the CPDN HadCM3L model.

Table 6.1: Information for each proxy-based paleoclimate reconstruction shown in Figure 6.5.

Region	Proxy Data	Climate Variable	Record (years)	Season	Source
SE Alaska	Tree Rings	Temp	1593-1992	Annual	Davi et al. 2003
NE Canada	Varves	Temp	971-2003	Summer	Thomas and Briner 2009
SW Canada	Tree Rings	Max Temp	950-1994	Summer	Luckman and Wilson 2005
SW USA	Tree Rings	Max Temp	1-1996	Annual	Salzer and Kipfmueller 2005
E USA	Varves	Temp	1700-1995	Spring	Cronin et al. 2003
S Canada	Tree Rings	Precip	1409-1998	Annual	St. George and Nielsen 2002
NW USA	Tree Rings	Precip	1705-1979	Annual	Garfin and Hughes 1996
SW USA	Tree Rings	Precip	570-1987	Annual	Salzer and Kipfmueller 2005
Mid USA	Tree Rings	Precip	1640-1982	Annual	Cleaveland and Duvick 1992
SE USA	Tree Rings	Precip	933-1985	Spring	Stahle and Cleaveland 1992

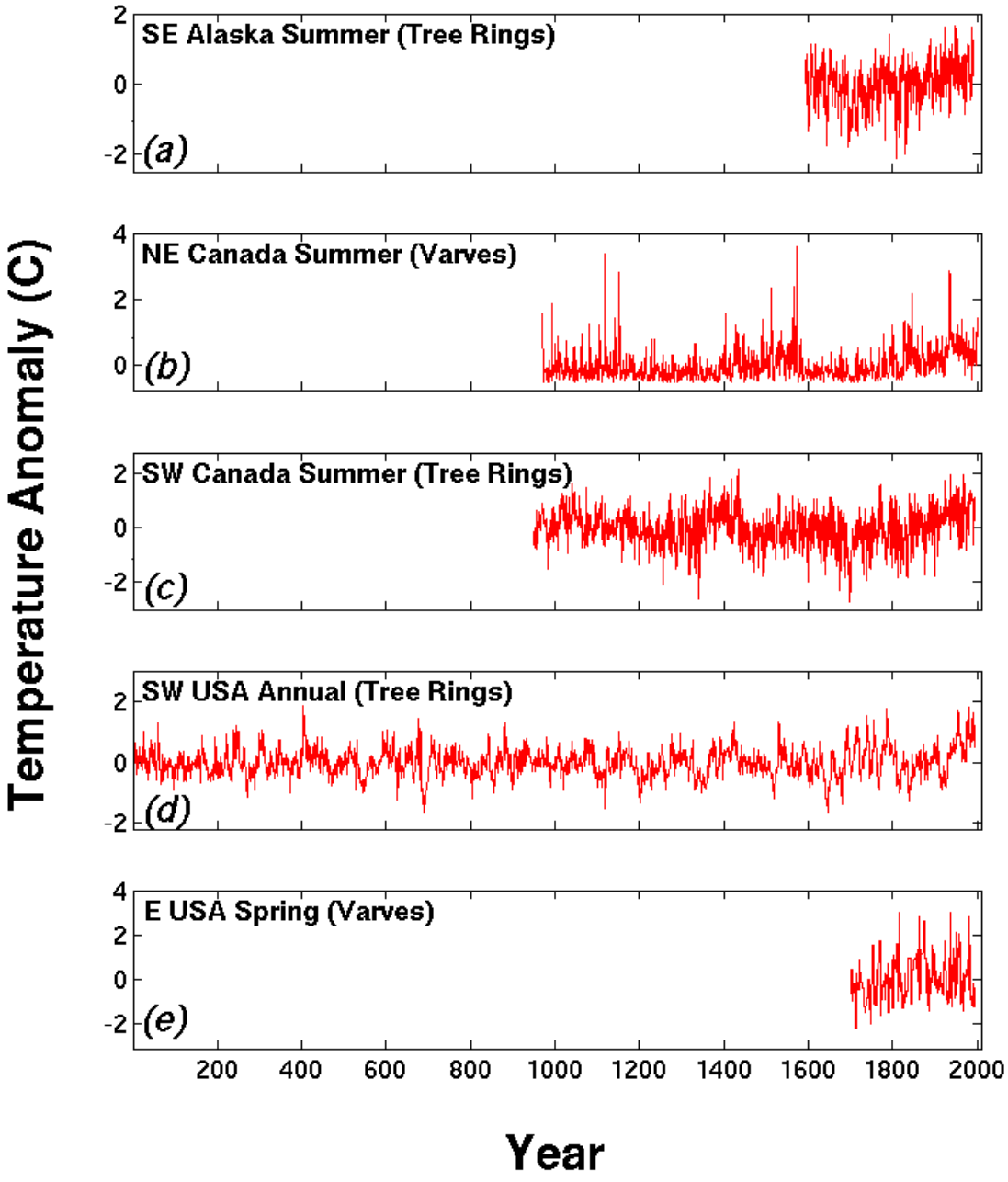


Figure 6.6: Annual average temperature anomaly (°C; anomaly from each data set's long-term mean) for *(a)* SE Alaska summer, *(b)* NE Canada summer, *(c)* SW Canada summer, *(d)* SW USA annual, and *(e)* E USA spring.

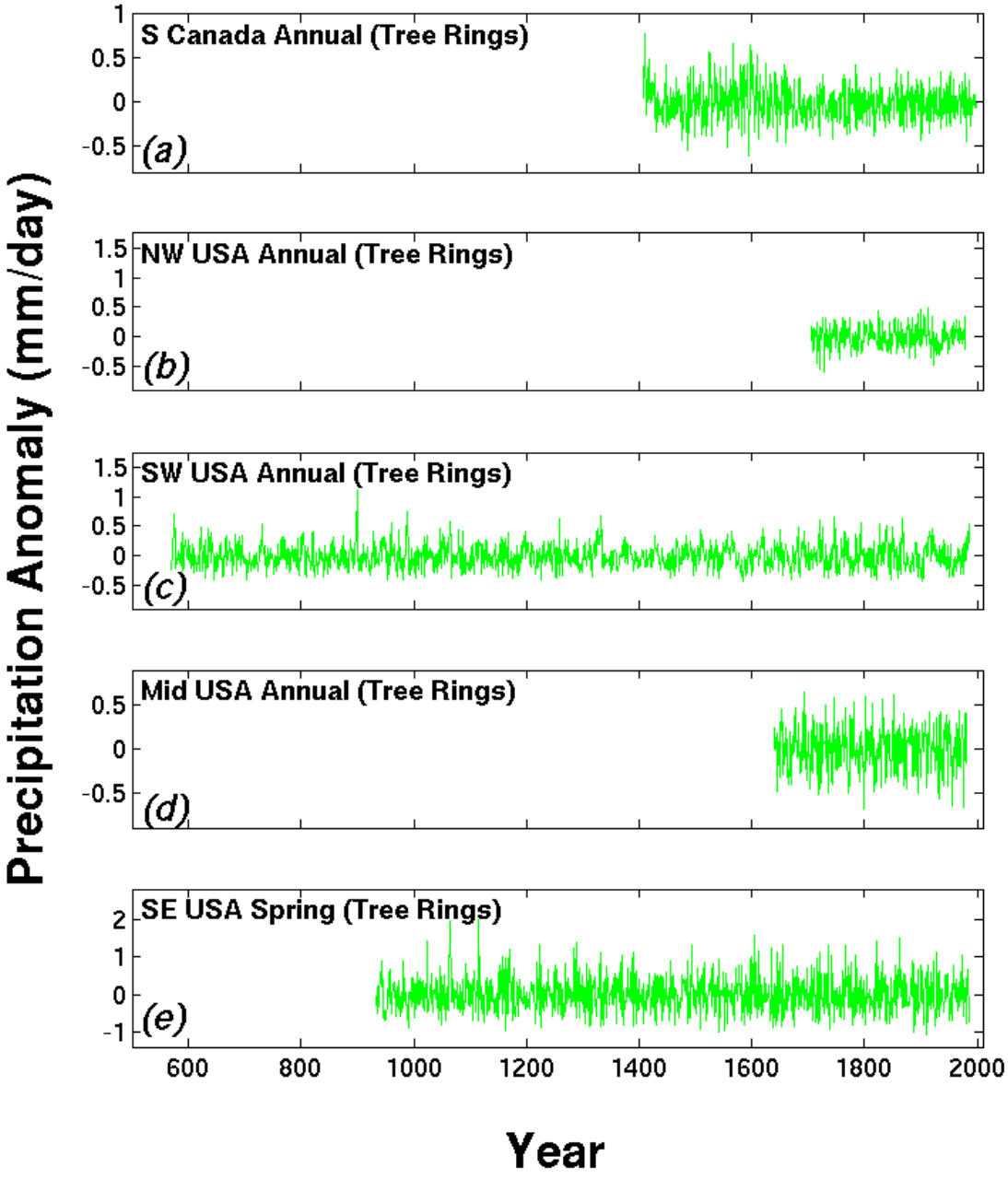


Figure 6.7: Annual average precipitation anomaly (mm/day; anomaly from each data set's long-term mean) for *(a)* S Canada annual, *(b)* NW USA annual, *(c)* SW USA annual, *(d)* Mid USA annual, and *(e)* SE USA spring.

Tree ring proxy data were used for all of the precipitation reconstructions as well as three of the five temperature reconstructions. The additional two temperature proxies were varved sediments from a glacial-lake in northeast Canada (NE Canada; Thomas and Briner 2009) and varved ocean sediments from the Chesapeake Bay in the eastern USA (E USA; Cronin et al. 2003). It should be noted that the E USA data set is unique from the rest because it was constructed to represent variations in Chesapeake Bay water temperature. However, it was still included because this was the only temperature reconstruction from within the CPDN ENA region and additionally because over half of that region in the model contained ocean grid cells and therefore the inclusion of a SST-based proxy estimate influenced by both oceanic water temperatures and regional atmospheric temperatures seemed appropriate.

Two pairs of temperature/precipitation reconstructions were included in the single CPDN WNA region because they provide information on both the Pacific Northwest (often cool/wet) and southwest United States (often warm/dry). Since both of these climatic regimes reside within the WNA region their resulting impacts may offset each other in a single, region-wide average calculation and therefor including both offered an opportunity to investigate this possibility. The two temperature reconstructions in this region were constructed to represent maximum temperature but it was assumed that the variability in maximum temperatures resembled that of mean temperatures.

Finally, it is important to keep in mind when using these proxy-based data sets that while the reconstructions are meant to represent larger regional average climate variations, they still could be representative of an area too small when compared to the

large CPDN NA regions. This could impact the resulting variability comparisons because variability changes as the area it is averaged over changes (i.e., averaging over a larger area reduces resulting variability estimates).

6.4 Paleoclimate Variability Compared to CPDN and Observations

The interannual and decadal variability of the proxy-based paleoclimate reconstructions are shown in Figure 6.8 and 6.9 respectively along with variability in CPDN control simulations and observational data sets. For interannual variability (Figure 6.8), the control simulation and observational distributions were constructed in the same manner discussed in the previous variability analysis in Chapter 5, Section 5.5.1 (i.e., five 30-year samples from each of the 1,214 control simulations with the same total number of observational bootstrap samples). Each proxy reconstruction had interannual variability calculated from 30-year time periods with 15-year overlapping blocks with the total number of samples depending on each data set's length.

In a similar manner, decadal variability (Figure 6.9) was calculated across three 100-year time periods within each control simulation and a single estimate calculated for each of the three 90-year temperature observational data sets. Decadal variability could not be calculated for any of the precipitation observational data sets because there were too few decadal samples available. Decadal variability for the proxy reconstructions was calculated from 100-year time periods with 50-year overlapping blocks, again resulting in a varying number of samples depending on record length.

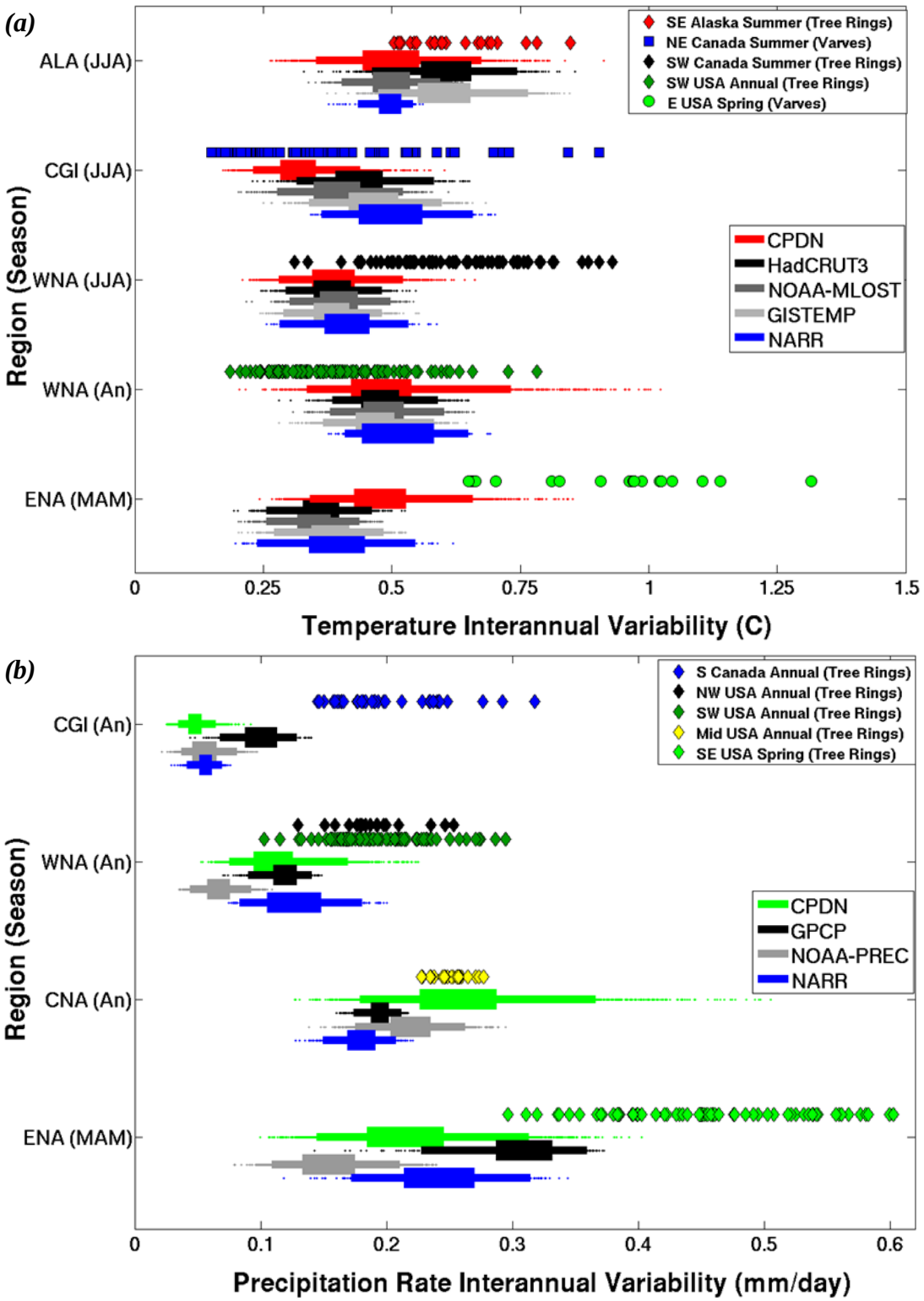


Figure 6.8: Interannual variability (30-yr) for *(a)* temperature (°C) and *(b)* precipitation rate (mm/day) for the 1,214 control simulations (five samples per simulation), observational bootstrap distributions (same number of samples) and paleoclimate reconstructions (number of samples vary depending on record length). Boxplots provide 25-75% (inner) and 2.5%-97% (outer) ranges and dots for samples outside the 95% range.

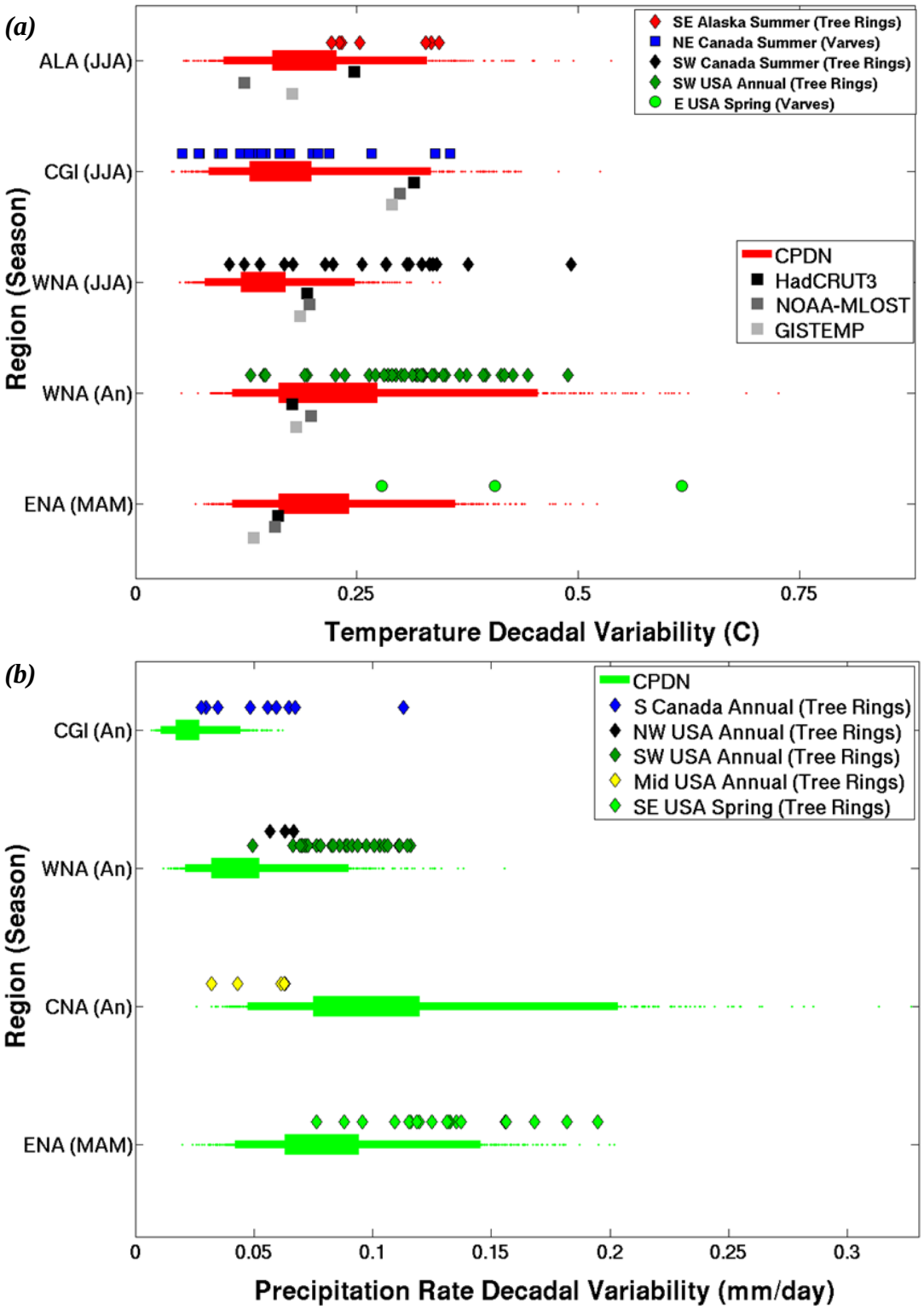


Figure 6.9: Decadal variability (100-yr) for *(a)* temperature (°C) and *(b)* precipitation rate (mm/day) for the 1,214 control simulations (three samples per simulation), three observational samples for temperature (one per 90-yr data set) and paleoclimate reconstructions (samples vary). Boxplots provide 25-75% (inner) and 2.5%-97% (outer) ranges and dots for samples outside the 95% range.

The interannual variability in proxy-based reconstructions of temperature (Figure 6.8(a)) generally aligned with control simulations and observations except for ENA (MAM) and possibly WNA (JJA). Recall that the temperature reconstruction for ENA (MAM) was the unique varved ocean sediments meant to represent water temperatures in the Chesapeake Bay (Cronin et al. 2003) and therefore that proxy may not be representative of the interannual variability of temperature over the entire ENA region. The WNA (JJA) temperature reconstruction has a number of samples within the range found for control simulations and observations but a majority of the samples show higher variability. This reconstruction was for maximum summer temperatures (Luckman and Wilson 2005) which may be causing a difference when comparing the variability to average summer temperature variability over the entire WNA region. This WNA region also contained a non-trivial amount of ocean within the regional average which may reduce the variability compared with a land-based reconstruction.

The interannual variability in proxy-based reconstructions of precipitation (Figure 6.8(b)) was generally larger in most cases except for the CNA (An) proxy data set which aligned with the control simulation 50% range (discussed further below). The proxy reconstruction for CGI (An) is located within the continental Canadian region (Figure 6.5) and therefore may have greater precipitation variability (e.g., more summertime convection) than the overall CGI regional average because of the large amount of water in the region. For WNA (An), both the northern (NW USA) and southern (SW USA) proxy reconstructions show similar variability in precipitation which was slightly larger than the controls simulations and observations. This could either indicate an underestimation of variability in the observational record and control

simulations or may just be due to the proxy data being representative of a smaller geographic region. For ENA (An), the reduced variability in the control simulations and observations may be due to size difference between the area represented by the reconstruction and the large ENA region.

Finally, the proxy reconstruction for CNA (An) aligns very well with the control simulation distribution (e.g., spans the 50% range). This is a landlocked region and relatively smaller in size compared to other regions and therefore would be less impacted by the presence of ocean water or a proxy reconstruction representing too small of an area compared to the larger CPDN region. The good alignment of the proxy reconstruction's interannual variability with the control simulations, which have slightly larger variability than the observed data sets, could indicate that the more recent observational period does not represent the full range of precipitation variability (e.g., underestimates variability). However, the reconstruction could just have larger variability due to a reduced area it actually represents, which would imply that the model is overestimating the variability. Either way, the control simulations contained a number of samples that extended to much higher variability which was not found in either the proxy reconstructions or observed data which indicates those simulations contained parameter variations leading to too large of interannual variability across CNA (also discussed in Section 5.5.1).

Temperature and precipitation decadal variability (Figure 6.9) contained similar features as those found in interannual variability (Figure 6.8) but this time proxy reconstructions aligned even better with control simulations because of the reduction of short-term variability in the decadal averages. With decadal variability in temperature

(Figure 6.9(a)) the proxy reconstruction ranges generally aligned with the full range of control simulations with most samples falling within the 95% range of the simulations. However the 50% range of the simulations tended to be on the lower end of most reconstructions probably due to the reconstructions being based on a smaller region. However it also could imply that the simulations are underestimating decadal variability. The proxy reconstruction for ENA (MAM) decadal variability was closer to the control simulations and observations than found in interannual variability (Figure 6.8) but with only three samples due to the shorter record length it is difficult to make any firm conclusions.

The decadal variability in precipitation generally was in better agreement with the control simulations than that found in interannual variability. CNA had a large number of simulations extending to larger variability, indicating its sensitivity to parameter variations but the other three regions all tended to have lower variability in their simulations, again, probably due to the reconstructions being based on a smaller region.

6.5 SUMMARY

A number of proxy-based paleoclimate reconstructions across NA were assessed to see whether the more recent observational period is representative of the full range of natural climate variability and if the HadCM3L control simulations reproduce this natural variability. While a number of similarities and differences were found, it is difficult to make any robust conclusions because of the many uncertainties involved

when using proxy-based data, particularly when comparing to the output from CPDN. Some of these uncertainties include the many factors, besides just climatic conditions, that affect tree ring and varved sediment growth, the sometimes combined impact of temperature and precipitation changes on the proxy, the true geographic area represented, and the reconstruction process itself which tends to reduce actual variability in the final reconstructed data set. Besides these uncertainties in the proxy data sets, another complicating factor is the large areal extent covered by the CPDN regions, which often contain ocean water (Figure 6.5). If the proxy reconstruction is representative of only a smaller regional area then it would be expected to have greater variability than that found in the larger CPDN region.

With all of these factors potentially impacting the variability estimates it was not possible to answer the question of whether the near-term observational record was over- or underestimating natural climate variability in temperature or precipitation with any certainty. What can be said is that many of the paleoclimate reconstructions had variability similar or slightly larger to that found in the control simulations and observations, especially in decadal variability. It may be possible to investigate this further and discern more robust results using the CMIP3 and CMIP5 gridded data sets or regionally downscaled gridded data sets over NA which would allow more flexibility in defining various geographic regions surrounding each proxy-based reconstruction to identify the impact variations in areal coverage has on the variability comparisons. Additionally, the CPDN globally gridded decadal average output could be evaluated at varying smaller regional scales across NA and compared to decadal variations in the paleoclimate reconstructions.

CHAPTER 7

TRANSIENT SIMULATION ANALYSIS

The goal of this chapter is to evaluate the performance of the HadCM3L transient simulations from the climate*prediction*.net (CPDN) British Broadcasting Corporation (BBC) Climate Change Experiment (CCE) over the observational time period. In addition these simulations are used to quantify uncertainties in future climate projections for the globe and North American (NA) regions and to constrain these projections based on a model's past performance. The transient simulations were forced using natural and anthropogenic historical forcings for the 1921-2000 time period and the SRES A1B scenario (Nakićenović and Swart 2000) for 2001-2080 future anthropogenic forcings along with a variety of natural forcing scenarios (see Chapter 3, Section 3.3.3 for full description).

Section 7.1 provides the quality control assessment of the transient ensemble and Section 7.2 describes the long-term drift removal procedure. Section 7.3 offers a comparison of the transient simulations to observational data sets while Section 7.4 assesses their past and future trends and Section 7.5 investigates relationships between these trends. Section 7.6 assesses future changes in the magnitude of the seasonal cycle and interannual variability. Section 7.7 evaluates the sensitivity of past and future trends to variations in model physics parameters, the results of which are used to constrain future climate projections, which is explored in Section 7.8 along with

projections constrained by model performance in the past. Finally Section 7.9 summarizes the key findings of this chapter.

7.1 Quality Control of Transient Simulation Ensemble

The initial transient simulation output acquired from CPDN was examined in the same manner as the control simulations (see Chapter 5, Section 5.1) to assure the quality of the simulations utilized. The NetCDF files were checked for errors and then temperature and precipitation output searched for errors, outliers, and duplicates as discussed below.

7.1.1 NetCDF File Errors

A total of 4,018 initial transient simulations were downloaded from the CPDN servers, 12 of which were immediately discarded due to NetCDF file generation errors in the CPDN archiving process. Of the remaining 4,006 simulations, 218 were missing at least one monthly output value within one of their annual NetCDF files and 187 of these were discarded. The other 31 simulations were left in the official ensemble because they were missing a monthly value within the first 20 years of the simulation, a period not used in analyses because the model's atmosphere and ocean are still in an initial adjustment period of the coupling process (see Chapter 5, Section 5.2).

Within the remaining 3,819 simulations containing output over the full time period of interest, an additional two simulations were identified with non-meteorological values (e.g., NaN, Inf, zero) but only one was removed because the

other had its error in the first 20 years. Therefore 3,818 transient simulations were identified as having a complete set of available model output.

7.1.2 Erroneous Outliers

Figure 7.1 displays the absolute temperature and precipitation over the globe and NA regions for all available transient simulations. A number of obvious outliers can be seen within the ensemble. The large "spikes" correspond with one or two year periods of anomalous output, most likely caused by a variable being saved incorrectly as another variable. And the sudden decreases followed by a slow return to its previous state correspond with the erroneous "sudden jumps" discussed in Stainforth et al. (2005) that also were found in the initial control simulations (Chapter 5, Section 5.1.2). As was done with the control simulations, an anomaly test was conducted to systematically identify these outliers from monthly and annual anomaly values as well as month-to-month and year-to-year anomaly differences within each simulation. The resulting anomalies were again standardized with respect to the full distribution of anomaly values across all simulations and then sorted to identify simulations with the largest outliers.

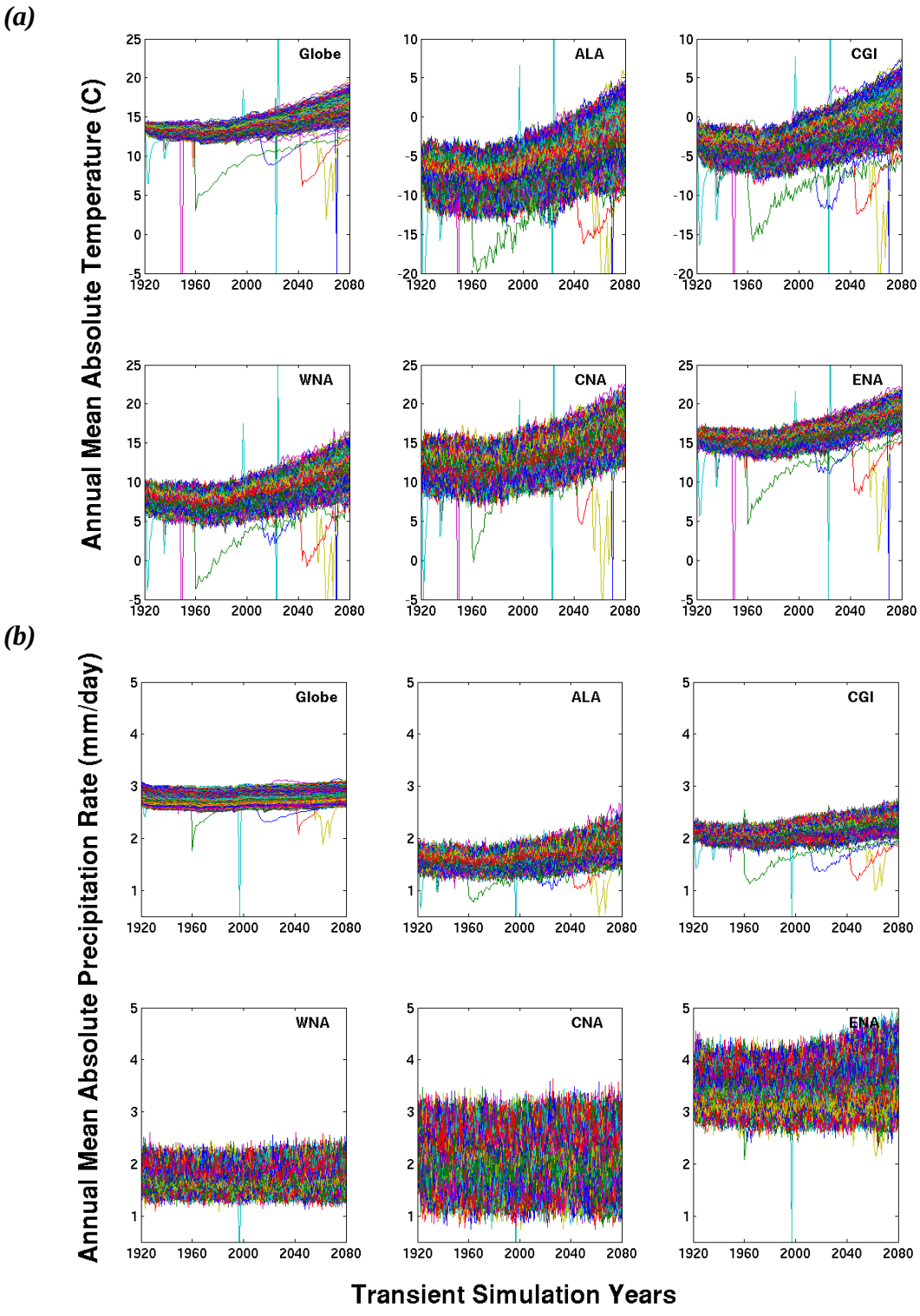


Figure 7.1: Initial ensemble of all transient simulations acquired from CPDN for annual mean *(a)* temperature (°C) and *(b)* precipitation rate (mm/day) for the globe and five NA regions. Each plot shows time series for 3,818 individual simulations. Temperature y-axis values are different across regions but all maintain a 30°C range. Precipitation y-axis values are the same.

Each anomaly test again identified a similar but not always consistent set of simulations containing the largest anomalies for a given variable and region and therefore the highest standard deviation anomalies were assessed individually to determine if they were caused by an error within the model or were simply larger fluctuations in the modeled climate. A total of 18 simulations were determined to contain non-climatic outliers. One metric that accurately distinguished 11 of those outliers was global mean annual average temperature anomalies greater than six standard deviations, which was the same metric used to identify control simulation outliers.[18] An additional six outliers were identified with global mean year-to-year anomaly differences greater than six standard deviations and three other outliers were found with more gradual transitions deemed anomalous.

7.1.3 Duplicates

After the 18 erroneous outlier simulations were removed, the remaining 3,800 transient simulations were searched for duplicates in their parameters. There were combinations of 153 atmospheres, ten oceans, ten initial conditions (DTHETA), five values for scaling anthropogenic sulfates (ANTHSCA), 15 solar forcing scenarios, and 50 volcanic forcing scenarios. Six simulations were found having a corresponding simulation with matching parameters, natural forcings and initial conditions. Of these six matching pairs only two had identical output, which were immediately removed

[18] As with the control simulations, a six standard deviation anomaly can be expected as an appropriate threshold for identifying outliers in such a large sample size. For the annual average and annual difference anomaly tests, the number of samples expected to be outside the range of standard deviations of 1, 2, 3, 4, 5 under a normal distribution for 610,880 samples (e.g., 3,818 simulations x 160 years) is 195,481 (32%), 28,100 (4.6%), 1,649 (0.27%), 38 (0.0063%) and 0.3 (0.000057%) samples respectively.

from the ensemble. The other four pairs had similar, but not identical, output and were kept in the ensemble as were three other simulation pairs having an initial time period of identical output. These two features also were found in the control simulations and reasoning for their retention is described in that section (e.g., possible initial condition restart issues; see Chapter 5, Section 5.1.3).

7.2 Long-Term Mean Drift Removal

Because of the method used to couple the atmosphere and ocean models together (see Chapter 3, Section 3.3.2), the transient simulations may contain a component of unforced long-term mean drift, as discovered in the control simulations (see Chapter 5, Sections 5.2.2 and 5.7.3). In order to investigate only the forced trends in transient simulations, the unforced model drift had to first be removed. This was accomplished by calculating the long-term mean drift (years 21-160) for a transient's matching control simulation (i.e., having the same atmosphere and ocean parameters) and then subtracting that drift off of the transient time period of 1941-2080, as the two should have the same background unforced model drift. The first 20 years of the simulations were not used because it corresponded with the period of adjustment for coupling the atmosphere and ocean models together as found in the control analysis (Chapter 5, Section 5.2.1). We do not attempt to match initial conditions on account of the possible issues already described in Chapter 5 (Section 5.1.3) and because it would vastly decrease the number of matched pairs available. Furthermore, initial condition variations have minimal impacts on long-term mean trends.

Figure 7.2 provides an example of the long-term mean drift being removed from a simulation's annual mean global temperature. The long-term mean trend in the original control simulation was calculated and then removed from the same control simulation to show the amount of drift to be removed (Figure 7.2(a)). The original (detrended) control simulation is shown in black (red). This same long-term mean trend was then removed from the original corresponding transient simulation having the same atmosphere and ocean parameters (black line in Figure 7.2(b)). The resulting transient with its unforced long-term mean drift removed is shown in red. Since the original unforced control simulation had a negative long-term mean trend, when it was removed from the transient simulation the resulting transient-minus-control (transient-control) simulation had a greater increase in temperature with time than the original transient (i.e., the transient-control simulation has a greater long-term mean trend). The impact of removing the unforced drift was different for each transient/control pair and depended on the magnitude and sign of the control drift. (See Chapter 5, Section 5.2.2 for the range of control long-term mean drift found.)

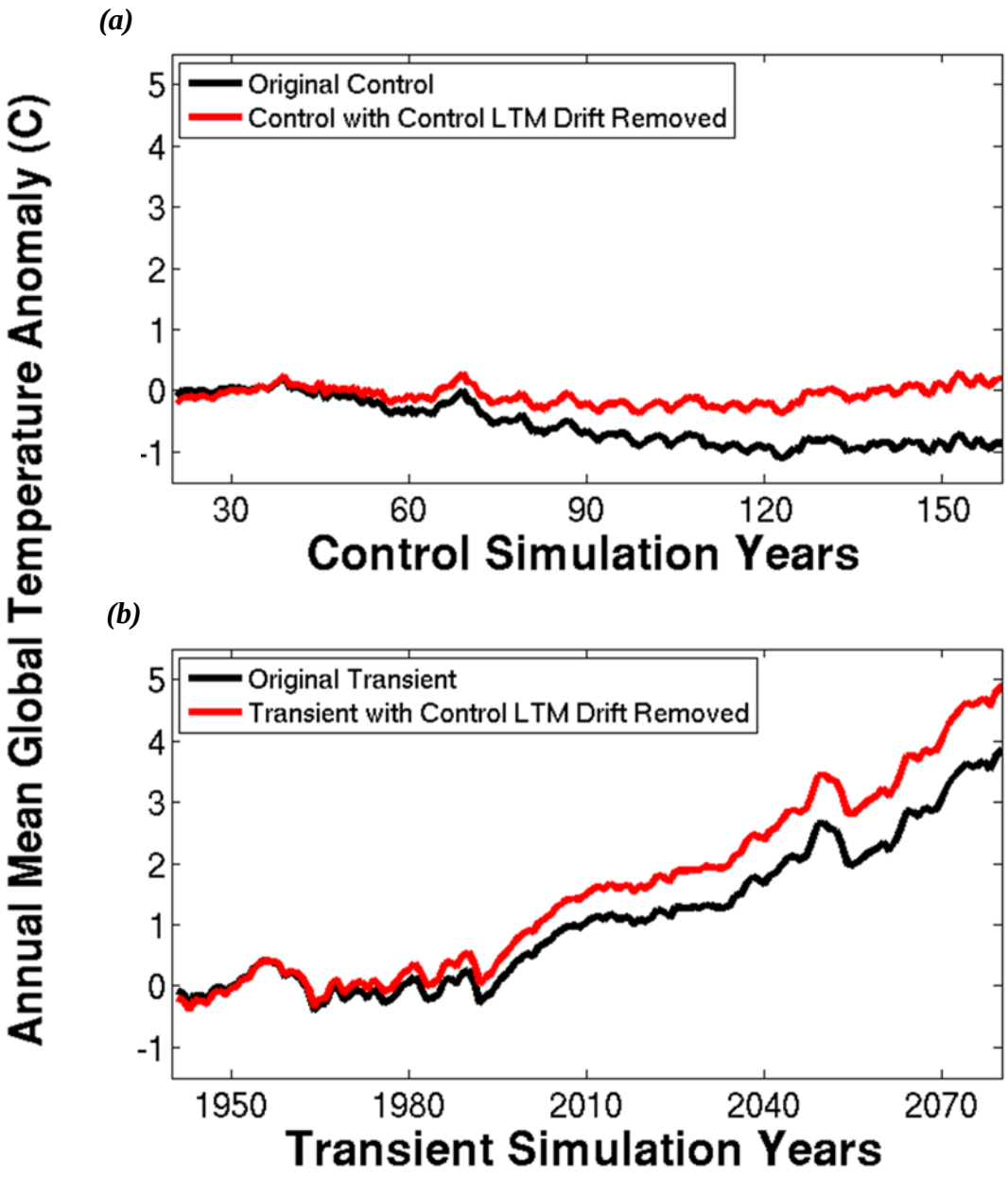


Figure 7.2: Long-term mean drift removal example in annual mean global temperature anomaly output for *(a)* control and *(b)* transient simulations having matching atmosphere and ocean parameter values. Original simulations are given in black and those with the control simulation's long-term mean trend from years 21-160 removed in red. Anomalies are relative to a 1941-1970 base period.

Unfortunately, a number of transient simulations did not have an available matching control simulation because they were either removed during the quality control assessment (Chapter 5: Section 5.1) or primarily because a large initial set of CPDN simulations needed to be discarded due to the fact they were generated with an error in the model code, resulting in unrealistic climates (Myles Allen and Dan Rowlands, 2010, Personal Communication). Of the 3,798 transient simulations, a total of 1,692 were found to have at least one control with matching atmosphere and ocean parameter settings from the 1,214 available control simulations. For this study, only these transients with matching controls are investigated because without a direct control match there is no way to identify the unforced background drift within a transient simulation. Using a transient that includes unforced drift would introduce an unquantifiable error in any assessment of the modeled climate that may or may not have a significant impact on the final results.

In Appendix A a potential alternative for estimating a control match for the other 2,106 unmatched transients is explored, a technique not requiring matching of all atmosphere and ocean parameters. This alternative matching procedure is only briefly discussed there and further investigation as to its usefulness is left as possible future work. The main conclusion from the discussion in Appendix A is that any alternative matching procedure increases the uncertainty in the unforced drift to be removed from each transient simulation and therefore increases uncertainty in any analysis performed on those transients. Fortunately, even when the 2,106 unmatched transients are removed from our analysis, all parameter values are still represented (see Table 7.1) and the relative proportion of simulations for any given value of a parameter is generally the

same as that found in the full original set of transient simulations (refer to Appendix A, Table A.1) meaning the original span of parameter variations is maintained.

Table 7.1: CPDN perturbed parameters and the number of transient simulations having each particular parameter value for the 1,692 transient simulations. Parameters are separated into their respective atmosphere, ocean, or initial condition groups. Default parameter values are highlighted in bold.

Parameter	Description	Values	Transient Simulations
ATMOSPHERE			
ALPHAM	Albedo at melting point of ice	**0.5**	**337**
		0.57	615
		0.65	740
ANTHSCA	Scaling factor for anthropogenic sulfates	0.5	354
		0.8	359
		1.0	**354**
		1.2	315
		1.5	310
CLOUDTAU	Time a circulating air parcel remains in cloud (s) [x 10^3]	3.6	404
		10.8	**785**
		32.4	503
CT	Accretion constant (s^{-1}) [x 10^{-4}]	0.5	505
		1	**540**
		4	647
CW_LAND [a]	Precipitation threshold over land (kg m^{-3}) [x 10^{-4}]	1	660
		2	**536**
		20	496
CW_SEA [a]	Precipitation threshold over sea (kg m^{-3}) [x 10^{-5}]	2	660
		5	**536**
		50	496
DTICE	Temperature range of ice albedo variation	2	740
		5	615
		10	**337**
EACF	Empirically adjusted cloud fraction [**]	**0.5**	**689**
		0.63	398
		0.67	605
ENTCOEF	Entrainment coefficient	0.6	513
		1.0	553
		3.0	**526**
		9.0	100

a, **b**, **c**, **d** Individual groups of parameters perturbed together

** Parameter values represent mean over 19 model levels (variations occur at each level)

Table 7.1: Continued

Parameter	Description	Values	Transient Simulations
I_CNV_ICE_LW [b]	Type of convective cloud ice crystal used in longwave radiation	**1**	**1459**
		7	233
I_CNV_ICE_SW [b]	Type of convective cloud ice crystal used in shortwave radiation	**3**	**1459**
		7	233
I_ST_ICE_LW [b]	Type of stratiform cloud ice crystal used in longwave radiation	**1**	**1459**
		7	233
I_ST_ICE_SW [b]	Type of stratiform cloud ice crystal used in shortwave radiation	**2**	**1459**
		7	233
ICE_SIZE	Ice crystal size (m) [x 10^{-4}]	2.5	543
		3.0	**660**
		4.0	489
L0 [c]	Sulfate mass scavenging parameter L0 (s^{-1}) [x 10^{-5}]	2.17	383
		6.5	**638**
		19.5	671
L1 [c]	Sulfate mass scavenging parameter L1 (s^{-1}) [x 10^{-5}]	0.99	383
		2.96	**638**
		8.86	671
NUM_STAR	Condensation threshold for accumulation [x 10^{6}]	0.1	593
		1.0	**789**
		10	310
RHCRIT	Critical relative humidity [**]	0.65	690
		0.73	**504**
		0.9	498
SO2_HIGH_LEVEL	Sulfur cycle: model level for SO2 (high level) emissions	1	251
		3	**1066**
		5	375
VF1	Ice fall speed (m s^{-2})	0.5	398
		1.0	**662**
		2.0	632
VOLSCA	Sulfur cycle: scaling factor for emission from natural (volcanic) emissions	1	939
		2	**486**
		3	267

a, **b**, **c**, **d** Individual groups of parameters perturbed together

** Parameter values represent mean over 19 model levels (variations occur at each level)

Table 7.1: Continued

Parameter	Description	Values	Transient Simulations
OCEAN			
HANEY	Haney heat forcing coefficient ($Wm^{-2}K^{-1}$)	**81.88**	**1499**
		163.76	193
HANEYSFACT	Haney salinity forcing factor	**0.25**	**1209**
		1.0	483
ISOPYC	Isopycnal diffusion of tracers (m^2s^{-1}) [x 10^3]	0.2	159
		1	**1214**
		2	319
MLLAM	Wind mixing energy scaling factor (m^2 s)	0.3	352
		0.7	**1340**
VDIFFDEPTH [d]	Ocean: increase of background vertical mixing of tracer with depth (ms^{-1}) [x 10^{-8}]	0.7	394
		2.8	**839**
		9.6	459
VDIFFSURF [d]	Ocean: background vertical mixing of tracer (diffusion) at surface (m^2s^{-1}) [x 10^{-5}]	0.5	394
		1	**839**
		2	459
VERTVISC	Ocean: background vertical mixing of momentum (viscocity) (m^2s^{-1}) [x10^{-5}]	0.5	369
		1.0	**1323**
INITIAL CONDITIONS			
DTHETA	Initial condition potential temperature perturbation applied to atmosphere (°C)	**0**	**195**
		0.01	163
		0.02	154
		0.03	178
		0.04	161
		0.05	176
		0.06	163
		0.07	153
		0.08	173
		0.09	176

a, **b**, **c**, **d** Individual groups of parameters perturbed together

****** Parameter values represent mean over 19 model levels (variations occur at each level)

The remainder of this section highlights the drift removal results for the 1,692 transient-control simulations generated using transients and controls with matching atmosphere and ocean parameters (from here on simply referred to as transient simulations or transients with the understanding that they actually are transients with their unforced long-term mean drift removed). These matches were comprised of 137 atmospheres and ten oceans with 614 unique atmosphere/ocean combinations. The remaining 1,078 simulations contained the same atmosphere/ocean combination as one of the unique 614 combinations but had variations to either their anthropogenic sulfate scaling factor (ANTHSCA), natural forcings (solar or volcanic), or initial conditions (DTHETA). Table 7.1 provides a summary of the number of transient simulations having each specific parameter value.

When identifying a transient simulation's control match, there often were multiple control simulations comprised of the same atmosphere and ocean parameters (i.e., multiple control simulation matches for a single transient simulation). These control matches were not exact duplicates of one another, but rather were generated using different initial conditions and therefore had slightly different simulated climates. In these instances, the long-term mean drift of all controls matching a single transient simulation were averaged together and used as the official drift removed from the corresponding transient.

Figure 7.3 shows example transient simulations before and after their corresponding control drift was removed. Each regional example corresponds with the largest control drift that was removed in that specific region/variable for all transients (i.e., the output shown for any given region/variable typically did not come from the

same transient simulation). As was seen in Figure 7.2, each temperature example in Figure 7.3(a) contains transient-control simulations with a larger trend than the original transients because of the removal of a negative control trend. The change in temperature after removing the long-term mean drift can be up to 2-3°C which substantiates the necessity of removing the drift prior to any analysis.

It is evident that the drift removal process had a limited impact on long-term changes in precipitation (Figure 7.3(b)), which can be attributed to the many factors affecting the formation of precipitation. Of all the regions, the two northernmost regions (ALA, CGI) appear to be most impacted which makes sense given that precipitation in those colder regions can be more sensitive to long-term changes in temperature which can affect the amount of moisture available in the regions. Note that precipitation for ALA and CGI originate from different simulations than those shown for the same regions in Figure 7.3(a). The actual corresponding temperature drift removed from ALA (CGI) was negative (positive), meaning the resulting transient minus control simulation was warmer (cooler) than the original which corresponds with a wetter (drier) simulation, as would be expected. One might anticipate a similar effect for greater drying across WNA and CNA with warmer temperatures but the drift removal had negligible impacts, especially with the larger variability seen across those regions.

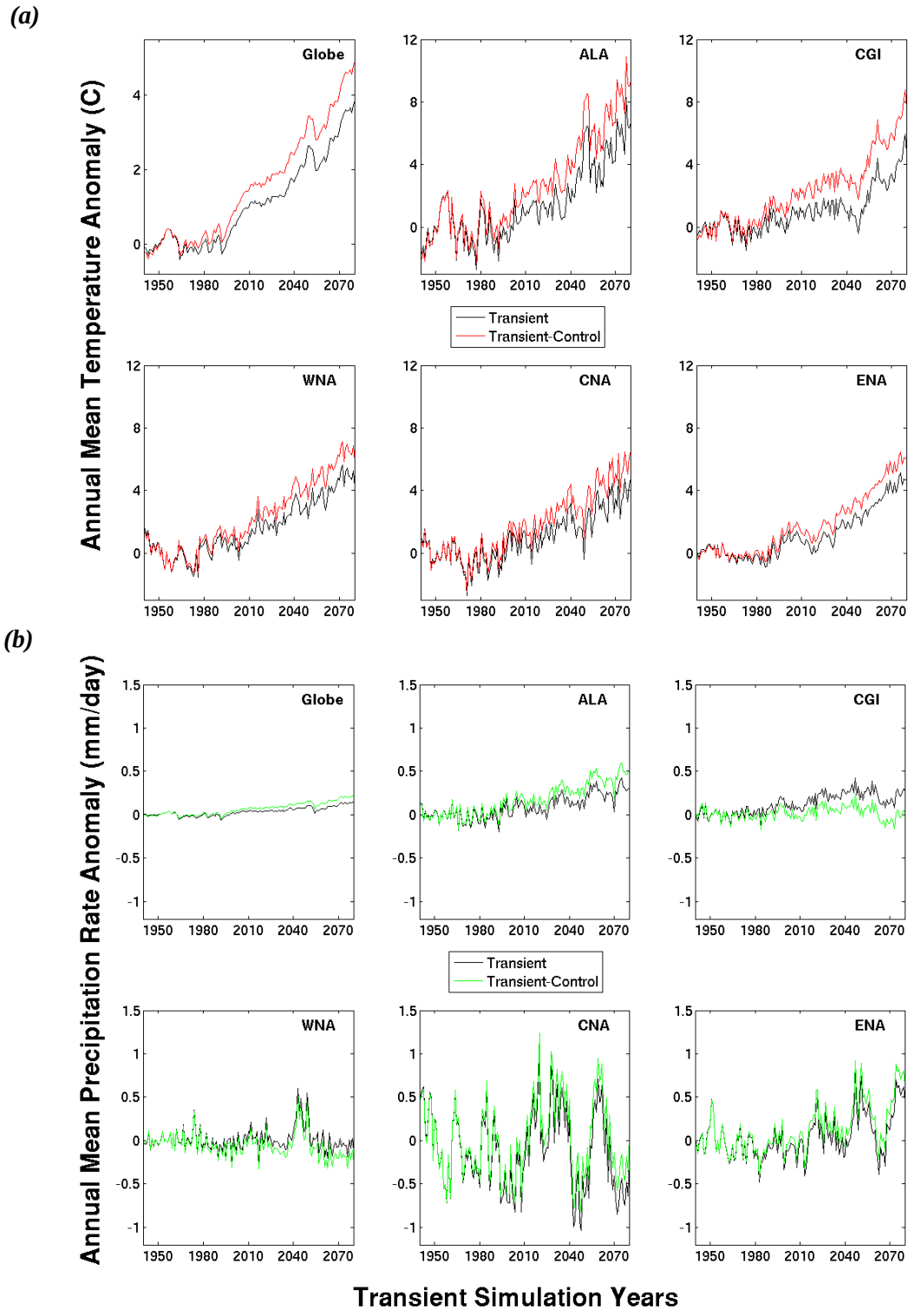


Figure 7.3: Transient (black) and Transient-Control (red, green) comparisons for those transients having the largest control drift removed for annual mean anomaly of *(a)* temperature (°C) and *(b)* precipitation rate (mm/day) for the globe and five NA regions from 1941-2080. Anomalies are relative to a 1941-1970 base period.

7.3 TRANSIENT SIMULATIONS VS. OBSERVATIONS

7.3.1 Transient Observational Period Ensemble

This section provides a comparison between the transient simulations and available observational data sets described in Chapter 4. Figure 7.4 shows the comparison between the transient simulation ensemble and observations for annual mean (December to November) global temperature anomalies covering the 1941-2010 observational time period. A mean base period of 1941-1970 was used instead of the more common 1961-1990 or other more recent 30 year periods in order to limit the impact of the three major volcanic eruptions across the 20th century (1963, 1982, 1991). This was because the perturbed physics ensemble can have a number of parameter value arrangements causing too large (small) of a response to the eruptions, most prominently in temperature at the global scale, which would make the 30-year mean base period too cool (warm), thus making the corresponding anomalies too warm (cool). The 1963 Agung eruption is still in this base period but by not including the other two eruptions, the overall volcanic impact is minimized. (The impact of a volcanic eruption on global climate is discussed further in the discussion below.) A person's choice of base period, however, does not impact the trends analysis, which is the focus of this chapter. It is more important when performing a direct comparison of model output to observed data at specific points in time (e.g., RMS error analysis).

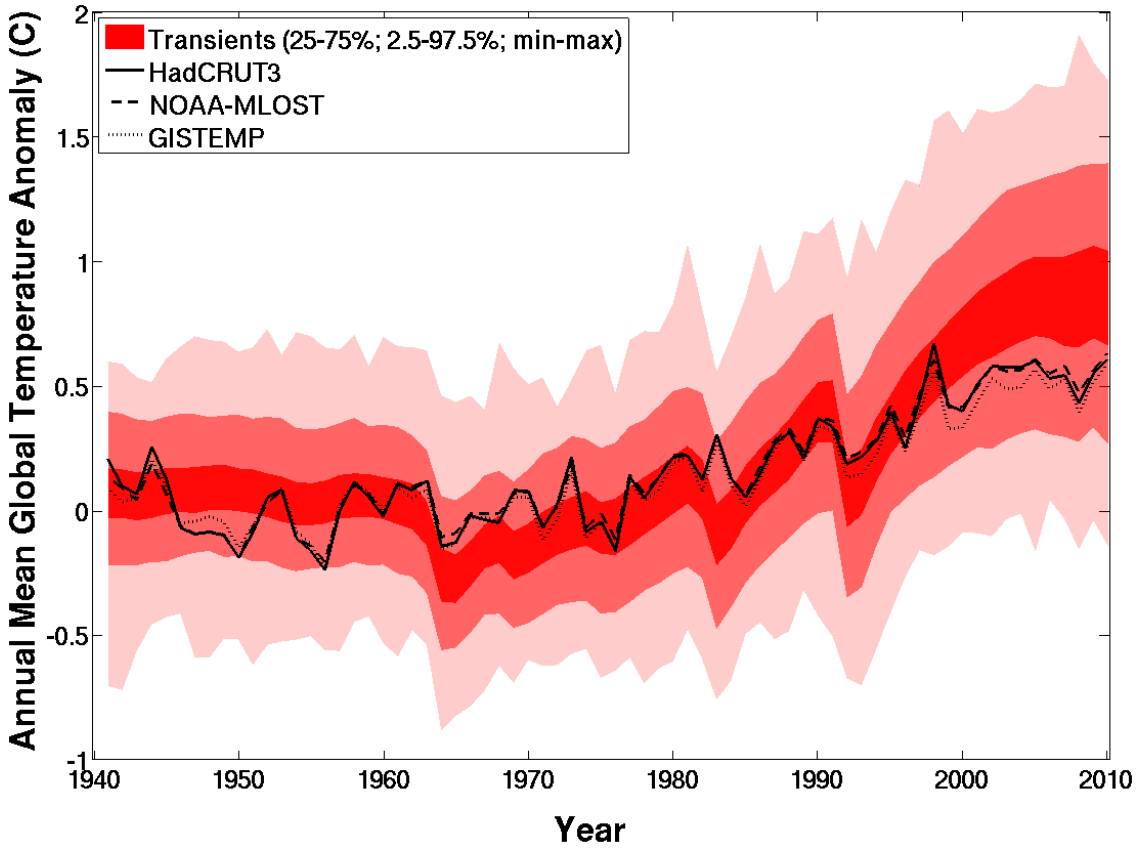


Figure 7.4: Annual mean global temperature anomaly for the 1,692 transient simulations (red shading) and three observational data sets (HadCRUT3, NOAA-MLOST, GISTEMP) over the 1941-2010 observational time period. The transient ensemble is shaded according to the 25-75%, 2.5-97.5%, and min-max ranges. Anomaly values are relative to a 1941-1970 base period.

The transient ensemble is plotted in density weighted terms, showing the 25-75% (defined as the 50% range), 2.5-97.5% (defined as the 95% range), and min-max range of all simulations in a given year. Therefore the 50% range (or in actuality the center of the 50% range) should not be interpreted as representing the actual evolution of a single simulation but rather the location of highest concentration of simulations for that year (i.e., a smoothed version not representing interannual variability). Temperature observations are from HadCRUT3, NOAA-MLOST, and GISTEMP (see Chapter 4). Even though the observations continue through 2010, recall that transient

simulation used observed natural and anthropogenic forcings to drive the simulations only up to the year 2000 and then use the SRES A1B scenario forcings starting in 2001 (Nakićenović and Swart 2000). Therefore, any observed variations in forcings from 2001-2010 were not included in the model.

The observations generally fall near the 50% range and within the 95% range of the transient ensemble. There are however three noteworthy features to discuss. The first is that the minimum to maximum spread in the transient simulation distribution is quite large, even in the 1941-1970 base period where the 30-year mean global temperature anomaly averages to zero. This can be attributed to some of the simulations having larger interannual variability, which was indeed identified within some of the control simulations in Chapter 5 (see Figure 5.16(a) in Section 5.5). This is only true for a limited number of simulations, however, as it can be seen that the interannual variability in the observational data sets over the base period appear to cover nearly the same relative spread as the 95% range.

The second feature in Figure 7.4 is the pronounced drop in temperature near the three major volcanic eruptions (Agung in 1963, El Chichon in 1982, and Pinatubo in 1991). These types of large explosive volcanic eruptions release sulfur dioxide (SO_2) into the stratosphere which is converted to sulfuric acid (H_2SO_4) and subsequently condenses to form sulfate aerosols. The stratospheric sulfate aerosols increase the reflection of solar radiation back into space (i.e., increases Earth's albedo) which in turn decreases the amount of radiation entering the troposphere, thus cooling tropospheric and surface temperatures. This effect can typically be observed at the global level and

generally lasts one to three years after which time the aerosols fall out of the stratosphere and temperatures return to their prior states.

Compared to observations, the models on average appear to have a larger drop in temperature associated with each volcanic eruption.[19] This can be caused either by the model having too large of a sensitivity to increases in sulfate aerosols in their stratospheres or by an incorrect amount of aerosols being present (i.e., incorrect volcanic radiative forcing applied). Recall that five different volcanic forcing scenarios from different data sets were used for the observational time period across the ensemble (see Chapter 3, Figure 3.3). The timing of these eruptions was the same in all five cases but the magnitude of the corresponding radiative forcing varied and therefore some of the simulations may have too large of forcing applied. The larger range of volcanic responses caused by either increased model sensitivity or variations in volcanic radiative forcing justifies our decision to use a base period of 1941-1970 to limit the impact of these modeled eruptions.

The third interesting feature in Figure 7.4 is the relatively warm simulations compared to observations near the end of the observational period starting around 2000. We cannot draw too much of a conclusion based solely on this shorter, roughly 10-year period because short-term natural variability may be at work (see below). Additionally, the observations still lie within the 95% range of the simulations. However, it may also indicate that some of the transient simulations have higher climate sensitivities and therefore have too large of warming during that period. This possibility will be

[19] It should be noted that the drop in temperature associated with the 1982 El Chichon eruption in Figure 7.4 appears to be aligned with an increase in observational temperature. This is because a large El Niño event occurred in the same year which is the likely cause for the global temperature increase

explored more throughout the rest of this chapter and considered in Section 7.8 when we utilize the performance of the models over the observational time period to constrain future climate projections.

In terms of a relative slowdown in warming from 2000-2010 caused by natural climate variability, Balmaseda et al. (2013) contend that increased oceanic absorption of heat from a fluctuation in the Pacific Decadal Oscillation (PDO) is the primary culprit. The PDO oscillates between a positive, warm, phase and negative, cool, phase approximately every 20-30 years reflecting the pattern of anomalies in sea surface temperature and surface air pressure between the north central and northeastern Pacific Ocean. The PDO index pattern can roughly be seen as a superimposed cycle within the long-term mean warming trend over the past century with cool phase development during the most recent time period (see Figure 7.5). Balmaseda et al. (2013) argue that during the PDO cool phase the prevailing winds shift causing increased mixing of the warm Pacific surface waters to deeper depths which in turn allow the surface waters to absorb more heat from the atmosphere that would have otherwise been available for warming the atmosphere and surface temperatures. Conversely, in times when the PDO is in a warm phase, the wind pattern is such that it reduces mixing to deeper waters, leaving the surface waters warmer and less apt to absorb as much atmospheric heat, allowing global temperatures to continue rising. They found that the PDO and corresponding wind patterns began to shift towards the cool phase around the year 2000 which coincided with a significant rise in deeper ocean temperatures. Therefore the decreased warming trend over the past decade could be attributed to an increase in absorption of heat by the Pacific Ocean. They also point out that when the PDO shifts

back to a warm phase, there is the potential for a substantial increase in warming across the globe due to the fact that the Pacific Ocean will no longer be absorbing as much heat from the atmosphere.

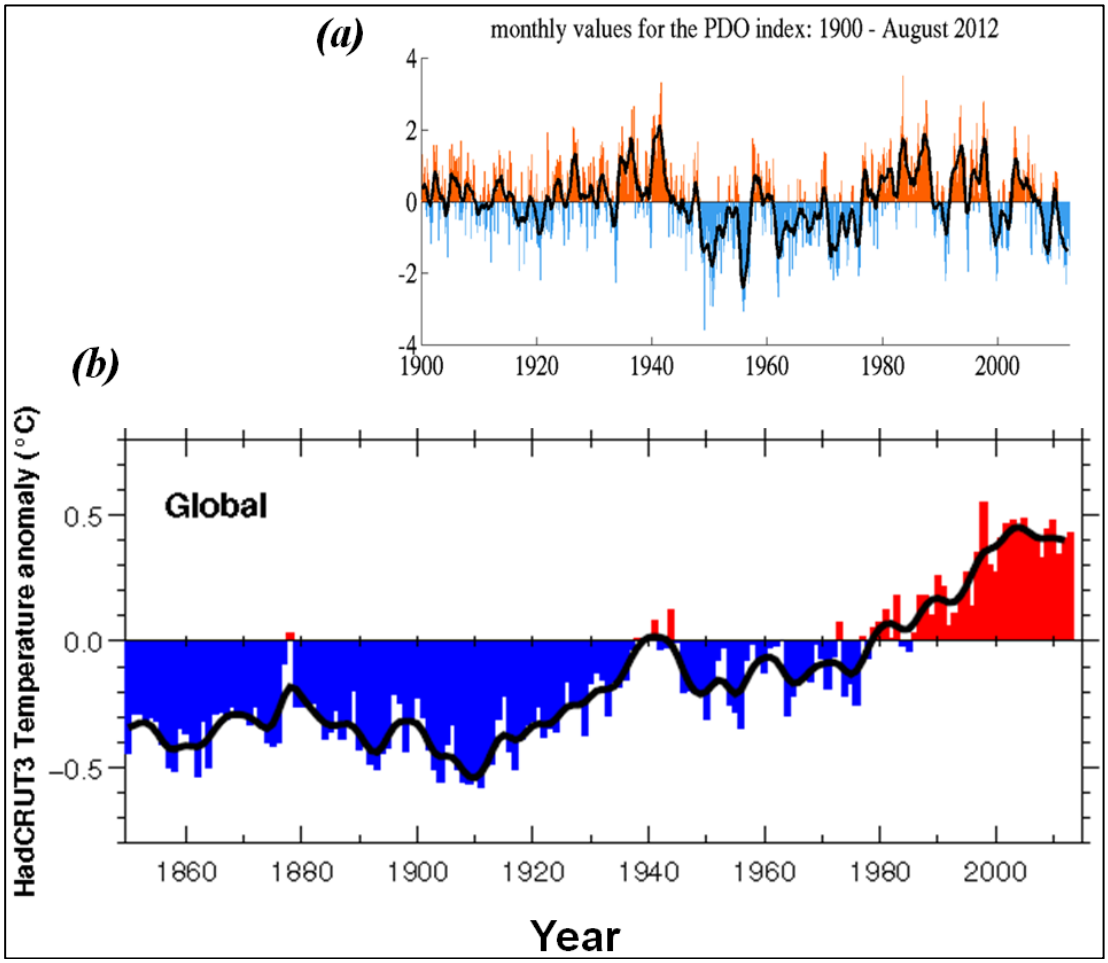


Figure 7.5: Comparison of (*a*) monthly values of the Pacific Decadal Oscillation (PDO) index and (*b*) the HadCRUT3 temperature anomaly (1961-1990 base period). The 1990-2012 time periods are aligned to allow for comparison. (HadCRUT3 from Met Office Hadley Center, based on Brohan et al. (2006); PDO from the Joint Institute for the Study of the Atmosphere and Ocean, University of Washington, based on Zhang et al. (1997) and Mantua et al. (1997)).

Figure 7.6 shows the same information as Figure 7.4 but includes the NA regions as well as precipitation comparisons to observations[20]. The regional temperatures (Figure 7.6(a)) generally compare well with observations, remaining close to the 50% range and typically within the 95% range. Similar to that found in global temperatures, there are some simulations with larger interannual variability causing a wider min-max distribution range. But again, the interannual variability of the observations roughly span close to the 95% range. The regional precipitation output generally aligns with observations except for CGI at the very end of the time period (specifically the GPCP data). This appears to be unique to this region only and is likely tied to insufficient observational coverage in this region that includes high latitude ocean grid cells. Also global precipitation is a very difficult quantity to estimate from observations given the very small percentage of the globe containing observing stations and therefore we will not focus on any comparisons of the model to these observations.

[20] Note that temperature anomalies are set relative to a 1941-1970 base period but the NARR data set only contains data from 1981-2010. In order to properly compare these different anomalies the NARR 1981-2010 base period was adjusted using the following formula to properly align it with the other data set anomalies having a 1941-1970 base period: NARR(1941-1970) = Obs(1981-2010) - Obs(1941-1970) + NARR(1981-2010) where Obs is the average 30-year mean value of all observational data sets over the specified period.

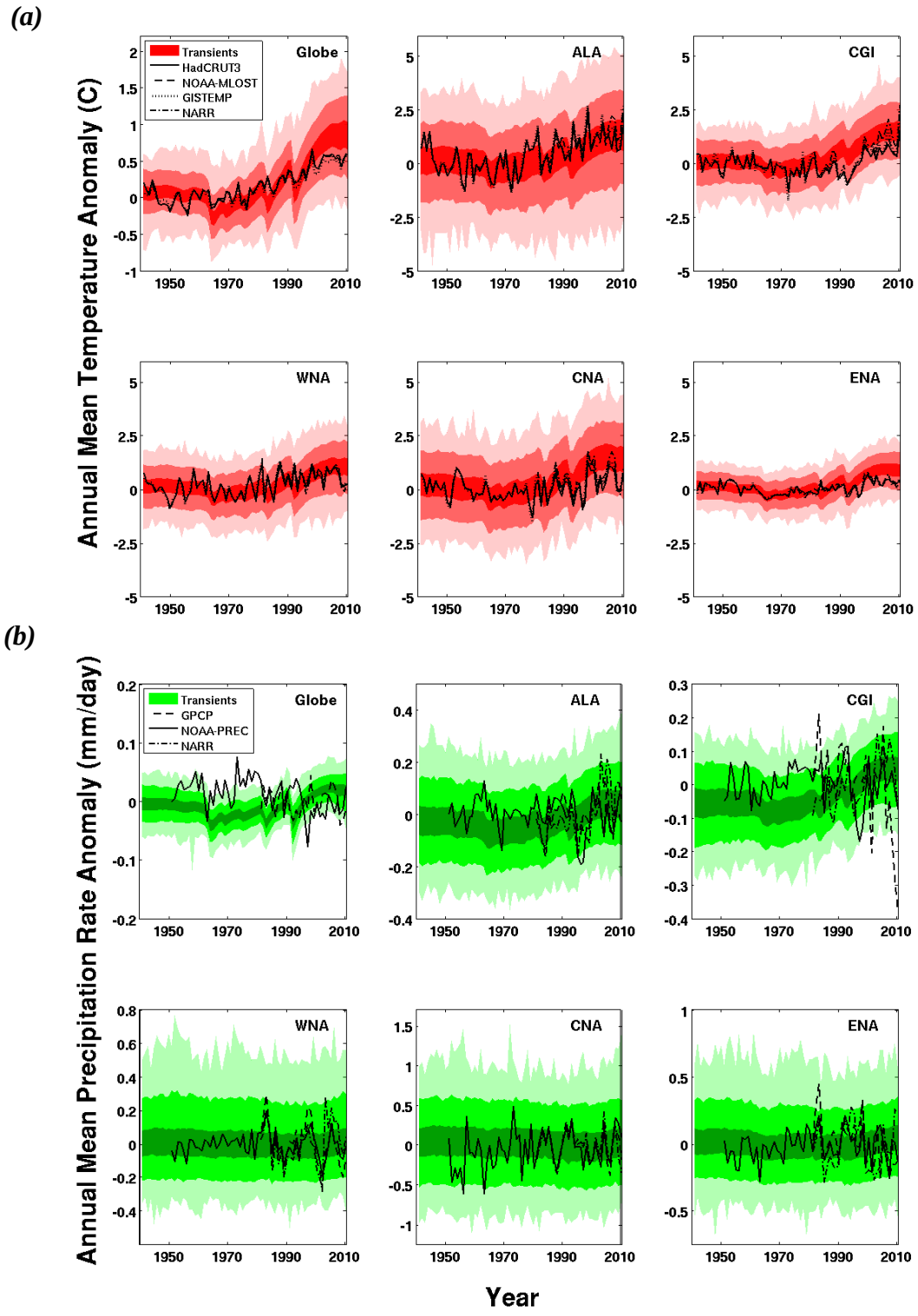
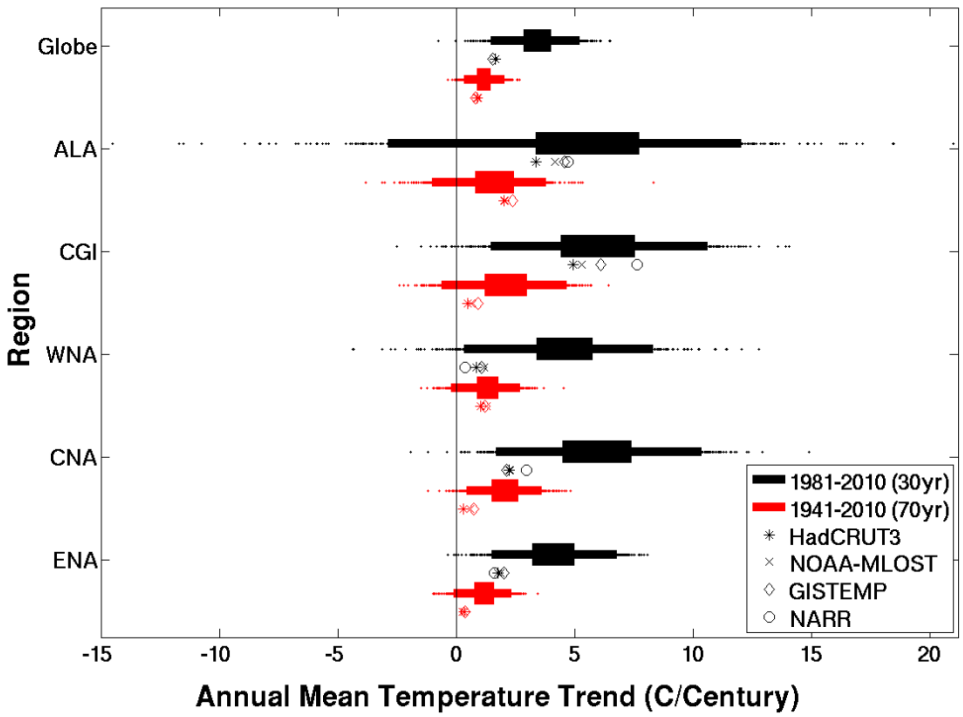


Figure 7.6: Same as Figure 7.4 but including regional comparisons for annual mean anomalies of *(a)* temperature(C) and *(b)* precipitation rate (mm/day). NARR data are included because it is available at the regional level and the precipitation data sets also include GPCP and NOAA-PREC. Temperature anomalies are relative to a 1941-1970 base period and precipitation anomalies are relative to 1981-2010.

7.3.2 Transient Observational Period Trends

Temperature and precipitation 30- and 70-year trends were calculated over the observational time period for all transient simulations. Figure 7.7 provides the resulting trend distributions along with observed trends for comparison. For temperature trends (Figure 7.7(a)), the majority of simulations show positive trends across all regions, as is seen in the observations. Trends over the most recent 30 years are larger than over the 70-year period, which is expected given the increase in warming over the latter half of the 20th century. Transient global 70-year temperature trends are close but slightly larger than observed trends while the 30-year trends are nearly all larger than observations. This general result can be seen in most NA regions as well. The partial slowdown of observed warming over the 2000's discussed in the previous section may be the root cause of this difference in the shorter-term trend. Importantly, with the distributions of both of these trends not centered on the observations, it may be possible to constrain future projections based on those simulations that line up best with observed trends (see Section 7.8).

(a)



(b)

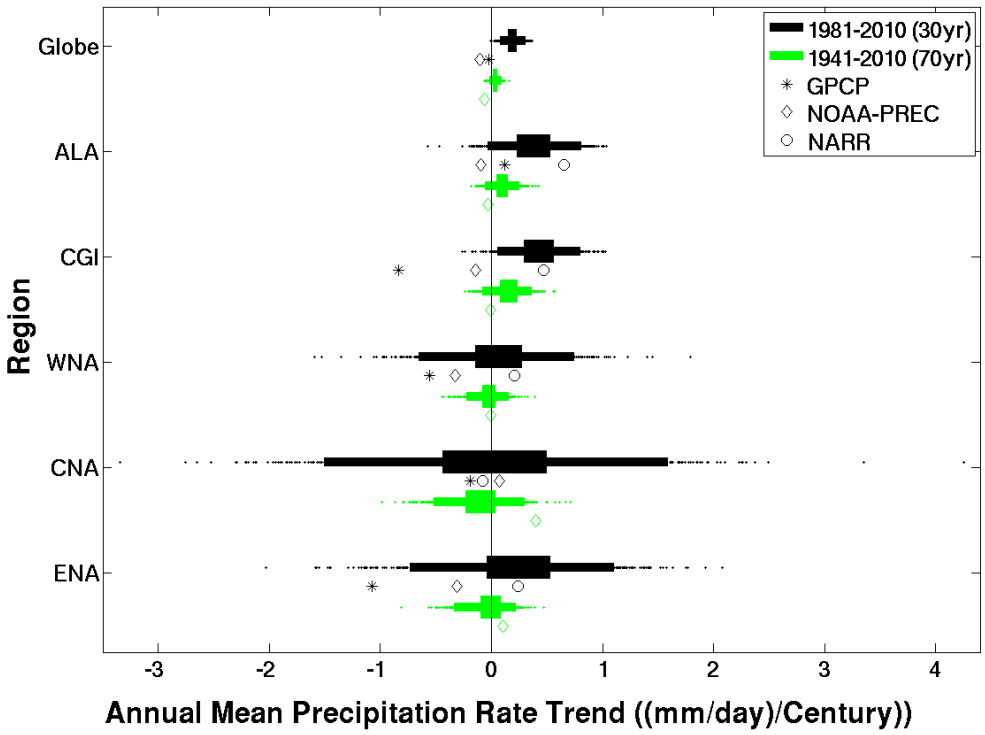


Figure 7.7: Annual mean (*a*) temperature (C/Century) and (*b*) precipitation rate ((mm/day)/Century) trends for observational periods 1941-2010 (colored) and 1981-2010 (black). Observed trends are plotted using same color scheme.

Figure 7.7(a) also shows that there were a few transient simulations with slightly negative global temperature trends in the observational period. These appeared to be caused by those simulations being overly sensitive to volcanic and anthropogenic aerosol forcings (i.e., cooling effect). Each of their trends became positive in the future after greenhouse gas forcings eventually overtook them (not shown).

Precipitation trends in Figure 7.7(b) show much less of a signal compared to temperature with most trends centered near zero for both the transient simulations and observations. The two northern regions (ALA, CGI) show a slight positive trend in the both the 30- and 70-year transient simulation trends which are not apparent in the observations. As discussed previously there could be errors in the observational estimates due to lack of sufficient observations in those regions. Whether the greater amount of simulated precipitation is realistic or not, the probable cause is an increase in moisture availability with modeled simulated warming.

One final note on Figure 7.7 is that the distributions for 30-year trends in ALA temperature and CNA precipitation are noticeably larger than the other distributions. This may be related to the larger range of interannual variability found in the same regions/variables in the control simulations (see Chapter 5, Figure 5.16) which implies they have greater sensitivity to variations in model parameters or possibly just larger natural variability.

7.4 TRANSIENT (PAST AND FUTURE) AND CONTROL TRENDS

In this section the full period of each transient simulation is assessed (1941-2080) and past and future trends compared to one another and to long-term mean trends found in control simulations. Figure 7.8 shows the same transient simulation ensemble of global mean temperature anomalies as in Figure 7.4 but extends the ensemble out to the year 2080. We see that the uncertainty range (or spread) in the ensemble increases with time into the future which emphasizes the variation in climate sensitivities of the various model parameter value combinations, further enhanced as atmospheric greenhouse gas concentrations continue increasing in the future. The majority of simulations show greater warming from 2011-2080 than was simulated from 1941-2010, the cause of which is linked to continued increases in anthropogenic greenhouse gases and the relatively reduced role of anthropogenic aerosols.

An interesting feature to point out is the drop in transient temperatures around 2015. As Figure 3.3 from Chapter 3 shows, this is a time when an arbitrary volcanic eruption was initiated in some of the models. Whether a volcanic eruption actually occurs near that time period is unknown but it is worth remembering that variations to volcanic and solar natural forcing were embedded within the transient simulations therefore provide additional variations to short-term natural variability.

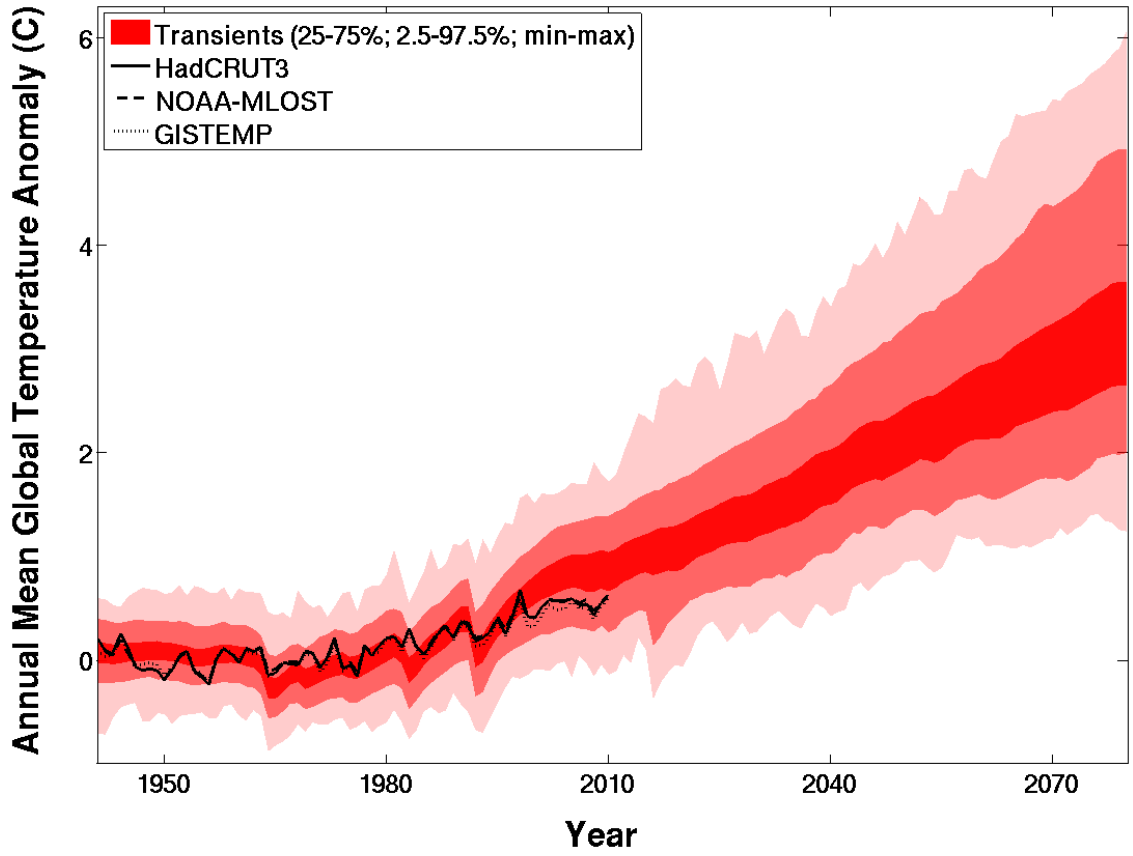


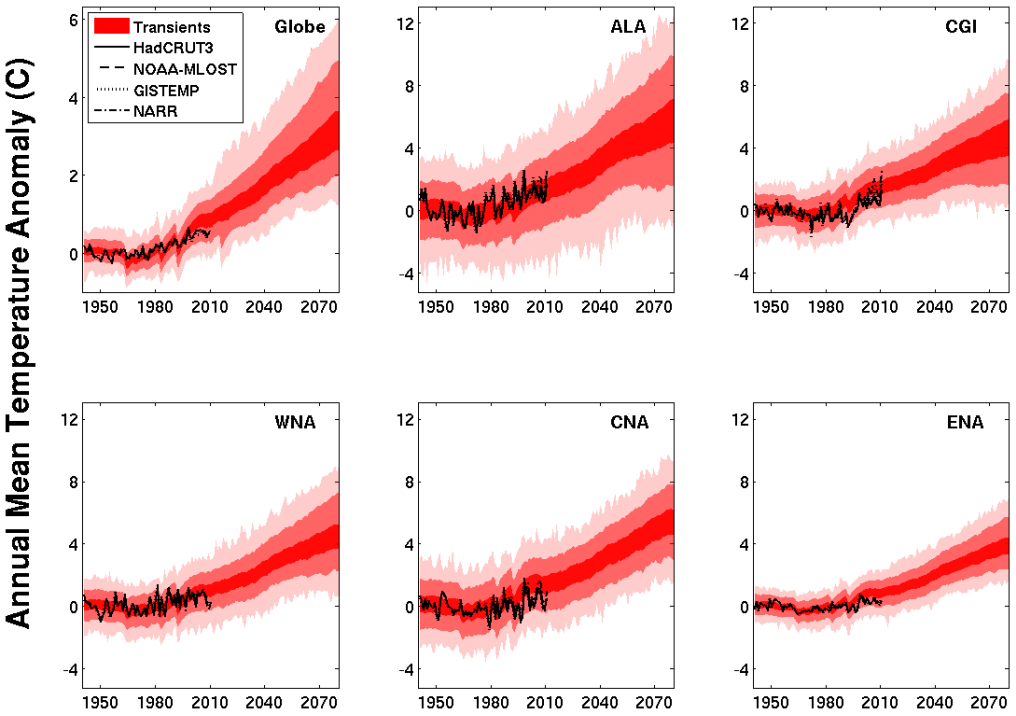
Figure 7.8: Annual mean global temperature anomaly for the 1,692 transient simulations (red shading) and three observational data sets over the 1941-2080 time period. The transient ensemble is shaded according to the 25-75%, 2.5-97.5%, and min-max ranges. Anomalies are relative to a 1941-1970 base period.

Another somewhat subtle feature to point out in Figure 7.8 is the general leveling off of simulated temperatures around 2000-2010 followed by more consistent upward trend thereafter. The interesting part is that the A1B SRES emissions scenario begins in 2001 and therefore this time period is not driven by observed forcings. While the observations in this same time period also appear to level off, that was presumably due to short-term variability, such as the PDO or ENSO, and such unforced natural variability occurs at random within the models and would not be anticipated to be a consistent feature across all models. One possible explanation could be that during this

period, an enhanced cooling effect of anthropogenic aerosols slowed the warming. Looking back at the A1B emissions scenario forcing in Chapter 3, Figure 3.3, we see that the anthropogenic sulfur dioxide (SO_2) emissions (Figure 3.3(c)) have a pronounced increase starting in the year 2000 and then peak around 2020 before declining. This is true for all values of ANTHSCA shown, which is simply a scaling factor of the original SO_2 emissions scenario shown as ANTHSCA = 1. During this same time greenhouse gases maintain a continuous increase in concentration (Figure 3.3(a)). Therefore the slowdown in model warming from 2000-2010 may be caused by this increase in SO_2 emissions which are then overtaken by the effect of the greenhouse gas forcing, presumably before the SO_2 emissions reach their peak in 2020, and a more linear increase in temperature ensues.

Figure 7.9 provides the same information as Figure 7.8 but includes the NA regions as well as precipitation comparisons to observations. As with the globe, Figure 7.9(a) shows uncertainties in future projections of temperature increasing in the future, with the possible exception being CNA. Each region also shows greater warming from 2011-2080 than simulated from 1941-2080. Precipitation in Figure 7.9(b) shows a general increase in uncertainty in the future with ALA, CGI, ENA, and the globe (relatively speaking) displaying an increase in precipitation in the future and WNA and CNA essentially showing no change.

(a)



(b)

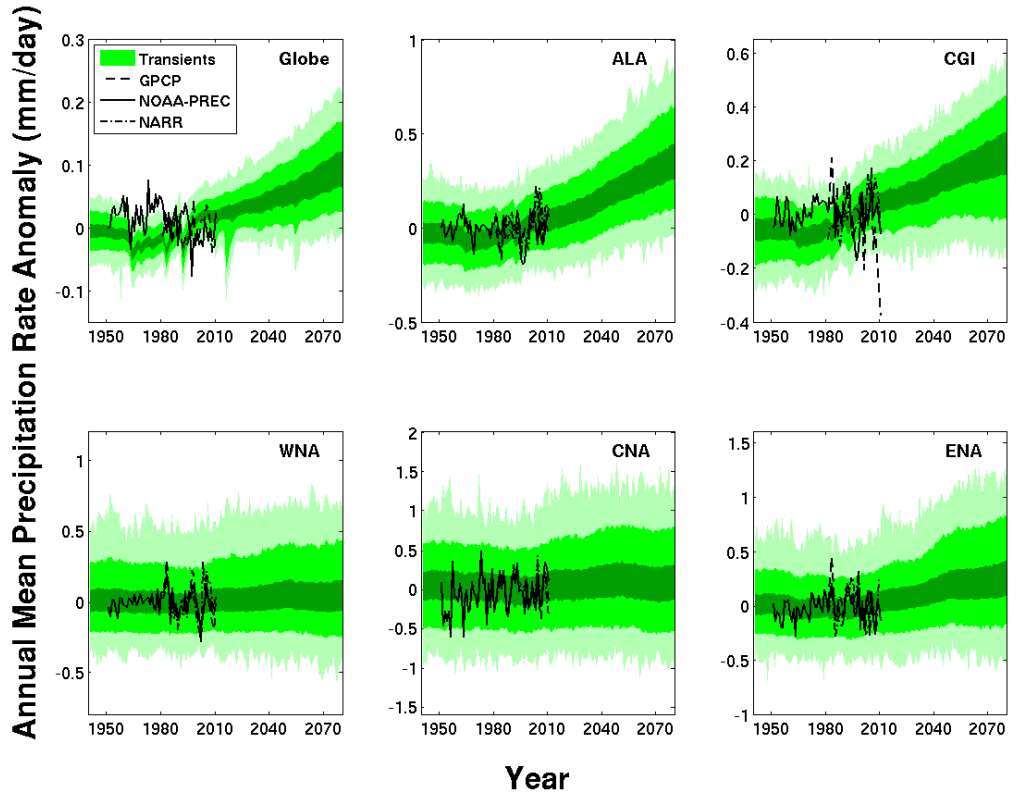


Figure 7.9: Same as Figure 7.8 but including regional comparisons for annual mean anomalies of *(a)* temperature(C) and *(b)* precipitation rate (mm/day). Temperature anomalies are relative to a 1941-1970 base period and precipitation anomalies are relative to 1981-2010.

To further explore changes in temperature and precipitation in the future, 30- and 70-year trends were calculated and compared against past trends and trends found in the control simulation ensemble. Figure 7.10 combines all of these trend distributions plus the observed trends from Figure 7.7 into a single plot for comparison. The initial feature to point out for both temperature and precipitation is that the control simulation 70-year mean trend distributions (three trends calculated for each control simulation; years 21-90, 56-126, 901-160) are all centered around zero and relatively small in magnitude.[21] And the 30-year control trend distributions (five 30-year trends calculated for each control simulation; years 21-50, 51-80, 81-110, 111-140, 131-160) are much larger than the 70-year trends because of the increasing influence of short-term variability.

All transient temperature trend distributions in Figure 7.10(a) are shifted in the positive direction compared to the control trend distributions which are centered on zero. This implies that the transient forced response trends are unlikely to be caused by natural variability in the model. While the past 70-year trends in temperature were smaller than the 30-year trends at the end of the observational period, the future 30- and 70-year trends are similar in magnitude (Figure 7.10(a)) because of the consistent, generally linear, increase in temperatures over the projection period (Figure 7.9(a)). These future trends resemble the late observational period (1981-2010) 30-year trend implying that temperatures are projected to continue increasing at a rate similar to later part of the observational period. The 70-year trends roughly double in the future in

[21] Note that the control trends are calculated after the long-term mean drift associated with imbalances from the atmosphere/ocean coupling process have been removed.

each region presumably due to the decreased influence of anthropogenic aerosols and increased influence of anthropogenic greenhouse gases.

The precipitation trend distributions shown in Figure 7.10(b) indicate minimal to no difference between control trends and past and future transient trends in WNA and CNA indicated no expected change in precipitation in the future over those regions. It should be noted however that these two regions are located in a position where most identify a transition zone of changing precipitation. Refer back to the CMIP3 future projections of precipitation across North America shown in Chapter 2, Figure 2.5 and compare to the regional locations of WNA and CNA (Chapter 3, Figure 3.4) and it becomes apparent that the regional means may be averaging together an increase in precipitation on the northern side of the region and a decrease on the southern side, thus resulting in a net zero trend. This point will be explored further in future work when an assessment is conducted on the CPDN decadal average gridded output.

The other regions show a slight increase in 70-year trends in the future, mostly in the northern regions of ALA and CGI possibly showing a future increase in moisture availability with increased temperature. The slight increase in global 70-year trends may be caused by a combination of increased high-latitude precipitation due to increased moisture availability and increased tropical convection.

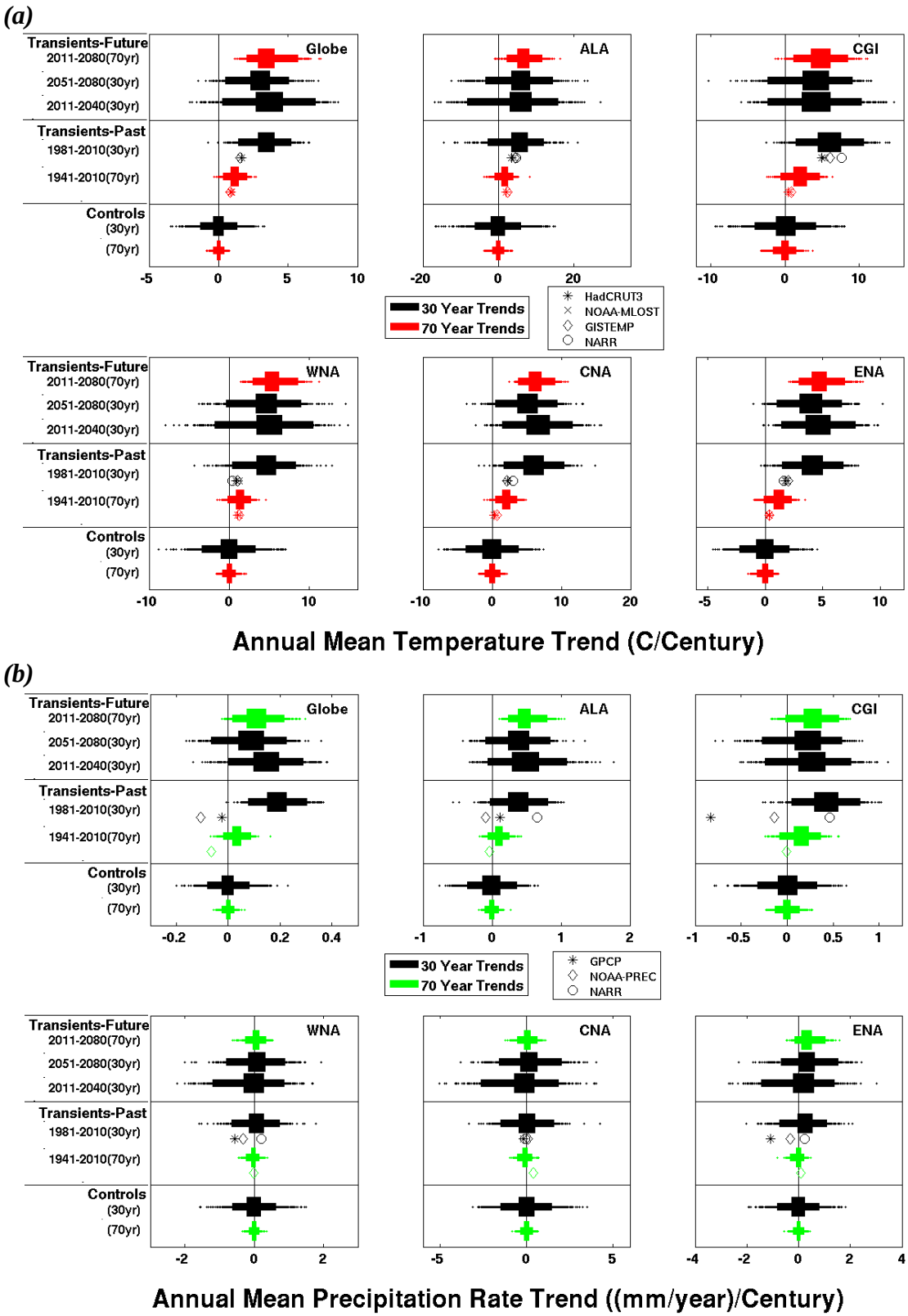


Figure 7.10: Annual mean *(a)* temperature (C/Century) and *(b)* precipitation rate ((mm/year)/Century) trends for past and future transients and controls for 30 year time periods (black) and 70 year periods (colored). Observed trends are plotted using the same color scheme.

7.5 TRANSIENT TREND RELATIONSHIPS

7.5.1 Global vs. Regional Trends (Same Time Period)

The relationship between global temperature trends and regional trends across the same time period are investigated in this sub-section to see if global changes correspond with changes at the regional level. Figure 7.11 shows scatter diagrams of the 70-year global temperature trend over the observational period versus regional 70-year trends across the same time period. We can see that a general relationship exists in each case. To quantify these relationships, the correlation was calculated for each case and is provided in Table 7.2. Also provided in Table 7.2 are the correlations for both 30- and 70-year trends during past and future time periods. Each correlation between the globe and an individual region is always calculated over the same time period.

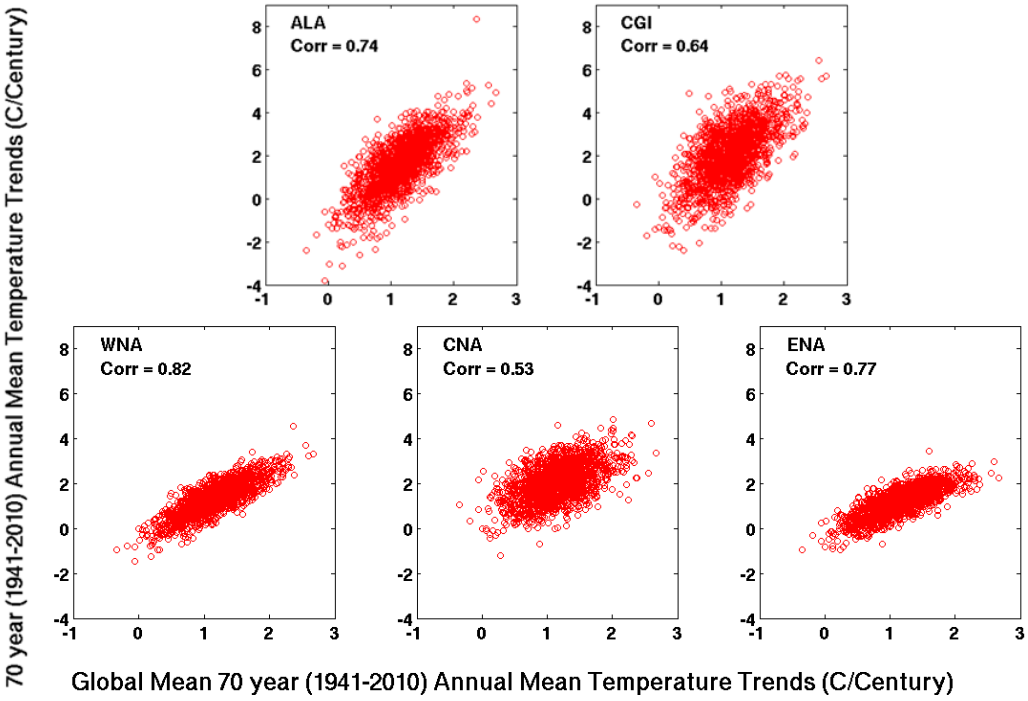


Figure 7.11: Comparison of 70 year trends (1941-2010) in annual mean temperature for the globe versus each region. A single point is plotted for each of the 1,692 transient simulations. P-values are all << 0.001.

Table 7.2: Correlations between simulated *global temperature trends* and *regional* temperature and precipitation rate trends *over the same time period* for the 1,692 transient simulations. Correlations are provided for 70 year past (1941-2010) and future (2011-2080) trends and for 30 year past (1981-2010) and two future time period (2011-2050; 2051-2080) trends. Correlations with magnitude ≥ 0.6 (0.8) are highlighted in gray (yellow). All p-values are <<0.001.

Region	**70 year Trends** (Globe vs. Region) *Past* 1941-2010 *[Future]* [2011-2080]	**30 year Trends** (Globe vs. Region) *Past* 1981-2010 *[Future]* [2011-2050; 2051-2080]
Temperature		
Globe	1.00 [1.00]	1.00 [1.00; 1.00]
ALA	0.74 [0.91]	0.70 [0.80; 0.86]
CGI	0.64 [0.72]	0.50 [0.57; 0.66]
WNA	0.82 [0.94]	0.78 [0.83; 0.89]
CNA	0.53 [0.74]	0.14 [0.11; 0.11]
ENA	0.77 [0.82]	0.56 [0.58; 0.69]
Precipitation Rate		
Globe	0.92 [0.79]	0.81 [0.83; 0.78]
ALA	0.63 [0.82]	0.47 [0.49; 0.51]
CGI	0.59 [0.68]	0.51 [0.53; 0.55]
WNA	0.31 [0.43]	0.49 [0.53; 0.60]
CNA	0.25 [0.36]	0.44 [0.55; 0.59]
ENA	0.33 [0.14]	0.46 [0.43; 0.55]

Table 7.2 shows that regional temperature trends correspond quite well to global temperature trends with the exception of CNA, possibly because of larger variability in that region. When comparing relationships between 70- and 30-year trends that share an overlapping period (e.g., past 70- and past 30-year trends) the 70-year trend relationship was almost always larger because of the increased variability over the shorter time span. The relationship in 70-year future trends was stronger for all regions than for 70-year past trends. This points to the increasing influence rising greenhouse gas concentrations had on regional temperature trends in the future as the impact of other forms of variability became reduced and the trends began to have a greater resemblance to the global long-term trend.

The global temperature trend has much weaker relationships to regional precipitation. The global temperature and global precipitation correspond well because global precipitation is highly dependent on global temperature (e.g., impacts on tropical rainfall and high-latitude moisture availability). Additionally, ALA and CGI have relatively higher correlations due to the fact that the higher latitudes respond more to temperature changes which alters moisture availability.

7.5.2 Past Global Trends vs. Future Global and Regional Trends

Whereas the previous sub-section looked at relationships over the same time period, this sub-section investigates the relationships of past global temperature trends with future global and future regional trends. This addresses the question of whether the magnitude of global trends simulated in the past are related to simulated future trends at both the global and regional scales. Table 7.3 provides the results for 70-year trends and the two different future 30-year time period trends, where an early and latter future 30-year period (2011-2040; 2051-2080) is compared to global temperature trends over the final 30 years of the observational period (1981-2010).

Table 7.3: Correlations between simulated *past global temperature* trends and *future regional* temperature and precipitation rate trends and for the 1,692 transient simulations. Correlations are provided for 70 year past (1941-2010) global and future (2011-2080) regional trends and for 30 year past (1981-2010) global and two future time period (2011-2050; 2051-2080) regional trends. Correlations with magnitude ≥ 0.25 are highlighted in blue. All p-values are <<0.001 except for those denoted with a (*).

Region	70 year Trends *Past Globe* | *Future Region* (1941-2010) vs (2011-2080)	30 year Trends *Past Globe* | *Future Region* (1981-2010) vs (2011-2040)	30 year Trends *Past Globe* | *Future Region* (1981-2010) vs (2051-2080)
Temperature			
Globe	0.18	0.34	0.34
ALA	0.24	0.26	0.28
CGI	0.45	0.17	0.33
WNA	0.20	0.30	0.31
CNA	0.14	0.09*	0.20
ENA	0.07*	0.23	0.29
Precipitation Rate			
Globe	0.18	0.26	0.25
ALA	0.14	0.19	0.22
CGI	0.42	0.14	0.33
WNA	0.17	0.17	0.13
CNA	-0.09*	0.17	0.08*
ENA	-0.30	0.06*	0.05*

It is immediately apparent that these correlations are generally much weaker than the correlations found comparing global temperature and regional trends across the same time period in the previous section (Table 7.2). This makes sense because when making comparisons across the same time period, both the globe and regions will be under the same forcings whereas comparisons from past to future will have additional uncertainty due to differences in forcings driving the simulations over the two time periods. Therefore we consider the relative differences in the correlations shown in Table 7.3 to get a general idea of the relationships of past global temperature trends to future regional trends.

The main conclusion from this analysis is that, in general, the 30-year relationships are stronger than the 70-year relationships, with the exception of CGI which may have to do with sea ice interactions and ENA precipitation. The implication of this is that when attempting to constrain future projections it will be better to use the recent past 30-year trend rather than past 70 year trends because they show a greater correlation to future trends. This is probably due to fact that greenhouse gas forcing has held greater importance in recent decades and it is expected to be a dominant factor in the future.

7.5.3 Past vs. Future Trends in Same Region

The previous two sub-sections assessed relationships between various regions and the global temperature trend. In this sub-section relationships are quantified between past and future trends within an individual region (Table 7.4). The most important aspect of these relationships is their comparison to the correlations calculated against past global temperatures in the previous section (Table 7.3). Again, the relationships in the same region (Table 7.4) have 30-year trend relationships that are generally stronger than for 70-year trends as was found when comparing past global temperatures to each future region. However, there is a difference in the magnitude of those 30-year trend correlations. The past global temperature trend appears to have a greater correlation to future regional climatic trends (Table 7.3) than the correlation found between past climatic trends to future trends from within the same region (Table 7.4).

This result will become useful when attempting to constrain future projections (Section 7.8) because it implies that past global temperature trends may be a better predictor of future regional climatic trends than past trends in the individual regions themselves. It also suggests that the 30-year trend in past global temperatures (1981-2010) may be more appropriate predictor to use for constraining than past 70-year trends (1941-2010).

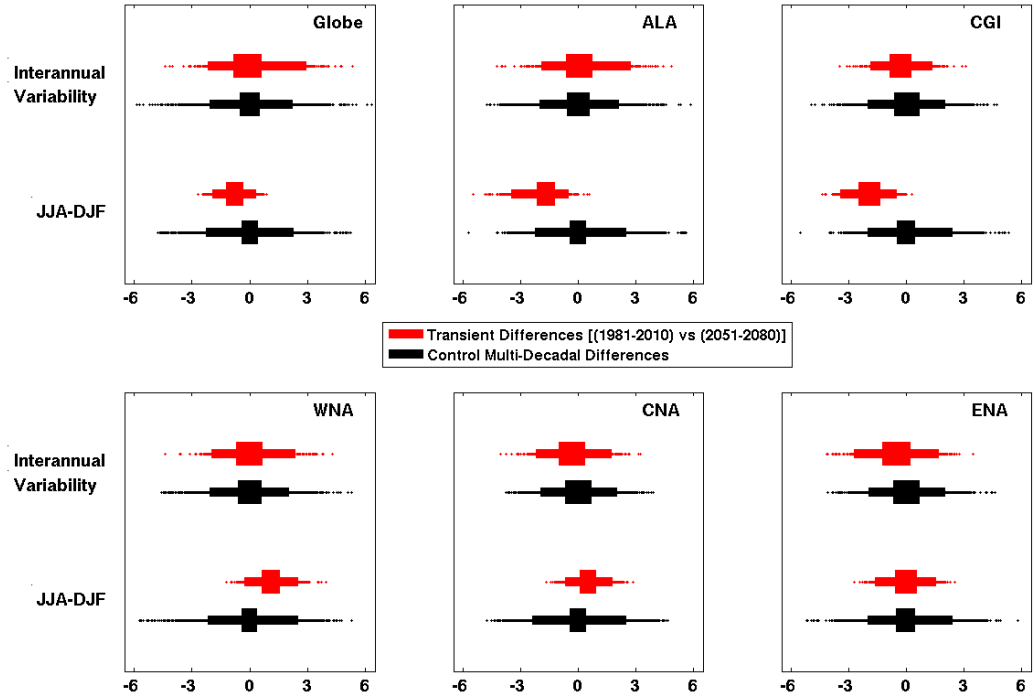
Table 7.4: Correlations between *past and future* trends within a given region for temperature and precipitation rate for the 1,692 transient simulations. The 70 year trends are compared between 1941-2010 and 2011-2080 and the 30 year trends are compared from the past time period 1981-2010 and future periods 2011-2040 and 2051-2080. Correlations ≥0.25 are highlighted in blue. All p-values are <<0.001 except for those with a (*).

Region	70 year Trends		30 year Trends		30 year Trends	
	Past	*Future*	*Past*	*Future*	*Past*	*Future*
	(1941-2010) vs (2011-2080)		*(1981-2010) vs (2011-2040)*		*(1981-2010) vs (2051-2080)*	
Temperature						
Globe	0.18		0.34		0.34	
ALA	0.24		0.25		0.20	
CGI	0.30		0.27		0.21	
WNA	0.14		0.27		0.23	
CNA	0.02*		0.13		0.08*	
ENA	0.03*		0.15		0.21	
Precipitation Rate						
Globe	0.11*		0.26		0.23	
ALA	0.14		0.11		0.13	
CGI	0.28		0.21		0.18	
WNA	0.23		0.15		0.04*	
CNA	0.15		0.20		0.02*	
ENA	-0.11		0.15		0.08*	

7.6 Changes in Seasonal Cycle and Variability

Next we assess whether there are changes in future projections of interannual variability or magnitude in the seasonal cycle (JJA-DJF). These two quantities were calculated in the transient simulations over the periods 1981-2010 and 2050-80 and then the difference found. The 30-year periods were detrended prior to the calculation to remove any impact the long-term mean trend might have. Figure 7.12 shows the distribution of these differences from all transients. To assess the significance of the change against natural variability, the same quantities were calculated over various 30-year periods in each control simulation (21-50, 51-80, 81-110, 111-140, 130-160) and differences between each period calculated from within a single control simulation. All of these differences were then combined into a single distribution representing all controls and shown as the black distribution in Figure 7.12.

(a)



(b)

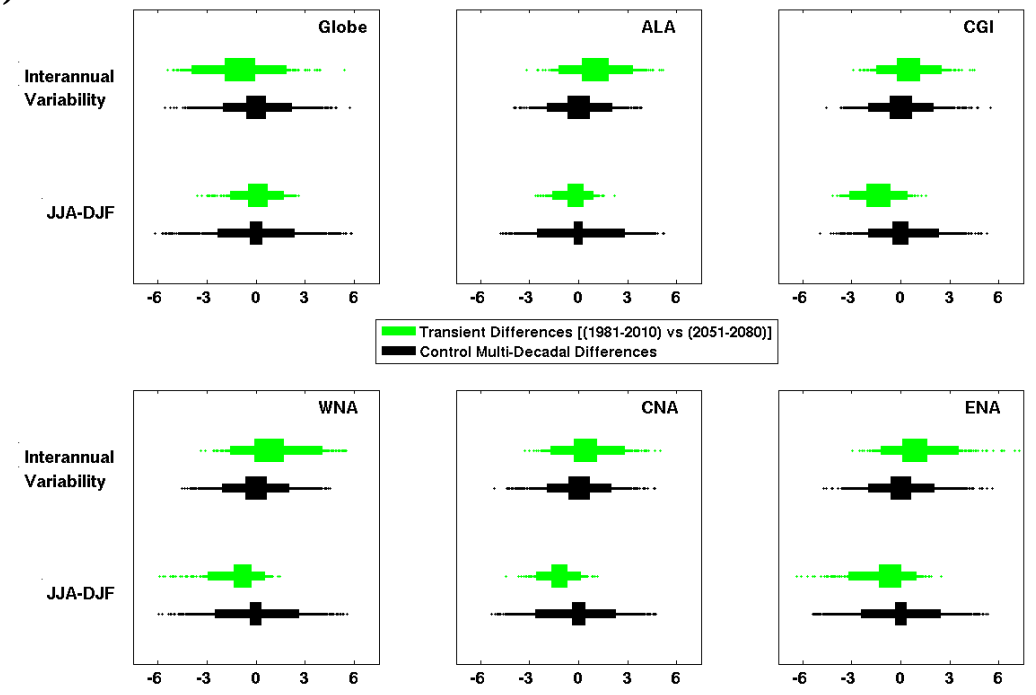


Figure 7.12: Differences in 30 year mean interannual variability and JJA-DJF from 1981-2010 to 2051-2080 for the 1,692 transient simulations (colored) and differences found across five different 30 year periods within all 1,214 control simulations. All values are standardized to the control difference distribution.

All changes in future projections of interannual variability and JJA-DJF are within the range of multi-decadal differences found in control simulation distributions which means that any single realization would not be considered outside the range of natural variability. However, there are instances when the entire distribution appears to be shifted and some instances where that shift leaves nearly all of the samples with the same sign. For interannual variability in temperature (Figure 7.12(a)) there was essentially no shift in the distributions but in interannual variability in precipitation (Figure 7.12(b) there was a slight positive shift in all NA regions and interestingly a negative shift in the globe. With all NA regions shifting one direction and the globe the other it implies that the global variability is being influenced by processes other than those predominantly affecting NA (e.g., the tropics).

JJA-DJF for temperature (Figure 7.12(a)) shows a reduction for ALA, CGI, and the globe which would be suggestive of greater warming in the winter than summer for the higher latitudes. WNA and CNA show an increase in JJA-DJF temperature which implies summer is warming more than winter which could be indicative of summer drying across the region.

JJA-DJF for precipitation (Figure 7.12(b)) shows a slight decrease in all regions except the globe and ALA. For the WNA, CNA, and ENA regions this may imply a reduction in summer rainfall, which would be consistent with the increased seasonal cycle in temperature seen in WNA and CNA (Figure 7.12(a)). The decrease in CGI is more difficult to explain because its maximum and minimum in precipitation do not align with JJA and DJF.

7.7 Sensitivity to Physical Parameter Values

The parameter perturbations applied to CPDN transient simulations are assessed to evaluate uncertainties in climate indices based on variations to these parameters. (For parameter perturbations see Table 7.1 and for further discussion of these perturbations refer to Chapter 3, Section 3.3.1) Section 7.7.1 assesses the sensitivity of 70- and 30- year trends to variations of each model parameter over the observational period while Section 7.7.2 assesses the same sensitivity over the future time period.

7.7.1 Parameter Variations and Observational Period Trends

An analysis was performed to identify the correlation between model parameter variations and simulated 30- and 70-year trends in both temperature and precipitation over the observational period. The top parameters with highest correlation magnitudes (≥ 0.3) are shown in Table 7.5. Compared to the parameter sensitivity analysis performed on control simulation mean and variability measures (Chapter 5, Table 5.5), these parameters are both fewer in number and have much weaker correlations. Therefore varying parameter settings has much less of an impact on trends than it does on natural variability measures. This is apparent in Figure 7.13 and 7.14 which show the limited variations in 30- and 70-year trends as these top parameters are varied. Therefore, attempting to constrain future projections based on model parameter values that best simulate climatic trends may be challenging (but was still attempted, see Section 7.8).

Table 7.5: Model physics parameters with correlation magnitude ≥ 0.3 between their variations and 30-year (1981-2010) or 70-year (1941-2010) observational period trends in annual mean temperature or precipitation rate over a defined region. Parameters are listed in order of generally higher sensitivity to lower. All correlations shown have p<<0.00001.

Parameter	Globe	ALA	CGI	WNA	CNA	ENA
ANTHSCA	70yr Precip [-0.41] 70yr Temp [-0.37]	70yr Precip [-0.34]		70yr Temp [-0.31]	70yr Temp [-0.30]	70yr Temp [-0.32]
HANEYSFACT	70yr Temp [-0.30]		70yr Precip [-0.41] 70yr Temp [-0.40]			
RHCRIT	30yr Precip [0.35] 30yr Temp [0.31]					

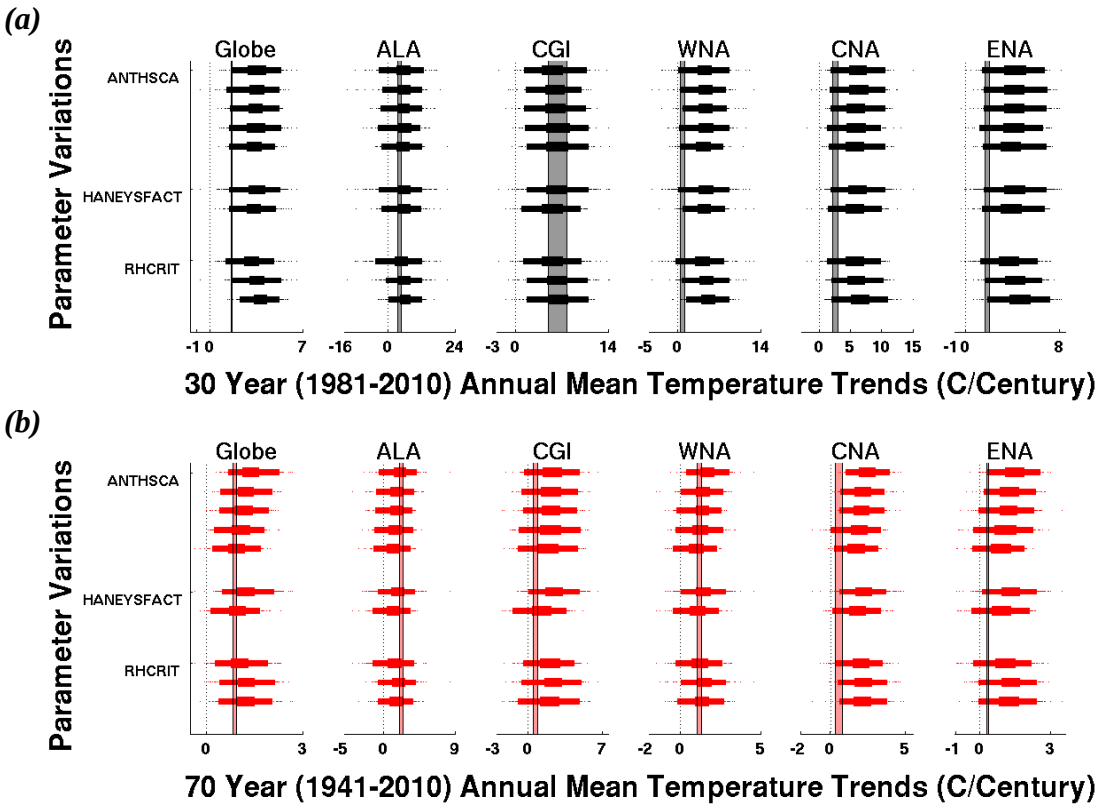


Figure 7.13: Annual mean temperature *(a)* 30 year trends, 1981-2010 and *(b)* 70 year trends, 1941-2010 (°C/Century) over the observational time period for the globe and five NA regions for the 1,692 transient simulations split into distributions corresponding with model parameter values. Actual parameter values are not listed but are arranged in the same order as that given in Table 7.1. Boxplots provide 25-75% (inner) and 2.5%-97% (outer) ranges and dots for samples outside the 95% range. The maximum and minimum range of corresponding observational data sets (including NARR) is shown as a vertical shaded bar. A vertical dotted line identifies zero trend.

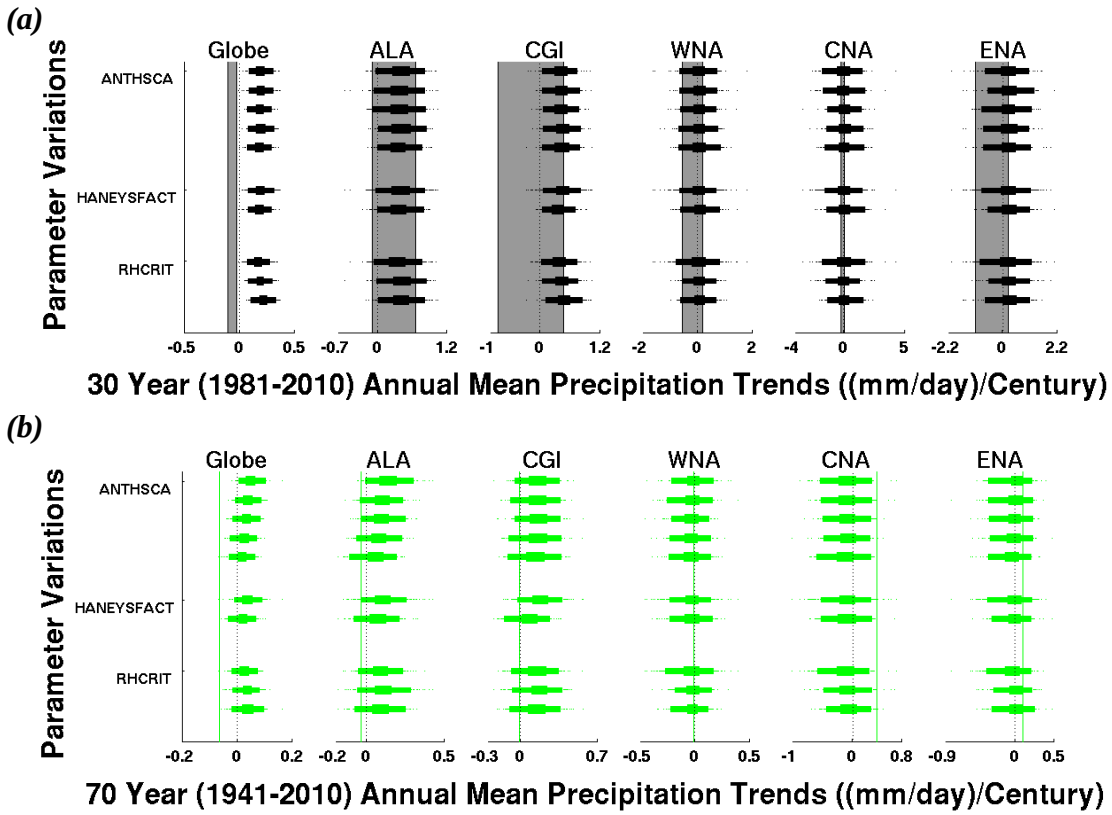


Figure 7.14: Annual mean precipitation rate *(a)* 30 year trends, 1981-2010 and *(b)* 70 year trends, 1941-2010 ((mm/year)/Century) over the observational time period for the globe and five NA regions for the 1,692 transient simulations split into distributions corresponding with model parameter values. Actual parameter values are not listed but are arranged in the same order as that given in Table 7.1. Boxplots provide 25-75% (inner) and 2.5%-97% (outer) ranges and dots for samples outside the 95% range. The maximum and minimum range of corresponding observational data sets (including NARR) is shown as a vertical shaded bar. The observational 70 year trend corresponds with a single data set (NOAA-MPREC) and is a 60 year average corresponding with the data set length. A vertical dotted line identifies zero trend.

One of the top parameters, ANTHSCA, is the scaling factor for anthropogenic sulfate aerosols (refer back to Chapter 3, Section 3.3.1 for all parameter discussions) and it is an important parameter because it directly alters the sulfate aerosols in the model which has a direct impact on solar radiation and therefore surface temperatures. When ANTHSCA is increased there is a greater amount of sulfate aerosols in the atmosphere which increases scattering and absorption of solar radiation thereby

reducing the amount of radiation reaching the surface (a cooling effect). When ANTHSCA is decreased, less sulfate aerosols are in the atmosphere and the opposite effect ensues. These effects can be seen in Figure 7.13(b) where the distributions in 70-year global temperature trends decrease as ANTHSCA increases. (Note that parameter distributions align with parameter values which are listed as smallest on top and largest on bottom to match the ordering in Table 7.1).

Parameter HANEYSFACT sets the time lag for the correction of model generated sea surface salinities (SSSs) to observed SSSs in the spin up phase of the model. This process attempts to reduce drift in the model and therefore varying it alters the long term mean model drift, which was supposedly removed, but evidently still plays a partial role in trends across the 20th century.

The parameter RHCRIT is the critical relative humidity and it sets the relative humidity threshold required for cloud water vapor to form in the model. When RHCRIT is set to a lower value, clouds form relatively faster (i.e., do not require as much moisture to form) which, in turn, increases the reflection of shortwave solar radiation in the clouds, thus decreasing the radiation reaching the ground (a cooling effect). This effect on temperature can be seen in the distribution changes of 30-year temperature trends with changing RHCRIT values in Figure 7.13(a) where increasing RHCRIT values result in larger trends (i.e., more moisture was required to form clouds so relatively less clouds form allowing more solar radiation to reach the surface.

7.7.2 Parameter Variations and Future Trends

While the main purpose of identifying influential parameters is to use that knowledge to constrain future projections it is still interesting to see which parameters are most important with regards to variations in future trends. In this sub-section a parameter sensitivity analysis is performed for variations in trends over the future projection time period. Table 7.6 lists the parameters found with highest correlation magnitudes (≥ 0.3) between their parameter variations and simulated 30-year (2051-2080) and 70-year (2011-2080) trends in temperature or precipitation. There are more parameters in this set than found for parameter sensitivities in past trends and the correlation magnitudes are slightly larger. This is probably due to the wider range of trend distributions in the future which further emphasizes differences in model climate sensitivities.

Table 7.6: Model physics parameters with correlation magnitude ≥ 0.3 between their variations and 30-year (2051-2080) or 70-year (2010-2080) future trends in annual mean temperature or precipitation rate over a defined region. Parameters are listed in order of generally higher sensitivity to lower and correlation magnitudes ≥ 0.4 are highlighted yellow. All correlations shown have p<<0.00001.

	Globe	ALA	CGI	WNA	CNA	ENA
EACF	70yr Precip [-0.51]	70yr Temp [-0.36]	70yr Temp [-0.42]	70yr Temp [-0.36]		
	70yr Temp [-0.38]	70yr Precip [-0.32]	70yr Precip [-0.41]	70yr Precip [-0.35]		
	30yr Temp [-0.36]	30yr Temp [-0.30]	30yr Temp [-0.32]	30yr Temp [-0.31]		
	30yr Precip [-0.36]		30yr Precip [-0.31]			
RHCRIT	70yr Precip [0.43]	70yr Temp [0.41]	70yr Temp [0.38]	70yr Temp [0.48]	70yr Temp [0.37]	70yr Temp [0.38]
	70yr Temp [0.42]	70yr Precip [0.36]	70yr Precip [0.37]	30yr Temp [0.36]		30yr Temp [0.32]
	30yr Temp [0.38]	30yr Temp [0.32]				
	30yr Precip [0.37]					
CT	70yr Precip [0.44]	70yr Temp [0.39]	70yr Temp [0.48]	70yr Temp [0.33]		70yr Precip [-0.30]
	70yr Temp [0.39]	30yr Temp [0.31]	70yr Precip [0.42]	70yr Precip [0.32]		
	30yr Temp [0.35]		30yr Temp [0.38]			
			30yr Precip [0.33]			
ENTCOEF			70yr Temp [0.36]	70yr Precip [0.38]		70yr Precip [-0.44]
			70yr Precip [0.33]			
CW_LAND; CW_SEA					70yr Precip [0.30]	70yr Precip [0.33]
VF1						70yr Precip [0.32]

It is interesting to note that while RHCRIT is still listed as a top parameter, ANTHSCA and HANEYSFACT are not. For ANTHSCA this is most likely due to the fact that the anthropogenic sulfate aerosols reach a peak in 2020 and then decrease throughout the rest of the simulation. Therefore, the impact these aerosols have on the climate would decrease with time, especially as the effects of increasing greenhouse gas concentrations began to dominate the modeled climate system. ANTHSCA is simply the scaling factor of the anthropogenic sulfate aerosols and therefore also would become less influential in the future. HANEYSFACT apparently was associated with model imbalances in the 20th century but was not as important as other parameters across the 21st century.

There were a few additional parameters of higher significance added that we can discuss further (EACF, CT). The parameter EACF is the empirically adjusted cloud fraction and identifies how much cloud cover there will be when the atmosphere is saturated over a given grid cell. When the EACF parameter is increased it means that there will be more cloud cover when the atmosphere is saturated and therefore more solar radiation will be absorbed or reflected, thus cooling the surface. This feature is seen in Figure 7.15(a,b) in all regions as a decreasing temperature trend with increasing values of EACF.

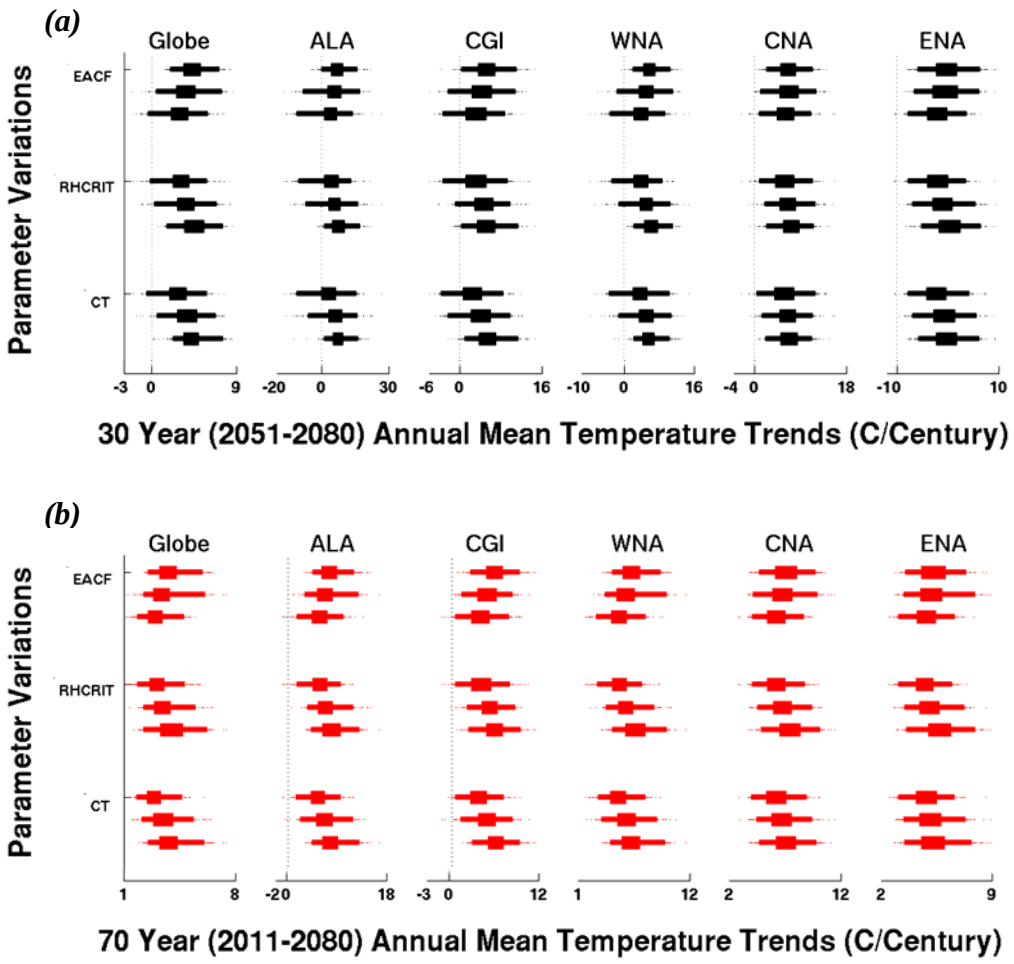


Figure 7.15: Annual mean temperature *(a)* 30 year trends, 2051-2080 and *(b)* 70 year trends, 2011-2010 (°C/Century) for the future time period for the globe and five NA regions for the 1,692 transient simulations split into distributions corresponding with model parameter values. Actual parameter values are not listed but are arranged in the same order as that given in Table 7.1. Boxplots provide 25-75% (inner) and 2.5%-97% (outer) ranges and dots for samples outside the 95% range. A vertical dotted line identifies zero trend.

The parameter CT is the accretion constant and identifies the cloud droplet to rain conversion rate (i.e., how long it takes to convert cloud droplets to rain). As discussed in Chapter 3, Section 3.3.1, a reduction in CT has been found to increase the amount of clouds for a given temperature and humidity, thereby decreasing surface temperatures. An increase in CT allows more cloud droplets to be removed by falling rain which increases the amount of precipitation falling. Both of these effects can be

seen with temperature trends generally decreasing when CT values are small (Figure 7.15) and precipitation trends increasing when CT values are large (Figure 7.16).

A major takeaway from this future trend analysis is the increasing importance of cloud parameters in the future projection period indicating the important role of cloud feedbacks on the climate sensitivity and the future warming trends

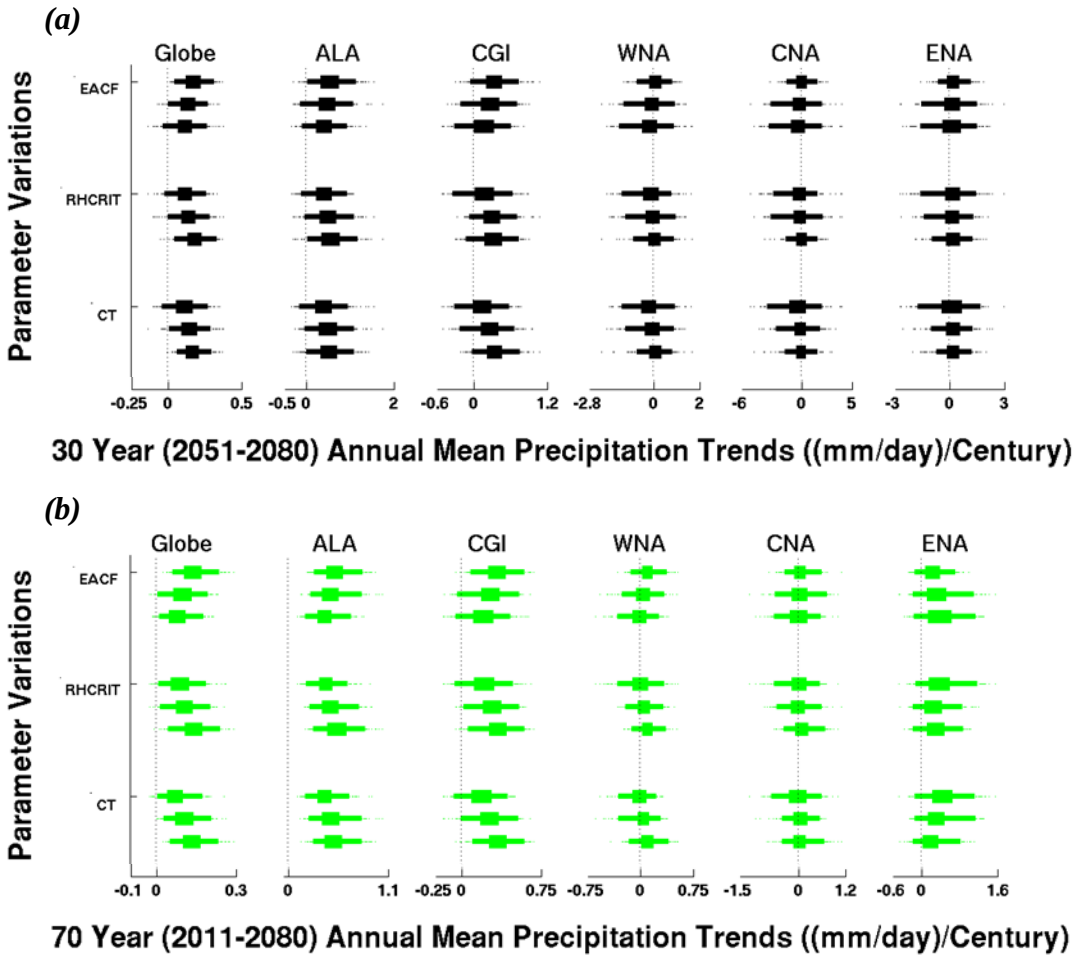


Figure 7.16: Annual mean precipitation rate *(a)* 30 year trends, 2051-2080 and *(b)* 70 year trends, 2011-2080 ((mm/year)/Century) for the future time period for the globe and five NA regions for the 1,692 transient simulations split into distributions corresponding with model parameter values. Actual parameter values are not listed but are arranged in the same order as that given in Table 7.1. Boxplots provide 25-75% (inner) and 2.5%-97% (outer) ranges and dots for samples outside the 95% range.

7.8 Constrained Transient Ensemble

Finally, the knowledge gained from the transient simulation assessments in this chapter is used to constrain future global and NA regional temperature and precipitation projections. The three sub-sections below provide transient simulation projections constrained by a simulation's ability to reproduce observed 30-year global temperature trends, observed 70-year global temperature trends, and by using model parameter value settings that are best suited to reproduce observed 70-year global temperature trends.

7.8.1 Constrained by 30 Year Global Temperature Trend

The first constrained future projection ensemble is constructed based on a transient simulation's ability to reproduce observed 30-year global temperature trends. As discussed in Section 7.5, 30-year global temperature trends had the highest correlation with future trends at both the global and regional scale and therefore would be the best metric to use for constraining future projections based on past performance. Figure 7.17 shows the constrained transient ensemble (shaded), which is comprised of all simulations that are within one standard deviation of the 30-year global temperature trend observed mean. The original transient ensemble is shown as the respective black lines. Using this constraint had an impact on future projections by generally reducing the average simulated future warming trend and its uncertainty range. It also improved the model's ability to simulate the more recent observed temperatures.

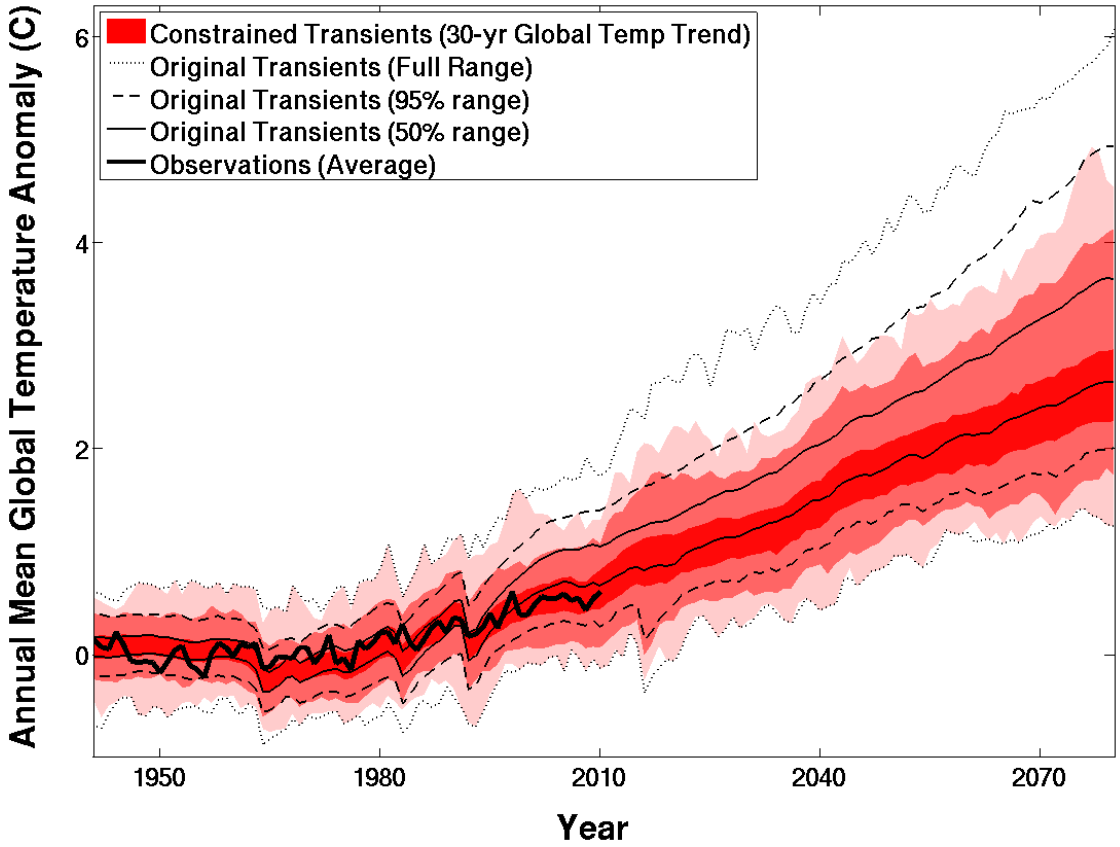


Figure 7.17: Annual mean global temperature anomaly for transient ensemble constrained by model performance for 30-year (1981-2010) global temperature trends (red shading; 255 simulations) and the original transient ensemble (black lines; 1,692 simulations). Both ensembles show the 25-75%, 2.5-97.5%, and min-max ranges. Observations are averaged together to give a single estimate. Anomalies are relative to a 1941-1970 base period.

Figure 7.18 shows the same constrained simulations as those shown in Figure 7.17 but for temperature and precipitation across the NA regions. A similar decrease in the average future warming trend is seen across the various regions as well as precipitation rate when a long-term trend originally existed. Performing this constraint therefore reduced the uncertainty in future projections of both temperature and precipitation at the global and NA regional levels.

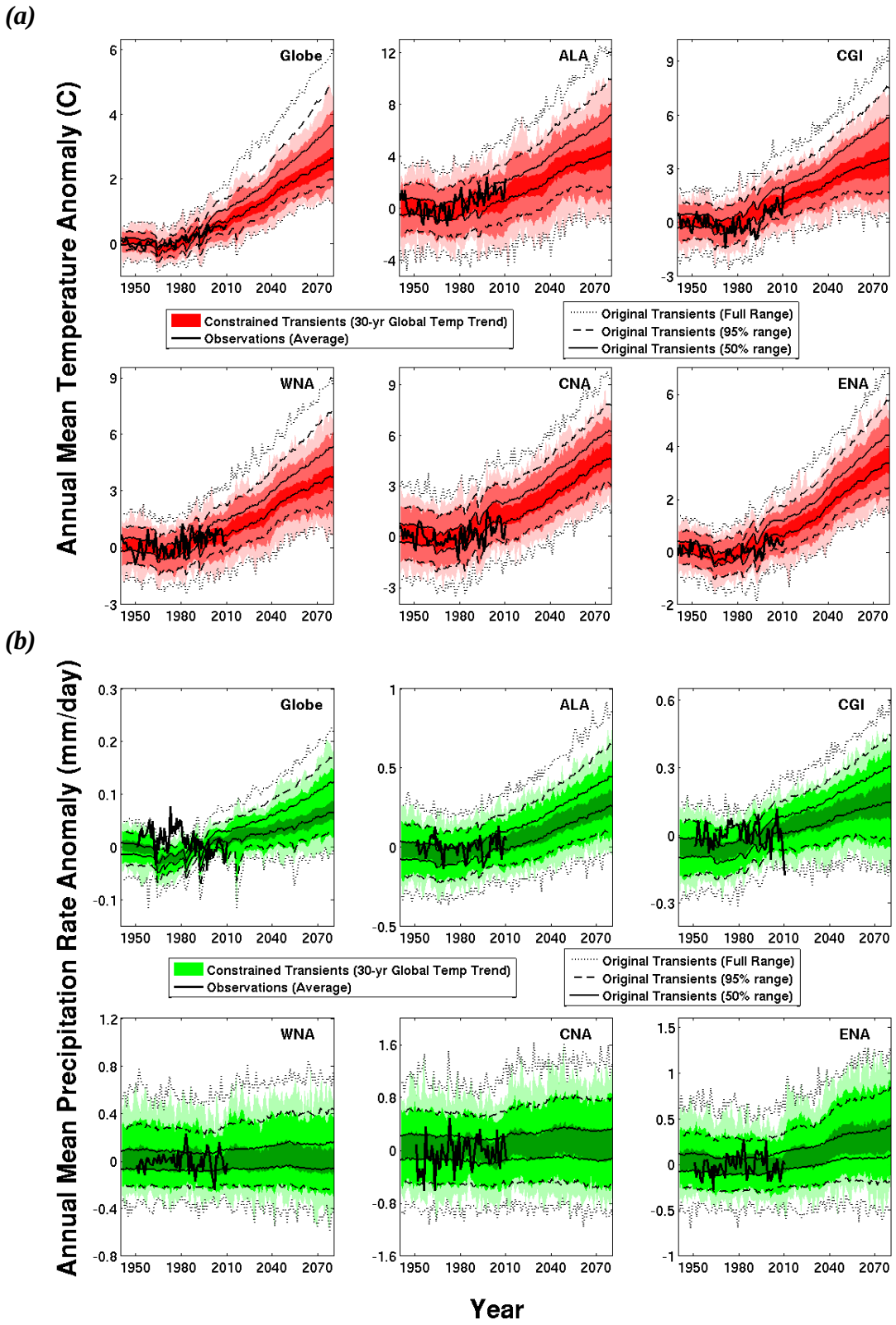


Figure 7.18: Same as Figure 7.17 but including regional comparisons for annual mean anomalies of *(a)* temperature (C) and *(b)* precipitation rate (mm/day). Temperature anomalies are relative to a 1941-1970 base period and precipitation anomalies are relative to 1981-2010.

7.8.2 Constrained by 70 Year Global Temperature Trend Performance

The next constrained future projection ensemble is constructed based on a transient simulation's ability to reproduce observed 70-year global temperature trends. Figure 7.19 shows the constrained transient ensemble (shaded), which is constructed in the same manner as Figure 7.17. Using this constraint appears not to have had an impact on the general pattern of the original ensemble. This is due to the fact that the observed 70-year global temperature trend was near the 50% range of the models and therefore less likely to identify a consistent set of simulations with the same bias in future trends compared to the observed 30-year global temperature trend which was closer to the 95% range of the modeled trends, thus having a greater number of simulations all containing the same trend bias (refer to Figure 7.7). The constrained regional temperature and precipitation showed virtually identical characteristics as the global constrained ensemble in Figure 7.19 (i.e., no changes to the original transient ensemble spread) and therefore are not shown.

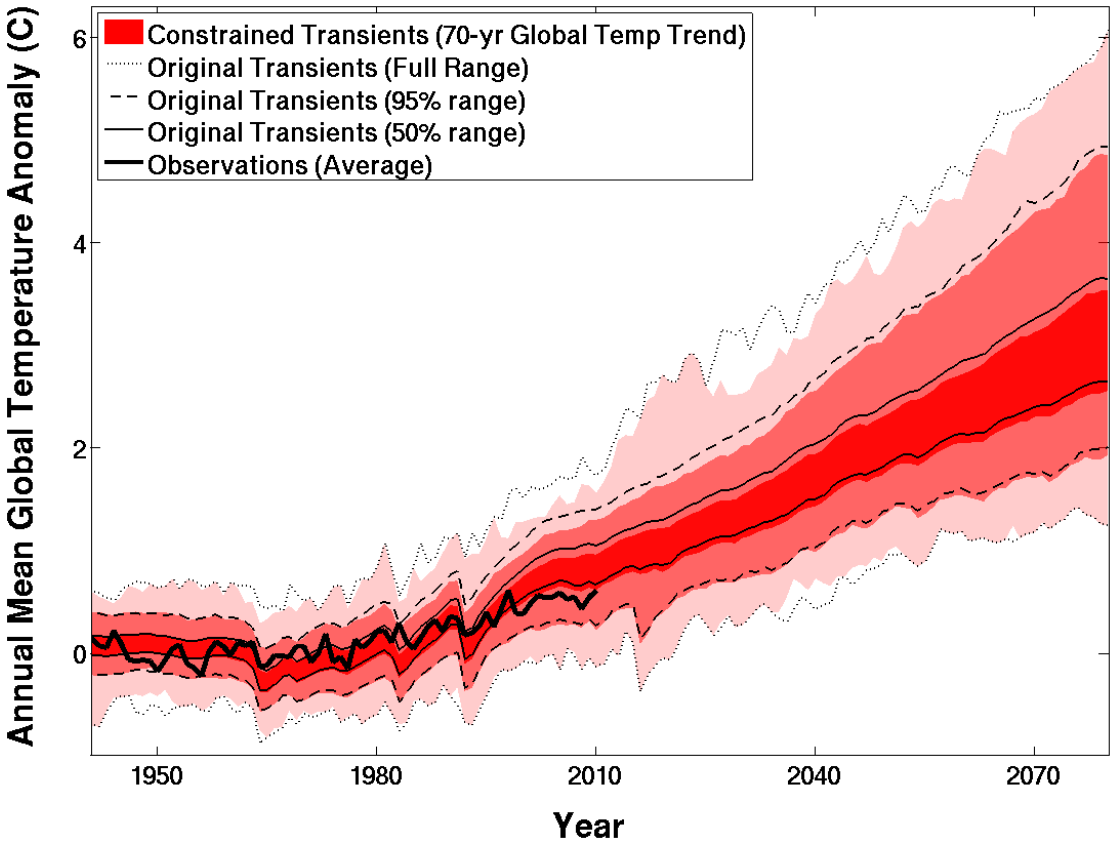


Figure 7.19: Annual mean global temperature anomaly for transient ensemble constrained by model performance for 70-year (1941-2010) global temperature trends (red shading; 997 simulations) and the original transient ensemble (black lines; 1,692 simulations). Both ensembles show the 25-75%, 2.5-97.5%, and min-max ranges. Observations are averaged together to give a single estimate. Anomalies are relative to a 1941-1970 base period.

7.8.3 Constrained by Parameters with Greatest Sensitivity (70yr Global Trends)

The final constrained future projection ensemble is constructed based on model parameter value settings that are best suited to reproduce observed 70-year global temperature trends. In Section 7.7.1 it was discovered that variations in three model parameters (ANTHSCA, HANEYSFACT, RHCRIT) had the largest impact on 30- and 70-year observed trends. By assessing the variations in these trends, a specific value for each parameter was found to maximize model performance, specifically the model's

ability to simulate 70-year global temperature trends (Figure 7.13(b)). These values were ANTHSCA = 1.5 (i.e., largest value), HANEYSFACT = 1.0 (largest value), and RHCRIT = 0.65 (smallest value). Constraining the transient ensemble to include only simulations with these specific values resulted in the ensemble shown in Figure 7.20 for annual mean global temperature anomaly. A significant reduction in the ensemble spread occurs with this constraint and the trends are all on the lower end of the long-term warming spectrum (similar to the results found by constraining based on a model's ability to reproduce observed 30-year global temperature trends shown in Figure 7.17). Using this constraint also provides a better representation of the more recent observed data. One thing to point out, though, is that using this constraint reduced the number of simulations in the ensemble to 37 which means there is the potential that the reduced ensemble spread is a result of the smaller number of simulations. Future work could include increasing the number of simulations by including those with parameter values within the most important parameters that are close to the settings chosen. For example, the next closest setting for ANTHSCA could be included to see how it impacts the final ensemble. Additionally, we could go back to the alternative "inferred" transient ensemble not used in this study (see Appendix A) and identify those simulations with the corresponding "best" values in the three top parameters and then also match those parameters required for an "inferred" match while letting all other parameters vary and see how the ensemble changes.

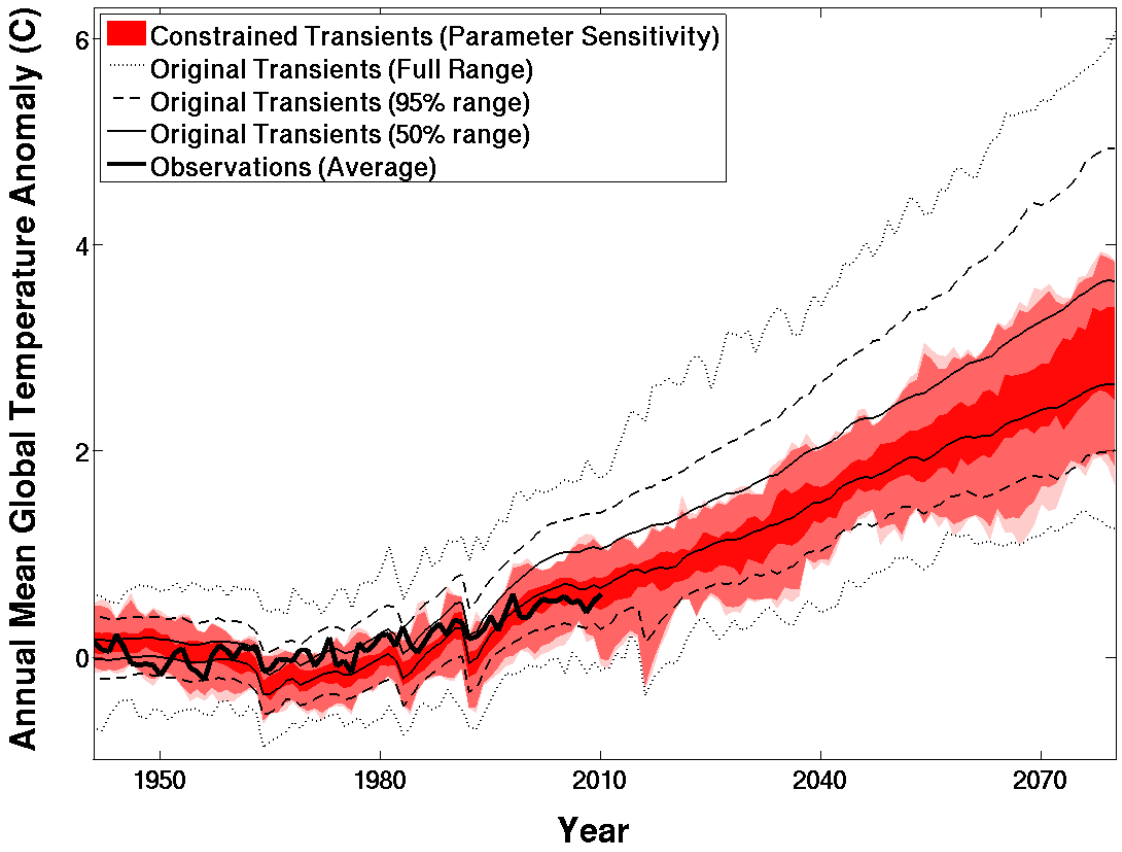


Figure 7.20: Annual mean global temperature anomaly for transient ensemble constrained by model parameters with greatest sensitivity for 70-year (1941-2010) global temperature trends (red shading; 37 simulations) and the original transient ensemble (black lines; 1,692 simulations). Both ensembles show the 25-75%, 2.5-97.5%, and min-max ranges. Observations are averaged together to give a single estimate. Anomalies are relative to a 1941-1970 base period.

The corresponding constrained regional ensembles are shown in Figure 7.21. Again, a similar decrease in the average warming trend is seen across the NA regions as well as a decrease in precipitation rate trend when a trend originally existed. The ensemble range also was decreased. Therefore, this constraint reduced the uncertainty in future climate projections at the global and NA regional levels. These constrained transient ensembles are discussed further, in terms of their comparison to the CMIP3 and CMIP5 ensembles, in Chapter 8.

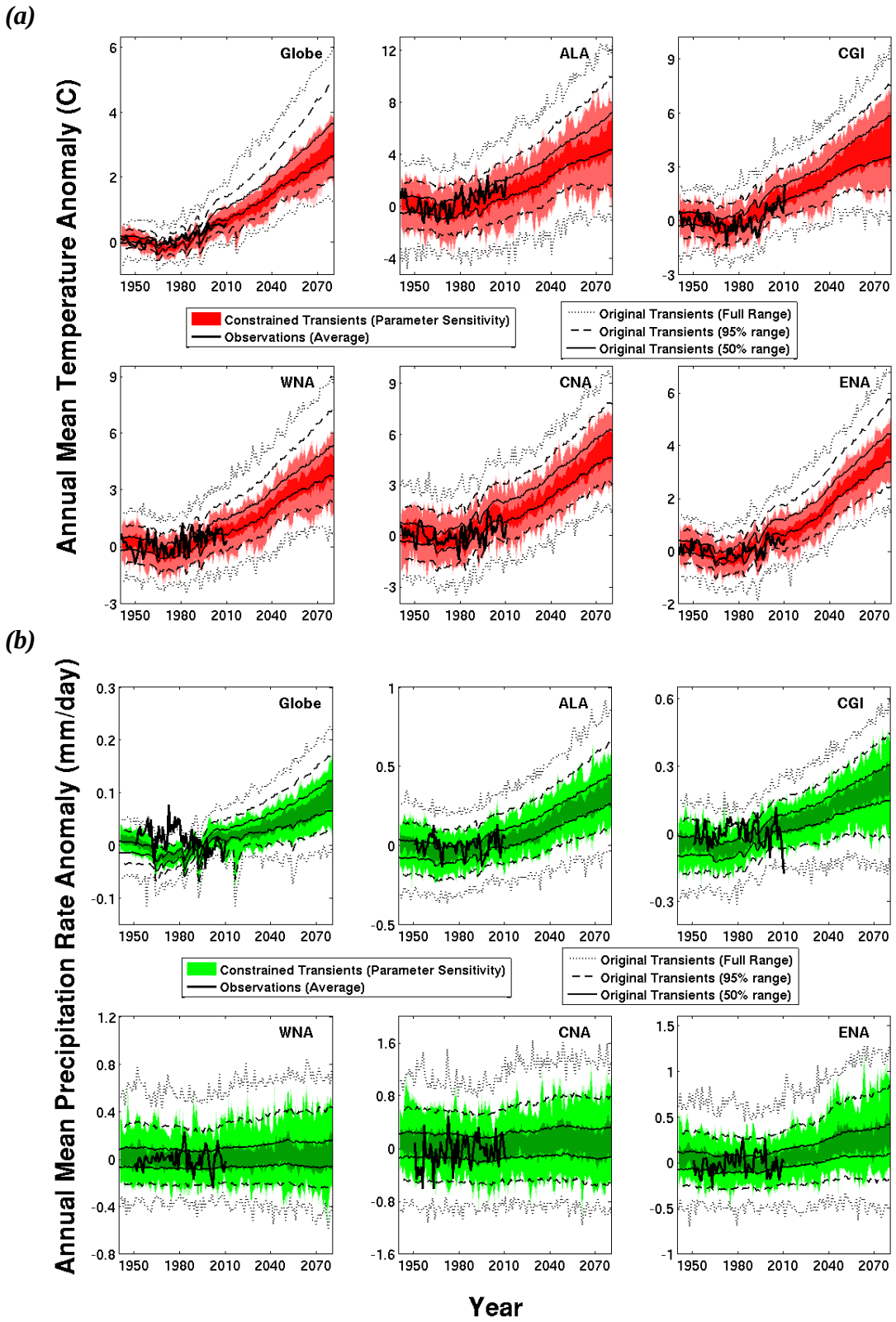


Figure 7.21: Same as Figure 7.19 but including regional comparisons for annual mean anomalies of *(a)* temperature (C) and *(b)* precipitation rate (mm/day). Temperature anomalies are relative to a 1941-1970 base period and precipitation anomalies are relative to 1981-2010.

In conclusion, both the near-term observational constraint (30-year global temperature trends) and the parameter sensitivity constraint (associated with parameter value performance over 70-year global temperature trend) generally reduced the temperature ensemble mean and decreased the range of possible future projections. This same conclusion was found in Stott et al. (2013) where they used an optimal fingerprint detection analysis (e.g., Allen and Tett 1999; Allen and Stott 2003; Stott et al. 2003) to observationally constrain future projections. In that analysis six CMIP5 models were used to assess the impact historical forcings of modeled anthropogenic greenhouse gases and other anthropogenic forcings (i.e., aerosols) had on warming and compared each to observed warming in order to generate scaling factors to represent how much a model's temperature response to the different forcings needed to be scaled up or downward. These scaling factors on temperature response were then applied to future forcings to produce observationally constrained projections.

Additionally, Rowlands et al. (2012) used a similar PPE from the same CPDN model (i.e., HadCM3L) and constrained future projections by a goodness-of-fit statistic based on the spatio-temporal pattern of surface temperatures from 1961 to 2010 and they also found that the constrained projection had a reduced ensemble spread and ensemble mean that was decreased (see Chapter 2, Figure 2.6).

7.8 Summary

This chapter evaluated the performance of the CPDN HadCM3L transient simulations over the observational time period and quantified uncertainties in future projections for the globe and NA regions and produced constrained future projections based on a model's performance over the observational time period.

There were a total of 1,692 transient simulations comprised of 137 atmospheres, ten oceans, ten initial conditions, five values for scaling anthropogenic sulfates, 15 solar forcing scenarios, and 50 volcanic forcing scenarios. This resulted in 614 unique atmosphere/ocean combinations with the remaining 1,078 containing duplicate atmosphere/ocean combinations with variations to their anthropogenic sulfate scaling factor, natural forcings (solar or volcanic), or initial conditions. The long-term mean drift caused by imbalances in the atmosphere/ocean coupling process was removed by identifying the drift in a transient's corresponding control simulation with matching atmosphere and ocean parameters. A number of available transient simulations could not be used because they did not have a matching control with the same atmosphere/ocean parameters and therefore the long-term mean drift to remove was unknown.

Observational estimates of temperature and precipitation generally were near the 50% range of the transient simulation ensemble and were almost always within the 95% range for both the globe and North American regions. The simulations tended to show greater warming across the most recent decade (i.e., 2000's) than found in observations possibly due to natural variability in the observations (i.e., heat going into the ocean within the PDO cycle or ENSO) or too large climate sensitivity in some models.

Future projections of temperature showed increased warming in all regions with greater warming occurring over the future projection period than seen over the observational period. Future projections of precipitation did not change for WNA or CNA but did show an increase in other regions, with only a minimal increase in ENA. The uncertainty range tended to increase with time for both temperature and precipitation across the future projection period.

There was no change found in future temperature interannual variability but a slight increase found in precipitation interannual variability for all NA regions. The magnitude of the temperature seasonal cycle was reduced in the future at higher latitudes, indicating greater winter warming, and increased in WNA and CNA, indicative of summer drying across the region.

Parameters ANTHSCA, HANEYSFACT, and RHCRIT were most sensitive with regards to 30- and 70-year trends over the observational period. ANTHSCA impacts temperature by scaling anthropogenic sulfates, HANEYSFACT is associated with imbalances between the atmosphere and ocean coupled model across the 20th century, and RHCRIT defines the rate at which clouds form based on the amount of moisture in a model grid cell. In future projected trends, the most important parameters included more cloud parameters indicating the important role of cloud feedbacks on the climate sensitivity and the future warming trends.

Past global temperature trends were the best identified predictors of future regional climatic trends (especially 30-year trends) and therefore used to constrain future projections. Also, future projections were constrained based on parameter sensitivity of the top three parameters (best reproducing 70-year past global temperature

trends). Constraining based on observed 30-year global temperature trends and by parameter sensitivity resulted in a reduction in the spread of the resulting constrained ensemble as well as a decrease in the ensemble mean (i.e., future projections resided within the lower/cooler part of the original ensemble). This result was similar to that found by Stott et al. (2013) and Rowlands et al. (2012) who used different approaches for constraining future projections.

Constraining future projections by observed 70-year global temperature trends did not change the general characteristics of the transient ensemble (i.e., maintained a similar ensemble mean, 50%, and 95% range).

CHAPTER 8

CPDN VERSUS CMIP ENSEMBLES

This chapter compares the results of the CPDN HadCM3L model analysis of the previous chapters to the multi-model ensembles of climate model simulations from the World Climate Research Programme (WCRP) Coupled Model Intercomparison Project Phase 3 (CMIP3; Meehl et al. 2007a) and Phase 5 (CMIP5 Taylor et al. 2011) described in Chapter 2, Section 2.3. CMIP3 and CMIP5 data were downloaded from the Koninklijk Netherlands Meteorological Institute (KNMI) Climate Explorer (http://climexp.knmi.nl). The goal of the chapter is to assess whether the uncertainty estimates from CMIP3 and CMIP5 adequately represent uncertainties in different climate metrics using a much larger ensemble of simulations. Section 8.1 investigates control simulation comparisons and Section 8.2 transient simulation comparisons. Section 8.3 summarizes the key findings.

8.1 CONTROL SIMULATIONS (CPDN VS. CMIP5)

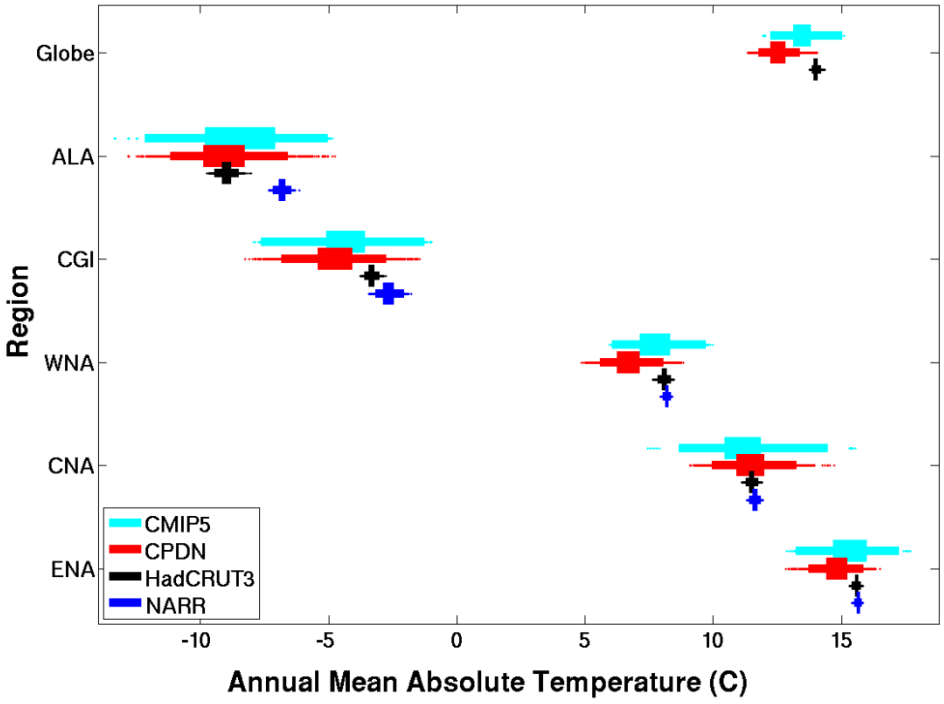
Select analyses from the CPDN HadCM3L control simulations were compared to CMIP5 control simulations to assess internal variability in the models. Only CMIP5 controls were utilized because they were readily available and contain the most recent model versions and therefore provide the most current estimates of natural variability in global climate models. There were 41 CMIP5 control simulations available for temperature and 37 for precipitation. All simulations were 190 years long and did not

contain model drift. These simulations were split into seven 30-year periods and climatic indices calculated and then placed into a single distribution for comparison to CPDN control simulations (287 samples for temperature and 259 samples for precipitation). It should be noted that while this provided a large sample size it was still significantly smaller than the 6070 samples available from the CPDN control simulation ensemble (1,214 simulations x 5 samples each). The subsections below investigate the comparisons of CPDN and CMIP5 model mean, seasonal cycle, and variability respectively.

8.1.1 Mean

The mean climate was assessed in the same manner as in Chapter 5, Section 5.3. Figure 8.1 provides annual mean distributions of absolute temperature and precipitation for CPDN, CMIP5, and observations. The annual mean temperature distributions (Figure 8.1(a)) of CPDN and CMIP5 were generally in good agreement except possibly for slightly warmer CMIP5 models in the global, WNA, and ENA distributions. In all three of these cases the CMIP5 distribution was closer to the observational distributions than CPDN, possibly pointing towards improved model performance with the newer generation of models in CMIP5 or better tuning of the model parameters to represent the observed climatology, recognizing that only limited tuning was done for the different parameter combinations for CPDN.

(a)



(b)

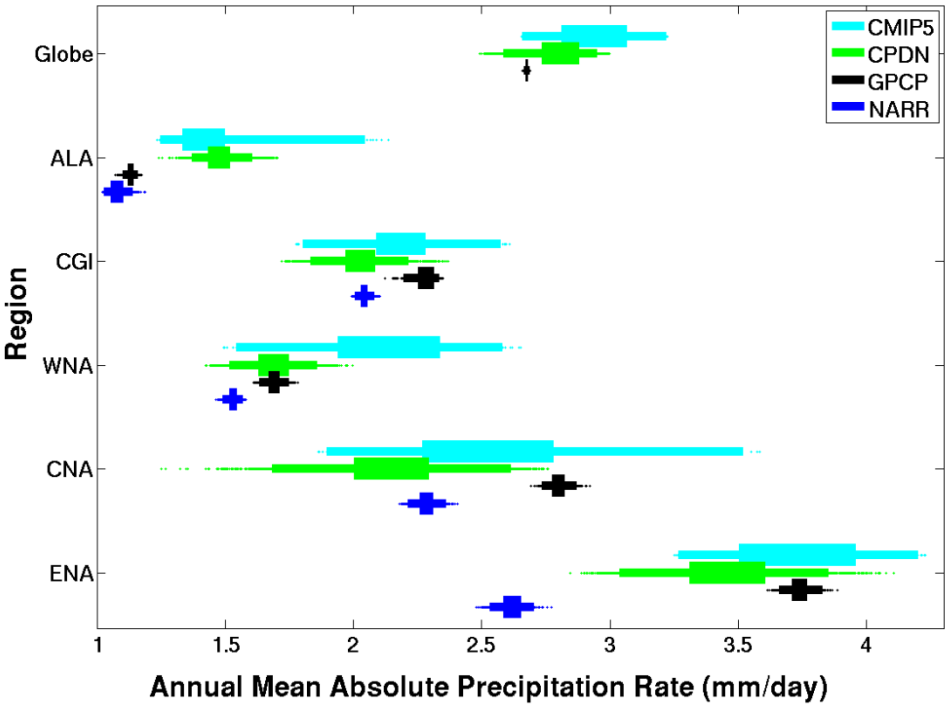


Figure 8.1: Annual 30-yr mean *(a)* temperature (°C) and *(b)* precipitation rate (mm/day) for the globe and five NA regions from the 1,214 CPDN control simulations (five samples per simulation), CMIP5 control simulations (seven 30-yr samples per simulation for 41 temperature and 37 precipitation simulations), and observational bootstrap distributions (6070 samples). Boxplots provide 25-75% (inner) and 2.5%-97% (outer) ranges and dots for samples outside the 95% range.

Annual mean precipitation (Figure 8.1(b)) for CMIP5 appeared to be relatively larger than CPDN. For the globe and high latitude regions this could be caused by the slightly warmer absolute temperatures found in some of the models which would allow for greater moisture availability. It is more difficult to identify an exact cause for the larger precipitation in the other, lower-latitude regions. The true cause may be from multiple factors tied to the variety of changes made in CMIP5 model development, that subsequently had an impact on precipitation processes (e.g., higher spatial resolution, more accurate topography, updated model physics, etc.). Or the CPDN HadCM3L model may simply be representative of the CMIP5 models in the lower range of the precipitation distributions.

In Figure 8.2 the same absolute annual mean temperature and precipitation distributions are shown except with the addition of winter (DJF) and summer (JJA) seasons. Again, the mean temperature (Figure 8.2(a)) of both CPDN and CMIP5 were generally in good agreement. The slightly warmer CMIP5 annual means could be seen in the globe for both seasons and in WNA and ENA mainly in winter. The slightly warmer CMIP5 winters were found in CNA as well (and even somewhat in ALA and CGI) which implies that some of the CMIP5 models generate warmer winters than CPDN across much of NA.

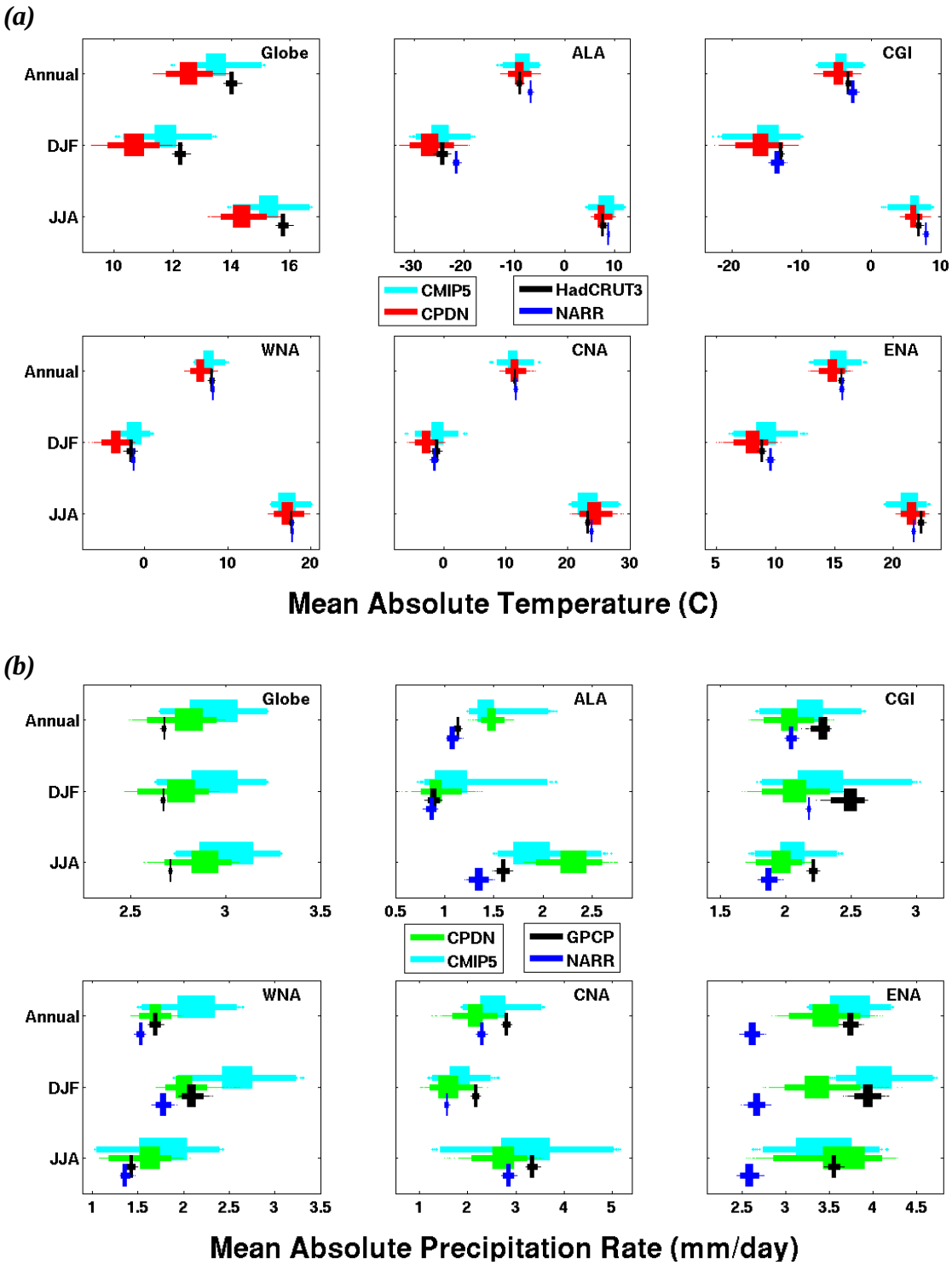


Figure 8.2: Same as Figure 8.1 but including winter (DJF) and summer (JJA) means.

The larger CMIP5 annual precipitation was found to occur mainly during winter except possibly for CNA (Figure 8.2(b)). With a number of the models found with higher temperatures this may point to greater moisture availability in those models leading to greater precipitation. The other feature worth noting with the precipitation distributions was the relatively larger distribution range found in some of the CMIP5 cases (e.g., ALA-annual and DJF; CGI-DJF; CNA-JJA). The reasoning for this was uncertain but it should be noted that some of the CMIP5 model simulations generated a wider range of absolute mean precipitation than CPDN.

8.1.2 Seasonal Cycle

Next the magnitude of the seasonal cycle (JJA-DJF) in temperature was assessed in the same manner as was done in Chapter 5, Section 5.4.2. Figure 8.3 provides the resulting distributions which show general agreement between CPDN and CMIP5 with the CPDN distributions slightly shifted to larger magnitudes. This makes sense given the slightly warmer temperatures found in CMIP5 DJF absolute mean distributions and the small differences found in the JJA distributions (Figure 8.2(a)).

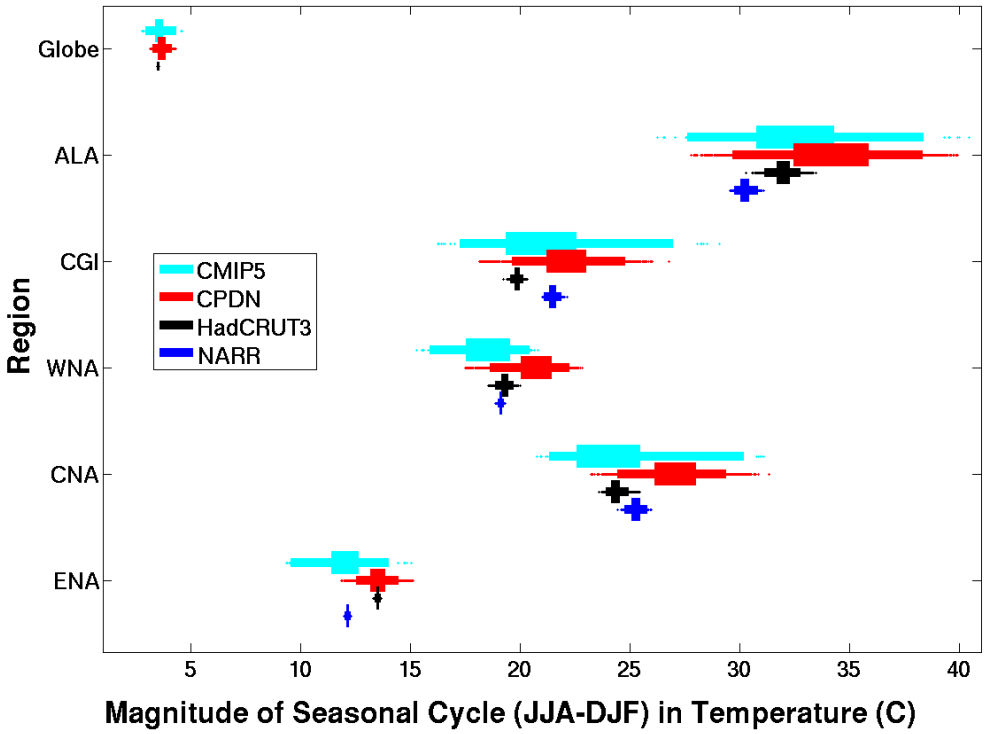


Figure 8.3: Magnitude of the seasonal cycle (JJA-DJF) of temperature for the globe and five NA regions for the 1,214 control simulations (five samples per simulation), CMIP5 control simulations (seven 30-yr samples per simulation for 41 temperature and 37 precipitation simulations), and observational bootstrap distributions (6070 samples). Boxplots provide 25-75% (inner) and 2.5%-97% (outer) ranges and dots for samples outside the 95% range.

8.1.3 Variability

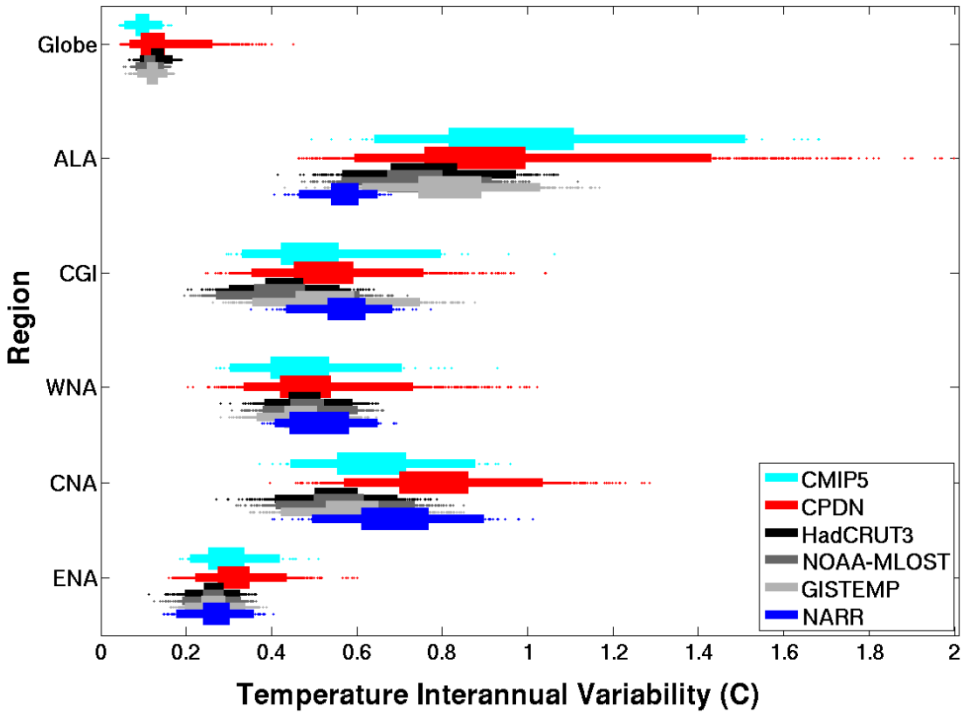
Next, interannual and decadal variability of CMIP5 control simulations were compared to CPDN control simulations and detrended observations (as was done in Chapter 5, Section 5.5.1). Figure 8.4 displays the resulting interannual variability distributions. The two ensembles agree well in most regions for both temperature and precipitation with CPDN distributions spanning as large or typically larger ranges of variability compared to CMIP5. This shows that the CPDN perturbed physics ensemble (PPE) did not underestimate the variability range found in the CMIP5 multi-model ensemble (MME).

As was found in CPDN temperature interannual variability (Section 5.5.1), CMIP5 extends to relatively larger variability in ALA compared to observations but this was not the case in global or CNA variability (Figure 8.4(a)). Therefore some of the physics parameter variations allowed for greater variability in these regions compared to CMIP5. In fact, the largest difference between CMIP5 and CPDN temperature interannual variability was found at the global level where CPDN extended to much larger values of variability. This could indicate that CMIP5 is underestimating global temperature variability. With precipitation interannual variability (Figure 8.4(b)), the main feature previously found with the CPDN distribution (Section 5.5.1) was the apparent shift to larger variability in CNA compared to observations. While a small shift in CMIP5 was found with extensions to larger variability it was not to the same extent as CPDN, again indicating parameter settings allowing larger variability in that region.

Figure 8.5 explores interannual variability further by providing variability for DJF and JJA. As with CPDN, the temperature interannual variability (Figure 8.5(a)) in the NA regions for CMIP5 was largest during winter, a feature previously found and resulting from the greater temperature difference between mid-latitudes and polar regions during northern hemisphere winter and the arctic frontal passages that traverse the region during that time period. CMIP5 did not contain larger variability for either season at the global level as seen in CPDN and for CNA it was found that JJA provided the main difference in variability between the two, with CPDN shifted to larger variability. Further, the shift to larger precipitation interannual variability in CPDN

CNA compared to CMIP5 was caused again by increased JJA variability (Figure 8.5(b)).

(a)



(b)

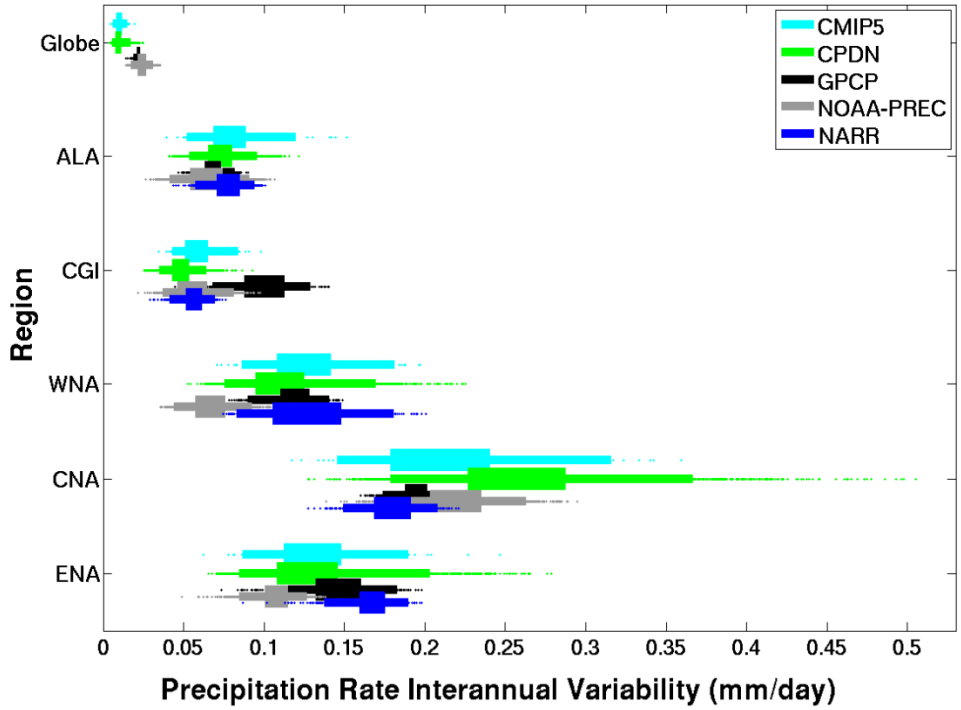
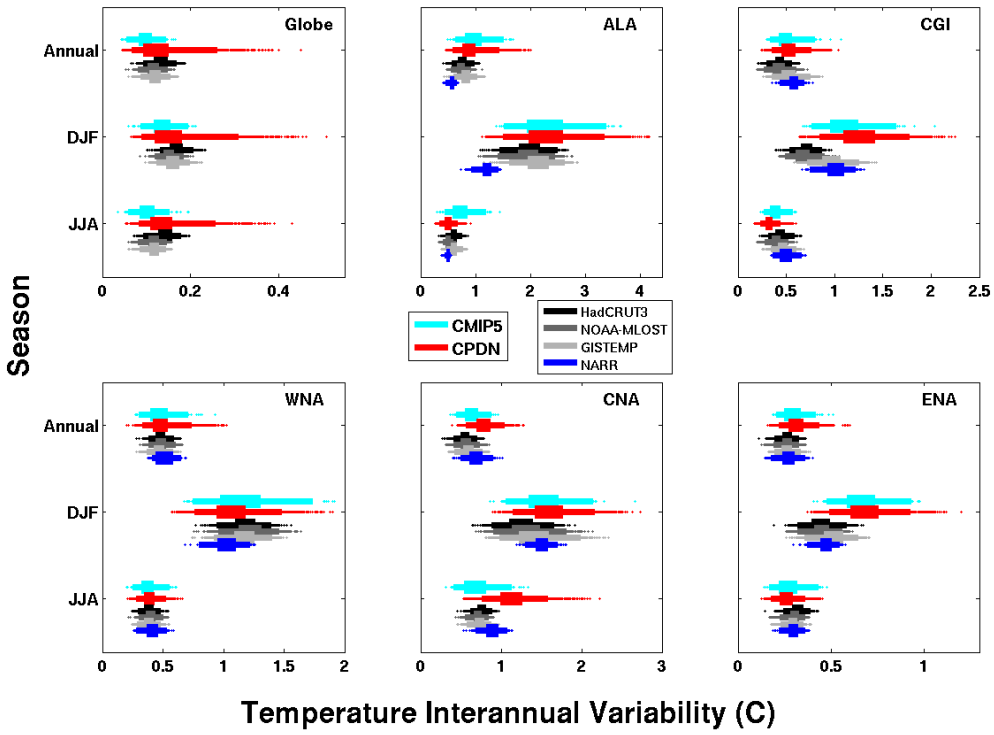


Figure 8.4: Annual 30-yr interannual variability for *(a)* temperature (°C) and *(b)* precipitation rate (mm/day) for the globe and five NA regions from the 1,214 control simulations (five samples per simulation), CMIP5 control simulations (seven 30-yr samples per simulation for 41 temperature and 37 precipitation simulations), and observational bootstrap distributions (6070 samples). Boxplots provide 25-75% (inner) and 2.5%-97% (outer) ranges and dots for samples outside the 95% range.

(a)



(b)

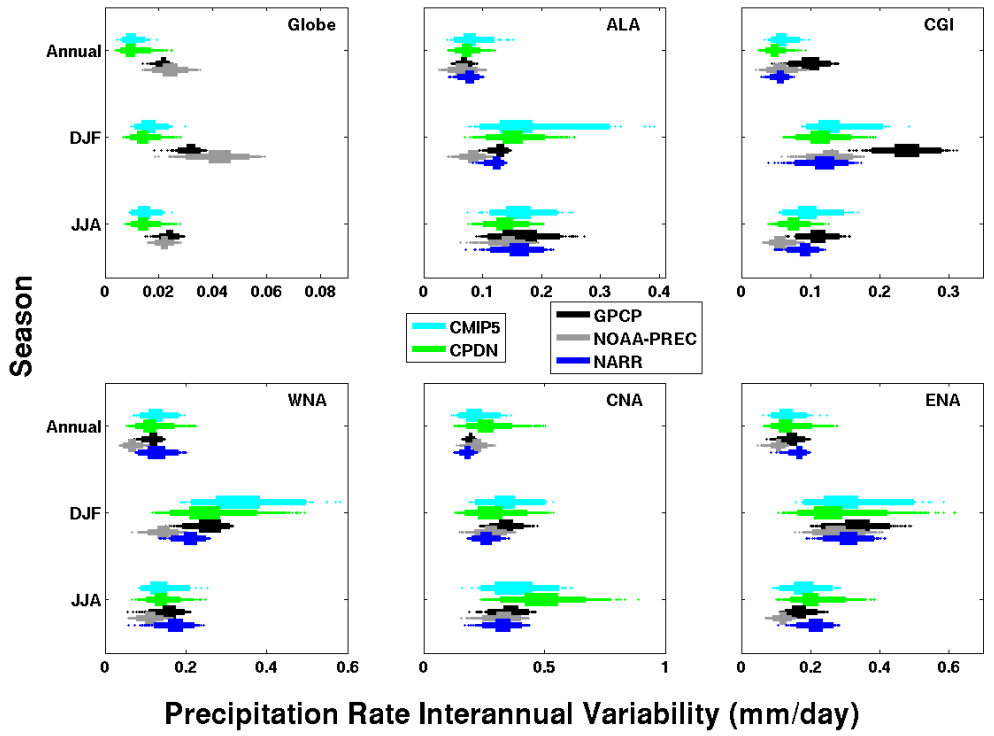
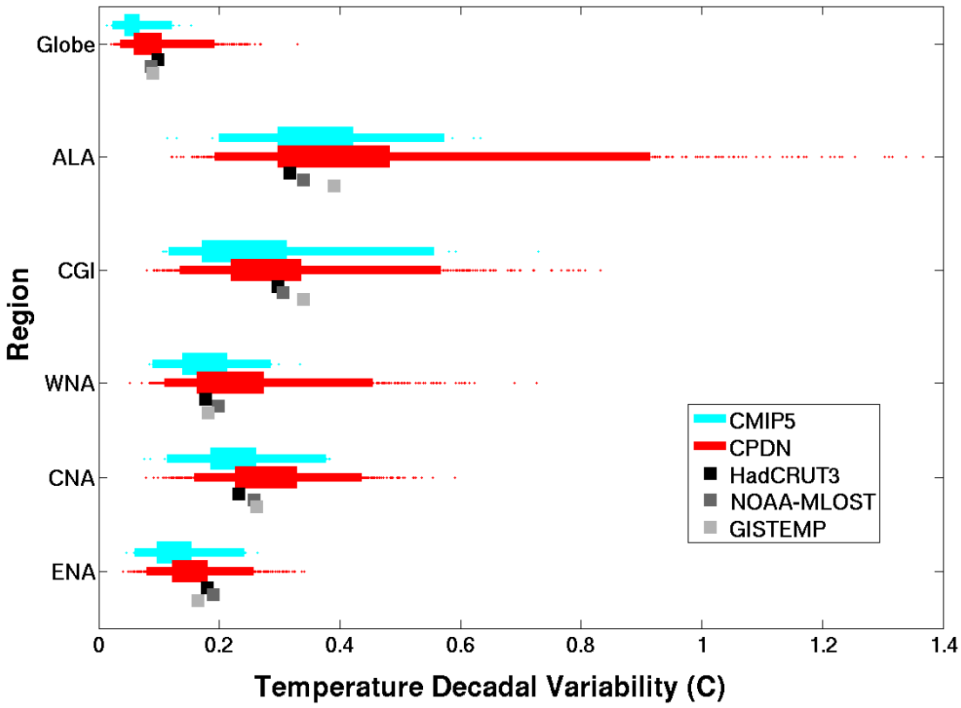


Figure 8.5: Same as Figure 8.4 but including winter (DJF) and summer (JJA) interannual variability.

Decadal variability distributions for annual mean output are shown in Figure 8.5. These resulting distributions show similar characteristics to those found for interannual variability (Figure 8.4) with fairly consistent agreement between CPDN and CMIP5. The only difference was a further extension to relatively larger variability in nearly every region for CPDN compared to CMIP5. The extension to relatively greater variability in CPDN compared to CMIP5 was even more amplified for the two more extreme cases of variability in ALA temperature (Figure 8.5(a)) and CNA precipitation (Figure 8.6(b)). This suggests that the CMIP5 model simulations may be underestimating the decadal variability of both temp and precipitation, possibly due to their smaller ensemble size and similarity in model components.

(a)



(b)

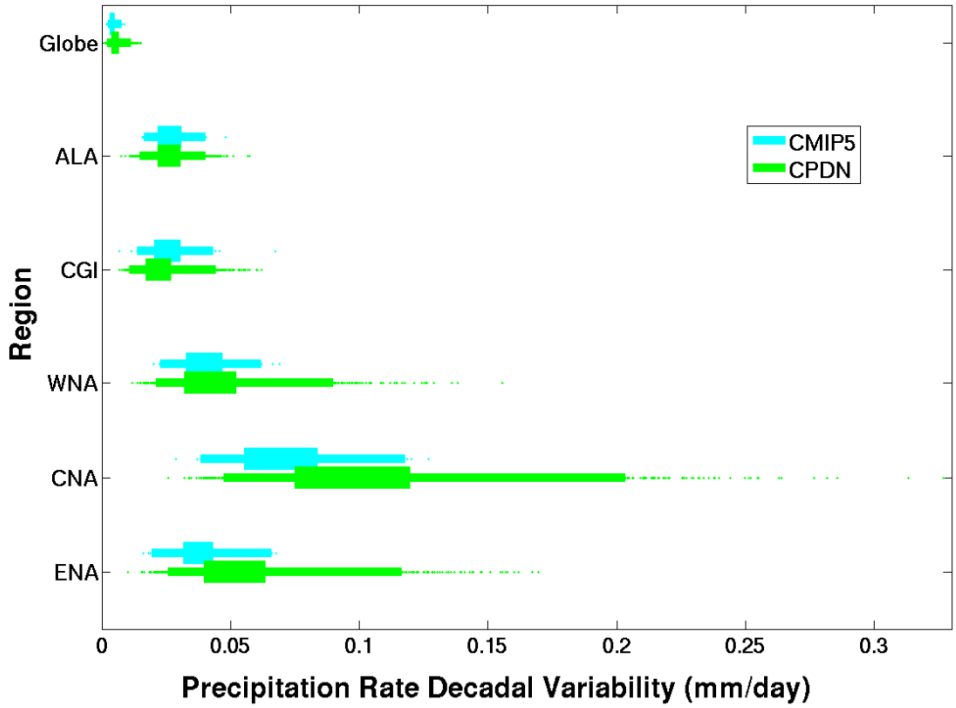


Figure 8.6: Annual 100-yr decadal variability for *(a)* temperature (°C) and *(b)* precipitation rate (mm/day) for the globe and five NA regions from the 1,214 control simulations (five samples per simulation), CMIP5 control simulations (three 100-yr samples per simulation for 41 temperature and 37 precipitation simulations), and one 90-year sample for each of the temperature observational data sets. Boxplots provide 25-75% (inner) and 2.5%-97% (outer) ranges and dots for samples outside the 95% range.

8.2 TRANSIENT SIMULATIONS (CPDN VS. CMIP3 & CMIP5)

The CPDN HadCM3L transient simulation ensemble was compared to CMIP3 and CMIP5 transient ensembles to assess any distribution differences. There were 52 CMIP3 transient simulations and 46 CMIP5 simulations available. Recall there were 1,692 CPDN transient simulations (Chapter 7). The subsections below provide the comparisons over the historical period, future projections, and constrained future projections respectively.

8.2.1 Historical Time Period

Figure 8.7 provides the CPDN annual mean global temperature anomaly ensemble and observational estimates for the 1941-2010 historical time period (discussed in Chapter 7, Section 7.3.1) as well as annual time series for each of the 52 CMIP3 transient simulations (Figure 8.7(a)) and 46 CMIP5 transient simulations (Figure 8.7(b)). The CMIP3 and CMIP5 simulations generally resided near the CPDN 95% range with CMIP5 in slightly better agreement with CPDN, at least prior to 2000. CMIP5 also appears to align slightly better with observations than CMIP3 (e.g., particularly between the mid-1960's to 2000). This could be associated with improved model development and the fact that CMIP5 operates under historical forcing through 2005 while CMIP3 only goes through 2000. Also, some of the CMIP3 models did not include volcanic forcing in their historical runs and therefore their simulations may be slightly warmer after the 1960's because of it. As was found in CPDN, most models within CMIP3 and CMIP5 produced warmer conditions across the 2000's than seen in

observations which was thought due to natural variability in the climate system driving short term observational estimates (refer to Section 7.3.1 for further discussion).

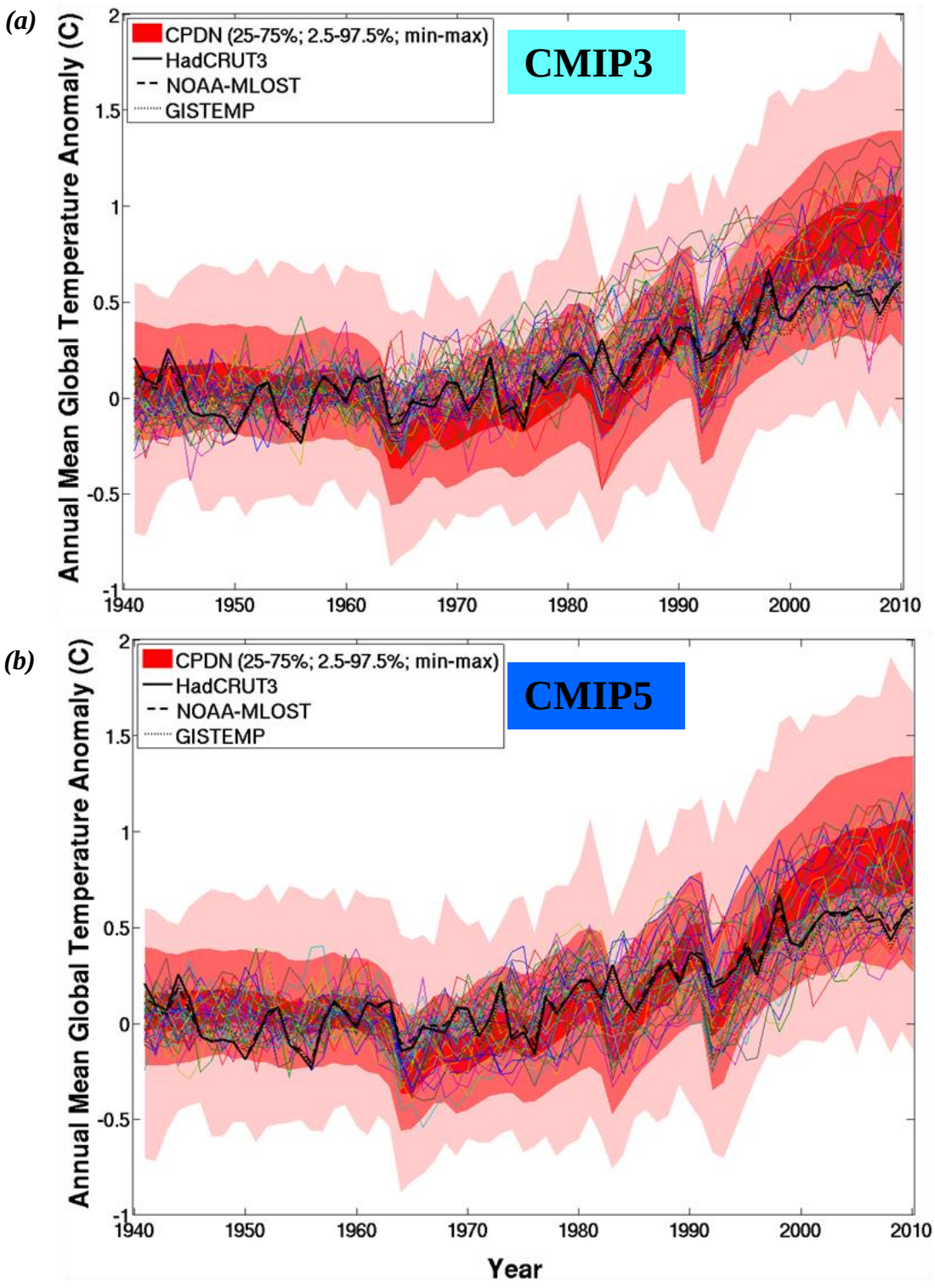


Figure 8.7: Annual mean global temperature anomaly for the 1,692 transient simulations (red shading), three observational data sets (HadCRUT3, NOAA-MLOST, GISTEMP), and *(a)* 52 CMIP3 and *(b)* 46 CMIP5 simulations (colored lines) over the 1941-2010 observational time period. The transient ensemble is shaded according to the 25-75%, 2.5-97.5%, and min-max ranges. Anomaly values are relative to a 1941-1970 base period.

Decadal average distribution ranges for both CMIP3 and CMIP5 are shown in Figure 8.8 with the same CPDN distribution and observations from Figure 8.7. The increase in temperatures over the latter half of the century was apparent in the CMIP distributions as well as CMIP5's slightly better agreement with observations. The same type of plot is shown for each NA region in Figure 8.9. For temperature (Figure 8.9(a)) the CMIP distributions were generally the same and show the same increase in the latter part of the time period in each region as found in CPDN and observations. The CMIP distributions remain centered near the CPDN 50% range except in the final decade for some regions where they are slightly cooler. For precipitation (Figure 8.9(b)), the CMIP distributions show the same increasing trend as CPDN in ALA and CGI and the relative no trend across the other three NA regions. With ALA and CGI, CMIP5 precipitation appears to remain closer to the CPDN 50% range than CMIP3.

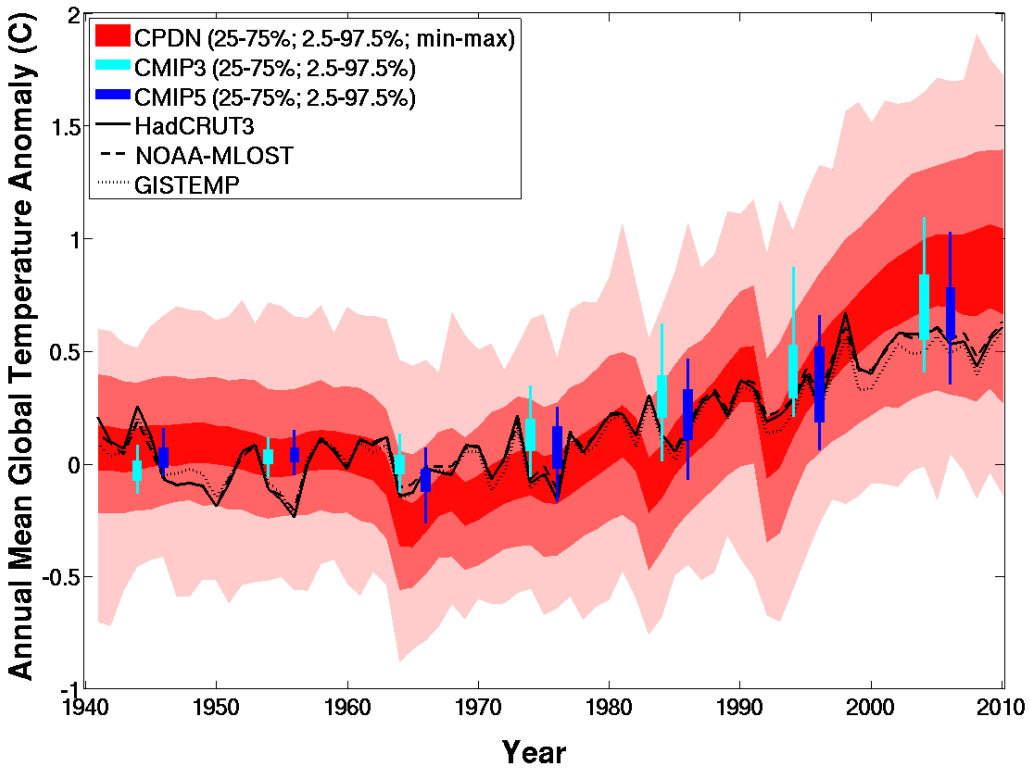


Figure 8.8: Same as Figure 8.7 but with CMIP3 and CMIP5 ensembles displayed as boxplots representing decadal means values. These boxplots include the 25-75% and 2.5-97.5% ranges.

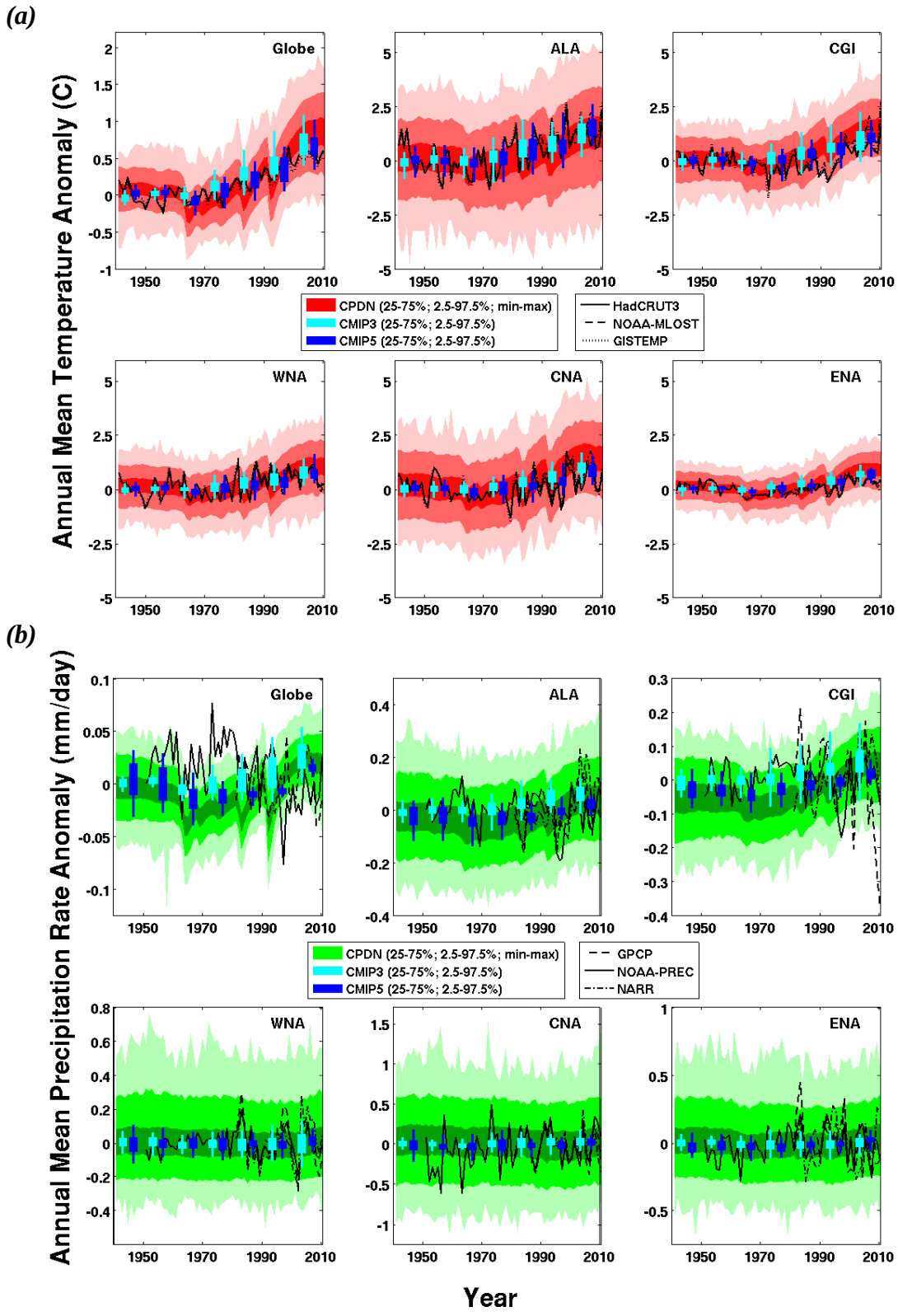


Figure 8.9: Same as Figure 8.8 but includes NA regional results for *(a)* temperature (°C) and *(b)* precipitation rate (mm/day). Temperature anomalies are relative to a 1941-1970 base period and precipitation anomalies are relative to 1981-2010.

8.2.2 Future Projections

In this sub-section the future projections of the CMIP ensembles are compared to the CPDN ensemble (discussed in Chapter 7, Section 7.4). Figure 8.10(a) shows annual mean global temperature for the CPDN ensemble and observations compared to time series of the 52 CMIP3 members under Special Report on Emissions Scenarios (SRES) A1B scenario Nakićenović and Swart 2000 and Figure 8.10(b) shows the same but with only the simulation from the CMIP3 HadCM3 model (Gordon et al. 2000) which is the parent model of the CPDN HadCM3L model. The full CMIP3 ensemble (Figure 8.10(a)) was generally within the CPDN 95% range but more within the range of lower projected warming while the HadCM3 model was similar to the CPDN mean in the future projections. The HadCM3 model was one of the models in the CMIP3 ensemble having slightly larger projecting warming compared to other models. However, as the CPDN HadCM3L distribution shows, the physic parameters within HadCM3 model could have been configured in alternative ways that could have led to results similar to the other CMIP3 simulations, or quite different (e.g., could have been even warmer comparatively).

This provides a good example as to the significance of perturbed physics ensembles compared to multi-model ensembles since it is apparent from Figure 8.10 that the single HadCM3 model simulation in the CMIP3 distribution can have its physics parameters changed across the range of uncertainty for each parameter and the resulting range of uncertainty in future projections (i.e., CPDN ensemble) can be even larger than the uncertainty range of the entire CMIP3 ensemble.

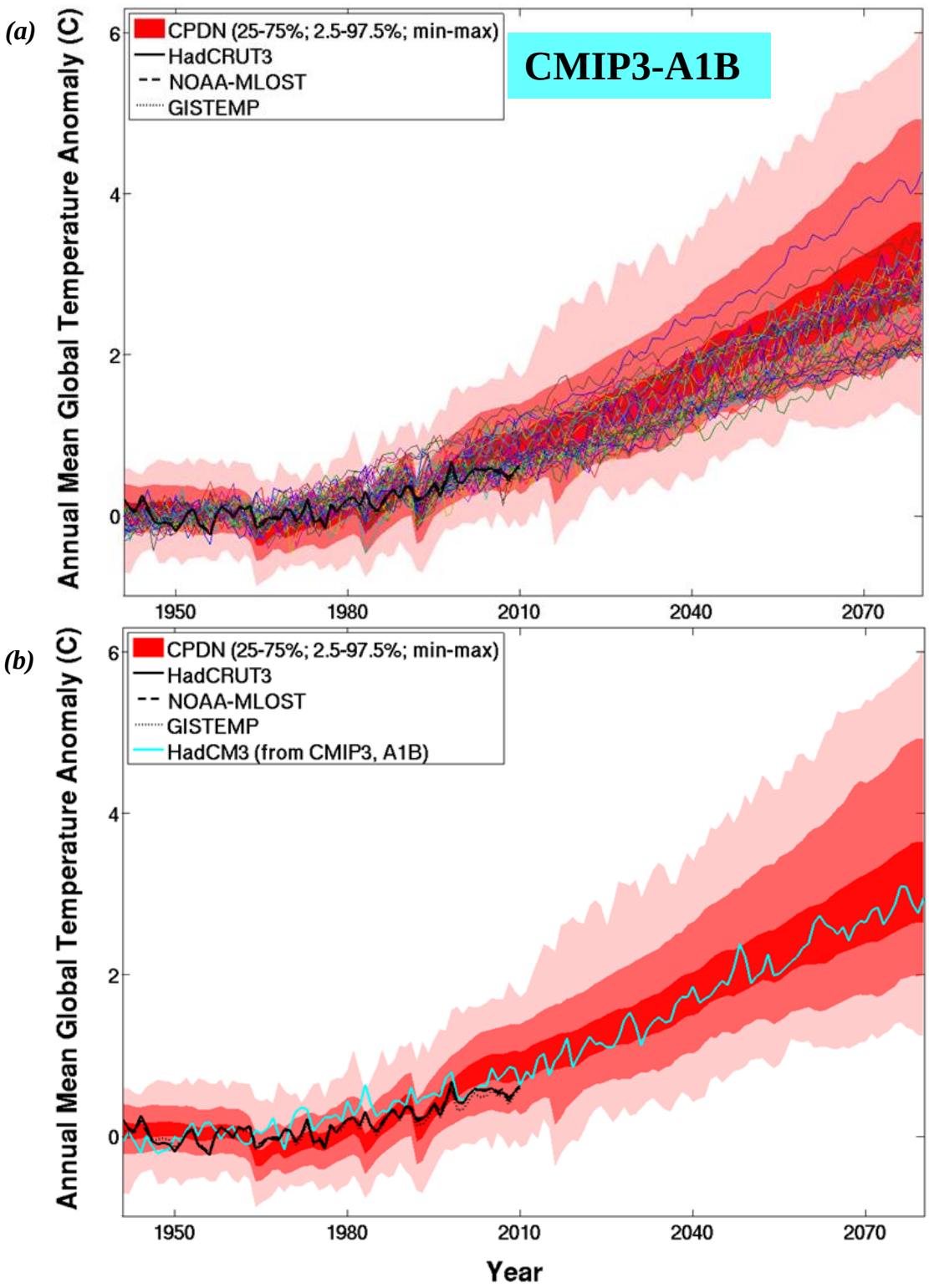


Figure 8.10: Annual mean global temperature anomaly from 1941-2080 for the 1,692 transient simulations (red shading), three observational data sets (HadCRUT3, NOAA-MLOST, GISTEMP), and *(a)* 52 CMIP3 simulations using SRES A1B and *(b)* the HadCM3 simulation from CMIP3. The transient ensemble is shaded according to the 25-75%, 2.5-97.5%, and min-max ranges. Anomaly values are relative to a 1941-1970 base period.

Figure 8.11(a) shows the comparison to the 46 CMIP5 members under the Representative Concentration Pathway (RCP) 6.0 Vuuren et al. 2011 and Figure 8.11(b) the next generation of the HadCM3 model named the Hadley Centre Global Environment Model version 2 (HadGEM2) Collins et al. 2008; Jones et al. 2011. Again, the future projections of the CMIP5 ensemble were on the cooler side of the CPDN ensemble's future projections and the HadGEM2 simulations had generally larger projected warming than most of the other CMIP5 members. It is difficult to make a true comparison between CMIP5 simulations and the CPDN ensemble since CMIP5 does not have a future forcing scenario that is exactly the same as CMIP3 and therefore CPDN. The CMIP3 SRES A1B scenario is close to but not the same as RCP 6.0 with the resulting future projections in global temperatures from RCP 6.0 simulations smaller than that of SRES A1B. This is further demonstrated in the discussion below.

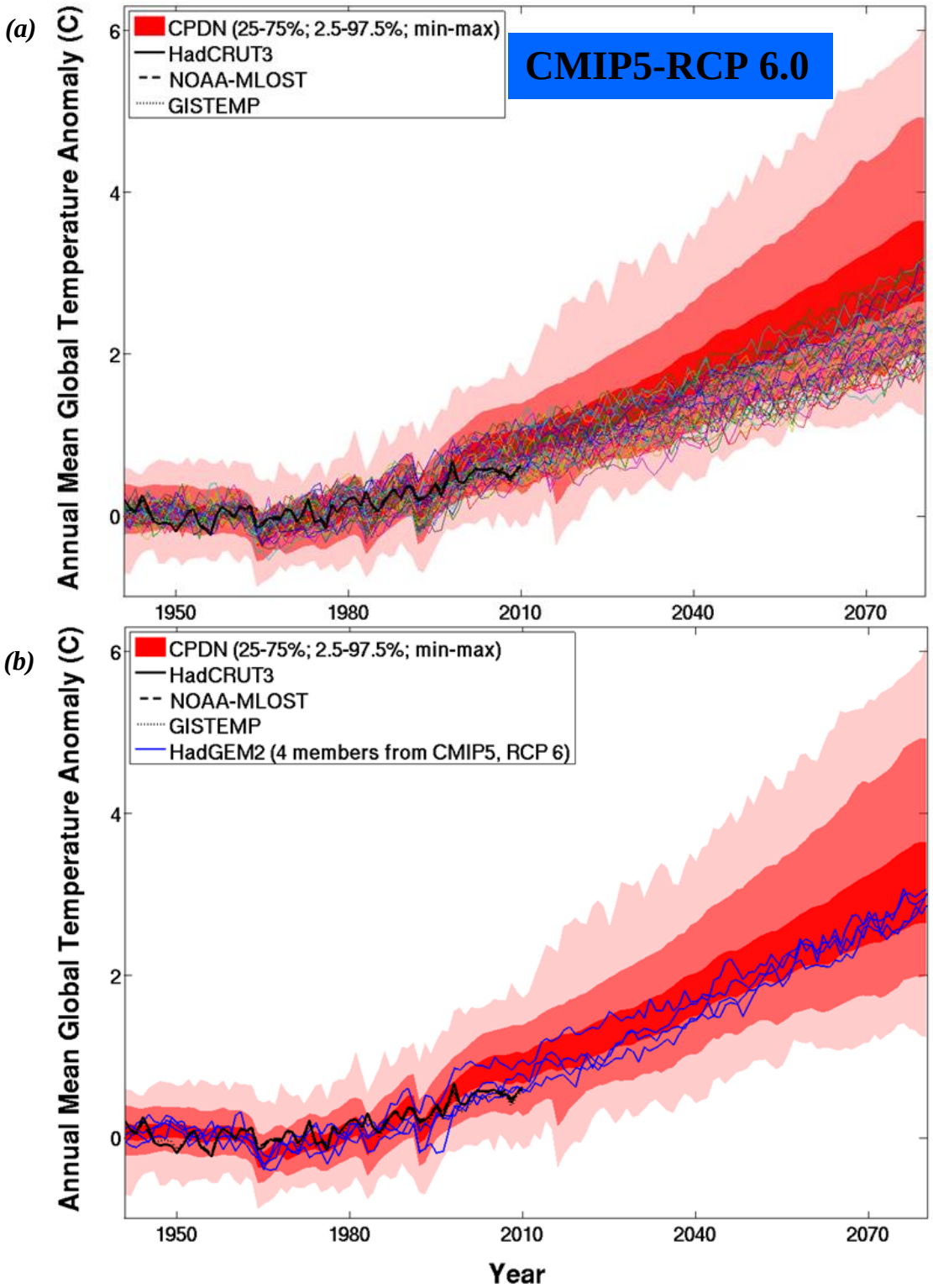


Figure 8.11: Annual mean global temperature anomaly from 1941-2080 for the 1,692 transient simulations (red shading), three observational data sets (HadCRUT3, NOAA-MLOST, GISTEMP), and *(a)* 46 CMIP5 simulations using RCP 6.0 and *(b)* four HadGEM2 simulations from CMIP5. The transient ensemble is shaded according to the 25-75%, 2.5-97.5%, and min-max ranges. Anomaly values are relative to a 1941-1970 base period.

To better compare the CMIP3 and CMIP5 ensembles to one another and to the CPDN ensemble, Figure 8.12 displays the CMIP ensembles as decadal mean distributions on top of the CPDN and observational annual mean global temperatures. The reduced warming in the CMIP5 ensemble compared to CMIP3 is immediately apparent. Again this does not imply that the CMIP3 simulations were projecting too warm temperatures, as the two ensembles simply were generated using two different future forcing scenarios. There was another RCP scenario producing global temperatures warmer than SRES A1B (i.e., RCP 8.5) but the difference between the resulting projected warming temperatures was much larger than differences between SRES A1B and RCP 6.0. Therefore RCP 6.0 was the best CMIP5 forcing scenario for comparing to CMIP3 SRES A1B. The reduction in future warming due to the different forcings used must be taken into account in any comparison.

Figure 8.13 displays the same information as the global temperature results in Figure 8.12 but includes the NA regions and precipitation ensembles. The CMIP ensembles for temperature across the NA regions showed similar characteristics as found in the global results (Figure 8.13(a)) with CMIP5 distributions at slightly lower values than CMIP3 except for ALA where the two are roughly the same. They both show continued warming across the projection time period in all regions with the warming being slightly less than the CPDN ensemble mean. The precipitation projections (Figure 8.13(b)) for the CMIP ensembles were similar to the CPDN projections with an increase in precipitation for the globe, ALA, and CGI regions and minimal change across WNA, CNA, and ENA. In almost every case, for both temperature and precipitation, the 95% range of CMIP3 and CMIP5 is smaller than the

95% range of the CPDN ensemble suggesting they underestimate uncertainties due to perturbed physics.

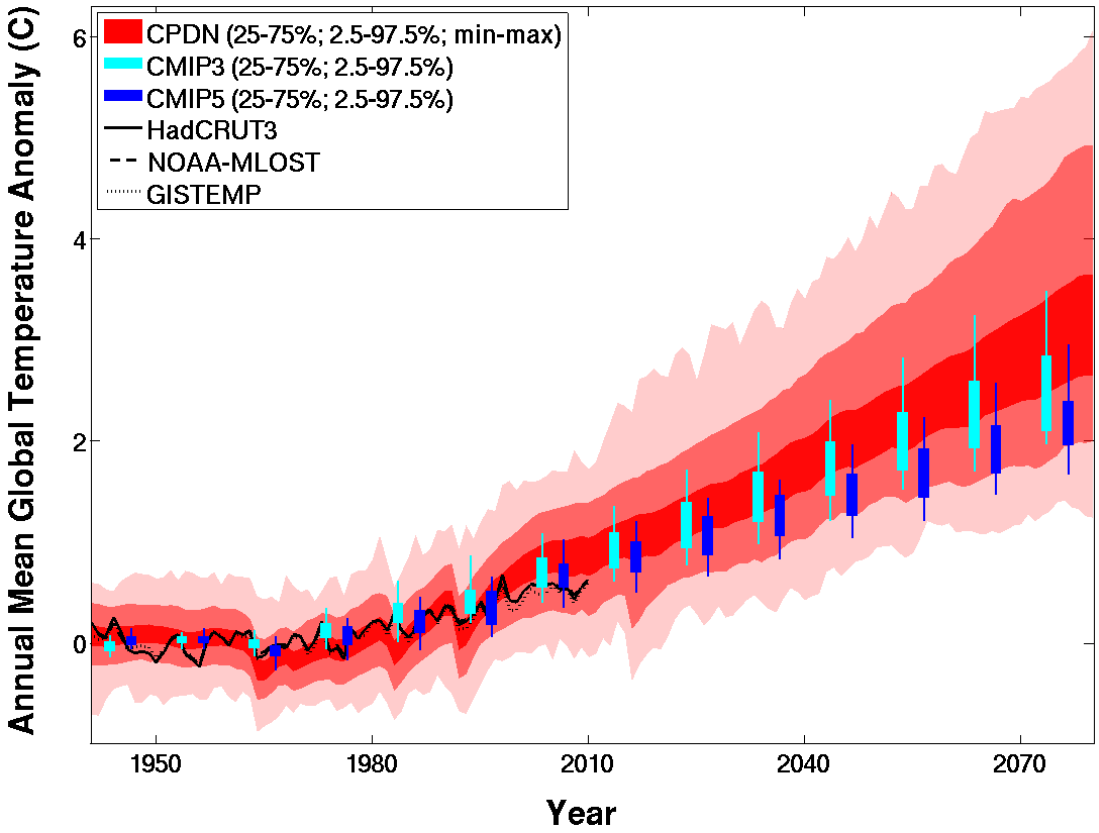


Figure 8.12: Same as Figure 8.11 but with CMIP3 (SRES A1B) and CMIP5 (RCP 6.0) ensembles displayed as boxplots representing decadal means values. These boxplots include the 25-75% and 2.5-97.5% ranges.

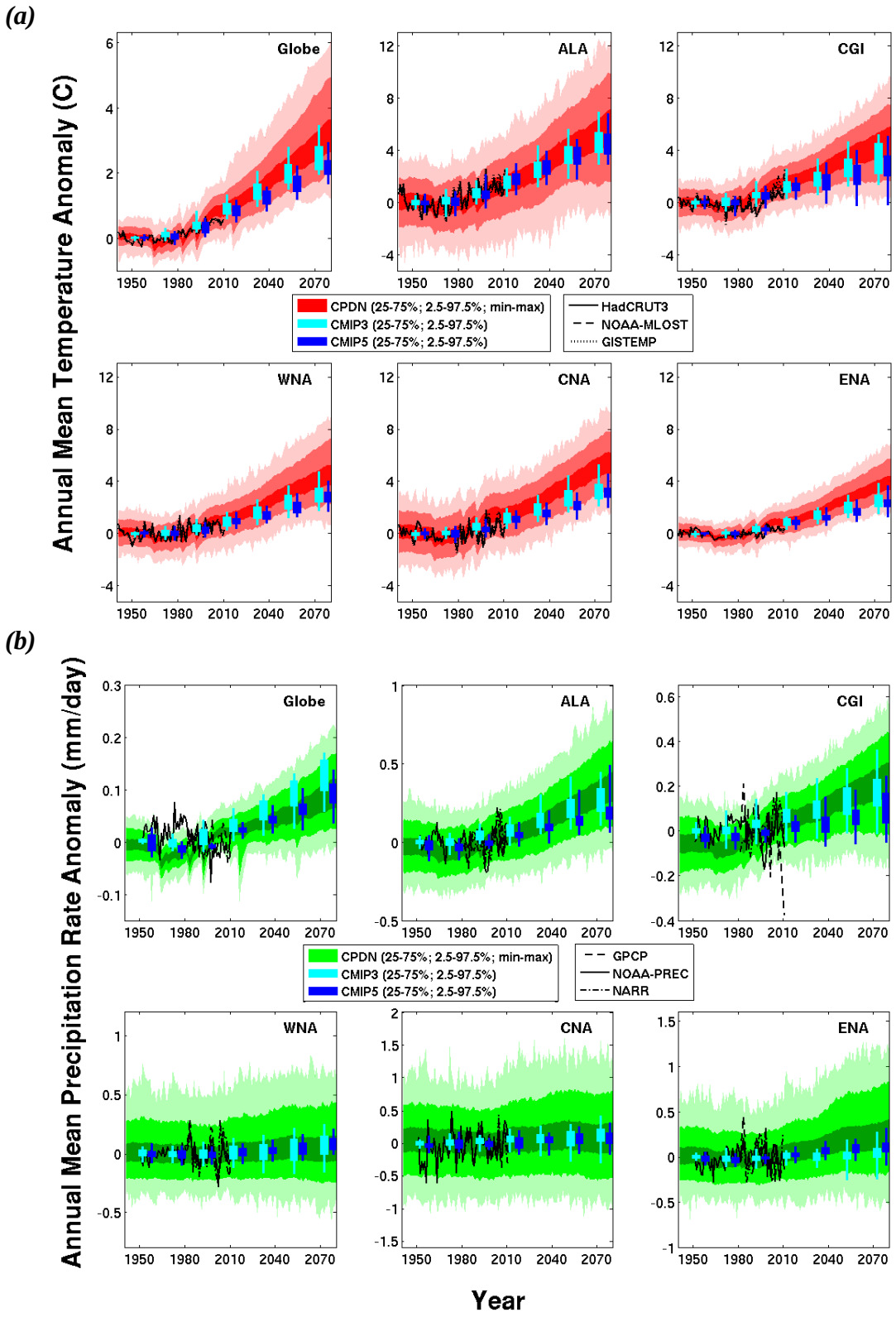
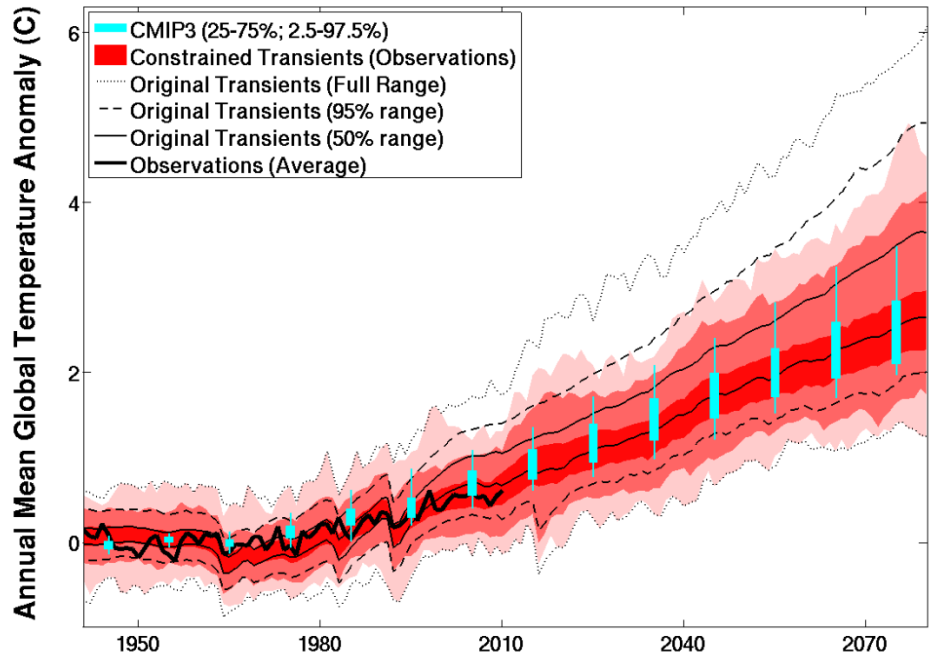


Figure 8.13: Same as Figure 8.12 but includes NA regional results for *(a)* temperature (°C) and *(b)* precipitation rate (mm/day). Temperature anomalies are relative to a 1941-1970 base period and precipitation anomalies are relative to 1981-2010.

8.2.3 CMIP3 versus Constrained CPDN Ensembles

Finally, the CMIP3 ensemble was compared to the constrained CPDN ensembles from Chapter 7, Section 7.8. Only the CPDN ensembles constrained by observed 30-year global temperature trends and by parameter sensitivity were assessed because the ensemble constrained by observed 70-year global temperature trends did not alter the general characteristics of the initial full CPDN ensemble (Section 7.8.2). Figure 8.14 shows annual mean global temperature anomalies for the initial CPDN full ensemble (background black lines), mean observations (heavy black line), CMIP3 decadal mean distributions and the CPDN ensembles constrained by performance with 30-year (i.e., 1981-2010) global temperature trends (Figure 8.14(a)) and constrained by parameter sensitivity (Figure 8.14(b)). Note that constraining by observed 30-year trends resulted in a relatively larger number of ensemble members (255 simulations) compared to constraining by parameter sensitivity (37 simulations). Therefore the ensemble spread of the 37 simulations could be much smaller simply because of the smaller sample size (i.e., conclusions made from the larger ensemble are more robust). However the CMIP3 ensemble also had a relatively smaller number of samples, comparatively, at 52 simulations.

(a)



(b)

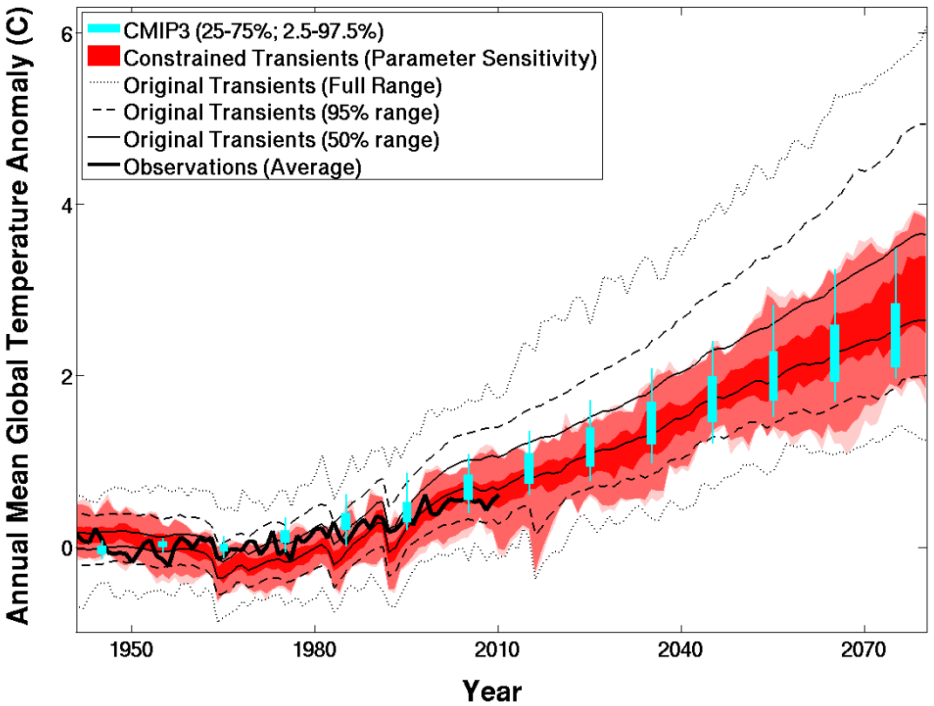


Figure 8.14: CMIP3 decadal mean global temperature distributions (52 simulations) with annual mean global temperature anomalies for transient ensemble constrained by (a) model performance compared to 30-year (1981-2010) observed trends (red shading; 255 simulations) and (b) model parameters with greatest sensitivity for 70-year (1941-2010) global temperature trends (red shading; 37 simulations) and the original transient ensemble (black lines; 1,692 simulations). Both sets of CPDN ensembles show the 25-75%, 2.5-97.5%, and min-max ranges. CMIP3 shows the 25-75% and 2.5-97.5% ranges and observations are averaged together to give a single estimate (heavy line). Anomalies are relative to a 1941-1970 base period.

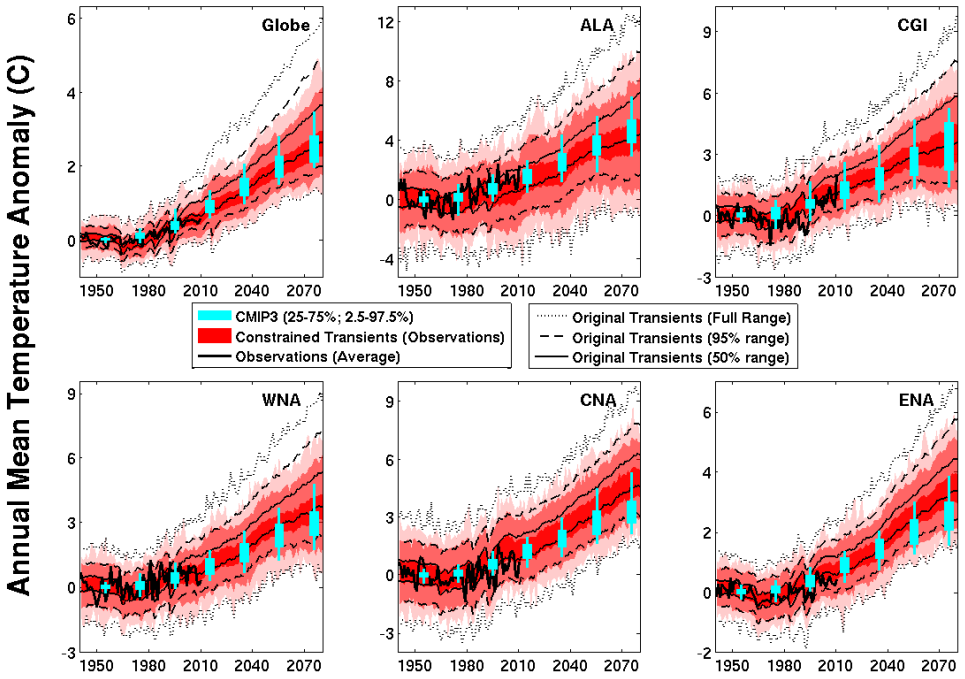
Looking at both constrained ensembles in Figure 8.14 (i.e., red shading) it is apparent that the mean of their projected warming was shifted to less warming compared to the original ensemble, bringing the 50% range in general agreement with that of the CMIP3 ensemble, especially for the observationally constrained CPDN ensemble containing the larger number of members (Figure 8.14(b)). The 95% range differences contained an interesting result. The extent of the greater warming side (i.e., top) of the CMIP3 95% range tended to align fairly well with the constrained ensembles, but the lower extent (less warming) of the 95% range did not reach as far as the CPDN 95% range, again especially for the observationally constrained ensemble. Therefore the uncertainty range of the CMIP3 ensemble was smaller than the constrained CPDN ensemble with an underestimation of the lower bound of the spread.

Focusing on the NA regions, Figure 8.15 and Figure 8.16 provide the same information as Figure 8.14 but for the regional and precipitation CPDN ensembles constrained by observations and parameter sensitivity respectively. As with the global results, the regional results of the two constrained ensembles show similar characteristics with the parameter sensitivity constrained ensemble exhibiting a relatively smaller range of uncertainty, again possibly due to the smaller number of samples. Therefore the two will be discussed together in general with a focus on the observationally constrained ensemble with larger sample size. The regional temperatures (Figure 8.15(a)) for the observationally constrained CPDN ensemble show similar comparison qualities to CMIP3 as found in the global results (Figure 8.14) with the CMIP3 50% range aligning fairly well in ALA and CGI but showing slightly less future warming for WNA, CNA, and ENA. The 95% range of CMIP3 was smaller than

CPDN for all regions except CGI with ALA underestimating the lower bound (i.e., less warming) and WNA, CNA, and ENA underestimating the upper bound (i.e., more warming). These same features were found in general for the CPDN ensemble constrained by parameter sensitivity but with less agreement between the 50% and 95% ranges within the CGI region (i.e., CPDN ensemble had greater warming).

For regional precipitation comparisons, both constrained CPDN ensembles displayed similar results (Figure 8.15(b) and Figure 8.16(b)). At the global level CMIP3 generally had a greater increase in precipitation than constrained CPDN. The 50% range was similar for both CMIP3 and constrained CPDN for ALA, CGI, and WNA but smaller for CMIP3 in CNA and ENA. The CMIP3 95% range was smaller than constrained CPDN in all regions except CGI, with ALA underestimating the lower bound and WNA, CNA, and ENA with all having much smaller ranges than CPDN. The general increasing trend in precipitation for ALA and CGI was found in both sets of ensembles as well as the minimal change found in WNA and CNA. The slight increasing trend in ENA in constrained CPDN ensembles was not found in CMIP3.

(a)



(b)

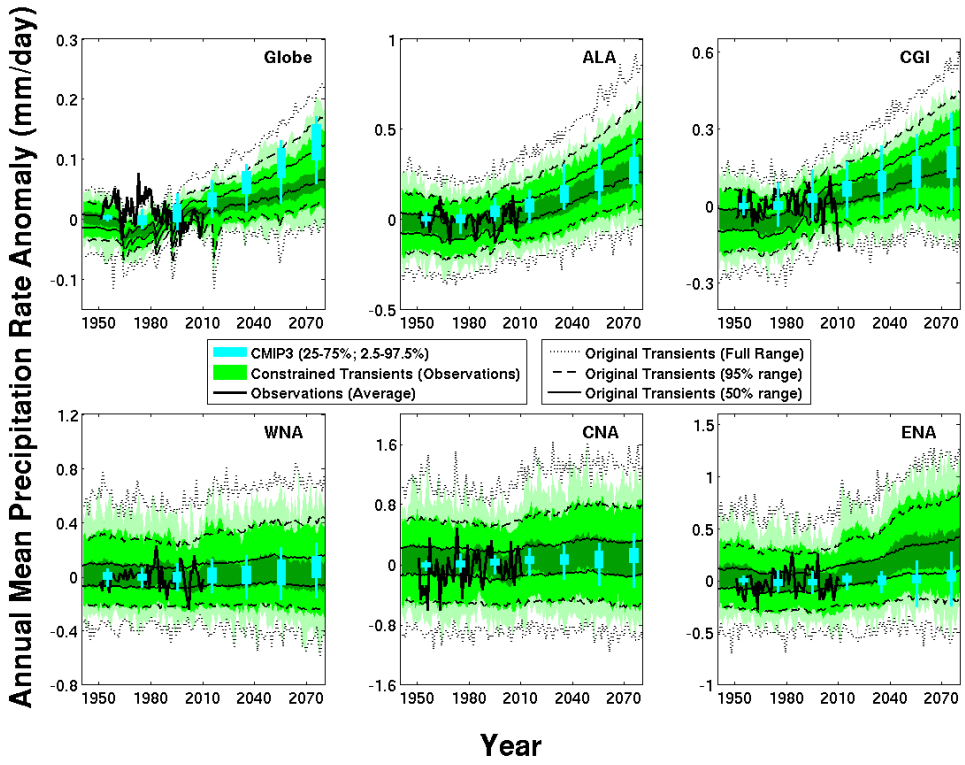
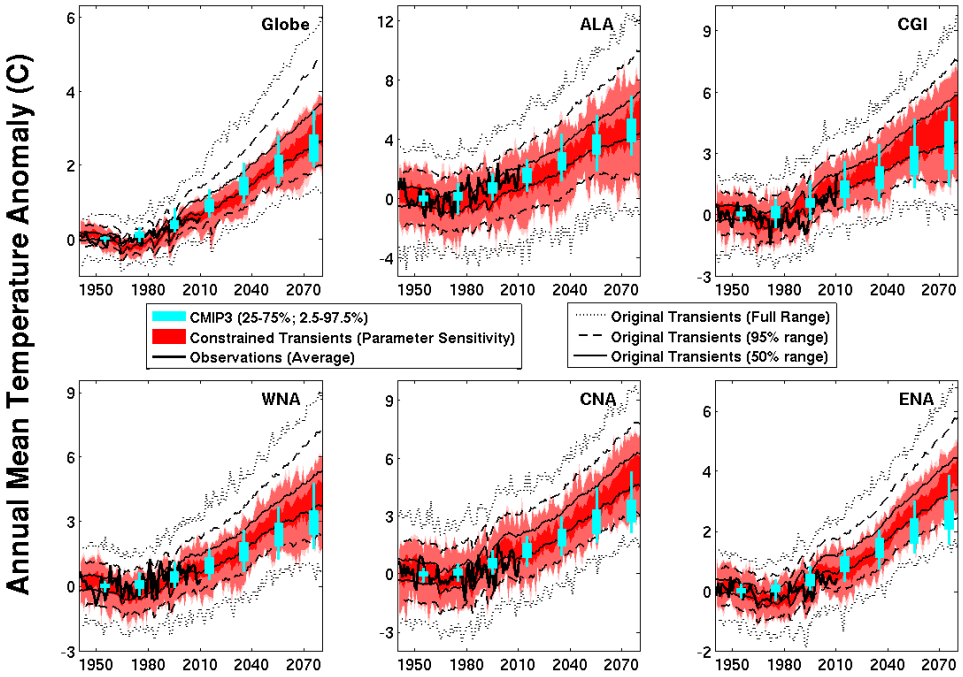


Figure 8.15: Same as Figure 8.14(a) (i.e., constraining by model performance compared to 30-year (1981-2010) observed trends) but includes NA regional results for *(a)* temperature (°C) and *(b)* precipitation rate (mm/day). Temperature anomalies are relative to a 1941-1970 base period and precipitation anomalies are relative to 1981-2010.

(a)



(b)

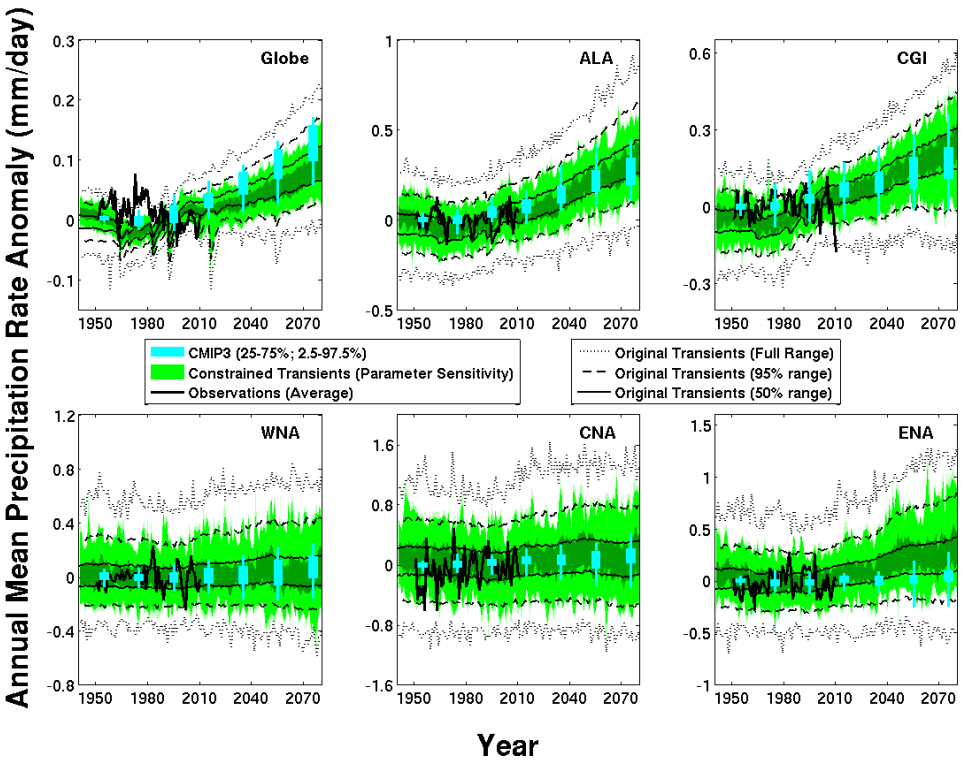


Figure 8.16: Same as Figure 8.14(b) (i.e., constraining by parameters with greatest impact on 70-year global temperature trends) but includes NA regional results for *(a)* temperature (°C) and *(b)* precipitation rate (mm/day). Temperature anomalies are relative to a 1941-1970 base period and precipitation anomalies are relative to 1981-2010.

The distribution differences between the original CPDN ensemble, both constrained CPDN ensembles, and the CMIP3 ensemble found in the previous figures and discussions were quantified by calculating decadal mean information for three decadal time periods: late historical (2001-2010), mid-future projection (2041-2050), and late-future projection (2071-2080). Table 8.1 and Table 8.2 provide each ensemble's mean, 2.5%, 25%, 75%, and, 97.5% value for temperature and precipitation respectively.

As an example on how to utilize the two tables, recall that when constraining the original CPDN ensemble there tended to be a reduction in both the ensemble mean and spread for future projections. The 50% range of these constrained ensembles aligned better with the 50% range of CMIP3 and the 95% range was closer to CMIP3 than the original CPDN ensemble but the CMIP3 95% range generally underestimated the uncertainty range. Looking at decadal mean global temperatures in Table 8.1 for both the mid- (2041-2050) and late-projection (2071-2080) time periods, the original CPDN ensemble's 50% ranges were (1.71, 2.27) and (2.54, 3.50) respectively. These ranges were reduced in both magnitude and spread when constrained by observations to (1.47, 1.96) and (2.19, 2.84) which brought them closer to the 50% ranges of the CMIP3 ensemble, (1.47, 2.00) and (2.10, 2.84). When comparing the 95% ranges, the original CPDN ensemble (i.e., [1.26, 2.98] and [1.88, 4.71]) still showed a reduction in both magnitude and spread after constraining by observations (i.e., [1.01, 2.58] and [1.61, 3.89]), but the CMIP3 ensemble's range was appreciably smaller (i.e., [1.22, 2.42] and [1.97, 3.50]).

Table 8.1: Decadal mean temperature anomalies for CMIP5, CPDN, CPDN constrained by 30-year global temperature trends (CPDN C-Trends), and CPDN constrained by parameters with greatest impact on 70-year global temperature trends (CPDN C-Parameters). Decadal means for each ensemble are given in terms of their mean [2.5% (25%-75%) 97.5%] and are given for three time periods (2001-2010), (2041-2050), and (2071-2080).

Decadal Temperatures	2001-2010	2041-2050	2071-2080
Globe			
CPDN	0.83 [0.29 (0.66, 1.00) 1.32]	1.98 [1.26 (1.71, 2.27) 2.98]	2.99 [1.88 (2.54, 3.50) 4.71]
CPDN C-Observations	0.57 [0.09 (0.41, 0.73) 1.03]	1.71 [1.01 (1.47, 1.96) 2.58]	2.51 [1.61 (2.19, 2.84) 3.89]
CPDN C-Parameters	0.62 [0.17 (0.48, 0.74) 0.99]	1.75 [1.25 (1.56, 1.92) 2.26]	2.78 [1.85 (2.42, 3.20) 3.65]
CMIP3	0.62 [0.41 (0.55, 0.84) 1.10]	1.67 [1.22 (1.47, 2.00) 2.42]	2.63 [1.97 (2.10, 2.84) 3.50]
ALA			
CPDN	1.25 [-1.15 (0.53, 1.95) 3.29]	3.65 [1.09 (2.82, 4.57) 6.55]	5.38 [1.51 (4.20, 6.80) 9.51]
CPDN C-Observations	0.62 [-2.06 (-0.23, 1.36) 2.70]	3.13 [0.36 (2.33, 3.95) 5.91]	4.24 [0.58 (3.16, 5.23) 7.81]
CPDN C-Parameters	0.97 [-1.68 (0.20, 1.69) 3.09]	3.41 [0.95 (2.69, 4.12) 5.45]	4.93 [1.15 (3.67, 6.12) 7.96]
CMIP3	1.07 [0.18 (0.83, 1.70) 2.07]	3.26 [1.55 (2.66, 3.80) 4.91]	4.63 [3.01 (3.87, 5.40) 7.03]
CGI			
CPDN	1.44 [0.18 (1.01, 1.87) 2.76]	3.17 [1.45 (2.52, 3.82) 4.98]	4.57 [1.68 (3.45, 5.62) 7.26]
CPDN C-Observations	1.11 [-0.10 (0.70, 1.53) 2.42]	2.57 [1.12 (2.07, 3.12) 4.20]	3.46 [1.24 (2.54, 4.32) 5.81]
CPDN C-Parameters	1.33 [0.13 (0.93, 1.75) 2.57]	3.09 [1.58 (2.46, 3.60) 4.58]	4.45 [1.62 (3.18, 5.48) 6.80]
CMIP3	0.86 [-0.03 (0.51, 1.35) 2.27]	2.24 [1.00 (1.65, 2.96) 3.96]	3.46 [1.44 (2.25, 4.57) 5.32]
WNA			
CPDN	1.03 [-0.25 (0.63, 1.42) 2.19]	2.86 [1.45 (2.37, 3.38) 4.61]	4.32 [2.21 (3.62, 5.11) 6.95]
CPDN C-Observations	0.66 [-0.64 (0.21, 1.06) 1.82]	2.53 [1.16 (2.08, 2.98) 4.08]	3.60 [1.68 (3.06, 4.19) 5.78]
CPDN C-Parameters	0.79 [-0.45 (0.39, 1.17) 1.92]	2.60 [1.43 (2.20, 3.00) 3.87]	4.04 [1.98 (3.27, 4.68) 5.59]
CMIP3	0.65 [0.20 (0.49, 1.05) 1.42]	2.09 [1.00 (1.60, 2.54) 3.20]	3.20 [1.78 (2.41, 3.50) 4.81]

Table 8.1: Continued.

	2001-2010	2041-2050	2071-2080
CNA			
CPDN	1.44 [-0.25 (0.85, 2.03) 3.12]	3.36 [1.44 (2.70, 4.01) 5.24]	5.27 [3.02 (4.47, 6.08) 7.61]
CPDN C-Observations	1.29 [-0.37 (0.71, 1.92) 3.05]	2.95 [1.23 (2.34, 3.57) 4.88]	4.67 [2.80 (3.99, 5.43) 6.91]
CPDN C-Parameters	1.17 [-0.42 (0.63, 1.72) 2.88]	2.94 [1.16 (2.34, 3.51) 4.82]	5.06 [2.84 (4.22, 5.96) 7.11]
CMIP3	0.91 [0.30 (0.73, 1.23) 1.72]	2.38 [1.39 (1.78, 2.92) 3.61]	3.43 [2.17 (2.68, 3.85) 5.38]
ENA			
CPDN	0.90 [0.050 (0.62, 1.18) 1.70]	2.40 [1.37 (2.04, 2.79) 3.62]	3.75 [2.35 (3.25, 4.29) 5.50]
CPDN C-Observations	0.68 [-0.16 (0.40, 0.96) 1.50]	2.19 [1.12 (1.78, 2.54) 3.33]	3.34 [2.04 (2.88, 3.85) 4.95]
CPDN C-Parameters	0.59 [-0.06 (0.36, 0.85) 1.41]	2.20 [1.30 (1.92, 2.47) 3.03]	3.76 [2.56 (3.32, 4.11) 4.68]
CMIP3	0.70 [0.15 (0.57, 0.83) 1.13]	1.79 [0.99 (1.41, 2.15) 2.64]	2.63 [1.56 (2.08, 3.01) 3.90]

Table 8.2: Decadal mean precipitation anomalies for CMIP5, CPDN, CPDN constrained by 30-year global temperature trends (CPDN C-Trends), and CPDN constrained by parameters with greatest impact on 70-year global temperature trends (CPDN C-Parameters). Decadal means for each ensemble are given in terms of their mean [2.5% (25%-75%) 97.5%] and are given for three time periods (2001-2010), (2041-2050), and (2071-2080).

Decadal Precipitation	2001-2010	2041-2050	2071-2080
Globe			
CPDN	0.02 [-0.01 (0.01, 0.03) 0.05]	0.05 [0.01 (0.03, 0.07) 0.10]	0.09 [0.02 (0.06, 0.12) 0.16]
CPDN C-Observations	0.01 [-0.01 (0.00, 0.02) 0.04]	0.04 [0.00 (0.02, 0.05) 0.08]	0.06 [0.02 (0.05, 0.08) 0.14]
CPDN C-Parameters	0.02 [-0.01 (0.010, 0.03) 0.04]	0.04 [0.01 (0.03, 0.06) 0.08]	0.08 [0.03 (0.06, 0.11) 0.14]
CMIP3	0.02 [0.00 (0.02, 0.04) 0.05]	0.07 [0.02 (0.06, 0.10) 0.11]	0.12 [0.06 (0.10, 0.16) 0.17]
ALA			
CPDN	0.04 [-0.11 (-0.01, 0.09) 0.20]	0.19 [0.00 (0.12, 0.26) 0.40]	0.33 [0.09 (0.24, 0.43) 0.62]
CPDN C-Observations	0.02 [-0.13 (-0.03, 0.070) 0.17]	0.15 [-0.03 (0.09, 0.22) 0.34]	0.26 [0.05 (0.19, 0.34) 0.52]
CPDN C-Parameters	0.04 [-0.12 (-0.02, 0.080) 0.18]	0.18 [0.03 (0.12, 0.24) 0.36]	0.32 [0.11 (0.24, 0.40) 0.54]
CMIP3	0.06 [-0.01 (0.04, 0.090) 0.13]	0.18 [0.04 (0.11, 0.22) 0.33]	0.29 [0.11 (0.20, 0.35) 0.45]
CGI			
CPDN	0.04 [-0.06 (0.01, 0.080) 0.15]	0.14 [-0.01 (0.08, 0.19) 0.28]	0.22 [-0.01 (0.14, 0.29) 0.42]
CPDN C-Observations	0.03 [-0.08 (-0.01, 0.06) 0.13]	0.11 [-0.03 (0.06, 0.15) 0.24]	0.15 [-0.05 (0.08, 0.23) 0.36]
CPDN C-Parameters	0.04 [-0.06 (0.00, 0.08) 0.14]	0.14 [0.00 (0.09, 0.18) 0.25]	0.23 [0.01 (0.16, 0.30) 0.40]
CMIP3	0.05 [-0.06 (0.02, 0.09) 0.17]	0.13 [-0.03 (0.08, 0.17) 0.28]	0.21 [-0.01 (0.11, 0.23) 0.37]
WNA			
CPDN	0.00 [-0.21 (-0.07, 0.08) 0.27]	0.04 [-0.21 (-0.05, 0.14) 0.40]	0.04 [-0.24 (-0.07, 0.15) 0.42]
CPDN C-Observations	-0.03 [-0.24 (-0.10, 0.05) 0.24]	0.04 [-0.22 (-0.05, 0.16) 0.39]	0.00 [-0.28 (-0.10, 0.11) 0.37]
CPDN C-Parameters	-0.01 [-0.22 (-0.08, 0.08) 0.27]	0.06 [-0.25 (-0.04, 0.15) 0.36]	0.02 [-0.31 (-0.10, 0.15) 0.44]
CMIP3	0.00 [-0.14 (-0.06, 0.05) 0.14]	0.05 [-0.11 (-0.02, 0.13) 0.22]	0.09 [-0.16 (-0.01, 0.15) 0.26]

Table 8.2: Continued.

	2001-2010	2041-2050	2071-2080
CNA			
CPDN	0.01 [-0.51 (-0.18, 0.19) 0.56]	0.11 [-0.48 (-0.10, 0.33) 0.79]	0.08 [-0.54 (-0.15, 0.30) 0.77]
CPDN C-Observations	-0.04 [-0.57 (-0.24, 0.14) 0.48]	0.16 [-0.45 (-0.060, 0.39) 0.82]	0.09 [-0.56 (-0.16, 0.32) 0.81]
CPDN C-Parameters	0.01 [-0.56 (-0.19, 0.17) 0.49]	0.18 [-0.47 (-0.070, 0.37) 0.79]	0.10 [-0.57 (-0.17, 0.34) 0.84]
CMIP3	0.04 [-0.08 (-0.01, 0.07) 0.19]	0.090 [-0.25 (0.020, 0.16) 0.27]	0.18 [-0.30 (0.03, 0.22) 0.43]
ENA			
CPDN	0.03 [-0.25 (-0.06, 0.12) 0.32]	0.17 [-0.17 (0.05, 0.30) 0.64]	0.23 [-0.18 (0.08, 0.40) 0.80]
CPDN C-Observations	-0.01 [-0.32 (-0.11, 0.09) 0.28]	0.24 [-0.15 (0.10, 0.40) 0.74]	0.29 [-0.15 (0.13, 0.48) 0.86]
CPDN C-Parameters	0.02 [-0.26 (-0.08, 0.11) 0.28]	0.22 [-0.09 (0.09, 0.36) 0.73]	0.28 [-0.11 (0.13, 0.46) 0.90]
CMIP3	0.01 [-0.09 (-0.03, 0.04) 0.07]	0.03 [-0.19 (-0.02, 0.07) 0.20]	0.05 [-0.24 (0.00, 0.10) 0.29]

8.3 SUMMARY

This chapter compared the CPDN HadCM3L ensemble to the CMIP3 and CMIP5 ensembles to assess whether the uncertainty estimates from CMIP3 and CMIP5 adequately represent uncertainties in different climate metrics using a much larger ensemble of simulations. In general, the control ensembles compared well between CPDN and CMIP5 (CMIP3 not available). The annual and seasonal mean absolute temperatures were in good agreement while the absolute precipitation was slightly larger for CMIP5, especially in the DJF season, except for CNA which saw larger amounts in JJA (Figures 8.1, 8.2). The magnitude of the seasonal cycles were similar but with the CMIP5 ensemble having a slightly smaller cycle (Figure 8.3) due to the slightly warmer DJF temperatures in conjunction with similar JJA temperatures as CPDN (Figure 8.2(a)).

The interannual variability was similar between the two ensembles for both temperature and precipitation with the CPDN distributions spanning as large or typically larger ranges of variability compared to CMIP5 (Figures 8.4, 8.5, 8.6). Therefore the CPDN PPE did not underestimate the interannual variability range found in the CMIP5 MME. For the decadal variability, however, the CPDN distributions for temperature and precipitation across all regions were larger with extensions to relatively greater variability. This suggests that the CMIP5 model simulations may be underestimating the decadal variability of both temperature and precipitation, possibly due to their smaller ensemble size and similarity in model components.

The transient simulation ensembles were compared between CPDN, CMIP3, and CMIP5. Over the historical period (1941-2010) both CMIP temperature

distributions displayed the same increasing temperature as CPDN at the global and regional scales and were centered near the 50% range of the CPDN ensemble in the NA regions but typically had smaller 50% and 95% ranges (Figures 8.7, 8.8, 8.9). The CMIP ensembles also tended to have relatively warmer temperatures compared to observations in the 2000's at the global scale as was found in CPDN (Figure 8.7). Historical precipitation in both CMIP ensembles followed a similar pattern to CPDN with increasing trends for the globe, ALA, and CGI but relatively no trend for WNA, CNA, and ENA.

The future projections of CMIP3 global temperatures were generally within the CPDN 95% range but had a 95% range that was much smaller than CPDN and more along the lower range of projected warming, especially near the end of the future period, while the HadCM3 model (CPDN parent model from CMIP3) resided along the CPDN mean, emphasizing the fact that the HadCM3 model was on the warmer side of the CMIP3 ensemble (Figure 8.10). This comparison provided a good example of the significance of a PPE versus an MME as each model simulation within an MME (i.e., CMIP3) has its own range of uncertainty that is not represented in the full MME. The single HadCM3 model simulation included in CMIP3 was shown, through the CPDN HadCM3L PPE experiment (i.e., red shading in Figure 8.10), to have a large range of uncertainty when varying the physics parameters across their range of uncertainty – a range found to be even larger than the entire CMIP3 ensemble itself.

The CMIP5 ensemble produced similar global temperature results but had slightly lower projected future warming than CMIP3 – generally found at both global and regional scales – because of the different future forcing scenario used (Figures 8.12,

8.13). However, the next generation version of the HadCM3 model, HadGEM2, again resided in the portion of the CMIP5 ensemble having larger warming, bringing it closer to the CPDN ensemble mean (Figure 8.11).

Regional temperatures projections in both CMIP ensembles followed similar patterns as that found at the global level with all regions increasing in temperature but at a slightly lower rate than CPDN on average. CMIP Regional precipitation projections generally continued the same characteristics found over the historical period with increasing trends in the globe, ALA, and CGI regions but very minimal change in WNA, CNA and ENA.

The CMIP3 ensemble was then compared to the constrained CPDN ensembles and it was found that constraining the CPDN ensemble reduced the global temperature ensemble mean and spread and brought the 50% range in general agreement with the CMIP3 50% range. However, the 95% range of the CMIP3 ensemble was considerably smaller than that of the constrained CPDN during most time periods, mostly underestimating the lower bound of the spread. At the regional level, CMIP3 appeared to underestimate the lower bound of the 95% spread for ALA, but then underestimate the upper bound for WNA, CNA, and ENA. For regional precipitation the 95% range of CMIP3 was significantly smaller than that for CPDN in WNA, CNA and ENA.

CHAPTER 9

CONCLUSIONS

This study investigated uncertainties in global and North American (NA) regional changes in temperature and precipitation over the observational and future time period (i.e., 1941-2080) using a multi-thousand member global climate model perturbed physics ensemble (PPE) in order to provide a better understanding of model uncertainties in projections of future climate change. The PPE was developed through the Climate*prediction*.net (CPDN) project and contained variations to 20 atmospheric and 10 ocean parameters as well as 5 alternative anthropogenic sulfate forcing scenarios, 15 solar forcing scenarios, 50 volcanic forcing scenarios, and the application of 10 different initial conditions. A total of 1,214 control simulations (i.e., constant annual but seasonally varying radiative forcing) and 1,692 transient simulations (i.e., including historic forcings and future emissions scenarios) were analyzed which equaled approximately 170,000 years and 237,000 years of modeled output respectively.

9.1 CONTROL ANALYSIS

The control analysis provided an evaluation of the performance of the CPDN HadCM3L control simulations across the globe and NA regions compared to observational data sets. The control simulations maintained a constant annual but seasonally varying radiative forcing and therefore were compared to detrended

observations to assess the modeled mean climate and its variability due to internal chaotic processes in the simulated climate system, including coupling between the atmosphere, ocean, land surface, and sea ice.

There were a total of 1,214 control simulations comprised of 138 atmospheres, ten oceans and eight initial condition variations resulting in 642 unique atmosphere/ocean combinations with the remaining 572 containing duplicate atmosphere/ocean combinations with variations to initial conditions. The controls contained relatively large drift in the first 20 years of their simulations due to atmosphere/ocean adjustments associated with the coupling process and therefore these initial 20 years were not used in any analysis (i.e., including the corresponding transient simulation years of 1921-1940). Control simulations also contained long-term mean drift from flux inequalities not removed by the flux adjustment process. This drift had to be removed from the corresponding transient simulations having the same atmosphere and ocean parameter values because a similar drift would exist in those forced simulations.

The absolute mean temperatures of the control simulations were generally aligned or slightly cooler than observational estimates potentially from poor representation of topography due to the models relatively coarse resolution. Additionally the observational estimates of absolute mean values may not have been representing the true value due to the difficulties in establishing absolute values compared to anomalies and because of limitations in ocean observations. The magnitude of the seasonal cycle in temperature in the simulations aligned generally well

will observations but with the range of CPDN distributions being significantly larger than the ranges of observations and extending to slightly larger magnitudes.

The interannual variability of the majority of the simulations and observations agreed well, with a general tendency in the model to extend to larger magnitudes of variability. However, with only 30-90 years of observational data to compare to, the full range of the climate system's natural variability may not be represented in the existing observational data sets. Therefore further analyses were performed on North American paleoclimate proxy reconstructions across the past 2,000 years to assess interannual and decadal variability. These analyses suggest greater variability of temperature and precipitation in proxy reconstructions than modern observations and the median estimate of the CPCN simulations in many regions. It was difficult, however, to identify significant differences between variability in the reconstructions and observational data sets or CPDN simulations because of the limitation in both the reconstruction process and the relatively smaller regional area that each proxy-based reconstruction may represent. However, using paleoclimate records to assess a climate model's internal variability offers fruitful prospects for future research which is discussed further in Section 9.5.

Parameter variations in control simulations did not always impact all regions or both temperature and precipitation in the same way and therefore a universal parameter value or set of parameter values could not be isolated and used to remove model simulations based on performance compared to observations.

Most of the model parameter uncertainty was found to be associated with two cloud physics parameters: the ice fall speed (VFI) which impacts cloudiness (and

therefore solar radiation and surface temperature) and precipitation by scaling the speed at which cloud ice particles fall out of the sky and the entrainment coefficient (ENTCOEF) which sets the rate at which convective clouds mix with their surrounding environmental air and impacts the transport of moisture to higher levels in the troposphere. These two parameters have been found important in previous studies as well (e.g., Knight et al. 2007; Sanderson et al. 2008a; Sanderson et al. 2008b; Sanderson et al. 2010).

The uncertainty in interannual variability was found to account for roughly half of the 50% uncertainty range in global 70-year control drift in both temperature and precipitation and a bit more than half for the 95% range. For regional temperatures this percentage remained roughly the same but for regional precipitation the internal variability uncertainty accounted for approximately 80-90% of the total uncertainty in most regions.

9.2 TRANSIENT ANALYSIS

The transient analysis evaluated the performance of the CPDN HadCM3L transient simulations over the observational time period and quantified uncertainties in future projections for the globe and NA regions and produced constrained future projections based on a model's performance over the observational time period.

There were a total of 1,692 transient simulations comprised of 137 atmospheres, ten oceans, ten initial conditions, five values for scaling anthropogenic sulfates, 15 solar forcing scenarios, and 50 volcanic forcing scenarios. This resulted in 614 unique atmosphere/ocean combinations with the remaining 1,078 containing duplicate

atmosphere/ocean combinations with variations to their anthropogenic sulfate scaling factor, natural forcings (solar or volcanic), or initial conditions. The long-term mean drift caused by imbalances in the atmosphere/ocean coupling process was removed by identifying the drift in a transient simulation's corresponding control simulation with matching atmosphere and ocean parameters. A number of available transient simulations could not be used because they did not have a matching control with the same atmosphere/ocean parameters and therefore the long-term mean drift to be removed could not be established.

Observational estimates of temperature and precipitation generally were near the 50% range of the transient simulation ensemble and were almost always within the 95% range for both the globe and North American regions. The simulations tended to show greater warming across the most recent decade (i.e., 2000's) than found in observations possibly due to natural variability in the observations (i.e., associated with ENSO and/or heat going into the ocean within the PDO cycle) or too large of climate sensitivity in some models.

Future projections of temperature showed increased warming in all regions with greater warming occurring over the future projection period than seen over the observational period. Future projections of precipitation did not change for WNA or CNA but did show an increase in other regions, with only a minimal increase in ENA. The uncertainty range tended to increase with time for both temperature and precipitation across the future projection period.

There was no change found in future temperature interannual variability but a slight increase found in precipitation interannual variability for all NA regions. The

magnitude of the temperature seasonal cycle was reduced in the future at higher latitudes, indicating greater winter warming, and increased in WNA and CNA, indicative of summer drying across the region.

Parameters ANTHSCA, HANEYSFACT, and RHCRIT were most sensitive with regards to 30- and 70-year trends over the observational period. ANTHSCA impacts temperature by scaling anthropogenic sulfates, HANEYSFACT is associated with imbalances between the atmosphere and ocean coupled model across the 20th century, and RHCRIT defines the rate at which clouds form based on the amount of moisture in a model grid cell. In future projected trends, the most important parameters included more cloud parameters indicating the important role of cloud feedbacks on the climate sensitivity and the future warming trends.

Past global temperature trends were the best identified predictors of future regional climatic trends (especially 30-year trends) and therefore used to constrain future projections. Also, future projections were constrained based on parameter sensitivity of the top three parameters (best reproducing 70-year past global temperature trends). Constraining based on observed 30-year global temperature trends and by parameter sensitivity resulted in a reduction in the spread of the resulting constrained ensemble as well as a decrease in the ensemble mean (i.e., future projections resided within the lower/cooler portion of the original ensemble). This result was similar to that found by Stott et al. (2013) and Rowlands et al. (2012) who used different approaches for constraining future projections.

Constraining future projections by observed 70-year global temperature trends did not change the general characteristics of the transient ensemble (i.e., maintained a similar ensemble mean, 50%, and 95% range).

9.3 Comparison to CMIP Ensembles

The CPDN HadCM3L ensemble was compared to the CMIP3 and CMIP5 ensembles to assess whether the uncertainty estimates from CMIP3 and CMIP5 adequately represent uncertainties in different climate metrics using a much larger ensemble of simulations. In general, the control ensembles compared well between CPDN and CMIP5 (CMIP3 not available). The annual and seasonal mean absolute temperatures were in good agreement while the absolute precipitation was slightly larger for CMIP5, especially in the DJF season, except for CNA which saw larger amounts in JJA. The magnitude of the seasonal cycles were similar but with the CMIP5 ensemble having a slightly smaller cycle due to the slightly warmer DJF temperatures in conjunction with similar JJA temperatures as CPDN.

The interannual variability was similar between the two ensembles for both temperature and precipitation with the CPDN distributions spanning as large or typically larger ranges of variability compared to CMIP5. Therefore the CPDN PPE did not underestimate the interannual variability range found in the CMIP5 MME. For the decadal variability, however, the CPDN distributions for temperature and precipitation across all regions were larger with extensions to relatively greater variability. This suggests that the CMIP5 model simulations may be underestimating the decadal

variability of both temperature and precipitation, possibly due to their smaller ensemble size and/or similarity in model components.

The transient simulation ensembles were compared between CPDN, CMIP3, and CMIP5. Over the historical period (1941-2010) both CMIP temperature distributions displayed the same increasing temperature as CPDN at the global and regional scales and were centered near the 50% range of the CPDN ensemble in the NA regions but typically had smaller 50% and 95% ranges. The CMIP ensembles also tended to have relatively warmer temperatures compared to observations in the 2000's at the global scale as was found in CPDN. Historical precipitation in both CMIP ensembles followed a similar pattern to CPDN with increasing trends for the globe, ALA, and CGI but relatively no trend for WNA, CNA, and ENA.

The future projections of CMIP3 global temperatures were generally within the CPDN 95% range but had a 95% range that was much smaller than CPDN and more along the lower range of projected warming, especially near the end of the future period, while the HadCM3 model (CPDN parent model from CMIP3) resided along the CPDN mean, emphasizing the fact that the HadCM3 model was on the warmer side of the CMIP3 ensemble. This comparison provided a good example of the significance of a PPE versus MME as each model simulation within an MME (i.e., CMIP3) has its own range of uncertainty that is not represented in the full MME. The single HadCM3 model simulation included in CMIP3 was shown, through the CPDN HadCM3L PPE experiment, to have a large range of uncertainty when varying the physics parameters across their range of uncertainty – a range found to be even larger than the entire CMIP3 ensemble itself.

The CMIP5 ensemble produced similar global temperature results but had slightly lower projected future warming than CMIP3 – generally found at both global and regional scales – because of the different future forcing scenario used. However, the next generation version of the HadCM3 model, HadGEM2, again resided in the portion of the CMIP5 ensemble having larger warming, bringing it closer to the CPDN ensemble mean.

Regional temperature projections in both CMIP ensembles followed similar patterns as that found at the global level with all regions increasing in temperature but at a slightly lower rate than CPDN on average. CMIP Regional precipitation projections generally continued the same characteristics found over the historical period with increasing trends in the globe, ALA, and CGI regions but very minimal change in WNA, CNA and ENA.

The CMIP3 ensemble was then compared to the constrained CPDN ensembles and it was found that constraining the CPDN ensemble reduced the global temperature ensemble mean and spread and brought the 50% range in general agreement with the CMIP3 50% range. However, the 95% range of the CMIP3 ensemble was considerably smaller than that of the constrained CPDN during most time periods, mostly underestimating the lower bound of the spread. At the regional level, CMIP3 appeared to underestimate the lower bound of the 95% spread for ALA, but then underestimate the upper bound for WNA, CNA, and ENA. For regional precipitation the 95% range of CMIP3 was significantly smaller than that of CPDN in WNA, CNA and ENA.

9.4 BROAD IMPLICATIONS

The larger implications of this study include the fact that a very large perturbed physics ensemble (PPE) was able to model many observed features in Earth's climate system. A subset of the PPE was identified as producing unrealistic historic climatic trends based on observed trends and that information was used to constrain future projections of climate change for the globe and North American regions. Additionally, climate indices were sensitive to changes in model parameter values and that information also was used to constrain future climate change projections.

With regards to comparing PPEs to multi-model ensembles (MMEs), the MMEs were found to underestimate the full range of uncertainties in physics parameters and therefore PPEs could be used to better quantify the full range of uncertainties in global and regional climate change. These results are important when considering which GCMs to use in regional downscaling studies where uncertainties in GCMs move downstream through regional projections for use in local impacts studies (e.g., ecosystems, hydrologic, agricultural). Climate scientists need to be able to quantify and effectively explain uncertainties originating from GCMs that may be present in regional and local impacts studies for their effective use and implementation by decision makers.

9.5 FUTURE WORK

Based on the current study, it would be useful if a similar large PPE experiment were conducted on different GCMs from other modeling groups to see if there are any additional physics parameter uncertainties based on differing model structures. Also, it

would be helpful if the PPE experiments were extended to other future emission scenarios besides SRES A1B. There may be uncertainties in parameter variations based on the atmospheric composition that can only be identified through investigation of different emission scenarios. And as a suggestion for others attempting to create a large PPE such as what CPDN has done, it would be useful to generate archived output for land-only regional means as well as land plus ocean regional means as the addition of ocean grid cells complicates assessing the performance of the PPE models because of the limitations in ocean observations.

And finally, in consideration of future work for myself, there is a great deal of analyses that could be done with regards to the CPDN globally gridded decadal mean output. Besides the global and five North American regional monthly mean time series output investigated in this study there are 2.5° lat by 3.75° long globally gridded decadal mean output available for all simulations. Therefore the next logical step would be to assess spatial patterns of temperature and precipitation across the historical period and compare them to future projections. The entire CPDN ensemble could be assessed as well as the constrained ensembles identified in this study. These results could then be compared to CMIP3 and CMIP5 globally gridded output.

Also, the higher spatial resolution CPDN decadal gridded output could be used to better assess decadal variability between the model and paleoclimate reconstructions across North American. The assessment described in Chapter 6 was limited because it attempted to compare the large CPDN regional means to relatively smaller regional reconstructed averages. With higher spatial resolution, a more robust assessment could be made between model and reconstructed observed decadal variability. This work

could be extended to the CMIP3 and CMIP5 gridded output to make further comparisons between paleoclimate reconstructions and MMEs and PPEs.

REFERENCES

Ackerley, D., E. J. Highwood, and D. J. Frame, 2009: Quantifying the effects of perturbing the physics of an interactive sulfur scheme using an ensemble of GCMs on the climateprediction.net platform. *Journal of Geophysical Research: Atmospheres*, **114,** D01203.

Adler, R. F., G. J. Huffman, A. Chang, R. Ferraro, P.-P. Xie, J. Janowiak, B. Rudolf, U. Schneider, S. Curtis, D. Bolvin, A. Gruber, J. Susskind, P. Arkin, and E. Nelkin, 2003: The Version-2 Global Precipitation Climatology Project (GPCP) Monthly Precipitation Analysis (1979–Present). *Journal of Hydrometeorology*, **4,** 1147-1167.

Alexander, L., S. Allen, N. Bindoff, F.-M. Bréon, J. Church, U. Cubasch, S. Emori, P. Forster, P. Friedlingstein, N. Gillett, J. Gregory, D. Hartmann, E. Jansen, K. K. Kanikicharla, B. Kirtman, R. Knutti, P. Lemke, J. Marotzke, V. Masson-Delmotte, G. Meehl, I. Mokhov, S. Piao, G.-K. Plattner, D. Qin, V. Ramaswamy, D. Randall, M. Rhein, M. Rojas, C. Sabine, D. Shindell, T. Stocker, L. Talley, D. Vaughan, and S.-P. Xie, 2013: Working Group I Summary for Policymakers. In Climate Change 2013: The Physical Climate Basis. 1-26.

Alexander, M., 2013: Extratropical Air-Sea Interaction, Sea Surface Temperature Variability, and the Pacific Decadal Oscillation. *Climate Dynamics: Why Does Climate Vary?* American Geophysical Union, 123-148.

Allen, M., 1999: Do-it-yourself climate prediction. *Nature*, **401,** 642-642.

Allen, M. R., and S. F. B. Tett, 1999: Checking for model consistency in optimal fingerprinting. *Climate Dynamics*, **15,** 419-434.

Allen, M. R., and P. A. Stott, 2003: Estimating signal amplitudes in optimal fingerprinting, part I: theory. *Climate Dynamics*, **21,** 477-491.

Ammann, C. M., G. A. Meehl, W. M. Washington, and C. S. Zender, 2003: A monthly and latitudinally varying volcanic forcing dataset in simulations of 20th century climate. *Geophysical Research Letters*, **30,** 1657.

Anderson, J. L., V. BalaJi, and A. J. Broccoli, 2004: The New GFDL Global Atmosphere and Land Model AM2–LM2: Evaluation with Prescribed SST Simulations. *Journal of Climate*, **17,** 4641-4673.

Annan, J. D., J. C. Hargreaves, R. Ohgaito, A. Abe-Ouchi, and S. Emori, 2005: Efficiently Constraining Climate Sensitivity with Ensembles of Paleoclimate Simulations. *SOLA*, **1,** 181-184.

Arakawa, A., and V. R. Lamb, 1977: Computational design of the basic dynamical processes. *Methods in Computational Physics: General Circulation Models of the Atmosphere*, J. Chang, Ed. Vol. 17, Academic Press, 174-267.

Arndt, D. S., M. O. Baringer, and M. R. Johnson, 2010: State of the Climate in 2009. *Bulletin of the American Meteorological Society*, **91,** s1-s222.

Balmaseda, M. A., K. E. Trenberth, and E. Källén, 2013: Distinctive climate signals in reanalysis of global ocean heat content. *Geophysical Research Letters*, **40,** 1754-1759.

Barnett, D., S. Brown, J. Murphy, D. H. Sexton, and M. Webb, 2006: Quantifying uncertainty in changes in extreme event frequency in response to doubled CO2 using a large ensemble of GCM simulations. *Climate Dynamics*, **26,** 489-511.

Becker, A., P. Finger, A. Meyer-Christoffer, B. Rudolf, K. Schamm, U. Schneider, and M. Ziese, 2013: A description of the global land-surface precipitation data products of the Global Precipitation Climatology Centre with sample applications including centennial (trend) analysis from 1901–present. *Earth Syst. Sci. Data*, **5,** 71-99.

Bindoff, N., and J. Willebrand, 2007: Observations: Oceanic Climate Change and Sea Level. *In: Climate Change 2007: The Physical Science Basis. Contribution of Working Group I to the Fourth Assessment Report of the Intergovernmental Panel on Climate Change*, S. Solomon, D. Qin, M. Manning, Z. Chen, M. Marquis, K.B. Averyt, M. Tignor and H.L. Miller, Ed. Cambridge University Press, Cambridge, United Kingdom, 385-432.

Blackmon, M., B. Boville, F. Bryan, R. Dickinson, P. Gent, J. Kiehl, R. Moritz, D. Randall, J. Shukla, S. Solomon, G. Bonan, S. Doney, I. Fung, J. Hack, E. Hunke, J. Hurrell, J. Kutzbach, J. Meehl, B. Otto-Bliesner, R. Saravanan, E. K. Schneider, L. Sloan, M. Spall, K. Taylor, J. Tribbia, and W. Washington, 2001: The Community Climate System Model. *Bulletin of the American Meteorological Society*, **82,** 2357-2376.

Boden, T., G. Marland, and R. Andres, 2010: Global, Regional, and National Fossil-Fuel CO2 Emissions. Carbon Dioxide Information Analysis Center, Oak Ridge National Laboratory, U.S. Department of Energy, Oak Ridge, Tenn., U.S.A. doi 10.3334/CDIAC/00001_V2010

Bradley, R., 1999: *Paleoclimatology: Reconstructing Climates of the Quaternary.* 2nd ed. Academic, San Diego, CA, 610 pp.

Briffa, K. R., F. H. Schweingruber, P. D. Jones, T. J. Osborn, S. G. Shiyatov, and E. A. Vaganov, 1998: Reduced sensitivity of recent tree-growth to temperature at high northern latitudes. *Nature*, **391,** 678-682.

Brohan, P., J. J. Kennedy, I. Harris, S. F. B. Tett, and P. D. Jones, 2006: Uncertainty estimates in regional and global observed temperature changes: A new data set from 1850. *Journal of Geophysical Research: Atmospheres,* **111,** D12106.

Brown, A., S. Milton, M. Cullen, B. Golding, J. Mitchell, and A. Shelly, 2012: Unified Modeling and Prediction of Weather and Climate: A 25-Year Journey. *Bulletin of the American Meteorological Society*, **93,** 1865-1877.

Bryan, K., 1969a: CLIMATE AND THE OCEAN CIRCULATION. *Monthly Weather Review*, **97,** 806-827.

——, 1969b: A numerical method for the study of the circulation of the world ocean. *Journal of Computational Physics*, **4,** 347-376.

Bukovsky, M. S., and D. J. Karoly, 2007: A Brief Evaluation of Precipitation from the North American Regional Reanalysis. *Journal of Hydrometeorology,* **8,** 837-846.

Chen, M., P. Xie, J. E. Janowiak, and P. A. Arkin, 2002: Global Land Precipitation: A 50-yr Monthly Analysis Based on Gauge Observations. *Journal of Hydrometeorology*, **3,** 249-266.

Chen, M., P. Xie, J. E. Janowiak, P. A. Arkin, and T. M. Smith, 2003: Reconstruction of the oceanic precipitation from 1948 to the present. *14th Symposium on Global Change and Climate Variations*, 83rd Annual AMS Meeting, Long Beach, CA.

Christensen, J. H., B. Hewitson, A. Busuioc, A. Chen, X. Gao, I. Held, R. Jones, R. K. Kolli, W. T. Kwon, R. Laprise, V. M. Rueda, L. Mearns, C. G. Menéndez, J. Räisänen, A. Rinke, A. Sarr, and P. Whetton, 2007: Regional Climate Projections. In: *Climate Change 2007:The Physical Science Basis. Contribution of Working Group I to the Fourth Assessment Report of the Intergovernmental Panel on Climate Change*. S. Solomon, D. Qin, M. Manning, Z. Chen, M. Marquis, K. B. Averyt, M.Tignor, and H. L. Miller, Eds. Cambridge University Press, Cambridge, United Kingdom and New York, NY, USA, 848-940.

Cleaveland, M. K., and D. N. Duvick, 1992: Iowa climate reconstructed from tree rings, 1640–1982. *Water Resources Research*, **28,** 2607-2615.

Collins, M., S. F. B. Tett, and C. Cooper, 2001: The internal climate variability of HadCM3, a version of the Hadley Centre coupled model without flux adjustments. *Climate Dynamics*, **17,** 61-81.

Collins, M., C. M. Brierley, M. MacVean, B. B. B. Booth, and G. R. Harris, 2007: The Sensitivity of the Rate of Transient Climate Change to Ocean Physics Perturbations. *Journal of Climate*, **20,** 2315-2320.

Collins, M., B. B. Booth, G. Harris, J. Murphy, D. H. Sexton, and M. Webb, 2006: Towards quantifying uncertainty in transient climate change. *Climate Dynamics*, **27,** 127-147.

Collins, M., B. B. Booth, B. Bhaskaran, G. Harris, J. Murphy, D. H. Sexton, and M. Webb, 2011: Climate model errors, feedbacks and forcings: a comparison of perturbed physics and multi-model ensembles. *Climate Dynamics*, **36,** 1737-1766.

Collins, W. J., N. Bellouin, M. Doutriaux-Boucher, N. Gedney, T. Hinton, C. D. Jones, S. Liddicoat, G. Martin, F. O'Connor, J. Rae, C. Senior, I. Totterdell, S. Woodward, T. Reichler, and J. Kim, 2008: Evaluation of the HadGEM2 model. Met Office Hadley Centre Technical Note no. HCTN 74.

Cox, M. D., 1984: A primitive equation, 3 dimensional model of the ocean. GFDL Ocean Group Technical Report 1, Princeton, NJ, USA, 143 pp.

Cox, P. M., R. A. Betts, C. B. Bunton, R. L. H. Essery, P. R. Rowntree, and J. Smith, 1999: The impact of new land surface physics on the GCM simulation of climate and climate sensitivity. *Climate Dynamics*, **15,** 183-203.

Cronin, T. M., G. S. Dwyer, T. Kamiya, S. Schwede, and D. A. Willard, 2003: Medieval Warm Period, Little Ice Age and 20th century temperature variability from Chesapeake Bay. *Global and Planetary Change*, **36,** 17-29.

Crossley, J. F., and D. L. Roberts, 1995: The thermodynamic/dynamic sea ice model. Technical Report UMDP 45, Hadley Centre for Climate Prediction and Research.

Crowley, T. J., 2000: Causes of Climate Change Over the Past 1000 Years. *Science*, **289,** 270-277.

Cullen, M. J. P., 1993: The Unified forecast/climate model. *The Meteorological Magazine*, **122,** 81-95.

Cullen, M. J. P., and T. Davies, 1991: A conservative split-explicit integration scheme with fourth-order horizontal advection. *Quarterly Journal of the Royal Meteorological Society*, **117,** 993-1002.

Cusack, S., J. M. Edwards, and J. M. Crowther, 1999: Investigating k distribution methods for parameterizing gaseous absorption in the Hadley Centre Climate Model. *Journal of Geophysical Research: Atmospheres*, **104,** 2051-2057.

Cusack, S., A. Slingo, J. M. Edwards, and M. Wild, 1998: The radiative impact of a simple aerosol climatology on the Hadley Centre atmospheric GCM. *Quarterly Journal of the Royal Meteorological Society*, **124,** 2517-2526.

Davi, N. K., G. C. Jacoby, and G. C. Wiles, 2003: Boreal temperature variability inferred from maximum latewood density and tree-ring width data, Wrangell Mountain region, Alaska. *Quaternary Research*, **60,** 252-262.

Davis, C. A., K. W. Manning, R. E. Carbone, S. B. Trier, and J. D. Tuttle, 2003: Coherence of Warm-Season Continental Rainfall in Numerical Weather Prediction Models. *Monthly Weather Review*, **131,** 2667-2679.

Delworth, T., S. Manabe, and R. J. Stouffer, 1993: Interdecadal Variations of the Thermohaline Circulation in a Coupled Ocean-Atmosphere Model. *Journal of Climate*, **6,** 1993-2011.

Deser, C., A. Phillips, V. Bourdette, and H. Teng, 2012: Uncertainty in climate change projections: the role of internal variability. *Climate Dynamics*, **38,** 527-546.

Dommenget, D., and M. Latif, 2008: Generation of hyper climate modes. *Geophysical Research Letters*, **35,** L02706.

Doswell, C. A., and P. M. Markowski, 2004: Is Buoyancy a Relative Quantity? *Monthly Weather Review*, **132,** 853-863.

Edwards, J. M., and A. Slingo, 1996: Studies with a flexible new radiation code. I: Choosing a configuration for a large-scale model. *Quarterly Journal of the Royal Meteorological Society*, **122,** 689-719.

ETOPO5, 1988: Data Announcement 88-MGG-02, Digital relief of the surface of the Earth. NOAA, National Geophysical Data Center, Boulder, CO, USA.

Feltham, D. L., 2008: Sea Ice Rheology. *Annual Review of Fluid Mechanics*, **40,** 91-112.

Fowler, H., D. Cooley, S. Sain, and M. Thurston, 2010: Detecting change in UK extreme precipitation using results from the climateprediction.net BBC climate change experiment. *Extremes*, **13,** 241-267.

Fowler, H. J., S. Blenkinsop, and C. Tebaldi, 2007: Linking climate change modelling to impacts studies: recent advances in downscaling techniques for hydrological modelling. *International Journal of Climatology*, **27,** 1547-1578.

Frame, D. J., T. Aina, C. M. Christensen, N. E. Faull, S. H. E. Knight, C. Piani, S. M. Rosier, K. Yamazaki, Y. Yamazaki, and M. R. Allen, 2009: The climateprediction.net BBC climate change experiment: design of the coupled model ensemble. *Philosophical Transactions of the Royal Society A: Mathematical, Physical and Engineering Sciences*, **367,** 855-870.

Fritts, H. C., 1971: Dendroclimatology and dendroecology. *Quaternary Research*, **1,** 419-449.

——, 1976: *Tree Rings and Climate.* Academic Press, San Diego, CA, 567 pp.

Garfin, G. M., and M. K. Hughes, 1996: Eastern Oregon Divisional Precipitation and Palmer Drought Severity Index from Tree-Rings. Report to the U.S. Forest Service Intermountain Research Station, USDA Forest Service Cooperative Agreement PNW, 90-174.

Gates, W. L., 1992: AMIP: The Atmospheric Model Intercomparison Project. *Bulletin of the American Meteorological Society*, **73,** 1962-1970.

Gent, P. R., and J. C. McWilliams, 1990: Isopycnal Mixing in Ocean Circulation Models. *Journal of Physical Oceanography*, **20,** 150-155.

Gerdes, R., C. Köberle, and J. Willebrand, 1991: The influence of numerical advection schemes on the results of ocean general circulation models. *Climate Dynamics*, **5,** 211-226.

Giorgi, F., and R. Francisco, 2000: Uncertainties in regional climate change prediction: a regional analysis of ensemble simulations with the HADCM2 coupled AOGCM. *Climate Dynamics*, **16,** 169-182.

Giorgi, F., and L. O. Mearns, 2002: Calculation of Average, Uncertainty Range, and Reliability of Regional Climate Changes from AOGCM Simulations via the "Reliability Ensemble Averaging" (REA) Method. *Journal of Climate*, **15,** 1141-1158.

Gleckler, P. J., K. E. Taylor, and C. Doutriaux, 2008: Performance metrics for climate models. *Journal of Geophysical Research: Atmospheres*, **113,** D06104.

Gordon, C., and M. Bottomley, 1985: The parametrisation of the upper ocean mixed layer in coupled ocean/atmosphere models. *Proc. 16th Liege Colloquium on Ocean Hydrodynamics*, Elsevier, Amsterdam.

Gordon, C., C. Cooper, C. A. Senior, H. Banks, J. M. Gregory, T. C. Johns, J. F. B. Mitchell, and R. A. Wood, 2000: The simulation of SST, sea ice extents and ocean heat transports in a version of the Hadley Centre coupled model without flux adjustments. *Climate Dynamics*, **16,** 147-168.

Grabowski, W. W., 2000: Cloud Microphysics and the Tropical Climate: Cloud-Resolving Model Perspective. *Journal of Climate*, **13,** 2306-2322.

Graybill, D. A., and S. B. Idso, 1993: Detecting the aerial fertilization effect of atmospheric CO2 enrichment in tree-ring chronologies. *Global Biogeochemical Cycles*, **7,** 81-95.

Greene, A. M., L. Goddard, and U. Lall, 2006: Probabilistic Multimodel Regional Temperature Change Projections. *Journal of Climate*, **19,** 4326-4343.

Gregory, D., 1995: A Consistent Treatment of the Evaporation of Rain and Snow for Use in Large-Scale Models. *Monthly Weather Review*, **123,** 2716-2732.

Gregory, D., and P. R. Rowntree, 1990: A Mass Flux Convection Scheme with Representation of Cloud Ensemble Characteristics and Stability-Dependent Closure. *Monthly Weather Review*, **118,** 1483-1506.

Gregory, D., and S. Allen, 1991: The effect of convective scale downdrafts upon NWP and climate simulations. *9th Conf. Numerical Weather Prediction*, Denver, CO, Amer. Meteor. Soc., 122-123.

Gregory, D., and D. Morris, 1996: The sensitivity of climate simulations to the specification of mixed phase clouds. *Climate Dynamics*, **12,** 641-651.

Gregory, D., R. Kershaw, and P. M. Inness, 1997: Parametrization of momentum transport by convection. II: Tests in single-column and general circulation models. *Quarterly Journal of the Royal Meteorological Society*, **123,** 1153-1183.

Gregory, D., G. J. Shutts, and J. R. Mitchell, 1998: A new gravity-wave-drag scheme incorporating anisotropic orography and low-level wave breaking: Impact upon the climate of the UK Meteorological Office Unified Model. *Quarterly Journal of the Royal Meteorological Society*, **124,** 463-493.

Griffies, S. M., A. Gnanadesikan, R. C. Pacanowski, V. D. Larichev, J. K. Dukowicz, and R. D. Smith, 1998: Isoneutral Diffusion in a z-Coordinate Ocean Model. *Journal of Physical Oceanography*, **28,** 805-830.

Grissino-Mayer, H. D., and H. C. Fritts, 1997: The International Tree-Ring Data Bank: an enhanced global database serving the global scientific community. *The Holocene*, **7,** 235-238.

Haney, R. L., 1971: Surface Thermal Boundary Condition for Ocean Circulation Models. *Journal of Physical Oceanography*, **1,** 241-248.

Hansen, J., and S. Lebedeff, 1987: Global trends of measured surface air temperature. *Journal of Geophysical Research: Atmospheres*, **92,** 13345-13372.

Hansen, J., R. Ruedy, J. Glascoe, and M. Sato, 1999: GISS analysis of surface temperature change. *Journal of Geophysical Research: Atmospheres*, **104,** 30997-31022.

Hansen, J., R. Ruedy, M. Sato, and K. Lo, 2010: GLOBAL SURFACE TEMPERATURE CHANGE. *Reviews of Geophysics*, **48,** RG4004.

Hansen, J., R. Ruedy, M. Sato, M. Imhoff, W. Lawrence, D. Easterling, T. Peterson, and T. Karl, 2001: A closer look at United States and global surface temperature change. *Journal of Geophysical Research: Atmospheres*, **106,** 23947-23963.

Harris, G. R., D. M. H. Sexton, B. B. B. Booth, M. Collins, J. M. Murphy, and M. J. Webb, 2006: Frequency distributions of transient regional climate change from perturbed physics ensembles of general circulation model simulations. *Climate Dynamics*, **27,** 357-375.

Hawkins, E., and R. Sutton, 2009: The Potential to Narrow Uncertainty in Regional Climate Predictions. *Bulletin of the American Meteorological Society*, **90,** 1095-1107.

——, 2011: The potential to narrow uncertainty in projections of regional precipitation change. *Climate Dynamics*, **37,** 407-418.

Hegerl, G. C., F. W. Zwiers, P. Braconnot, N. P. Gillett, Y. Luo, J. A. M. Orsini, N. Nicholls, J. E. Penner, and P. A. Stott, 2007: Understanding and Attributing Climate Change. In: *Climate Change 2007: The Physical Science Basis. Contribution of Working Group I to the Fourth Assessment Report of the Intergovernmental Panel on Climate Change*. S. Solomon, D. Qin, M. Manning, Z. Chen, M. Marquis, K. B. Averyt, M.Tignor, and H. L. Miller, Eds. Cambridge University Press, Cambridge, United Kingdom and New York, NY, USA, 663-745.

Heymsfield, A. J., 1977: Precipitation Development in Stratiform Ice Clouds: A Microphysical and Dynamical Study. *Journal of the Atmospheric Sciences*, **34,** 367-381.

Hibler, W. D., 1979: A Dynamic Thermodynamic Sea Ice Model. *Journal of Physical Oceanography*, **9,** 815-846.

Holdaway, D., J. Thuburn, and N. Wood, 2012: Comparison of Lorenz and Charney–Phillips vertical discretisations for dynamics–boundary layer coupling. Part I: Steady states. *Quarterly Journal of the Royal Meteorological Society***,** n/a-n/a.

Houghton, J. T., Y. Ding, D. J. Griggs, M. Noguer, P. J. van der Linden, X. Dai, K. Maskell, and C. A. Johnson, 2001: *Climate Change 2001: The Scientific Basis: Contributions of Working Group I to the Third Assessment Report of the*

Intergovernmental Panel on Climate Change. Cambridge Univ. Press, New York, 881 pp.

Hoyt, D. V., and K. H. Schatten, 1993: A discussion of plausible solar irradiance variations, 1700-1992. *Journal of Geophysical Research: Space Physics*, **98,** 18895-18906.

Huffman, G. J., R. F. Adler, D. T. Bolvin, and G. Gu, 2009: Improving the global precipitation record: GPCP Version 2.1. *Geophysical Research Letters*, **36,** L17808.

Huffman, G. J., R. F. Adler, P. Arkin, A. Chang, R. Ferraro, A. Gruber, J. Janowiak, A. McNab, B. Rudolf, and U. Schneider, 1997: The Global Precipitation Climatology Project (GPCP) Combined Precipitation Dataset. *Bulletin of the American Meteorological Society*, **78,** 5-20.

Hurrell, J. W., 1995: Decadal Trends in the North Atlantic Oscillation: Regional Temperatures and Precipitation. *Science*, **269,** 676-679.

Hurrell, J. W., Y. Kushnir, G. Ottersen, and M. Visbeck, 2013: An Overview of the North Atlantic Oscillation. *The North Atlantic Oscillation: Climatic Significance and Environmental Impact* American Geophysical Union, 1-35.

Ingram, W. J., 1990: Unified Model Documentation Paper no. 23: Radiation, Tech. Rep. UK Met Office.

IPCC, 1990: *Climate Change: The IPCC Scientific Assessment.* [Houghton, J.T., G.J. Jenkins, and J.J. Ephraums (eds.))], Cambridge University Press, Cambridge, United Kingdom and New York, NY, USA, 365 pp.

——, 1996: *Climate Change 1995: The Science of Climate Change.* [Houghton, J.T., et al. (eds.)], Cambridge University Press, Cambridge, United Kingdom and New York, NY, USA, 572 pp.

——, 2001: *Climate Change 2001: The Scientific Basis. Contribution of Working Group I to the Third Assessment Report of the Intergovernmental Panel on Climate Change.* [Houghton, J.T., et al. (eds.)], Cambridge University Press, Cambridge, United Kingdom and New York, NY, USA, 881 pp.

——, 2007: *Climate Change 2007: The Physical Science Basis. Controbution of Working Group I to the Fourth Assessment Report of the Intergovernmental Panel on Climate Change, 2007.* [S. Solomon et al. (eds.)], Cambridge University Press, Cambridge, United Kingdom and New York, NY, USA, 996 pp.

——, 2013: *(Draft Report) Climate Change 2013: The Physical Science Basis. Controbution of Working Group I to the Fifth Assessment Report of the Intergovernmental Panel on Climate Change, 2013.* [T. Stocker and D. Qin (eds.)], Cambridge University Press, Cambridge, United Kingdom and New York, NY, USA.

Jansen, E., J. Overpeck, K. R. Briffa, J.-C. Duplessy, F. Joos, V. Masson-Delmotte, D. Olago, B. Otto-Bliesner, W. R. Peltier, S. Rahmstorf, R. Ramesh, D. Raynaud, D. Rind, O. Solomina, R. Villalba, and D. Zhang, 2007: Palaeoclimate. *In: Climate Change 2007: The Physical Science Basis. Contribution of Working Group I to the Fourth Assessment Report of the Intergovernmental Panel on Climate Change* S. Solomon, D. Qin, M. Manning, Z. Chen, M. Marquis, K.B. Averyt, M. Tignor and H.L. Miller, Ed. Cambridge University Press, Cambridge, United Kingdom 433-497.

Jerlov, N. G., 1968: *Optical Oceanography.* Elsevier, 194 pp.

Johns, T. C., R. E. Carnell, J. F. Crossley, J. M. Gregory, J. F. B. Mitchell, C. A. Senior, S. F. B. Tett, and R. A. Wood, 1997: The second Hadley Centre coupled ocean-atmosphere GCM: model description, spinup and validation. *Climate Dynamics*, **13,** 103-134.

Johns, T. C., C. F. Durman, H. T. Banks, M. J. Roberts, A. J. McLaren, J. K. Ridley, C. A. Senior, K. D. Williams, A. Jones, G. J. Rickard, S. Cusack, W. J. Ingram, M. Crucifix, D. M. H. Sexton, M. M. Joshi, B. W. Dong, H. Spencer, R. S. R. Hill, J. M. Gregory, A. B. Keen, A. K. Pardaens, J. A. Lowe, A. Bodas-Salcedo, S. Stark, and Y. Searl, 2006: The New Hadley Centre Climate Model (HadGEM1): Evaluation of Coupled Simulations. *Journal of Climate*, **19,** 1327-1353.

Jones, C., 2003: A Fast Ocean GCM without Flux Adjustments. *Journal of Atmospheric and Oceanic Technology*, **20,** 1857-1868.

Jones, C. D., and J. R. Palmer, 1998: Spinup methods for HadCM3L. Technical Report CRTN 84, Hadley Centre for Climate Prediction and Research

Jones, C. D., J. K. Hughes, N. Bellouin, S. C. Hardiman, G. S. Jones, J. Knight, S. Liddicoat, F. M. O'Connor, R. J. Andres, C. Bell, K. O. Boo, A. Bozzo, N. Butchart, P. Cadule, K. D. Corbin, M. Doutriaux-Boucher, P. Friedlingstein, J. Gornall, L. Gray, P. R. Halloran, G. Hurtt, W. J. Ingram, J. F. Lamarque, R. M. Law, M. Meinshausen, S. Osprey, E. J. Palin, L. Parsons Chini, T. Raddatz, M. G. Sanderson, A. A. Sellar, A. Schurer, P. Valdes, N. Wood, S. Woodward, M. Yoshioka, and M. Zerroukat, 2011: The HadGEM2-ES implementation of CMIP5 centennial simulations. *Geosci. Model Dev.*, **4,** 543-570.

Jones, P. D., and M. E. Mann, 2004: Climate over past millennia. *Reviews of Geophysics*, **42,** RG2002.

Jones, P. D., T. Jonsson, and D. Wheeler, 1997: Extension to the North Atlantic oscillation using early instrumental pressure observations from Gibraltar and south-west Iceland. *International Journal of Climatology*, **17,** 1433-1450.

Knight, C. G., S. H. E. Knight, N. Massey, T. Aina, C. Christensen, D. J. Frame, J. A. Kettleborough, A. Martin, S. Pascoe, B. Sanderson, D. A. Stainforth, and M. R. Allen, 2007: Association of parameter, software, and hardware variation with large-scale behavior across 57,000 climate models. *Proceedings of the National Academy of Sciences*, **104,** 12259-12264.

Knutti, R., G. A. Meehl, M. R. Allen, and D. A. Stainforth, 2006: Constraining Climate Sensitivity from the Seasonal Cycle in Surface Temperature. *Journal of Climate*, **19,** 4224-4233.

Korpela, E., D. Werthimer, D. Anderson, J. Cobb, and M. Leboisky, 2001: SETI@home – massively distributed computing for SETI. *Computing in Science and Engineering*, **3,** 78-83.

Kraus, E. B., and J. S. Turner, 1967: A one-dimensional model of the seasonal thermocline II. The general theory and its consequences. *Tellus*, **19,** 98-106.

Lacis, A. A., G. A. Schmidt, D. Rind, and R. A. Ruedy, 2010: Atmospheric CO2: Principal Control Knob Governing Earth's Temperature. *Science*, **330,** 356-359.

Lambert, S. J., and G. J. Boer, 2001: CMIP1 evaluation and intercomparison of coupled climate models. *Climate Dynamics*, **17,** 83-106.

Lamoureux, S., and R. Bradley, 1996: A late Holocene varved sediment record of environmental change from northern Ellesmere Island, Canada. *J Paleolimnol*, **16,** 239-255.

Large, W. G., J. C. McWilliams, and S. C. Doney, 1994: Oceanic vertical mixing: A review and a model with a nonlocal boundary layer parameterization. *Reviews of Geophysics*, **32,** 363-403.

Lean, J., J. Beer, and R. Bradley, 1995: Reconstruction of solar irradiance since 1610: Implications for climate change. *Geophysical Research Letters*, **22,** 3195-3198.

Ledley, T. S., 1985: Sea ice: Multiyear cycles and white ice. *Journal of Geophysical Research: Atmospheres*, **90,** 5676-5686.

Leonard, E., 1997: The relationship between glacial activity and sediment production: evidence from a 4450-year varve record of neoglacial sedimentation in Hector Lake, Alberta, Canada. *J Paleolimnol*, **17,** 319-330.

Lorenz, E. N., 1960: Energy and Numerical Weather Prediction. *Tellus*, **12,** 364-373.

Luckman, B. H., and R. J. S. Wilson, 2005: Summer temperatures in the Canadian Rockies during the last millennium: a revised record. *Climate Dynamics*, **24,** 131-144.

Luthi, D., M. Le Floch, B. Bereiter, T. Blunier, J.-M. Barnola, U. Siegenthaler, D. Raynaud, J. Jouzel, H. Fischer, K. Kawamura, and T. F. Stocker, 2008: High-resolution carbon dioxide concentration record 650,000-800,000[thinsp]years before present. *Nature*, **453,** 379-382.

Manabe, S., and R. J. Stouffer, 1988: Two Stable Equilibria of a Coupled Ocean-Atmosphere Model. *Journal of Climate*, **1,** 841-866.

Mann, M. E., 2007: Climate Over the Past Two Millennia. *Annual Review of Earth and Planetary Sciences*, **35,** 111-136.

Mantua, N. J., S. R. Hare, Y. Zhang, J. M. Wallace, and R. C. Francis, 1997: A Pacific Interdecadal Climate Oscillation with Impacts on Salmon Production. *Bulletin of the American Meteorological Society*, **78,** 1069-1079.

Martin, G. M., D. W. Johnson, and A. Spice, 1994: The Measurement and Parameterization of Effective Radius of Droplets in Warm Stratocumulus Clouds. *Journal of the Atmospheric Sciences*, **51,** 1823-1842.

Massey, N., T. Aina, M. R. Allen, C. M. Christiansen, D. J. Frame, D. Goodman, J. A. Kettleborough, A. Martin, S. Pascoe, and D. A. Stainforth, 2006: Data access and analysis with distributed federated data servers in climateprediction.net. *Advances in Geosciences*, **8,** 49-56.

Masson, D., and R. Knutti, 2011: Spatial-Scale Dependence of Climate Model Performance in the CMIP3 Ensemble. *Journal of Climate*, **24,** 2680-2692.

McGuffie, K., and A. Henderson-Sellers, 2005: *A Climate Modeling Primer.* John Wiley & Sons Ltd, West Sussex, England, 280 pp.

McSweeney, C. F., R. G. Jones, and B. B. B. Booth, 2012: Selecting Ensemble Members to Provide Regional Climate Change Information. *Journal of Climate*, **25,** 7100-7121.

Mearns, L. O., R. Arritt, S. Biner, M. S. Bukovsky, S. McGinnis, S. Sain, D. Caya, J. Correia, D. Flory, W. Gutowski, E. S. Takle, R. Jones, R. Leung, W. Moufouma-Okia, L. McDaniel, A. M. B. Nunes, Y. Qian, J. Roads, L. Sloan, and M. Snyder, 2012: The North American Regional Climate Change Assessment Program: Overview of Phase I Results. *Bulletin of the American Meteorological Society*, **93,** 1337-1362.

Meehl, G. A., J. M. Arblaster, and G. Branstator, 2012: Mechanisms Contributing to the Warming Hole and the Consequent U.S. East–West Differential of Heat Extremes. *Journal of Climate*, **25,** 6394-6408.

Meehl, G. A., G. J. Boer, C. Covey, M. Latif, and R. J. Stouffer, 2000: The Coupled Model Intercomparison Project (CMIP). *Bulletin of the American Meteorological Society*, **81,** 313-318.

Meehl, G. A., C. Covey, K. E. Taylor, T. Delworth, R. J. Stouffer, M. Latif, B. McAvaney, and J. F. B. Mitchell, 2007a: THE WCRP CMIP3 Multimodel Dataset: A New Era in Climate Change Research. *Bulletin of the American Meteorological Society*, **88,** 1383-1394.

Meehl, G. A., T. F. Stocker, W. D. Collins, P. Friedlingstein, A. T. Gaye, J. M. Gregory, A. Kitoh, R. Knutti, J. M. Murphy, A. Noda, S. C. B. Raper, I. G. Watterson, A. J. Weaver, and Z. C. Zhao, 2007b: Global Climate Projections. In: *Climate Change 2007: The Physical Science Basis. Contribution of Working Group I to the Fourth Assessment Report of the Intergovernmental Panel on Climate Change*. S. Solomon, D. Qin, M. Manning, Z. Chen, M. Marquis, K. B. Averyt, M.Tignor, and H. L. Miller, Eds. Cambridge University Press, Cambridge, United Kingdom and New York, NY, USA, 747-845.

Mesinger, F., G. DiMego, E. Kalnay, K. Mitchell, P. C. Shafran, W. Ebisuzaki, D. Jović, J. Woollen, E. Rogers, E. H. Berbery, M. B. Ek, Y. Fan, R. Grumbine, W. Higgins, H. Li, Y. Lin, G. Manikin, D. Parrish, and W. Shi, 2006: North American Regional Reanalysis. *Bulletin of the American Meteorological Society*, **87,** 343-360.

Mo, K. C., M. Chelliah, M. L. Carrera, R. W. Higgins, and W. Ebisuzaki, 2005: Atmospheric Moisture Transport over the United States and Mexico as Evaluated in the NCEP Regional Reanalysis. *Journal of Hydrometeorology*, **6,** 710-728.

Morice, C. P., J. J. Kennedy, N. A. Rayner, and P. D. Jones, 2012: Quantifying uncertainties in global and regional temperature change using an ensemble of observational estimates: The HadCRUT4 data set. *Journal of Geophysical Research: Atmospheres*, **117,** D08101.

Murphy, J. M., 1995a: Transient Response of the Hadley Centre Coupled Ocean-Atmosphere Model to Increasing Carbon Dioxide. Part 1: Control Climate and Flux Adjustment. *Journal of Climate*, **8,** 36-56.

——, 1995b: Transient Response of the Hadley Centre Coupled Ocean-Atmosphere Model to Increasing Carbon Dioxide. Part III: Analysis of Global-Mean Response Using Simple Models. *Journal of Climate*, **8,** 496-514.

Murphy, J. M., and J. F. B. Mitchell, 1995: Transient Response of the Hadley Centre Coupled Ocean-Atmosphere Model to Increasing Carbon Dioxide. Part II: Spatial and Temporal Structure of Response. *Journal of Climate*, **8,** 57-80.

Murphy, J. M., B. B. B. Booth, M. Collins, G. R. Harris, D. M. H. Sexton, and M. J. Webb, 2007: A methodology for probabilistic predictions of regional climate change from perturbed physics ensembles. *Philosophical Transactions of the Royal Society A: Mathematical, Physical and Engineering Sciences*, **365,** 1993-2028.

Murphy, J. M., D. M. H. Sexton, D. N. Barnett, G. S. Jones, M. J. Webb, M. Collins, and D. A. Stainforth, 2004: Quantification of modelling uncertainties in a large ensemble of climate change simulations. *Nature*, **430,** 768-772.

Nakićenović, N., and R. Swart, 2000: *Special Report on Emissions Scenarios. A Special Report of Working Group III of the Intergovernmental Panel on Climate Change.* Cambridge University Press, Cambridge, United Kingdom, 599 pp.

NAS, 2006: Surface Temperature Reconstructions for the Last 2,000 Years. National Academy of Sciences, National Research Council, National Academies Press, 145 pp.

Pacanowski, R. C., and S. G. H. Philander, 1981: Parameterization of Vertical Mixing in Numerical Models of Tropical Oceans. *Journal of Physical Oceanography*, **11,** 1443-1451.

Palmer, T. N., G. J. Shutts, and R. Swinbank, 1986: Alleviation of a systematic westerly bias in general circulation and numerical weather prediction models through an orographic gravity wave drag parametrization. *Quarterly Journal of the Royal Meteorological Society*, **112,** 1001-1039.

Pan, Z., R. W. Arritt, E. S. Takle, W. J. Gutowski, C. J. Anderson, and M. Segal, 2004: Altered hydrologic feedback in a warming climate introduces a "warming hole". *Geophysical Research Letters*, **31,** L17109.

Paulson, C. A., and J. J. Simpson, 1977: Irradiance Measurements in the Upper Ocean. *Journal of Physical Oceanography*, **7,** 952-956.

Pennell, C., and T. Reichler, 2010: On the Effective Number of Climate Models. *Journal of Climate*, **24,** 2358-2367.

Peterson, T. C., and R. S. Vose, 1997: An Overview of the Global Historical Climatology Network Temperature Database. *Bulletin of the American Meteorological Society*, **78,** 2837-2849.

Piani, C., D. J. Frame, D. A. Stainforth, and M. R. Allen, 2005: Constraints on climate change from a multi-thousand member ensemble of simulations. *Geophysical Research Letters*, **32,** L23825.

Pope, V. D., M. L. Gallani, P. R. Rowntree, and R. A. Stratton, 2000: The impact of new physical parametrizations in the Hadley Centre climate model: HadAM3. *Climate Dynamics*, **16,** 123-146.

Portmann, R. W., S. Solomon, and G. C. Hegerl, 2009: Spatial and seasonal patterns in climate change, temperatures, and precipitation across the United States. *Proceedings of the National Academy of Sciences*, **106,** 7324-7329.

Puma, M. J., and B. I. Cook, 2010: Effects of irrigation on global climate during the 20th century. *Journal of Geophysical Research: Atmospheres*, **115,** D16120.

Racherla, P. N., D. T. Shindell, and G. S. Faluvegi, 2012: The added value to global model projections of climate change by dynamical downscaling: A case study over the continental U.S. using the GISS-ModelE2 and WRF models. *Journal of Geophysical Research: Atmospheres*, **117**.

Randall, D. A., R. A. Wood, S. Bony, R. Colman, T. Fichefet, J. Fyfe, V. Kattsov, A. Pitman, J. Shukla, J. Srinivasan, R. J. Stouffer, A. Sumi, and K. E. Taylor, 2007: Clmate Models and Their Evaluation. In: *Climate Change 2007: The Physical Science Basis. Contribution of Working Group I to the Fourth Assessment Report of the Intergovernmental Panel on Climate Change*. S. Solomon, D. Qin, M. Manning, Z. Chen, M. Marquis, K. B. Averyt, M.Tignor, and H. L. Miller, Eds. Cambridge University Press, Cambridge, United Kingdom and New York, NY, USA, 589-662.

Rayner, N. A., D. E. Parker, E. B. Horton, C. K. Folland, L. V. Alexander, D. P. Rowell, E. C. Kent, and A. Kaplan, 2003: Global analyses of sea surface temperature, sea ice, and night marine air temperature since the late nineteenth century. *Journal of Geophysical Research: Atmospheres*, **108,** 4407.

Redi, M. H., 1982: Oceanic Isopycnal Mixing by Coordinate Rotation. *Journal of Physical Oceanography*, **12,** 1154-1158.

Reichhardt, T., 1999: A million volunteers join the online search for extraterrestrial life. *Nature*, **400,** 804-804.

Reynolds, R. W., N. A. Rayner, T. M. Smith, D. C. Stokes, and W. Wang, 2002: An Improved In Situ and Satellite SST Analysis for Climate. *Journal of Climate*, **15,** 1609-1625.

Robinson, W. A., R. Reudy, and J. E. Hansen, 2002: General circulation model simulations of recent cooling in the east-central United States. *Journal of Geophysical Research: Atmospheres*, **107,** 4748.

Robinson, W. J., 1976: Tree-ring dating and archaeology in the American Southwest. *Tree Ring Bulletin*, **36,** 9-20.

Roether, W., V. M. Roussenov, and R. Well, 1994: A tracer study of the thermohaline circulation of the eastern Mediterranean. . Kluwer Academic Press, 371-394.

Rogers, J. C., 1984: The Association between the North Atlantic Oscillation and the Southern Oscillation in the Northern Hemisphere. *Monthly Weather Review*, **112,** 1999-2015.

Rougier, J., D. M. H. Sexton, J. M. Murphy, and D. Stainforth, 2009: Analyzing the Climate Sensitivity of the HadSM3 Climate Model Using Ensembles from Different but Related Experiments. *Journal of Climate*, **22,** 3540-3557.

Rowlands, D. J., D. J. Frame, D. Ackerley, T. Aina, B. B. B. Booth, C. Christensen, M. Collins, N. Faull, C. E. Forest, B. S. Grandey, E. Gryspeerdt, E. J. Highwood, W. J. Ingram, S. Knight, A. Lopez, N. Massey, F. McNamara, N. Meinshausen, C. Piani, S. M. Rosier, B. M. Sanderson, L. A. Smith, D. A. Stone, M. Thurston, K. Yamazaki, Y. Hiro Yamazaki, and M. R. Allen, 2012: Broad range of 2050 warming from an observationally constrained large climate model ensemble. *Nature Geosci*, **5,** 256-260.

Ruddiman, W. F., 2007: *Earth's Climate: Past and Future.* 2nd ed. W. H. Freeman, New York, 388 pp.

Salzer, M., and K. Kipfmueller, 2005: Reconstructed Temperature And Precipitation On A Millennial Timescale From Tree-Rings In The Southern Colorado Plateau, U.S.A. *Climatic Change*, **70,** 465-487.

Sanderson, B., K. Shell, and W. Ingram, 2010: Climate feedbacks determined using radiative kernels in a multi-thousand member ensemble of AOGCMs. *Climate Dynamics*, **35,** 1219-1236.

Sanderson, B., C. Piani, W. J. Ingram, D. A. Stone, and M. R. Allen, 2008a: Towards constraining climate sensitivity by linear analysis of feedback patterns in thousands of perturbed-physics GCM simulations. *Climate Dynamics*, **30,** 175-190.

Sanderson, B. M., R. Knutti, T. Aina, C. Christensen, N. Faull, D. J. Frame, W. J. Ingram, C. Piani, D. A. Stainforth, D. A. Stone, and M. R. Allen, 2008b: Constraints on Model Response to Greenhouse Gas Forcing and the Role of Subgrid-Scale Processes. *Journal of Climate*, **21,** 2384-2400.

Sato, M., J. E. Hansen, M. P. McCormick, and J. B. Pollack, 1993: Stratospheric aerosol optical depths, 1850–1990. *Journal of Geophysical Research: Atmospheres*, **98,** 22987-22994.

Schneider, E. K., and J. L. Kinter, III, 1994: An examination of internally generated variability in long climate simulations. *Climate Dynamics*, **10,** 181-204.

Schneider, U., A. Becker, P. Finger, A. Meyer-Christoffer, M. Ziese, and B. Rudolf, 2013: GPCC's new land surface precipitation climatology based on quality-controlled in situ data and its role in quantifying the global water cycle. *Theor Appl Climatol***,** 1-26.

Schneider von Deimling, T., H. Held, A. Ganopolski, and S. Rahmstorf, 2006: Climate sensitivity estimated from ensemble simulations of glacial climate. *Climate Dynamics*, **27,** 149-163.

Semtner, A. J., 1976: A Model for the Thermodynamic Growth of Sea Ice in Numerical Investigations of Climate. *Journal of Physical Oceanography*, **6,** 379-389.

Senior, C. A., and J. F. B. Mitchell, 1993: Carbon Dioxide and Climate. The Impact of Cloud Parameterization. *Journal of Climate*, **6,** 393-418.

Sexton, D. H., J. Murphy, M. Collins, and M. Webb, 2012: Multivariate probabilistic projections using imperfect climate models part I: outline of methodology. *Climate Dynamics*, **38,** 2513-2542.

Simmons, A. J., and D. M. Burridge, 1981: An Energy and Angular-Momentum Conserving Vertical Finite-Difference Scheme and Hybrid Vertical Coordinates. *Monthly Weather Review*, **109,** 758-766.

Slingo, A., 1989: A GCM Parameterization for the Shortwave Radiative Properties of Water Clouds. *Journal of the Atmospheric Sciences*, **46,** 1419-1427.

Smith, R., D. Gregory, J. Mitchell, A. Bushell, and C. Wilson, 1998: UM Documentation No. 26: Large Scale Precipitation. Tech. Rep. U.K. Met Office.

Smith, R. N. B., 1990: A scheme for predicting layer clouds and their water content in a general circulation model. *Quarterly Journal of the Royal Meteorological Society*, **116,** 435-460.

——, 1993: Experience and developments with the layer cloud and boundary layer mixing schemes in the UK Meteorological Office Unified Model. *ECMWF/GCSS Workshop on Parametrization of the Cloud-Topped Boundary Layer*, Reading, UK, ECMWF, 319-339.

Smith, T. M., and R. W. Reynolds, 2005: A Global Merged Land–Air–Sea Surface Temperature Reconstruction Based on Historical Observations (1880–1997). *Journal of Climate*, **18,** 2021-2036.

Smith, T. M., R. W. Reynolds, T. C. Peterson, and J. Lawrimore, 2008: Improvements to NOAA's Historical Merged Land–Ocean Surface Temperature Analysis (1880–2006). *Journal of Climate*, **21,** 2283-2296.

Solanki, S. K., and N. A. Krivova, 2003: Can solar variability explain global warming since 1970? *Journal of Geophysical Research: Space Physics*, **108,** 1200.

St. George, S., and E. Nielsen, 2002: Hydroclimatic Change in Southern Manitoba Since A.D. 1409 Inferred from Tree Rings. *Quaternary Research*, **58,** 103-111.

Stahle, D. W., and M. K. Cleaveland, 1992: Reconstruction and Analysis of Spring Rainfall over the Southeastern U.S. for the Past 1000 Years. *Bulletin of the American Meteorological Society*, **73,** 1947-1961.

Stainforth, D. A., J. A. Kettleborough, M. R. Allen, M. Collins, A. Heaps, and J. M. Murphy, 2002: Distributed computing for public interest climate modeling research. *Computing in Science and Engineering*, **4,** 2-9.

Stainforth, D. A., M. R. Allen, D. J. Frame, J. A. Kettleborough, C. M. Christiansen, T. Aina, and M. Collins, 2004: *Climateprediction.net: A Global Community for Research in Climate Physics.* Springer-Verlag London Ltd.

Stainforth, D. A., T. Aina, C. Christensen, M. Collins, N. Faull, D. J. Frame, J. A. Kettleborough, S. Knight, A. Martin, J. M. Murphy, C. Piani, D. Sexton, L. A. Smith, R. A. Spicer, A. J. Thorpe, and M. R. Allen, 2005: Uncertainty in predictions of the climate response to rising levels of greenhouse gases. *Nature*, **433,** 403-406.

Steele, M., J. Zhang, D. Rothrock, and H. Stern, 1997: The force balance of sea ice in a numerical model of the Arctic Ocean. *Journal of Geophysical Research: Oceans*, **102,** 21061-21079.

Stensrud, D. J., 2007: *Parameterization Schemes: Keys to Understanding Numerical Weather Prediction Models.* Cambridge University Press, New York, 459 pp.

Stocker, T., 2011: *Introduction to Climate Modeling.* Springer Berlin Heidelberg, 179 pp.

Stott, P., P. Good, G. Jones, N. Gillett, and E. Hawkins, 2013: The upper end of climate model temperature projections is inconsistent with past warming. *Environmental Research Letters*, **8,** 014024.

Stott, P. A., M. R. Allen, and G. S. Jones, 2003: Estimating signal amplitudes in optimal fingerprinting. Part II: application to general circulation models. *Climate Dynamics*, **21,** 493-500.

Taylor, K. E., R. J. Stouffer, and G. A. Meehl, 2011: An Overview of CMIP5 and the Experiment Design. *Bulletin of the American Meteorological Society*, **93,** 485-498.

Tebaldi, C., and R. Knutti, 2007: The use of the multi-model ensemble in probabilistic climate projections. *Philosophical Transactions of the Royal Society A: Mathematical, Physical and Engineering Sciences*, **365,** 2053-2075.

Tebaldi, C., R. L. Smith, D. Nychka, and L. O. Mearns, 2005: Quantifying Uncertainty in Projections of Regional Climate Change: A Bayesian Approach to the Analysis of Multimodel Ensembles. *Journal of Climate*, **18,** 1524-1540.

Thomas, E., and J. Briner, 2009: Climate of the past millennium inferred from varved proglacial lake sediments on northeast Baffin Island, Arctic Canada. *J Paleolimnol*, **41,** 209-224.

Thrasher, B., J. Xiong, W. Wang, F. Melton, A. Michaelis, and R. Nemani, 2013: Downscaled Climate Projections Suitable for Resource Management. *Eos, Transactions American Geophysical Union*, **94,** 321-323.

Turekian, K. K., 1978: Bioturbation in deep-sea deposits: rates and consequenses. *Oceanus*, **21,** 34-41.

Visbeck, M., J. Marshall, T. Haine, and M. Spall, 1997: Specification of Eddy Transfer Coefficients in Coarse-Resolution Ocean Circulation Models*. *Journal of Physical Oceanography*, **27,** 381-402.

Vose, R. S., D. Arndt, V. F. Banzon, D. R. Easterling, B. Gleason, B. Huang, E. Kearns, J. H. Lawrimore, M. J. Menne, T. C. Peterson, R. W. Reynolds, T. M. Smith, C. N. Williams, and D. B. Wuertz, 2012: NOAA's Merged Land–Ocean Surface Temperature Analysis. *Bulletin of the American Meteorological Society*, **93,** 1677-1685.

Vuuren, D., J. Edmonds, M. Kainuma, K. Riahi, A. Thomson, K. Hibbard, G. Hurtt, T. Kram, V. Krey, J.-F. Lamarque, T. Masui, M. Meinshausen, N. Nakicenovic, S. Smith, and S. Rose, 2011: The representative concentration pathways: an overview. *Climatic Change*, **109,** 5-31.

Webb, M. J., C. A. Senior, D. M. H. Sexton, W. J. Ingram, K. D. Williams, M. A. Ringer, B. J. McAvaney, R. Colman, B. J. Soden, R. Gudgel, T. Knutson, S. Emori, T. Ogura, Y. Tsushima, N. Andronova, B. Li, I. Musat, S. Bony, and K.

E. Taylor, 2006: On the contribution of local feedback mechanisms to the range of climate sensitivity in two GCM ensembles. *Climate Dynamics*, **27,** 17-38.

Weigel, A. P., R. Knutti, M. A. Liniger, and C. Appenzeller, 2010: Risks of Model Weighting in Multimodel Climate Projections. *Journal of Climate*, **23,** 4175-4191.

WMO, 1983: *Guide to Climatological Practices (WMO No. 100).* 2nd ed. World Meteorological Organization, Geneva.

——, 1988: *Technical Regulations.* Vol. 1- General Meteorological Standards and Recommended Practices (WMO-No. 49), World Meteorological Organization, Geneva.

Woodage, M., P. Davison, and D. Roberts, 2003: Aerosol processes (sulphur cycle and soot aerosol scheme) version 2, model version 5.5. Unified Model Doc. Pap. 20, Met Office, Exeter, U.K.

Woodruff, S. D., H. F. Diaz, J. D. Elms, and S. J. Worley, 1998: COADS Release 2 data and metadata enhancements for improvements of marine surface flux fields. *Physics and Chemistry of the Earth*, **23,** 517-526.

Wu, X., 2002: Effects of Ice Microphysics on Tropical Radiative–Convective–Oceanic Quasi-Equilibrium States. *Journal of the Atmospheric Sciences*, **59,** 1885-1897.

Zhang, Y., J. M. Wallace, and D. S. Battisti, 1997: ENSO-like Interdecadal Variability: 1900–93. *Journal of Climate*, **10,** 1004-1020.

APPENDIX A

INFERRED TRANSIENT SIMULATION ENSEMBLE

The 2,106 transients not having a corresponding control with matching atmosphere and ocean parameters and thus not having a known unforced model drift to be removed could potentially still be utilized if a pseudo-match could be established. This subsection briefly describes a possible method for identifying a transient's pseudo or "inferred" control match but then will leave any further analysis for potential future work.

Table A.1 provides a summary of the number of transient simulations having each specific parameter value for both the transients having a matching control with the same atmosphere and ocean parameter settings ("direct" match) and those that do not ("inferred" match). From comparing the number of "direct" and "inferred" simulations in Table A.1 it is clear that all parameter values are represented in the "direct" match simulations and that the relative proportion of simulations for any given value of a parameter is similar for both the "direct" and "inferred" groups, further supporting the use of only "direct" match simulations in this study.

Table A.1: CPDN perturbed parameters and the number of transient simulations having each particular parameter value for the 1,692 transients with a "direct" atmosphere/ocean matching control and for the 2,106 transients with an "inferred" match based on parameter sensitivity to control simulation long-term drift (see Chapter 5, Section 5.7.2). Default parameter values are highlighted in bold.

Parameter	Description	Values	Transient Simulations Direct (Inferred)
ATMOSPHERE			
ALPHAM	Albedo at melting point of ice	**0.5**	**337 (513)**
		0.57	615 (674)
		0.65	740 (921)
ANTHSCA	Scaling factor for anthropogenic sulfates	0.5	354 (398)
		0.8	359 (393)
		1.0	**354 (430)**
		1.2	315 (418)
		1.5	310 (469)
CLOUDTAU	Time a circulating air parcel remains in cloud (s) [x 10^3]	3.6	404 (554)
		10.8	**785 (1042)**
		32.4	503 (512)
CT	Accretion constant (s^{-1}) [x 10^{-4}]	0.5	505 (492)
		1	**540 (702)**
		4	647 (914)
CW_LAND [a]	Precipitation threshold over land (kg m^{-3}) [x 10^{-4}]	1	660 (910)
		2	**536 (735)**
		20	496 (463)
CW_SEA [a]	Precipitation threshold over sea (kg m^{-3}) [x 10^{-5}]	2	660 (910)
		5	**536 (735)**
		50	496 (463)
DTICE	Temperature range of ice albedo variation	2	740 (921)
		5	615 (674)
		10	**337 (513)**
EACF	Empirically adjusted cloud fraction [**]	**0.5**	**689 (1014)**
		0.63	398 (449)
		0.67	605 (645)
ENTCOEF	Entrainment coefficient	0.6	513 (662)
		1.0	553 (536)
		3.0	**526 (686)**
		9.0	100 (224)

a, **b**, **c**, **d** Individual groups of parameters perturbed together

** Parameter values represent mean over 19 model levels (variations occur at each level)

Table A.1: Continued

Parameter	Description	Values	Transient Simulations Direct (Inferred)
I_CNV_ICE_LW [b]	Type of convective cloud ice crystal used in longwave radiation	**1**	**1459 (1723)**
		7	233 (385)
I_CNV_ICE_SW [b]	Type of convective cloud ice crystal used in shortwave radiation	**3**	**1459 (1723)**
		7	233 (385)
I_ST_ICE_LW [b]	Type of stratiform cloud ice crystal used in longwave radiation	**1**	**1459 (1723)**
		7	233 (385)
I_ST_ICE_SW [b]	Type of stratiform cloud ice crystal used in shortwave radiation	**2**	**1459 (1723)**
		7	233 (385)
ICE_SIZE	Ice crystal size (m) [x 10^{-4}]	2.5	543 (827)
		3.0	**660 (746)**
		4.0	489 (535)
L0 [c]	Sulfate mass scavenging parameter L0 (s^{-1}) [x 10^{-5}]	2.17	383 (489)
		6.5	**638 (872)**
		19.5	671 (747)
L1 [c]	Sulfate mass scavenging parameter L1 (s^{-1}) [x 10^{-5}]	0.99	383 (489)
		2.96	**638 (872)**
		8.86	671 (747)
NUM_STAR	Condensation threshold for accumulation [x 10^{6}]	0.1	593 (563)
		1.0	**789 (1061)**
		10	310 (484)
RHCRIT	Critical relative humidity [**]	0.65	690 (751)
		0.73	**504 (813)**
		0.9	498 (544)
SO2_HIGH_LEVEL	Sulfur cycle: model level for SO2 (high level) emissions	1	251 (274)
		3	**1066 (1220)**
		5	375 (614)
VF1	Ice fall speed (m s^{-2})	0.5	398 (626)
		1.0	**662 (783)**
		2.0	632 (699)
VOLSCA	Sulfur cycle: scaling factor for emission from natural (volcanic) emissions	1	939 (990)
		2	**486 (662)**
		3	267 (456)

a, **b**, **c**, **d** Individual groups of parameters perturbed together

** Parameter values represent mean over 19 model levels (variations occur at each level)

Table A.1: Continued

Parameter	Description	Values	Transient Simulations Direct (Inferred)
OCEAN			
HANEY	Haney heat forcing coefficient ($Wm^{-2}K^{-1}$)	**81.88**	**1499 (1902)**
		163.76	193 (206)
HANEYSFACT	Haney salinity forcing factor	**0.25**	**1209 (1421)**
		1.0	483 (687)
ISOPYC	Isopycnal diffusion of tracers (m^2s^{-1}) [x 10^3]	0.2	159 (211)
		1	**1214 (1439)**
		2	319 (458)
MLLAM	Wind mixing energy scaling factor (m^2 s)	0.3	352 (377)
		0.7	**1340 (1731)**
VDIFFDEPTH [d]	Ocean: increase of background vertical mixing of tracer with depth (ms^{-1}) [x 10^{-8}]	0.7	394 (358)
		2.8	**839 (1100)**
		9.6	459 (650)
VDIFFSURF [d]	Ocean: background vertical mixing of tracer (diffusion) at surface (m^2s^{-1}) [x 10^{-5}]	0.5	394 (358)
		1	**839 (1100)**
		2	459 (650)
VERTVISC	Ocean: background vertical mixing of momentum (viscocity) (m^2s^{-1}) [x10^{-5}]	0.5	369 (425)
		1.0	**1323 (1683)**
INITIAL CONDITIONS			
DTHETA	Initial condition potential temperature perturbation applied to atmosphere (°C)	**0**	**195 (208)**
		0.01	163 (210)
		0.02	154 (232)
		0.03	178 (209)
		0.04	161 (205)
		0.05	176 (207)
		0.06	163 (213)
		0.07	153 (203)
		0.08	173 (214)
		0.09	176 (207)

a, **b**, **c**, **d** Individual groups of parameters perturbed together

** Parameter values represent mean over 19 model levels (variations occur at each level)

It may be possible to estimate the model drift to be removed from a transient simulation using knowledge gained from the assessment of model parameter variations having the greatest influence in changes to model drift (see Chapter 5, Section 5.7.2). When matching transient and controls directly, there were a total of 28 atmosphere and ocean parameters needing to be identical. For this set of "inferred" match transient simulations, that total was reduced to the top six parameters from Section 5.7.2 whose variations were found to be the most influential in changes to long-term mean drift in control simulations (see Table 5.11)[22]. These six parameters had a correlation magnitude greater than or equal to (≥) 0.2 between their variations and long-term mean drift in temperature and/or precipitation.

This requirement allowed all 2,106 "inferred" transients to have at least one control with the same value across all six of those parameters. These transients were comprised of 152 atmospheres and ten oceans with 796 unique atmosphere/ocean combinations. Increasing the number of required matching parameters decreased the number of transients-control matches (see Table A.2) while decreasing the number of parameters increased the uncertainty range in drift values covered by the matching controls (Figure A.1). Figure A.1 illustrates the increased uncertainty when varying the number of parameters requiring a match (i.e., varying the required correlation threshold). In that figure the long-term mean drift in global temperature for all control simulations is given as the black distribution at the bottom. (Only global results are given and discussed because regional characteristics are all similar.) This distribution was not centered upon zero and therefore the bias was subtracted off in order to better

[22] There are actually seven parameters that must match but VDIFFDEPTH and VDIFFSURF vary together and therefore can be considered a single parameter.

compare the range in these drift value magnitudes to the other distributions shown in Figure A.1 which are anomaly values. These anomaly distributions correspond with the "direct" (blue) and "inferred" (red) transient-control matching cases and represent anomalies from the average long-term mean drift within each set of control simulations that match a single transient simulation. For example, a transient simulation may have five matching control simulations. The long-term mean drift was calculated for all five simulations and then averaged together to create a single estimate used as the official drift value removed from the matching transient simulation. An anomaly value, from that average control drift value, was then calculated for each of the five control simulations (i.e., actual drift of the control simulation minus the average value of all five). This was done for all control sets that match an individual transient and then all these anomalies were combined into a single anomaly distribution. That anomaly distribution is what is shown in Figure A.1.

Table A.2: Model parameter matching information for matching all atmosphere and ocean parameters ("Direct") and multiple options for matching a reduced number of parameters ("Inferred"). The number of parameters matched, number of transient-control matches, and average number of controls matching a single transient are given. The "Inferred" match options originate from the parameter sensitivity analysis for control long-term mean drift in Chapter 5 (Section 5.7.2).

	"Direct" Matches	**"Inferred" Matches (Correlation magnitude ≥)**								
		0.1	**…**	**0.125**	**0.15**	**0.175**	**…**	**0.2**	**0.3**	**0.4**
Number of Parameters	28	13	…	9	6	6	…	6	5	2
Number of Matches	1692	626	…	1827	2106	2106	…	2106	2106	2106
Average # Controls per Match	2	3	…	9	54	54	…	54	60	462

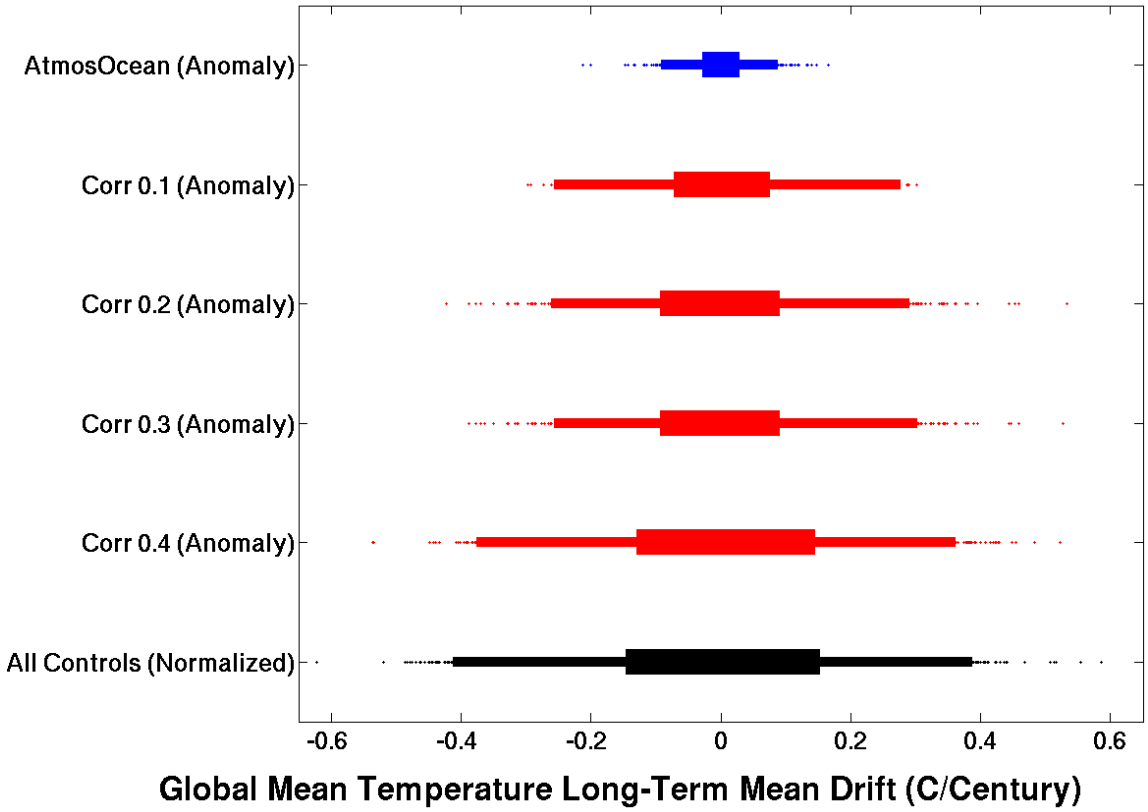


Figure A.1: Comparison of normalized (i.e., mean of distribution subtracted off) long-term mean drift in global mean temperature for all control simulations (black bottom distribution) to anomalies from the average long-term mean drift for each set of control simulations matching one of the transient simulations in the "direct" match cases (top blue distribution) and for four different correlation threshold examples in the "inferred" match cases (four middle red distributions). All distributions are in units of (°C/Century).

The main takeaway point from Figure A.1 is that when a large number of parameters are used to match transients and controls, the long-term mean drift differences found in the control simulation matching sets are smaller (e.g., all 28 atmosphere/ocean parameters from the "direct" match cases shown as the blue distribution at top) than if a smaller number of parameters are used to match (e.g., 2 parameters from correlation magnitude ≥ 0.4 from the "inferred" match cases shown as the bottom red distribution) when comparing against the full range of actual long-term mean drift values (black distribution at bottom). The figure, along with the information

given in Table A.2, also show us that using six parameters (i.e., correlation magnitude ≥ 0.2) to match transients and controls is the most useful threshold to use. Using more than six parameters (i.e., correlation magnitude ≥ 0.1 or 0.125) decreases the number of total transient-control matches available (Table A.2) while using less parameters increases the average number of controls used to estimate the long-term mean drift to be removed from each matching transient (Table A.2) which increases the uncertainty in the control drift values removed from the matched transients. Additionally, there are only minimal anomaly distribution differences between correlation magnitude thresholds of 0.2 and 0.1 which mean the uncertainty in drift removed does not change that much when using fewer parameters. The uncertainty range, however, is still significantly larger than matching all atmosphere and ocean parameters (i.e., "direct" matches shown in blue at top of Figure A.1) which is why we have decided to investigate only the "direct" match group in this study.

As a consequence, there are 15 atmospheres and 796 unique atmosphere/ocean combinations in the "inferred" match group that are not in the "direct" match group and therefore not available for analysis. But as already discussed and shown in Table A.1, all individual parameters are still represented and the relative proportion of parameter value variations remain consistent with the original full set of transient simulations. Future studies may explore this alternative "inferred" match group of transients and compare the results to the current study.